ASME
SETTING THE STANDARD

Transactions of the ASME, Journal of Fluids Engineering (ISSN 0098-2202) is published monthly by The American Society of Mechanical Engineers, Three Park Avenue, New York, NY 10016. Periodicals postage paid at New York, NY and additional mailing offices.
POSTMASTER: Send address changes to Transactions of the ASME, Journal of Fluids Engineering, c/o THE AMERICAN SOCIETY OF MECHANICAL ENGINEERS, 22 Law Drive, Box 2300, Fairfield, NJ 07007-2300.
CHANGES OF ADDRESS must be received at Society headquarters seven weeks before they are to be effective. Please send old label and new address.
STATEMENT from By-Laws. The Society shall not be responsible for statements or opinions advanced in papers or ... printed in its publications (B7.1, Par. 3).

Journal of Fluids Engineering

Published Monthly by ASME

VOLUME 130 • NUMBER 12 • DECEMBER 2008

RESEARCH PAPERS

Flows in Complex Systems

121101 Hydrodynamic Characterization of a Nozzle Check Valve by Numerical Simulation
Stefano Sibilla and Mario Gallati

121102 The Impact of Manifold-to-Orifice Turning Angle on Sharp-Edge Orifice Flow Characteristics in Both Cavitation and Noncavitation Turbulent Flow Regimes
W. H. Nurick, T. Ohanian, D. G. Talley, and P. A. Strakey

121103 Numerically Investigating the Effects of Cross-Links in Scaled Microchannel Heat Sinks
Minh Dang, Ibrahim Hassan, and Sung In Kim

121104 Hydraulic Circuit Design Rules to Remove the Dependence of the Injected Fuel Amount on Dwell Time in Multijet CR Systems
Mirko Baratta, Andrea Emilio Catania, and Alessandro Ferrari

121105 Instabilities of Nonreturn Valves in Low-Speed Air Systems
Mark Potter, Marko Bacic, Phil Ligrani, and Matthew Plackett

121106 Experimental Study on the Amplitude of a Free Surface Fluctuation
Ho-Yun Nam, Byoung-Hae Choi, Jong-Man Kim, and Byung-Ho Kim

Fundamental Issues and Canonical Flows

121201 Computational Dynamics of a Thermally Decomposable Viscoelastic Lubricant Under Shear
T. Chinyoka

Multiphase Flows

121301 Experiments and Models of the Magneto Rheological Behavior of High Weight Percent Suspensions of Carbonyl Iron Particles in Silicone Oil
Farzad Ahmadkhanlou, Monon Mahboob, Stephen Bechtel, and Gregory Washington

Techniques and Procedures

121401 A Three-Equation Eddy-Viscosity Model for Reynolds-Averaged Navier–Stokes Simulations of Transitional Flow
D. Keith Walters and Davor Cokljat

121402 Instantaneous Liquid Flow Rate Measurement Utilizing the Dynamics of Laminar Pipe Flow
Bernhard Manhartsgruber

121403 Grid Independence Via Automated Unstructured Adaptation
Ronald J. Chila and Deborah A. Kaminski

(Contents continued on inside back cover)

This journal is printed on acid-free paper, which exceeds the ANSI Z39.48-1992 specification for permanence of paper and library materials. ♾™
♻ 85% recycled content, including 10% post-consumer fibers.

(**Contents continued**)

Journal of Fluids Engineering **Volume 130, Number 12** **DECEMBER 2008**

TECHNICAL BRIEFS

124501 The Influence of Slip Boundary Conditions on Peristaltic Pumping in a Rectangular Channel
X. Mandviwalla and R. Archer

i Author Index

The ASME Journal of Fluids Engineering is abstracted and indexed in the following:

Applied Science & Technology Index, Chemical Abstracts, Chemical Engineering and Biotechnology Abstracts (Electronic equivalent of Process and Chemical Engineering), Civil Engineering Abstracts, Computer & Information Systems Abstracts, Corrosion Abstracts, Current Contents, Ei EncompassLit, Electronics & Communications Abstracts, Engineered Materials Abstracts, Engineering Index, Environmental Engineering Abstracts, Environmental Science and Pollution Management, Excerpta Medica, Fluidex, Index to Scientific Reviews, INSPEC, International Building Services Abstracts, Mechanical & Transportation Engineering Abstracts, Mechanical Engineering Abstracts, METADEX (The electronic equivalent of Metals Abstracts and Alloys Index), Petroleum Abstracts, Process and Chemical Engineering, Referativnyi Zhurnal, Science Citation Index, SciSearch (The electronic equivalent of Science Citation Index), Shock and Vibration Digest, Solid State and Superconductivity Abstracts, Theoretical Chemical Engineering

Hydrodynamic Characterization of a Nozzle Check Valve by Numerical Simulation

Stefano Sibilla[1]
e-mail: stefano.sibilla@unipv.it

Mario Gallati

Dipartimento di Ingegneria Idraulica
e Ambientale,
Università di Pavia,
via Ferrata 1,
27100 Pavia, Italy

The ability to obtain correct estimates of the hydraulic characteristics of a nozzle check valve by finite-volume numerical simulation is discussed. The evaluation of the numerical results is performed by comparison of the computed pressure drops inside the valve with experimental measurements obtained on an industrial check valve. It is shown that, even with high mesh refinement, the obtained result is highly dependent on the choice of the turbulence model. The renormalization group theory (RNG) k-ε model proves to be the more accurate to describe the flow inside the valve, which is characterized by repeated flow decelerations and accelerations and by boundary layer development under adverse pressure gradient. Pressure-drop and flow coefficients computed by adopting the RNG model agree well with the experimental values at different positions of the plug. The opening transient of the valve is also analyzed by an unsteady flow simulation where the motion of the plug is taken into account. The characteristic curve of the valve obtained in steady flow conditions is finally compared with the transient opening characteristic, highlighting a temporary increase in the pressure drop, which occurs because of a large unsteady separation region downstream of the plug. [DOI: 10.1115/1.3001065]

1 Introduction

Check valves allow fluid flow in one direction only by use of a moving plug (either a disk, a wedge, or a plate), which opens when forward flow starts in the pipeline. When pressure drops, due to gravity, back pressure, or a mechanical spring force, the moving element moves back to its seal to prevent reversal of flow (backflow). Check valves are largely employed in industrial hydraulic systems and are classified according to the different types and geometries of plugs.

Swing check valves have a disk-shaped plug hinged on its edge, which closes due to the backflow. They are usually employed in pumping stations, and the overpressure generated by the slam of the plug against the valve body has been the subject of experimental measurement and modeling [1,2]. Numerical simulations of the flow in a swing check valve have shown that (1) the hydraulic characteristics such as pressure drop and hydraulic torque on the plug cannot be estimated by assuming successive quasi-steady flow conditions, and (2) the pressure distribution associated with the angular acceleration of the plug cannot be neglected due to water hammer effects [3].

Dual plate (wafer) check valves have a two-piece disk hinged down the diameter of the pipe. The forward flow pushes the disk into the open position while a spring pushes it back to prevent backflow. Experiments show that a careful design of the valve body and of the plate can reduce pressure surges. The pressure drop during normal operation is slightly higher than that generated by swing valves because of the presence of the plate across the main flow [4].

Nozzle check valves designed to operate in large-diameter pipelines consist of a hydrodynamically shaped flow contraction and an annulus-shaped plug. The position of the plug is regulated by three to six springs. These valves usually provide lower pressure surges during shutting off compared with swing and dual plate check valves [5,6], although they introduce higher pressure drops in normal flow conditions.

In fact, the flow around the valve body is partitioned by the plug and the spring housing into two annular channels whose cross section increases in the downstream direction. The hydrodynamic design of the body and the annular channel shapes is essential to minimize the pressure drop across the valve or to maximize the flow coefficient C_v at design conditions with the valve fully open.

Several computational fluid dynamics (CFD) analyses [7–13] in the prediction of incompressible and compressible flows inside different kinds of valves have been performed in recent years. Many of these analyses have focused on the ability of different turbulence models to correctly reproduce the features of the complex flows.

Stevenson and Chen [7] studied the flow in a high-pressure homogenizing valve for dairy industry applications. They modeled the axisymmetric flow in the plug-seat region by a finite-volume approach with the standard k-ε turbulence model by Launder and Spalding [14]. The results obtained by varying the valve gaps between 10^{-3} and 10^{-4} times the valve diameter show good agreement between measured and computed head losses. The results show, however, that with such reduced gap dimensions the pressure drop only occurs in the laminar flow in the gap and the effects of the turbulent jet downstream the valve gap appear to be negligible.

Agaphonov et al. [8] and Badur et al. [9] studied the three-dimensional flow inside steam-turbine control valves using finite-volume Navier–Stokes solvers for compressible gas flows. Agaphonov et al. adopted the standard high-Re model [14] and found that the predicted levels of turbulent kinetic energy in the contraction region were too high. They therefore introduced a simple limitation of the eddy viscosity by allowing a maximum turbulent kinetic energy level in the plug region equal to the maximum level in the inlet pipe. The predicted pressure drops across the valve were in good agreement with measured data, even for an axisymmetric assumption of the valve. Morita et al. [10] performed large eddy simulations in a steam control valve to produce flow fluctuations, which induce vibrations in the valve.

Davis and Stewart [11] performed finite-volume numerical

[1]Corresponding author.

Contributed by the Fluids Engineering Division of ASME for publication in the JOURNAL OF FLUIDS ENGINEERING. Manuscript received July 28, 2006; final manuscript received March 14, 2008; published online October 23, 2008. Assoc. Editor: Yu-Tai Lee.

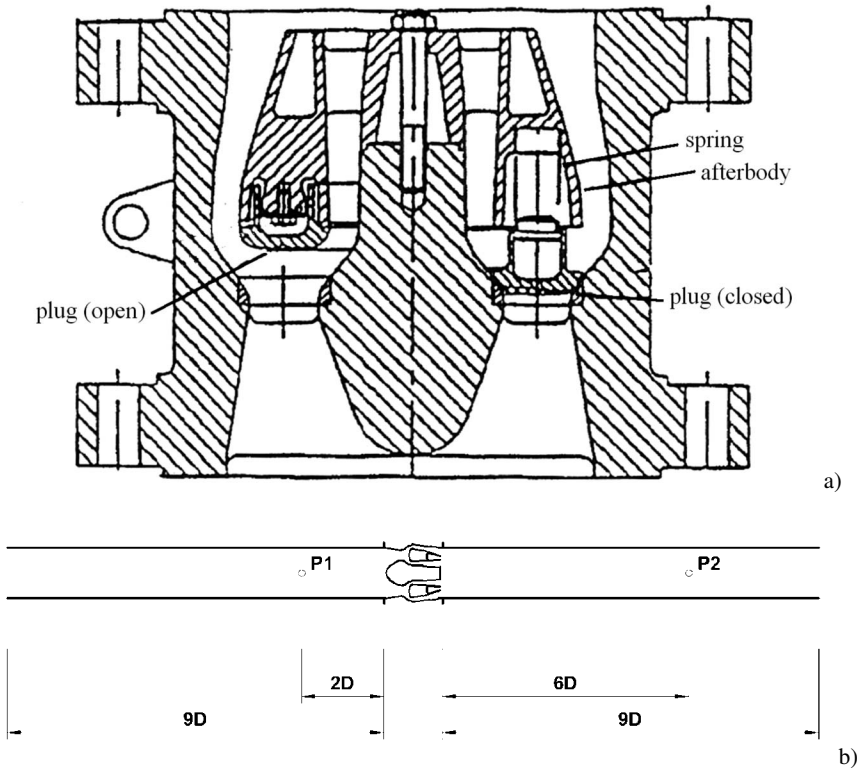

Fig. 1 Experimental setup: (*a*) nozzle check valve geometry; (*b*) sketch of the test section with upstream and downstream pressure probes P1 and P2

simulations of an axisymmetric flow in the plug-seat region of different globe control valves and validated their results with proper experiments [12]. Their results show clear descriptions of flow separation and recirculation regions at different valve openings. The predicted valve characteristic (i.e., the law relating the flow coefficient C_v to the valve opening) was well produced by numerical simulations, except at fully open conditions. No major differences between the different turbulence models were found.

The use of CFD codes to compute torque and forces on a 2D model of a butterfly valve disk was performed by Leutwyler and Dalton [13]. Although differences were noted between the predicted pressure profiles on the disk wall by various turbulence models, numerical results yielded satisfactory predictions of the total forces on the disk.

No detailed analysis has been performed using CFD to predict the flow inside a nozzle check valve. This flow, characterized by repeated flow decelerations and accelerations, poses specific challenges to flow simulation. This paper is aimed at verifying the capability and limitations of numerical flow simulations in predicting the hydraulic performance of a nozzle check valve. As discussed above, one of the main issues about numerical simulation concerns the accuracy in estimating the pressure drop in a fully open valve condition during the normal operation of a check valve. The accuracy appears to be related to the adequacy of the turbulence model.

Numerical simulations of the flow in a commercial nozzle check valve have been performed. The fully open valve configuration has been assumed to be the most critical case for pressure-drop prediction. It has been adopted as a reference case for the evaluation of different k-ε turbulence models by comparing measured and computed pressure-drop values. Flow field details have been studied for the best obtained solution.

The hydraulic characteristics of the valve at different plug positions have been predicted numerically and compared with the steady-state hydraulic characteristics measured during experiments. A dynamic simulation of the unsteady flow during a simplified opening transient has also been performed. The simulations highlighted the presence of unsteady flow separations, resulting in a departure of the characteristic curve of the valve from that obtained in quasisteady conditions.

2 Description of the Reference Experiments

The present analysis has been performed on a commercial nozzle check valve (Mannesmann Demag DRV-B) with a nominal diameter of 600 mm (Fig. 1(*a*)). The position of the plug is regulated by three springs, housed in a tapered afterbody behind the plug itself. The discrete model of the geometry has been produced from design drawings and has been limited to an axisymmetric schematization of the valve. The details of the supports of the inner body and of the plug springs have not been modeled.

Numerical results have been compared with the hydraulic characteristics in valve flow and head loss coefficients at maximum opening obtained during closed-loop experiments [15]. These measurements were obtained in steady-state conditions, by a gradual increase in the flow rate at each pressure loss evaluation. Upstream and downstream pressures were measured by piezoelectric pressure transducers, with an overall accuracy of $\pm 0.25\%$ of the measured value. The transducers were located 1.2 m upstream of the inlet section and 3.6 m downstream of the outlet section of the valve, respectively (Fig. 1(*b*)). The flow rate was measured in the feeding pipe by an electromagnetic flow-meter with an accuracy of $\pm 1\%$ of the full scale value.

3 Flow Simulation Method

3.1 Numerical Solution. The simulation of the fluid flow inside the valve has been obtained by use of STAR-CD code [16]. The code solves the three-dimensional Navier–Stokes equations, discretized by a finite-volume second order upwind-differencing scheme. Higher-order schemes have also been tested, as discussed

Table 1 k-ε model parameters

Model	C_μ	σ_k	σ_ε	$C_{\varepsilon 1}$	$C_{\varepsilon 2}$	$C_{\varepsilon 3}$	η_0	β
Standard	0.09	1.0	1.22	1.44	1.92	-	-	-
Chen	0.09	0.75	1.15	1.15	1.9	0.25	-	-
RNG	0.085	0.719	0.719	1.42	1.68	-	4.38	0.012

in Sec. 5.

Steady-state solutions have been obtained iteratively by the use of the predictor-corrector semi-implicit pressure linked equations (SIMPLE) algorithm [17]. Time integration for unsteady flow simulations has been obtained by the implicit predictor-corrector pressure implicit splitting of operators (PISO) algorithm [18].

3.2 Turbulence Models. Different versions of the k-ε turbulence models have been tested during this study. The values of the coefficients of the different models are given in Table 1.

Standard k-ε model. The equation for the turbulent kinetic energy k was obtained by modeling the terms of production, diffusion, and dissipation as follows:

$$\frac{D}{Dt}(\rho k) = P + \frac{\partial}{\partial x_j}\left[\left(\mu + \frac{\mu_T}{\sigma_k}\right)\frac{\partial k}{\partial x_j}\right] - \rho\varepsilon \tag{1}$$

where ρ is the density, μ is the dynamic viscosity,

$$P = 2\mu_T\left(\frac{\partial u_i}{\partial x_j} + \frac{\partial u_j}{\partial x_i}\right)\frac{\partial u_i}{\partial x_j} \tag{2}$$

is the production rate of turbulent kinetic energy from the mean flow velocity gradient, μ_T is the dynamic eddy viscosity, σ_k is the turbulent Prandtl number, and ε is the dissipation rate of the turbulent kinetic energy.

The closure of the model was obtained by using the equation for the turbulent dissipation rate ε as follows:

$$\frac{D}{Dt}(\rho\varepsilon) = C_{\varepsilon 1}\frac{\varepsilon}{k}P + \frac{\partial}{\partial x_j}\left[\left(\mu + \frac{\mu_T}{\sigma_\varepsilon}\right)\frac{\partial \varepsilon}{\partial x_j}\right] - C_{\varepsilon 2}\rho\frac{\varepsilon^2}{k} \tag{3}$$

Here σ_ε is the dissipation Prandtl number, and $C_{\varepsilon 1}$ and $C_{\varepsilon 2}$ are empirical coefficients. Dynamic eddy viscosity is then obtained by dimensional considerations

$$\mu_T = \frac{C_\mu \rho k^2}{\varepsilon} \tag{4}$$

where C_μ is also an empirical coefficient.

RNG k-ε model. Yakhot et al. [19] applied concepts based on the renormalization group theory to turbulence and derived a RNG k-ε model. An additional term $\Re$ is added to the right-hand side of the dissipation equation (3) to account for the effects of rapid strain of vortex structures in locally anisotropic turbulent flows. The additional term is modeled as

$$\Re = -\frac{C_\mu \eta^3(1 - \eta/\eta_0)}{1 + \beta\eta^3}\frac{\rho\varepsilon^2}{k} \tag{5}$$

and is a function of the empirical coefficients C_μ, η_0, and β and of a nondimensional rate-of-strain

$$\eta = \frac{k}{\varepsilon}\sqrt{2\left(\frac{\partial u_i}{\partial x_j} + \frac{\partial u_j}{\partial x_i}\right)\left(\frac{\partial u_i}{\partial x_j} + \frac{\partial u_j}{\partial x_i}\right)} \tag{6}$$

based on the turbulent time scale k/ε.

Chen k-ε model. Chen and Kim [20] developed an alternative k-ε model where an additional production term

$$\Re = C_{\varepsilon 3}\frac{\mu_T^2}{\rho}\frac{P^2}{k} \tag{7}$$

in the ε equation represents the effect of energy transfer from large-scale to small-scale turbulence. This transfer is controlled by the production-range time scale k/P. The standard production term in Eq. (3) is modified by reducing the value of $C_{\varepsilon 1}$.

3.3 Computational Mesh. The volume inside the nozzle check valve and the spring housing has been discretized into an unstructured mesh with hexahedral cells. A single cell layer has been produced in the circumferential direction because of the axial symmetry of the analyzed geometry. Symmetry conditions have been adopted on the boundary meridian planes.

The mesh was refined in the regions where high-pressure gradients or strong shear flows were expected, i.e., in front of the valve body and the plug, in the gap between the plug and the spring housing, in the boundary layer, and in the wake regions.

Different grid refinement levels were tested. The number of needed cells ranged between 16,000 and 45,000. A detail of the coarsest and the finest meshes in the fully open valve configuration is shown in Fig. 2. Further discussion on grid independence is given in Sec. 5.

Unsteady flow simulations involved also the movement of boundaries (the plug walls). The computational mesh was created by moving the internal mesh nodes. Node movement was handled by an arbitrary Lagrangian–Eulerian (ALE) formulation [21,22]. An ALE method allows arbitrary motion of mesh points with respect to their frame of reference by taking the convection of these points explicitly into account in the solution of the equations of motion. The velocity and position of each mesh node are assigned at each time step according to the moving boundary position and requiring a uniform distribution of the cell sizes in the direction of the boundary movement. New cell layers near the moving boundary (i.e., near the plug surface) are generated or removed at given intervals to avoid excessive distortion of the mesh cells.

3.4 Boundary Conditions. All the simulations have been performed with the following boundary conditions:

(1) uniform velocity at the initial section of the inlet pipe
(2) inlet values of k and ε assigned according to a 10% turbulence intensity level
(3) zero pressure at the outlet
(4) zero axial gradient of k and ε at the outlet
(5) no-slip conditions at the solid walls, and wall velocity profile assigned according to the logarithmic law on smooth walls

$$\frac{u}{u_*} = \frac{1}{\kappa}\ln\frac{\rho y u_*}{\mu} + C \tag{8}$$

where u is the flow velocity at a distance y from the wall, $\kappa = 0.4$ is the von Kàrmàn constant, $C = 5.5$, $u_* = \sqrt{\tau_w/\rho}$ is the friction velocity, and τ_w is the wall stress; $y^+ = y u_*/\nu$ has been adjusted between 80 and 100.

Different choices for the inflow boundary condition have been tested on the simulation of the fully open valve configuration with the RNG turbulence model. Axial velocity profiles at the inlet have been assigned according to 1/7 power or to a logarithmic law. Figure 3 shows that, in the throat section upstream of the plug, the computed velocities differ only slightly from those computed by assuming a uniform inflow profile. The difference in the computed flow coefficient amounts to 3.1% in the case of a logarithmic velocity profile. Since the exact inlet velocity profile from the experiments is unknown, it is considered reasonable to perform all of the following calculations with the uniform inflow velocity.

4 Hydraulic Characteristics of the Valve

The hydraulic behavior of the valve in operational conditions is characterized by the local pressure drop introduced by the valve itself. This pressure drop is made nondimensional by the mean dynamic pressure in the pipeline, leading to the definition of a pressure-drop coefficient

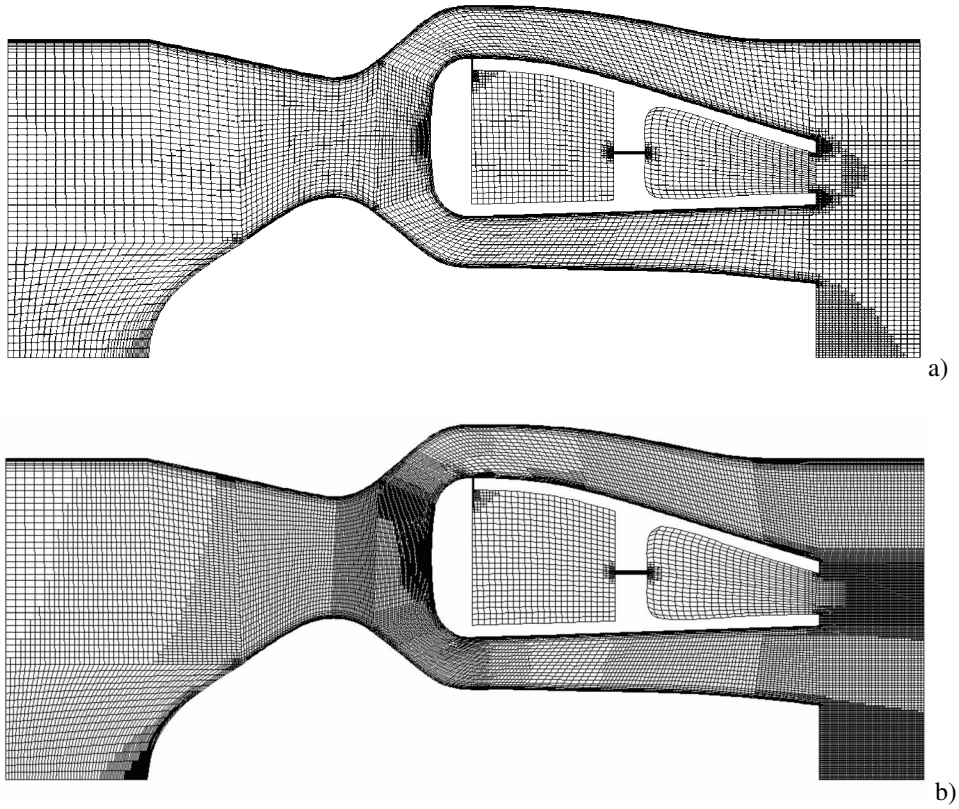

Fig. 2 Computational mesh, full valve opening: coarse mesh (*a*) and fine mesh (*b*)

$$\alpha = \frac{2\Delta p}{\rho V^2} \tag{9}$$

where Δp is the pressure drop between an upstream and a downstream section of the flow where uniform flow conditions can be assumed. V is here the mean velocity in the pipe. However, valve manufacturers usually evaluate hydraulic characteristics by a dimensional flow coefficient

$$C_v = \frac{Q}{\sqrt{\Delta p}} \tag{10}$$

where the flow rate is expressed in US gpm and the pressure drop in psi.

In control valves, where the plug travel is imposed, a characteristic curve expressing C_v as function of the valve travel can be defined; for check valves, where the travel is a function of the flow rate and is usually an unknown for the valve characterization, it seems more convenient to define a characteristic curve C_v versus Q.

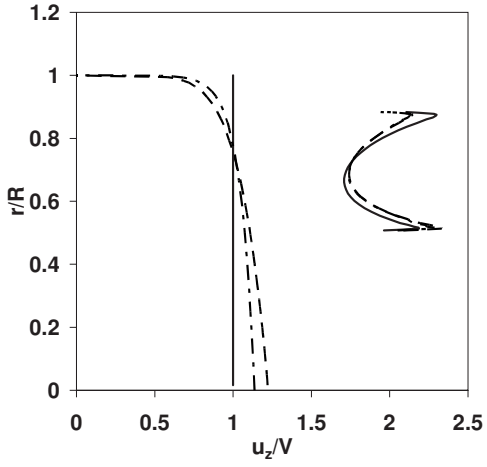

Fig. 3 Effect of the inflow boundary condition: axial velocity profiles at the inlet (left) and in the throat section upstream of the plug (right). Uniform flow (solid), 1/7 power profile (dashed); logarithmic profile (dash-dot).

5 Choice of the Turbulence Model

The pressure drop in the fully open valve configuration is the relevant engineering parameter to qualify the hydrodynamic design of the valve. The choice of the "best" turbulence model has been therefore performed by comparing measured α values with those computed by the k-ε turbulence models described in Sec. 3.2. These models must correctly represent all the principal flow features: The turbulent boundary layers around the spring housing and the valve body develop under adverse pressure gradient; the shape and extension of the turbulent wakes determine the base drag of the valve.

The grid independence of the numerical simulations has been first checked. Figure 4 shows that solutions obtained from coarse meshes lead, in general, to an underestimation of the pressure drop in comparison with the solutions obtained from finer meshes. On the other hand, the solutions on the two finest meshes differ only slightly, allowing us to assume that the finest mesh is adequate for the present study.

The influence of the differencing schemes for the convective terms in the equations of motion has also been tested. A second order upwind scheme, which adopts a linear interpolation for the

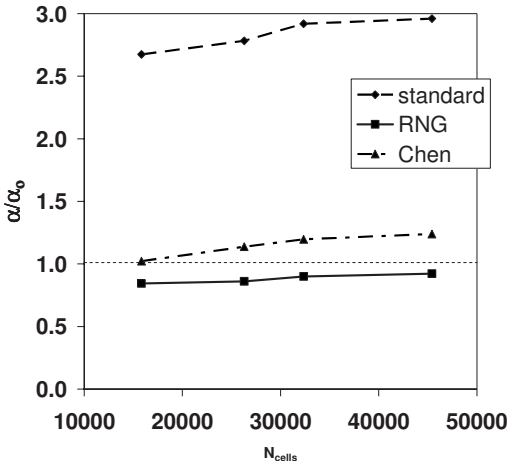

Fig. 4 Dependency of the valve pressure-drop coefficient on the turbulence model and on the mesh refinement

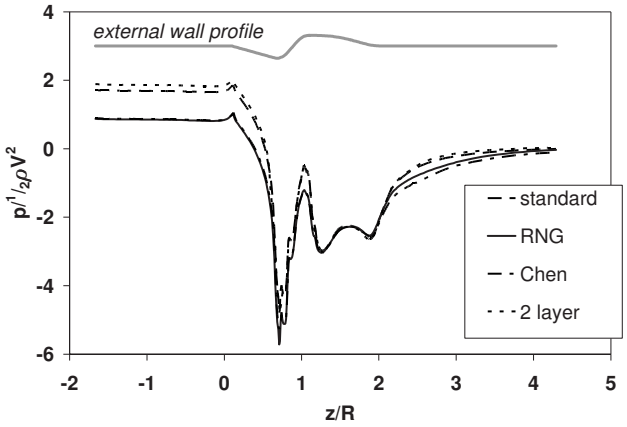

Fig. 6 Pressure profile along the external valve wall: comparison between different *k*-ε turbulence models

evaluation of convective fluxes on the mesh cell faces, has been compared with the higher-order QUICK scheme, which adopts quadratic interpolation formulas for flux evaluation. The two schemes yielded almost the same results and the second order upwind scheme has been used for the rest of the calculations.

The pressure-drop coefficient α and the flow coefficient C_v computed on the finest mesh have been compared with the values α_o and C_{vo} obtained from Ref. [15] at the critical flow rate Q_o, i.e., the minimal flow rate sufficient to guarantee fully open conditions. Table 2 shows that the standard and Chen's k-ε models tend to overestimate α, while the RNG model prediction is only slightly lower than the experimental value.

Table 2 Pressure-drop and flow coefficients in the fully open valve configuration, computed with different *k*-ε models

Model	α/α_o	C_v/C_{vo}
Standard	2.96	0.58
RNG	0.92	1.04
Chen	1.24	0.90

An explanation to the failure of the standard k-ε model can be found by observing the high levels of turbulent kinetic energy predicted close to the stagnation point on the plug (Fig. 5(*a*)). A further growth of k is computed downstream of the stagnation point, when a reduction of turbulence intensity should occur due to flow acceleration. Both the RNG (Fig. 5(*b*)) and Chen's (not shown) models predict high levels of turbulent energy only in the boundary layers under adverse pressure gradient and in the wakes. The comparison of the pressure fields inside the valve (Fig. 6) shows that downstream of the plug the standard k-ε model predicts a negative pressure gradient with a steeper slope than that predicted by the RNG model. The higher pressure drop appears to be a direct consequence of the dissipation introduced by the higher turbulence intensity.

It is well known that the standard high Reynolds number k-ε model overestimates the turbulent energy production rate in the near-wall region, and that large errors in the evaluation of k can arise in regions of large strain such as those occurring downstream of the stagnation point on the plug. Two-layer formulations with finer near-wall discretizations and damping functions are usually adopted to avoid these errors. Here, a Norris and Reynolds [23] algebraic dissipation function has been coupled in the near-wall region to the standard k-ε model in a simulation performed on a

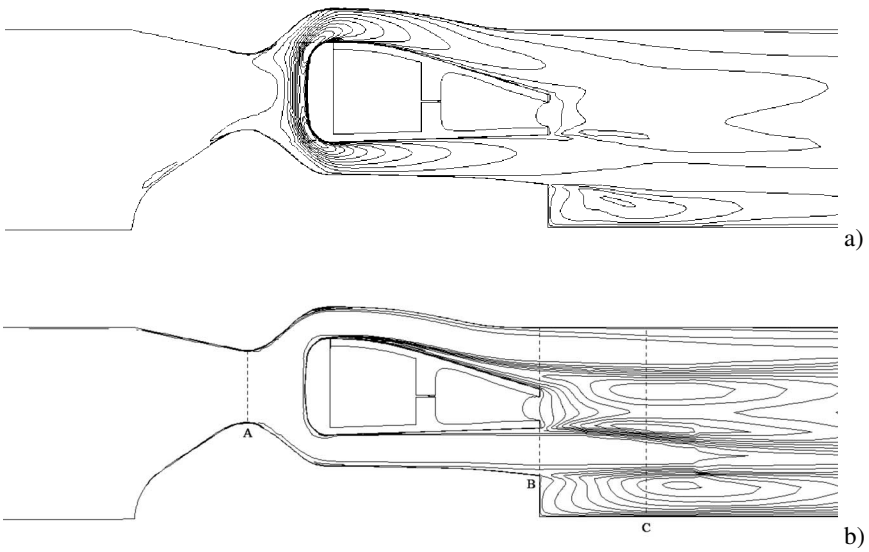

Fig. 5 Turbulent kinetic energy field. Simulation with (*a*) standard and (*b*) RNG *k*-ε models. Isolines range (*a*) from 0 to 0.36V^2, step 0.03V^2; (b) from 0 to 0.12V^2, step 0.01V^2.

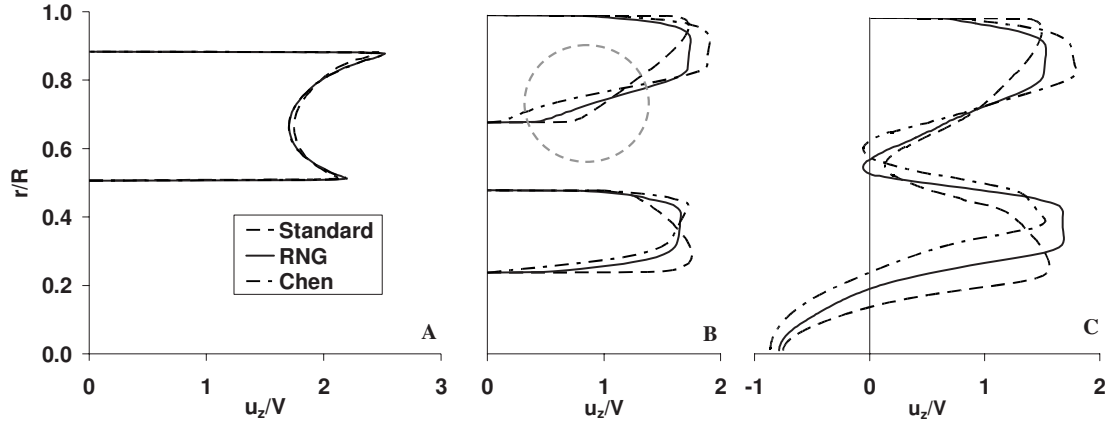

Fig. 7 Axial velocity profiles of three sections shown by dashed lines in Fig. 5(*b*): simulation with different *k*-ε turbulence models

refined mesh of 61,000 cells and $y^+ \approx 2$. However, the results show the same turbulent kinetic energy distributions and even higher pressure drops across the valve (Fig. 6). Far better results have been obtained by the RNG model, which avoids excessive production of k by reducing the destruction rate of ε in the high rate-of-strain regions, and by Chen's model, which increases the production rate of ε in the regions of high P. The result obtained with the RNG model appears, in particular, to be the closest one to the measured value. This result, which underestimates the experimental α by 8%, can be considered a reasonable approximation of the experimental value. In fact, the axisymmetric schematization of the valve adopted in the numerical simulation neglects the additional drag introduced by the streamlined bearings of the plug-spring housing and of the inner body of the valve. The RNG model has been therefore considered the most reliable one and has been adopted in the following.

A possible explanation of the differences between RNG and Chen's turbulence models can be envisaged in the different predictions of boundary layer thickening along the annular channels downstream of the plug. Axial velocity profiles in three sections (shown in Fig. 5(*b*)) of the valve are compared in Fig. 7. The influence of the different turbulence models is negligible in the throat section upstream of the plug (section A). Downstream of the plug, the high turbulence intensity predicted by the standard *k*-ε model leads to steep velocity gradients in the boundary layers along the walls of the annular channels (section B). The peak of the velocity profile is shifted toward the outer walls, eventually leading to the prediction of a wider wake (section C). The prediction of such a wide wake accounts for the large overestimate of the valve drag, which depends on the pressure on the downstream surface of the valve and hence on the shape and width of the wake itself.

Chen's and RNG models seem to better reproduce the velocity profile expected for the retarded flow in the boundary layers and for the wake. However, it can be noted that the effects of the adverse pressure gradient are enhanced by Chen's model in the inner boundary layer of the outer channel (circled area). This leads to a thicker boundary layer with higher turbulent intensities (Fig. 8), which causes the higher drag predicted by Chen's model.

6 Flow Details in the Open Valve

The numerical solution obtained using the RNG model shows that the turbulent flow in the pipe initially undergoes a favorable pressure gradient (Fig. 9(*a*)) while approaching the stagnation point on the inner valve body. An expansion around the inner valve body leads to an acceleration of the flow followed by a second stagnation region on the plug. Turbulence intensities are here very low.

The flow accelerates around the plug after the second stagnation point and enters the annular channels around the spring housing at maximum velocity (Fig. 9(*b*)). Pressure is minimum around the curved edges of the plug. The correct prediction of this value is essential to the evaluation of the force experienced by the plug because it determines the base pressure on the plug through the

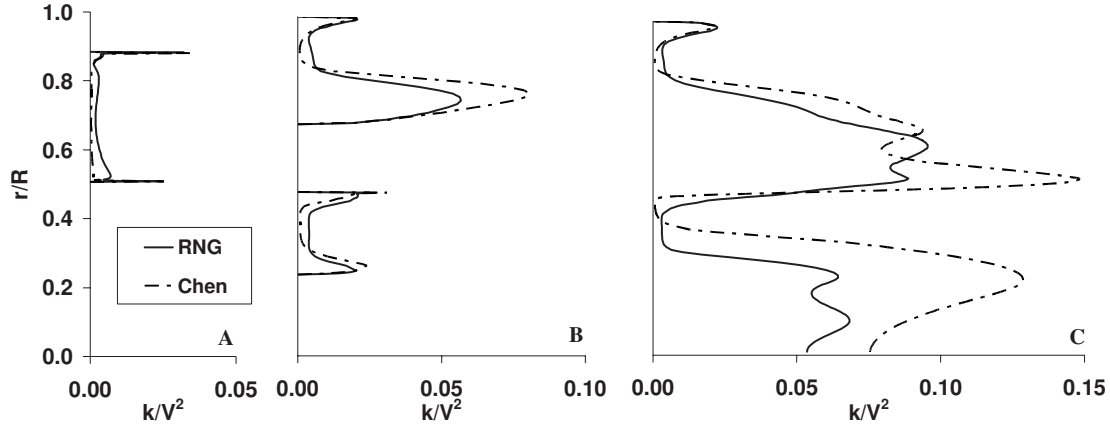

Fig. 8 Turbulent kinetic energy profiles of three sections shown by dashed lines in Fig. 5(*b*): simulation with Chen's and RNG *k*-ε turbulence models

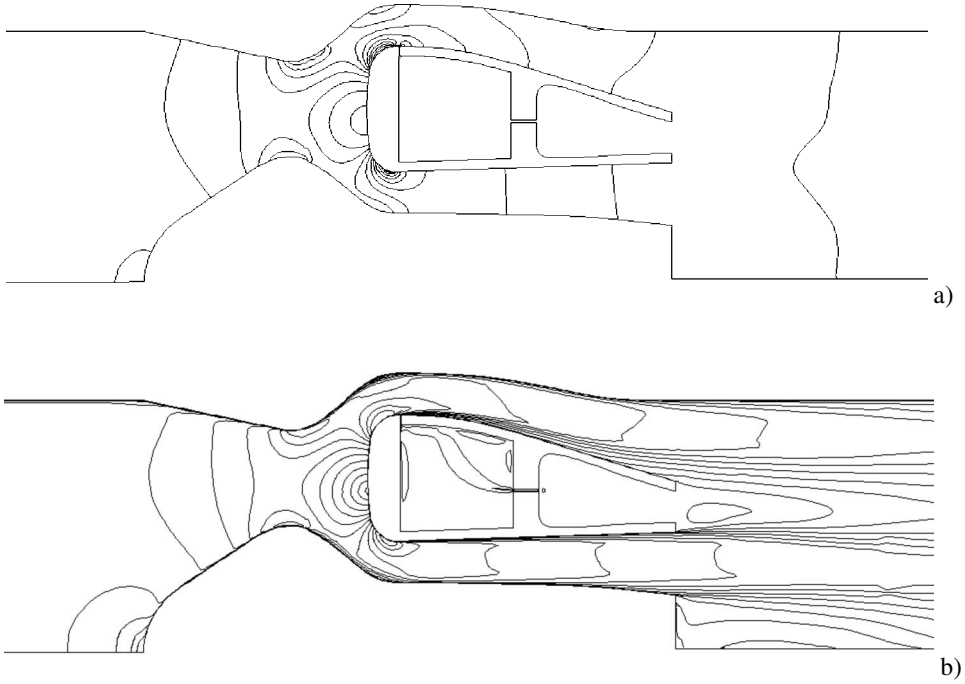

Fig. 9 Flow field in the fully open valve configuration. (*a*) Pressure: isolines range from $-5\rho V_0^2$ to $2\rho V_0^2$, step $(1/2)\rho V_0^2$. (*b*) Velocity magnitude: isolines range from 0 to $3V_0$, step $0.25V_0$.

slot below the outer edge of the plug. Downstream of the plug, turbulent boundary layers start to develop on the valve walls.

As discussed in Sec. 5, the increasing section of the annular channels leads to flow deceleration, resulting in an adverse pressure gradient, which causes a thickening of the boundary layers and an increase in the near-wall turbulence intensity (Fig. 5(*b*)).

The higher turbulence levels found in the outer boundary layer (Fig. 7) are due to the impact of the plane radial jet, which flows from the slot at the base of the plug. This jet is injected into the boundary layer, normal to the direction of the mean flow.

Two recirculation regions are formed in the downstream section of the pipe, just behind the inner valve body and behind the plug-spring housing (Fig. 10). These regions lead to the development of two separate turbulent wakes, which merge farther downstream.

7 Prediction of the Characteristic Curve

7.1 Quasisteady Flow Assumption. As discussed in Sec. 4, the characteristic of a check valve is better presented by comparing the flow coefficient C_v with the flow rate Q, rather than the plug travel, which is usually an unknown function of the flow rate itself.

Consistently, in the reference experiments on the check valve analyzed in the present work, pressure drops across the valve were measured at assigned flow rates [15]. The characteristic curves exhibit slight differences when measured during increasing or decreasing flow (Fig. 11). These differences may be attributed to friction effects in the sliding surfaces, which become more relevant near the fully open position of the plug. The presence of a

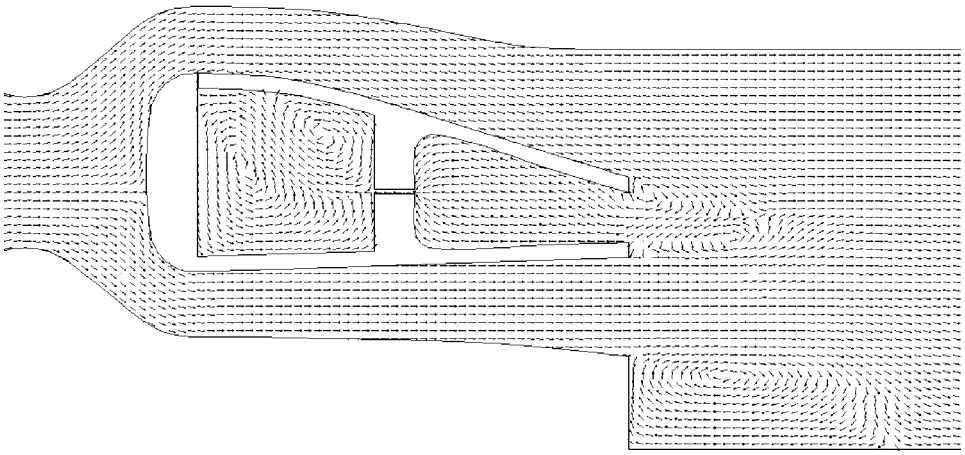

Fig. 10 Velocity vector field in the wake region of the fully open check valve. The vector length is uniform to highlight flow direction and recirculation regions.

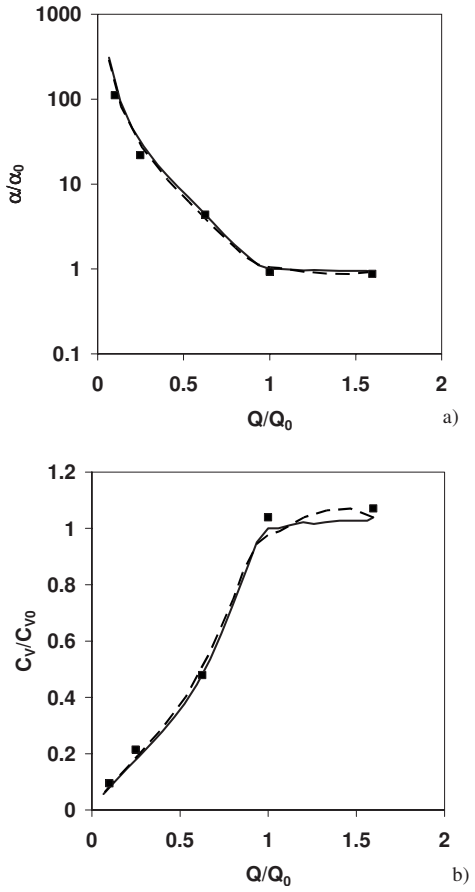

Fig. 11 Check valve characteristic curves: (*a*) pressure-drop coefficient; (*b*) flow coefficient. The symbols indicate results corresponding to the plug positions analyzed by numerical simulation; the lines indicate experimental results obtained by increasing the flow rate from zero to the maximum value (solid) and then decreasing again to zero (dashed).

slight Reynolds number effect can be also noted, as the flow coefficient tends to increase when the flow rate is increased beyond the minimal value Q_o necessary to ensure fully open conditions.

The quasisteady characteristic curve obtained by these experiments has been produced numerically by imposing a fixed plug travel. The exact flow rate in each case has been determined iteratively by requiring that the pressure load on the plug be equal to the reaction force of the springs. With the finest computational mesh adopted for the fully open configuration, simulations were built for 10%, 25%, and 50% plug travels. In accordance with the discussion reported in Sec. 5, the RNG k-ε model has been adopted in all the simulations. Figure 11(*b*) shows that the computed $Q-C_v$ conditions reproduce with good accuracy the experimental values. The Reynolds number dependency of α and C_v in fully open conditions is also simulated satisfactorily.

When the plug is partially closed the pressure drop occurs almost entirely near the gap between the plug and the valve body (Fig. 12). This is evident especially at low travels (Fig. 12(*b*)) and might suggest that the prediction of the characteristics of a partially closed valve does not require an accurate simulation of the flow downstream of the plug. However, if the plug position for a given flow rate is not known a priori, as in this case, the evaluation of the pressure load on the plug is essential to determine the equilibrium position of the plug (or, equivalently, the flow rate generating a given plug position). The numerical solutions show that the whole spring housing lies within the wake of the plug (Fig. 13). A correct simulation of the turbulent flow in the wake of the plug and of the resulting recirculation regions (Fig. 14) is therefore necessary because the load on the plug is directly dependent on the base pressure on the plug itself.

7.2 Simulation of the Opening Transient. The steady-state simulations discussed in Sec. 7.1 neglect the dynamic effects due to rapid plug displacement. These effects have been evaluated numerically by performing an unsteady simulation of the plug opening transient by the ALE formulation described in Sec. 3.3. A time step $\Delta t=1.06\times10^{-2}R/V_0$, corresponding to a maximum Courant number (CFL) of about 20, has been selected. The RNG k-ε model has been adopted also in this case.

The computational mesh for the unsteady flow simulation has

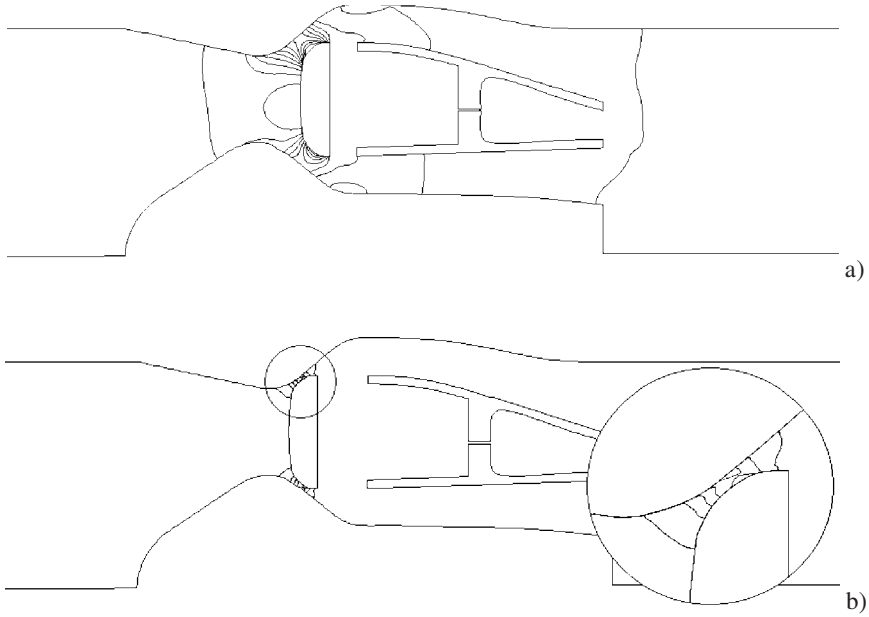

Fig. 12 Pressure field in steady flow at different plug positions. (*a*) 50% travel; (*b*) 10% travel; detail of the plug region in the circle. Isolines range from $-5\rho V_0^2$ to $2\rho V_0^2$, step $(1/2)\rho V_0^2$.

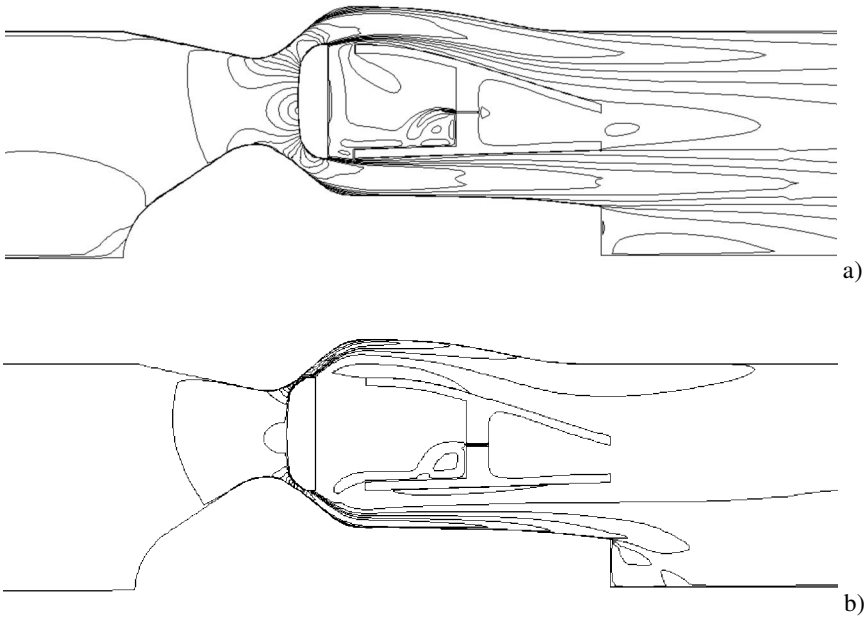

Fig. 13 Velocity magnitude field in steady flow at different plug positions. (*a*) 50% travel; (*b*) 10% travel. Isolines range from 0 to $3V_0$, step $0.25V_0$.

been built in order to account for the plug motion (Fig. 15), i.e., to allow the generation or removal of cell layers close to the plug surface in order to reduce mesh distortion. A linear law has been adopted for the displacement of the plug (Fig. 16). The 100% plug travel has been reached at $t_o=4.24R/V_0$, which corresponds to an opening transient of 0.4 s in the experiment on the real valve. At times higher than t_o the plug is fixed in the fully open position.

The inlet flow rate has also been increased linearly. The mini-

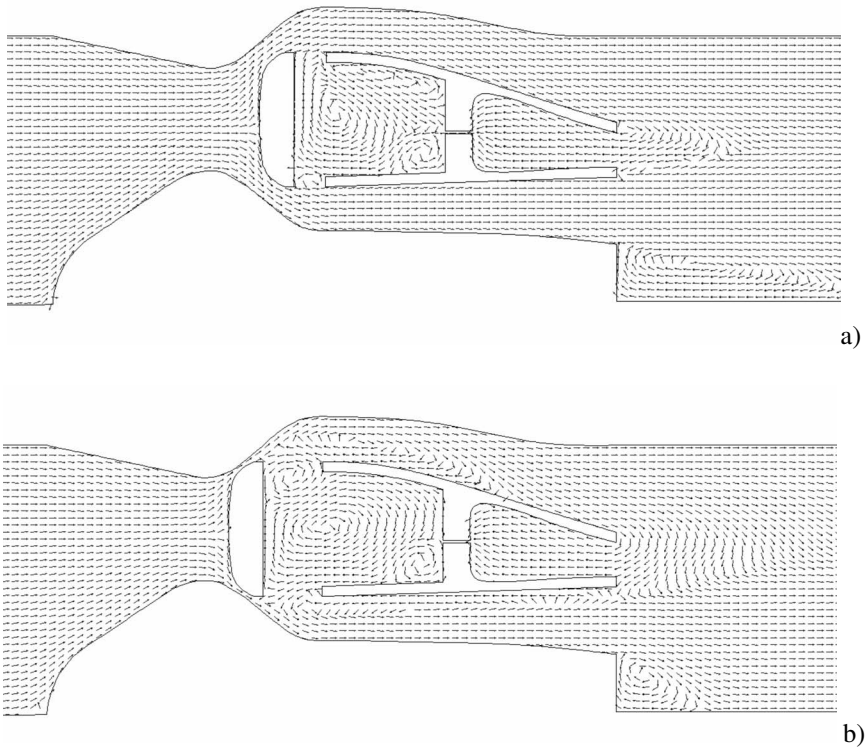

Fig. 14 Velocity vector field in steady flow at different plug positions. (*a*) 50% travel; (*b*) 10% travel. The vector length is uniform to highlight flow direction and recirculation regions.

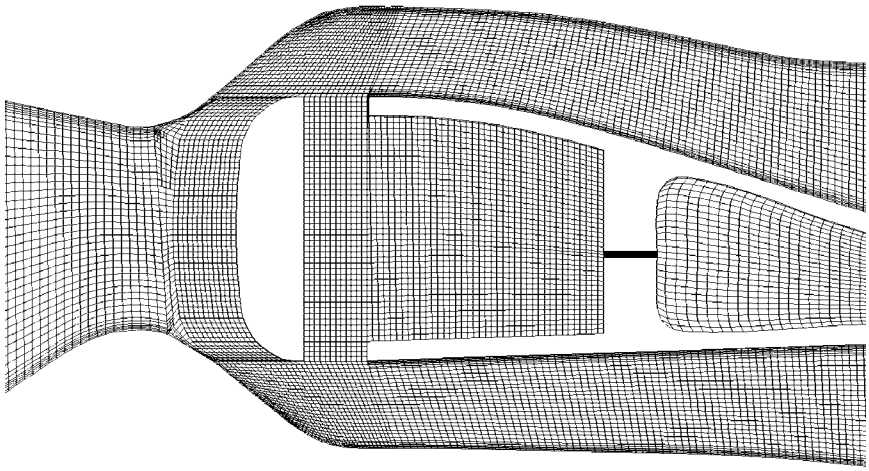

Fig. 15 Computational mesh for ALE simulation: detail at $t=2.12R/V_0$ (50% open, i.e., after 200 time steps)

mal value Q_o necessary to guarantee fully open conditions is reached at $t=t_o$. The rate of increase in the flow rate is kept constant until $t=1.15t_o$, when the maximum flow rate occurred during the tests is reached. The transient simulation has been then extended up to $t=1.4t_o$ at constant maximum flow rate. It must be recognized that it is not entirely correct to provide the variation of the mass flow rate during the opening of the valve instead of a constant head condition upstream of the valve. However, the pressure drop adjusted according to the assigned flow rate and the true transient flow coefficient is recovered in this way.

The velocity fields at different instants highlight some of the dynamic flow effects caused by the plug movement. The separation region downstream of the plug at 50% travel is larger in the unsteady case (Fig. 17(*b*)) than in the steady one (Fig. 13(*b*)). This separation region is still present in the outer channel when the plug reaches its final position (Fig. 17(*d*)). Later, the flow slowly reattaches to the afterbody wall. At the end of the analyzed transient the flow field (Fig. 17(*f*)) is the same as that found in the steady-state solution for the fully open configuration (Fig. 13(*a*)).

A pressure-drop coefficient can still be defined in this case as

$$\alpha = \frac{2}{\rho V^2}\left(\Delta p - \rho \frac{dV}{dt} L\right) \tag{11}$$

where the pressure gradient necessary to accelerate the flow during the transient (which is constant and equal to $3.54\rho V_0^2 L^{-1}$) is taken into account. A flow coefficient can be defined likewise.

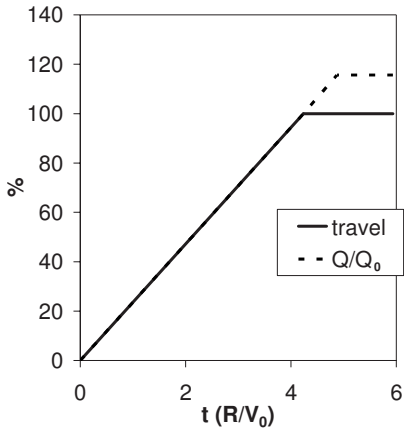

Fig. 16 Time history for plug travel and flow rate in the opening transient simulation

Figure 18 shows that the flow separation caused by the plug motion introduces an additional pressure drop, which could not be taken into account in the steady-state analysis. At the end of the transient, the separated region is convected downstream and the pressure drop computed for the steady-state case is recovered. The vertical lines at the end of the transient characteristics in Fig. 18 represent this final stage, when the flow rate is constant while the flow coefficient gradually recovers its steady-state value.

8 Conclusions

The turbulent flow inside an industrial check valve with an annular plug has been simulated by a finite-volume CFD solver. The comparison between the pressure drops estimated by the numerical simulation and the measurement has shown that the computational model must rely on a properly designed mesh with adequate grid nodes in the regions of high-pressure gradients (stagnation regions and expansions around the plug edges) and of high velocity gradients (boundary layers and wakes behind the valve body). Insufficient meshing can lead to overestimation of the valve flow coefficient in the fully open configuration.

The peculiar geometry of a nozzle check valve leads to a flow characterized by two stagnation regions, successive expansion and compression regions and a boundary layer, which develops under a strong adverse pressure gradient. These flow features pose severe requirements to the turbulence model used to simulate turbulent stresses in the flow. Actually, the standard high Reynolds number k-ε model is unable to simulate turbulence effects in the valve, even with a low Reynolds number near-wall model.

Far better results have been obtained by the use of the RNG k-ε model, which proves to be adequate in predicting the hydrodynamic characteristics of the valve. The calculated pressure drops and flow coefficients at different positions of the plug agree well with experimental measurements in steady-state conditions, thus confirming the validity of the numerical simulation of the flow.

The validated numerical model has been employed also to study the unsteady flow inside the valve during the opening transient of the plug. This analysis has shown the onset of dynamic effects, which consist mainly of a flow separation occurring downstream of the plug and persisting for some time after the end of the opening transient. The main consequence of this unsteady separation is an additional increase in the pressure drop in the upper half of the valve travel, leading to a departure from the quasisteady characteristic curve of the valve.

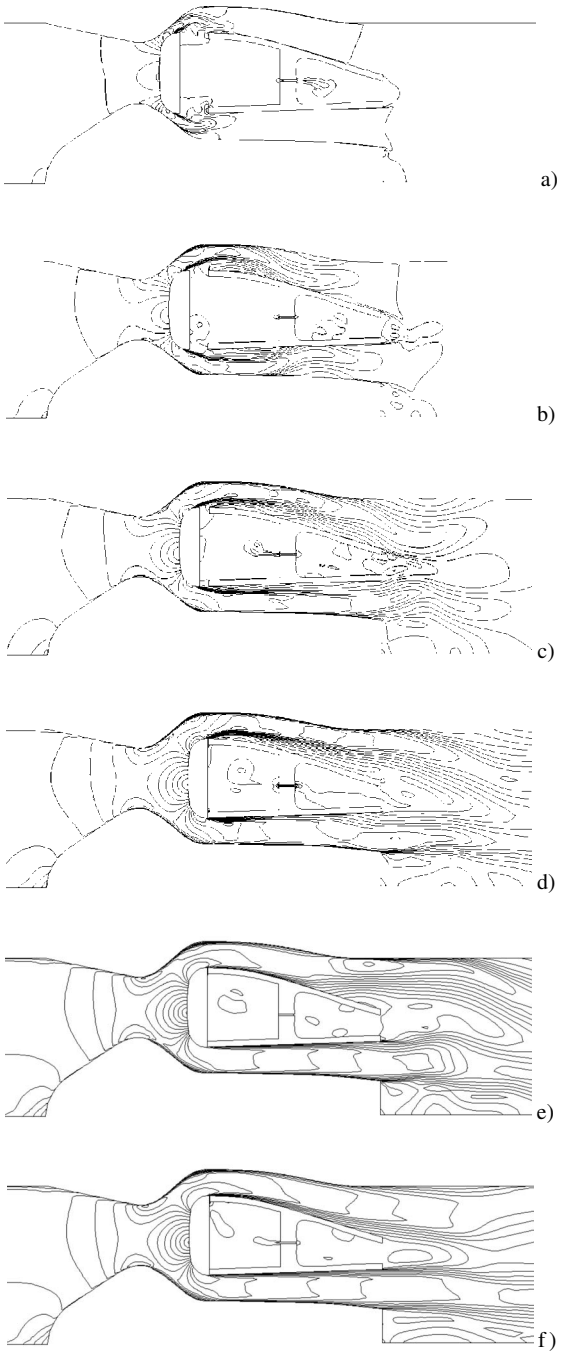

Fig. 17 Velocity magnitude fields during plug opening. (*a*) $t=0.25t_o$, (*b*) $t=0.5t_o$, (*c*) $t=0.75t_o$, (*d*) $t=t_o$, (*e*) $t=1.15t_o$, and (*f*) $t=1.4t_o$. Isolines range from 0 to $3V_0$, step $0.25V_0$.

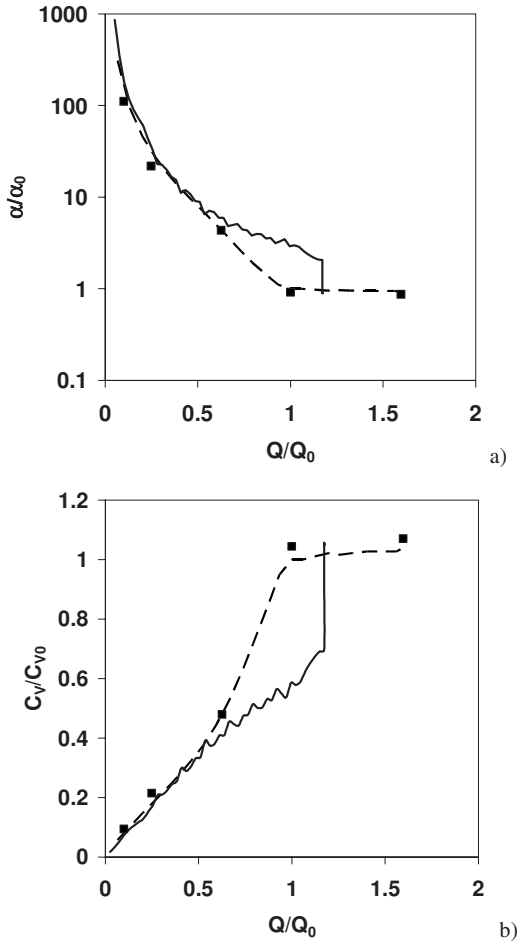

Fig. 18 Check valve characteristic curves during plug opening: (*a*) pressure-drop coefficient; (*b*) flow coefficient. Transient simulation (symbols) compared with steady-state simulations (dashed) and with experimental results obtained by increasing the flow rate from zero to the maximum value (solid).

Acknowledgment

The authors are grateful to Mr. Giuseppe Bianchi and to Dresser Italia S.p.A. for their support to this research and to Dr. Sara Lazzarini for her valuable help in the setup of the first numerical simulations.

Nomenclature

$C_{\varepsilon 1}$, $C_{\varepsilon 2}$, $C_{\varepsilon 3}$, C_μ, η_0, β = turbulence model coefficients
C_v = valve flow coefficient
C_{vo} = valve flow coefficient measured in fully open conditions
k = specific turbulent kinetic energy
L = axial distance between pressure probes
P = production rate of k
Q = flow rate
Q_o = minimal flow rate, which guarantees fully open conditions
R = pipe radius
u_i' = vector of velocity fluctuations
u_* = friction velocity
t = time
t_o = duration of plug opening transient
V = mean velocity in the pipe
V_0 = mean velocity in the pipe at flow rate Q_o
y^+ = near-wall cell height in wall units
α = pressure-drop coefficient
α_o = pressure-drop coefficient measured in fully open conditions
Δp = pressure drop across the valve
ε = dissipation rate of k
η = nondimensional rate of strain
κ = von Kàrmàn constant
μ = dynamic viscosity
μ_T = dynamic eddy viscosity
ρ = fluid density
σ_k, σ_ε = turbulent Prandtl numbers for k and ε
τ_w = wall stress

References

[1] Pandula, Z., and Halász, G., 2002, "Dynamic Model for Simulation of Check Valves in Pipe Systems," Period. Polytech., Mech. Eng.-Masinostr., **46**, pp. 91–100.

[2] Lee, T. S., and Leow, L. C., 2001, "Numerical Study on Effects of Check Valve Closure Flow Conditions on Pressure Surges in Pumping Station With Air Entrainment," Int. J. Numer. Methods Fluids, **35**, pp. 117–124.

[3] Li, G., and Liou, J. C. P., 2003, "Swing Check Valve Characterization and Modeling During Transients," ASME J. Fluids Eng., **125**, pp. 1043–1050.

[4] Goodwin, R., and Jenkins, K., 2000, "Anti-Pressure Surge Developments on Dual Plate Check Valves," *Proceedings of the Eighth International Conference on Pressure Surges*, BHRA, Harrogate, England.

[5] Hannah, B., Sponsel, J., Gormley, R., and Kostelnik, M., 2001, "Detailed Performance Comparisons Between Swing Type and In-Line Nozzle Check Valves," *Proceedings of the Eighth EPRI/NMAC Valve Technology Symposium*.

[6] Gormley, R., and Michel, I., 2002, "Axial Flow Check Valve Dynamic Response: Using Test Results to Select Optimum Valve Design," *Proceedings of the Seventh NRC/ASME Valve and Pump Testing Symposium*, Vol. 4, pp. 2A–77, Paper No. NUREG/CP-0152,.

[7] Stevenson, M. J., and Chen, X. D., 1997, "Visualization of the Flow Patterns in a High-Pressure Homogenizing Valve Using a CFD Package," J. Food. Eng., **33**, pp. 151–165.

[8] Agaphonov, B. N., Goryachev, V. D., Kolyvanov, V. G., Ris, V. V., Smirnov, E. M., and Zaitsev, D. K., 1999, "Simulation of 3d Turbulent Flow Through Steam-Turbine Control Valves," *Proceedings of the Second International Symposium on Finite Volumes for Complex Applications*, R. Vielsmeer, F. Benkhaldoun, and D. Hanel, eds., Hermes Science, London, pp. 743–750.

[9] Badur, J., Banaszkiewicz, M., Karcz, M., and Winowiecki, M., 1999, "Numerical Simulation of 3D Flow Through a Control Valve," Cieplne Maszyny Przepływowe-Turbomachinery, **115**, pp. 29–36.

[10] Morita, R., Inada, F., Mori, M., Tezuka, K., and Tsujimoto, Y., 2007, "CFD Simulations and Experiments of Flow Fluctuations Around a Steam Control Valve," ASME J. Fluids Eng., **129**, pp. 48–54.

[11] Davis, J. A., and Stewart, M., 2002, "Predicting Globe Control Valve Performance, Part I: CFD Modeling," ASME J. Fluids Eng., **124**, pp. 772–777.

[12] Davis, J. A., and Stewart, M., 2002, "Predicting Globe Control Valve Performance, Part II: Experimental Validation," ASME J. Fluids Eng., **124**, pp. 778–783.

[13] Leutwyler, Z., and Dalton, C., 2006, "A Computational Study of Torque and Forces Due to Compressible Flow on a Butterfly Valve Disk in Mid-Stroke Position," ASME J. Fluids Eng., **128**, pp. 1074–1082.

[14] Launder, B. E., and Spalding, D. B., 1974, "The Numerical Computation of Turbulent Flows," Comput. Methods Appl. Mech. Eng., **3**, pp. 269–289.

[15] Kruisbrink, A. C. H., 1999, "Mannesmann Demag Nozzle Check Valve DN 600 Type DRV-B PN 10; Test Report," WL Delft Hydraulics.

[16] CD Adapco Group, 2001, *StarCD Version 3.15 User Guide*, Computational Dynamics Ltd., London.

[17] Issa, R. I., Gosman, A. D., and Watkins, A. P., 1986, "The Computation of Compressible and Incompressible Recirculating Flows by a Non-Iterative Implicit Scheme," J. Comput. Phys., **62**, pp. 66–82.

[18] Issa, R. I., 1986, "Solution of the Implicitly Discretised Fluid Flow Equations by Operator-Splitting," J. Comput. Phys., **62**, pp. 40–65.

[19] Yakhot, V., Orszag, S. A., Thangam, S., Gatski, T. B., and Speziale, C. G., 1992, "Development of Turbulence Models for Shear Flows by a Double Expansion Technique," Phys. Fluids A, **4**(7), pp. 1510–1520.

[20] Chen, Y. S., and Kim, S. W., 1987, "Computation of Turbulent Flows Using an Extended k-ε Turbulence Closure Model," NASA, Report No. CR-179204.

[21] Hirt, C. W., Amsden, A. A., and Cook, J. L., 1974, "An Arbitrary Lagrangian-Eulerian Computing Method for All Speeds," J. Comput. Phys., **14**, pp. 227–253.

[22] Demirdzic, I., and Peric, M., 1988, "Space Conservation Law in Finite Volume Calculations of Fluid Flow," Int. J. Numer. Methods Fluids, **8**, pp. 1037–1050.

[23] Norris, L. H., and Reynolds, W. C., 1975, "Turbulent Channel Flow With a Moving Wavy Boundary," Department of Mechanical Engineering, Stanford University, Report No. FM–10.

W. H. Nurick
e-mail: wnurick@verizon.net

T. Ohanian

Science and Technology Applications LLC (STA),
Moorpark, CA 93021

D. G. Talley
Air Force Research Laboratory Edwards Air Force Base,
AFRL/PRSA,
10 East Saturn Boulevard,
Edwards AFB, CA 93524-7660

P. A. Strakey
Energy Systems Dynamics Division,
National Energy Technology Laboratory,
Morgantown, WV 26505

The Impact of Manifold-to-Orifice Turning Angle on Sharp-Edge Orifice Flow Characteristics in Both Cavitation and Noncavitation Turbulent Flow Regimes

The approach taken was to analyze the results in a manner consistent with application by design engineers to new and existing applications, while providing some insight into the processes that are occurring. This paper deals with predicting the initiation of cavitation, cavitation impacts on the contraction coefficient (C_c), as well as noncavitation impacts on discharge coefficient (C_d) from L/D of five sharp-edge orifices over a turning angle range between 60 deg and 120 deg. The results show that in the cavitation regime, C_c is controlled by the cavitation parameter (K_{cav}), where the data follow the 1/2 power with K_{cav}, and inception of cavitation occurs at a K_{cav} of 1.8. In the noncavitation regime for conditions where the cross velocity is 0 the data are consistent with the first order equation relating head loss (H_L) to the dynamic pressure where K_L is constant and is consistent with in-line orifices. Cross flow has a significant impact on loss coefficient and depends on both the turning angle and manifold inlet to orifice exit velocity ratio.
[DOI: 10.1115/1.2978999]

1 Introduction

Cavitation occurs in a wide variety of applications from diesel and gas injectors for the automotive industry to prop wake flow associated with water propulsion. Rocket engine injectors can also experience cavitation when the propellants are injected into the combustion chamber from impinging type elements utilizing sharp-edge orifices. The ability for cavitation to occur depends on the specific manifold and injection orifice design and operating conditions. The actual onset of cavitation depends on the orifice edge sharpness, L/D, upstream pressure, cross velocity, orifice entrance angle, and back pressure. In application where the engine is "deep" throttled cavitation can occur if the chamber pressure is sufficiently low and/or the upstream flow causes a contraction/expansion to support separation. The inability to predict the occurrence of cavitation and/or separation can lead to combustion instability, jet misimpingement that result in loss in performance, and potential wall propellant impingement. All of these impacts can result in a catastrophic failure of an engine and/or loss of mission.

In 1976 Nurick [1] published a paper discussing cavitation for in-line sharp-edge orifices and proposed a simple first order model for predicting cavitation. Photographic evidence was also presented, showing that after the inception of cavitation, the vena-contracta reattachment point started to move downstream toward the exit of the orifice. This also resulted in a decrease in discharge coefficient (C_d) until it reached the separation value. In some cases the orifice remained attached even at a cavitation parameter of 1 while in other cases hydraulic flip occurred in the region of K_{cav} of 1.8 or less. In 2007 Nurick et al. [2] (in review for publication) wrote a paper specifically dealing with sharp-edged orifices having a 90 deg orientation relative to the manifold feed. This study revealed that the simple relationship could be extended to 90 deg orifices in cross flow although the C_c and K_L relationships needed to account for the manifold-to-orifice velocity ratio.

The early Nurick [1] results were subsequently utilized in other studies [3–6] that included computational fluid dynamics (CFD) modeling to extend model applicability and in some cases verify codes. In the past 10–15 years CFD modeling has improved considerably, and predictions are now being made that show the impact of key design/operating variables on both the discharge coefficient (C_d) and contraction coefficient (C_c). Unfortunately, there is little if any test data that can be utilized to verify these predictions. It is the hope of the authors that the results presented in this paper will be useful in that goal.

This paper is an extension of the earlier work [1,2] and includes varying the turning angle from as low as 60 deg up to 120 deg for an orifice L/D of 5. The approach taken in this paper is to present the results in a manner consistent with application by design engineers to new and existing applications, while providing some insight into the processes that are occurring. This paper deals with predicting the initiation of cavitation and the impact of the variables listed above on C_c, C_d, and K_L. In addition the impact of the same variables in the turbulent flow regime is also discussed, and correlations are provided.

2 Test Facility and Test Setup

2.1 Facility Design. The experimental investigation was carried out at the Air Force Research Laboratory cold-flow injector characterization facility, a simplified schematic of which is shown in Fig. 1. Water, which is used as a simulant for liquid oxygen, is stored and pressurized in a 1 m^3 tank. The injector inlet flow rate is controlled with a throttling valve and measured with one of several turbine flow meters arranged in parallel to cover a wide range of flow rates. Downstream of the injector, another turbine flow meter measures the outlet flow rate, and a back-pressure regulator maintains the injector fluid pressure. Fluid pressures of up to 13.79 MPa and manifold velocities up to 40 m/s may be produced in this manner. The injector, as illustrated in Fig. 2,

Contributed by the Fluids Engineering Division of ASME for publication in the JOURNAL OF FLUIDS ENGINEERING. Manuscript received June 26, 2007; final manuscript received July 25, 2008; published October 23, 2008. Assoc. Editor: Steven Ceccio.

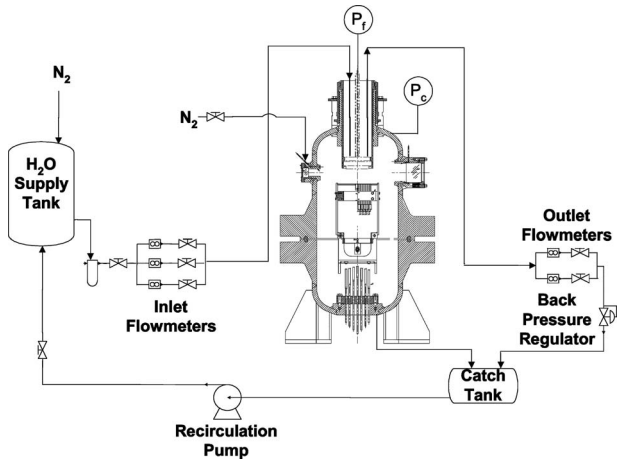

Fig. 1 Schematic of AFRL cold flow test facility

consists of an interchangeable stainless steel plate with a sharp-edged hole machined in the center of the plate. This is mounted against the fluid manifold, which contains a 6.35 mm square channel machined into the manifold. A plenum and screen at the inlet and exit of the manifold reduce the velocity before the flow enters the manifold in order to generate a reproducible flow field at the entrance to the orifice. The distance from the manifold inlet screen to the orifice entrance is 63.5 mm or ten manifold channel widths. The entire arrangement is secured inside an optically accessible pressure chamber, which is rated to 13.79 MPa.

The orifices are either pilot drilled and reamed or made by electrical discharge machining with a diameter tolerance of ± 13 μm and inlet edge radius to orifice diameter ratio of less than 0.003, ensuring a sharp-edged inlet. Chamber pressure, orifice pressure drop, and inlet and outlet flow rates are recorded by a 12 bit analog to digital conversion board, and the data are stored on a personal computer. Experiments are typically conducted by setting the fluid pressure and flow rates to a predetermined value, with the chamber pressure being gradually increased while the data acquisition system records flow rates and pressures. This allows for a large amount of data to be collected in a relatively short period of time. Orifice pressure drop and chamber gas pressure are measured within an accuracy of $\pm 0.25\%$. Manifold velocities are held constant to within $\pm 1.5\%$ during the experiment. Because of the difficulty associated with directly measuring the orifice flow rate inside the pressurized vessel, the orifice flow rate is measured by subtracting the manifold outlet flow rate from the manifold inlet flow rate.

The experimental error associated with the discharge coefficient measurement is limited by the accuracy of the flow meters, which is $\pm 0.5\%$. This translates to an error on the discharge coefficient

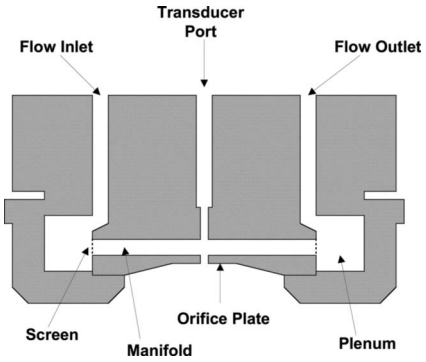

Fig. 2 Injector schematic

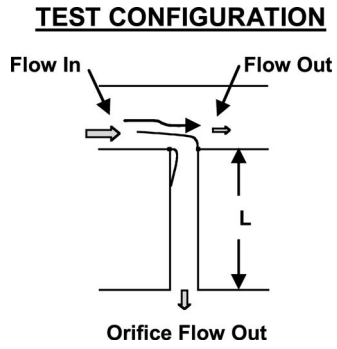

Fig. 3 Cross flow test configuration for 90 deg orifices

data of about $\pm 0.5\%$ at the lowest manifold flow rates and highest orifice flow rates to $\pm 10\%$ at the lowest orifice flow rates and highest manifold flows. A typical error for the intermediate flow rates is on the order of $\pm 4\%$.

2.2 Manifold Configuration. For the data in this paper the manifold was operated such that fluid enters the inlet port, and a portion of the flow exits the manifold and the remainder enters the orifice. A sketch of the configuration is shown in Fig. 3.

2.3 Orifice Configurations. Both single and compound angle orifice designs were tested. As shown in Fig. 4, for the single angle direction feed, the orifice is oriented such that the flow enters the orifice by turning in the direction of its angle; while for the compound angle direction flow the flow must first turn 90 deg while also turning in the direction of the orifice angle.

The range of operating conditions and orifice geometries typical of liquid rocket injectors was studied and is given in Table 1.

3 Analysis Approach

3.1 Cavitation Regime (Turbulent Flow). In 1976 Nurick [1] introduced a cavitation parameter that takes into account all the dynamic variables that impact the process such as (1) the manifold-to-orifice area ratio, (2) flow turning losses, (3) friction losses, (4) contraction and expansion losses, etc. Consistent with this the definition of a cavitation parameter stated by Nurick and utilized in this study is

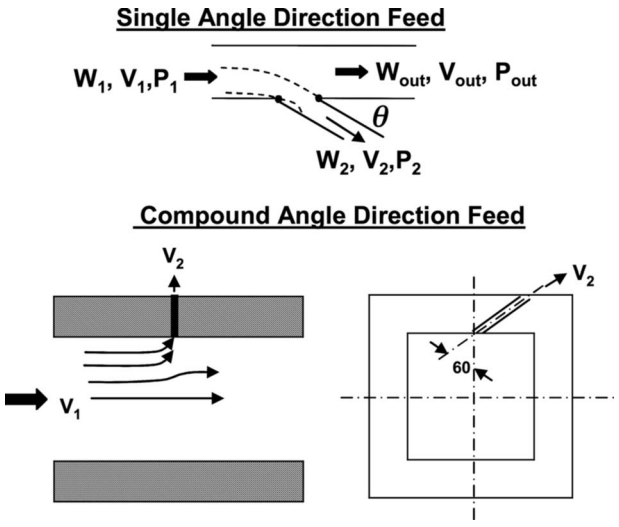

Fig. 4 Illustration of flow turning for single and compound angle orifices

Table 1 Test variables and range of testing

Orifice diameter (mm)	1.19–2.03
Length to diameter ratio	3–10
Fluid pressure (MPa)	0.69–10.3
Back pressure (MPa)	0.09–10.3
Cross-velocity (m/s)	0–18.5
Orifice Re_d	1.0×10^4–3.0×10^5
Manifold Re_w	6.0×10^3–1.1×10^5
Manifold dynamic head to orifice static D_p ratio	5.0×10^{-5}–6.0×10^0

$$K_{\text{cav}} = \frac{P_1 - P_v}{P_1 - P_2} \tag{1}$$

The derivation of relationships between C_d and C_c depends on various assumptions unique to the flow characteristics of the configuration tested. For the tests in this program the manifold velocity cannot be neglected in the definition of the discharge coefficient. For this case the discharge coefficient is defined as

$$C_d = \frac{V_2}{[(2/\rho)(P_1 - P_2) + V_1^2]^{1/2}} \tag{2}$$

When the flow entering the manifold exits by two paths (i.e., the manifold exit and the orifice), the velocity at the vena-contracta is defined by

$$V_c = \frac{V_2}{C_c} \tag{3}$$

Utilizing the above equations and the Bernoulli equation, with the assumption that the head loss between the manifold and the vena-contracta is small, the resulting discharge coefficient can be shown to as

$$C_d = \frac{C_c K_{\text{cav}}^{1/2}}{\left[1 + \left(\frac{V_1}{V_2}\right)^2 C_c^2 (K_{\text{cav}} - 1)\right]^{1/2}} \tag{4}$$

Equation (4) can be rearranged to

$$C_c = \frac{1}{\left[\frac{K_{\text{cav}}}{C_d^2} - \left(\frac{V_1}{V_2}\right)^2 (1 - K_{\text{cav}})\right]^{1/2}} \tag{5}$$

Equation (5) was used to define C_c for all tests.

3.2 Noncavitation Regime (Turbulent Flow). In basic fluid dynamics texts, the flow around bends is defined by a loss coefficient, which is included in the specification of the overall head loss. Consistent with this tradition the data in the noncavitation turbulent flow are both analyzed and correlated in terms of the impact on the overall head loss (H_L).

The head loss defined by the Bernoulli equation is

$$H_L = (P_1 - P_2) + \frac{\rho}{2}(V_1^2 - V_2^2) \tag{6}$$

This formulation of the energy equation is per unit of flow. Not including the flow exit energy in Eq. (6) separates the problem into two parts: (1) the manifold inlet through the orifice and (2) the manifold inlet to the manifold exit. The latter is not included in this paper.

Equation (6) assumes that the flow rate "1" is equal to the flow rate "2" so that the inlet flow included in the equation is only that portion that flows into the orifice (i.e., shown by the boundary line in Fig. 3). Although the energy out is not included it does not follow that the impact of the transition from the manifold inlet to the outlet does not impact the losses.

The loss coefficient as defined in most textbooks in the U.S. is

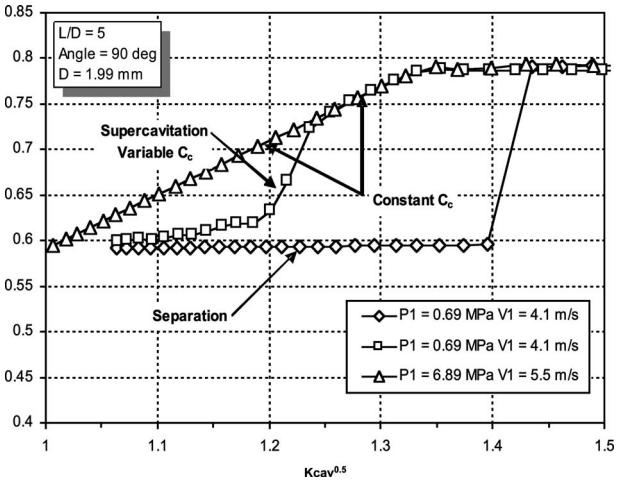

Fig. 5 Sharp-edge orifice data depicting all flow regimes

$$H_L = K_L \frac{\rho V_2^2}{2} \tag{7}$$

Then substitution into Eq. (6) defines the loss coefficient as

$$K_L = \frac{\Delta P}{\frac{\rho V_2^2}{2}} + \left(\frac{V_1}{V_2}\right)^2 - 1 \tag{8}$$

Utilizing Eqs. (2) and (8) the loss coefficient can be related to the discharge coefficient as

$$C_d = \frac{1}{\sqrt{K_L + 1}} \tag{9}$$

4 Results and Discussion

4.1 Cavitation Regime. It is important to first define the flow regimes so that the data can be related to specific processes. There are three flow regimes of interest in the cavitation regime. The first is the onset of cavitation (inception of cavitation) where bubbles are formed at the orifice entrance and continue to flow downstream until they are converted back to liquid in the recovery area. The second is full cavitation where the bubbles coalesce, forming a vapor cavity, the length of which varies as the cavitation parameter is lowered. The third is supercavitation where the vapor pocket attachment has moved to the orifice exit and beyond but the flow still acts as attached. For this study only the 90 deg orifice angle configuration experienced supercavitation. For all other angles it did not appear to occur. The physical reason is unknown at this time, and its determination would require additional measurements including photographic evidence of the vapor cavity characteristics.

All three of these regimes, in addition to separation, are illustrated in Fig. 5.

Note that the hydraulic flip can occur at any point in the cavitation regime depending on the orifice L/D as well as flow conditions. There also appears to be potential for "hysteresis" to also occur at start-up, as indicated by the two identical run conditions shown in Fig. 5. Note that in one case the orifice was separated at the outset, but at about the point where cavitation inception occurs it immediately flips to the noncavitation condition. In the other test it appears that the flow is attached at the onset but not in separation since the data curve upward until about a $(K_{\text{cav}})^{0.5}$ of 1.18 where C_c becomes constant. In the regime where C_c varies the flow is supercavitated and is impacted by the ability of the flow to remain attached and other processes most likely occurring at the orifice exit. Then as the cavitation parameter is further in-

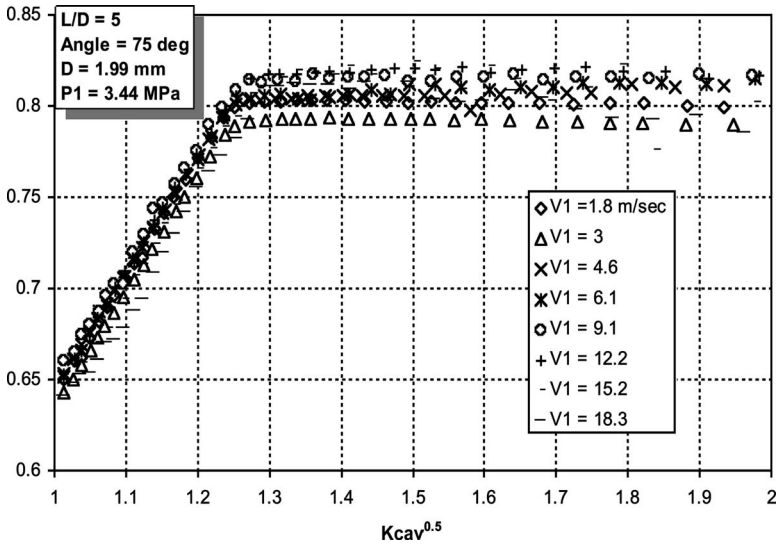

Fig. 6 Cavitation parameter versus discharge coefficient

creased (C_c constant), as is normal, transitions to the noncavitation condition. These resulting impacts on the cavitation characteristics are noted in Fig. 5. Also shown is the constant C_c condition where the flow smoothly transitions from noncavitation to cavitation and remains attached. This latter condition is the basis for the correlations presented in this paper.

4.1.1 Single Angle Direction. Inception of Cavitation. The inception of cavitation occurs where the discharge coefficient either abruptly changes to a decreasing value with decreasing cavitation parameter or more smoothly transitions, both resulting in a constant slope consistent with Eq. (3). Both characteristics are illustrated in Fig. 6. Interestingly the cavitation data all follow the relationship of Eq. (3), suggesting that the denominator for a given test is constant.

For each test sequence, where the upstream conditions were set and the back pressure systematically increased, the data were analyzed to determine the point where the data deviated from the straight line relationship. This is also the point where the flow is no longer choked and transitions into the noncavitation turbulent regime. Analysis of the data revealed that the cavitation parameter where cavitation inception begins remains constant (within experimental error) at all conditions regardless of turning angle or upstream conditions at $K_{\text{cav}} \sim 1.8$. In some cases there is a transition region where C_c varies until the flow fully chokes and C_c remains constant. When this occurs C_c becomes constant at K_{cav} between $\sim 1.5-1.6$.

Full Cavitation. The impact of upstream conditions on the contraction coefficient should be related to the nonsymmetric nature of the flow due to acceleration from bending as well as both area reduction and attachment on the far wall. These characteristics should impact the vena-contracta formation process. Equation (4) can be solved for C_c and the result is

$$C_c = \frac{1}{\left(\frac{K_{\text{cav}}}{C_d^2} - b\right)^{1/2}} \tag{10}$$

where

$$b = \left(\frac{V_1}{V_2}\right)^2 (K_{\text{cav}} - 1) \tag{11}$$

Therefore, in addition to K_{cav} and C_d, it is expected that C_c will also be a function of the velocity ratio (the area ratio is constant for these tests and the ratio V_{out}/V_2 is dependent on V_1/V_2). For different turning angles it would also be expected that C_c would be a function of angle. The contraction coefficient will therefore be a function of

$$C_c = f\left[C_d, K_{\text{cav}}, \theta, \frac{V_1}{V_2}\right] \tag{12}$$

The test data were reduced to define C_c using Eq. (10) for each turning angle. The results are plotted in Fig. 7 as a function of V_1/V_2. For the 60 deg turning angle the results show that C_c initially increases with velocity ratio then decreases similar to that of the other angles. As the manifold exit flow rate approaches zero the C_c appears to "sense" the resistance of a wall being formed and therefore seek the value for no exit flow.

Note that for all angles the data approach a value of C_c of ~ 0.62, which conforms to that of an in-line orifice (no cross flow) [7]. The significant impact of turning angle and velocity ratio on C_c suggests that increasing either variable result in a decrease in the vena-contracta area. This further suggests that the ability of the accelerating flow to reach vapor pressure increases as the flow turning angle and/or the velocity ratio increases. This decrease in the vena-contracta area increases the vapor area. A hypothesis for this phenomenon is that it is related to the dynamics of the flow impacting on the far wall, creating a vapor pocket only on the near wall. Best-fit curves were fitted to each angle in the form

$$C_c = A\left(\frac{V_1}{V_2}\right)^2 + B\frac{V_1}{V_2} + C \tag{13}$$

The resulting equations for each angle are given in Table 2 in addition to the R^2 root mean square error. Application of this equation is only valid within the limits of the data, as indicated in Fig. 7.

Utilizing the results from the cavitation study for analysis and design is straightforward. For example, given an orifice and manifold design as well as the expected operating conditions, K_{cav} can be calculated using Eq. (1). The value of K_{cav} can then be compared with that required to achieve incipient cavitation (i.e., 1.8) and if equal to or less than this value operation will be in the cavitation regime. Then based on the design variables such as (1) manifold/orifice area ratio, (2) flow rate ratio, and (3) turning angle, C_c can be calculated using Eq. (13). The orifice discharge coefficient can then be calculated from Eq. (4).

It is important to note that since the area ratio was not varied, the equations have only been validated at the ratio A_2/A_1 used in this study. Therefore Eq. (14) has only been validated for this value of area ratio.

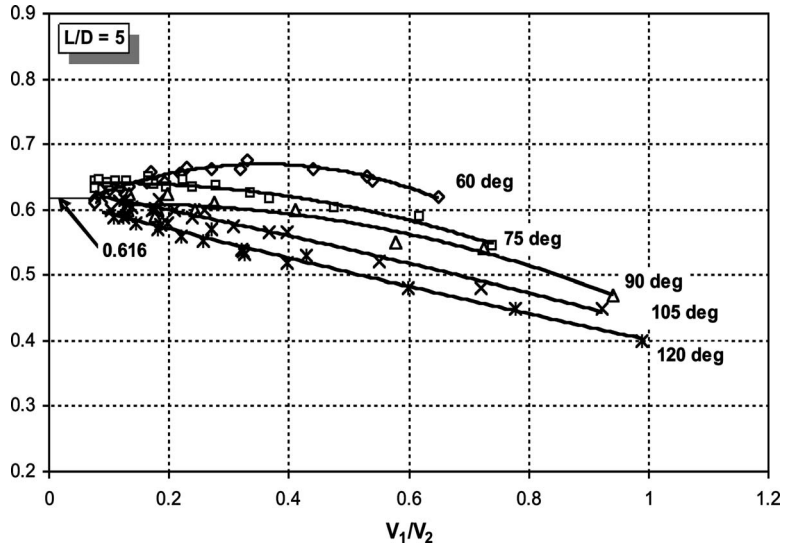

Fig. 7 Impact of cross velocity and turning angle on C_c

4.1.2 Compound Angle Direction Feed. Inception of Cavitation. The designation of 90_xx for the compound angle orifices designates that the flow must turn 90 deg relative to the manifold wall while also turning in the direction of the orifice angle (xx).

The compound angle direction feed data, Fig. 8, followed the identical trends as the single angle direction feed data. Within the experimental accuracy, cavitation inception was between 1.7 and 1.8, as shown in Fig. 8 ($K_{cav}^{0.5}$=1.3–.34). The inception of cavitation for both the 90_60 deg and 90_75 deg data again is taken at the beginning of the rollover from the turbulent regime to the cavitation regime. It should be noted that the full cavitation is not achieved until $\sim K_{cav}^{0.5}$=1.3. The sharp decline in C_d in the noncavitation regime is due to the definition of C_d that includes V_1.

Full Cavitation. The variation in the contraction coefficient with velocity ratio for the compound angle direction feed is shown in Fig. 9. The data are compared with the single angle direction feed data of 60 deg and 75 deg. Note that both the 90_60 and the 90_75 data nearly fit to a single curve. In addition note that as the manifold exit flow rate approaches zero the C_c tends to approach a constant at a value equal to that determined for the approach velocity case.

Since there are only two compound angle configurations tested individual equations are provided. The equation is

$$C_c = A\left(\frac{V_1}{V_2}\right)^2 + B\frac{V_1}{V_2} + C \tag{14}$$

The constants for each configuration are provided in Table 3.

Table 2 Contraction coefficient equations for specific turning angles

Turning angle (deg)	Equations	R^2
60	$C_c=-0.5419(V_1/V_2)^2+0.4397(V_1/V_2)+0.5881$	0.87
75	$C_c=-0.2298(V_1/V_2)^2+0.0486(V_1/V_2)+0.6365$	0.95
90	$C_c=-0.1443(V_1/V_2)^2+0.0468(V_1/V_2)+0.5928$	0.93
105	$C_c=-0.0366(V_1/V_2)^2-0.0734V_1/V_2+0.6342$	0.98
120	$C_c=-0.0203(V_1/V_2)^2-0.2364(V_1/V_2)+0.6164$	0.98

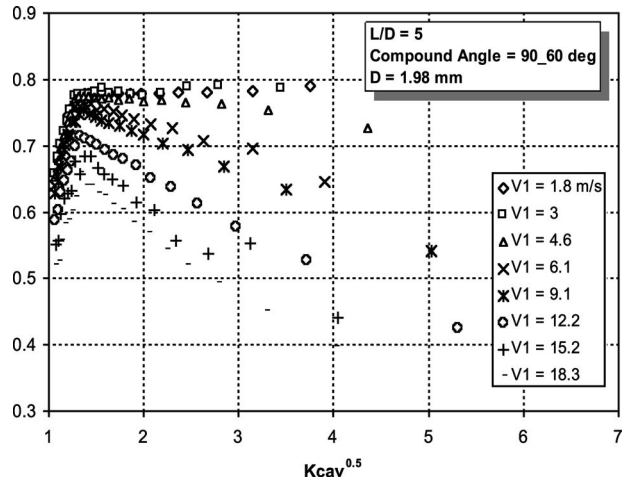

Fig. 8 C_d versus cavitation parameter for compound angle 90_60 deg

4.2 Noncavitation Regime (Attached Turbulent Flow). The results for the noncavitation turbulent flow regime are divided into two areas. The first section deals with the single angle direction feed and the last section deals with the compound angle orifice design.

4.2.1 Single Angle Direction. Feed Impact of Orifice Variables

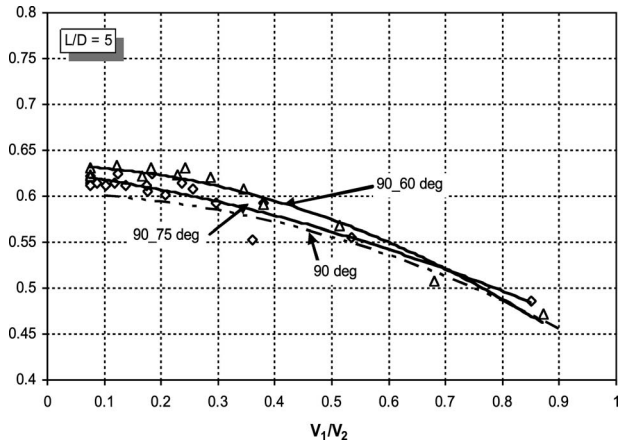

Fig. 9 Impact of manifold-to-orifice velocity ratio on C_c

Table 3 Constants for Eq. (15)

Angle	*A*	*B*	*C*
90_60	−0.2125	−0.0.114	0.6324
90_75	−0.1058	−0.0771	0.6259

Table 4 Loss coefficient equations for specific turning angles

Turning angles (deg)	Equations	R^2
All	$W_1=W_2: K_L=0.62+(V_1/V_2)^2$	0.992
60	$W_1\neq W_2: K_L=0.686+1.344(V_1/V_2)^2-1.152(V_1/V_2)$	0.995
75	$W_1\neq W_2: K_L=0.568+1.23(V_1/V_2)^2-0.4755(V_1/V_2)$	0.982
90	$W_1\neq W_2: K_L=0.62+(V_1/V_2)^2$	0.992
105	$W_1\neq W_2: K_L=0.534+0.837(V_1/V_2)^2+0.784V_1/V_2$	0.998
120	$W_1\neq W_2: K_L=0.554+0.7564(V_1/V_2)^2+1.040(V_1/V_2)$	0.998

on K_L. For each test the manifold inlet velocity was constant, and the data plotted as head loss versus the orifice exit dynamic pressure resulted in a linear relationship. For the case where all flow went through the orifice the data intersected at the origin, and an offset occurred when the flow was diverted through the manifold exit. The data were initially analyzed using Eq. (7). In all cases the results were consistent with that shown in Fig. 10. For convenience $\rho V_2^2/2$ in Eq. (7) is termed the dynamic head.

For each test the loss coefficient (K_L) was determined using Eq. (7), utilizing the experimental data. The results are shown in Fig. 11. The data fall in distinct patterns with K_L increasing with turning angle as well as manifold-to-orifice velocity ratio. This is consistent with expectations in that as (1) the manifold velocity increases the acceleration forces increase then energy losses should increase and (2) increasing turning angle should increase the turning loss coefficient, contraction coefficient, as well as the expansion losses. Since the data for each angle do not fit an exponential or log function the best fit equations for each angle tested are provided in Table 4 for convenience of analysis.

Of particular interest is that the intercept is ~0.6 as compared with an in-line orifice (i.e., with 0 cross velocity) of 0.5 for the contraction and expansion processes only. The difference is probably related to the friction (~0.01) and turbulence losses, which at

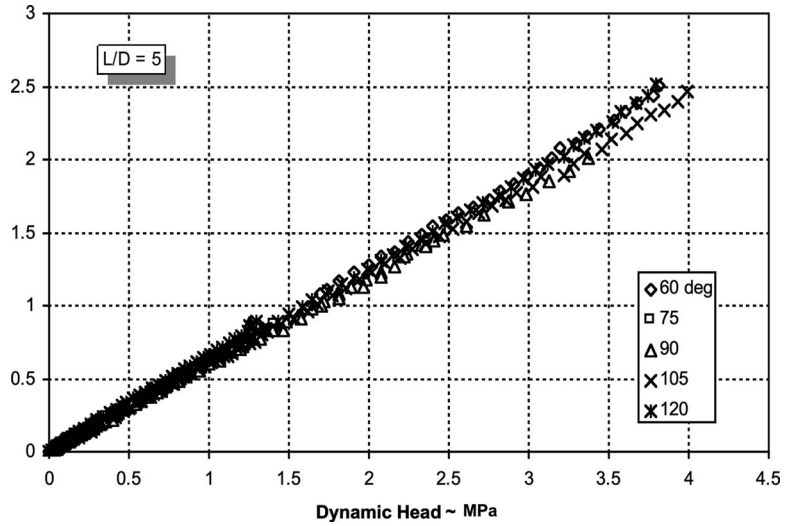

Fig. 10 Illustration of the linearity of the slope (K_L) with the dynamic head

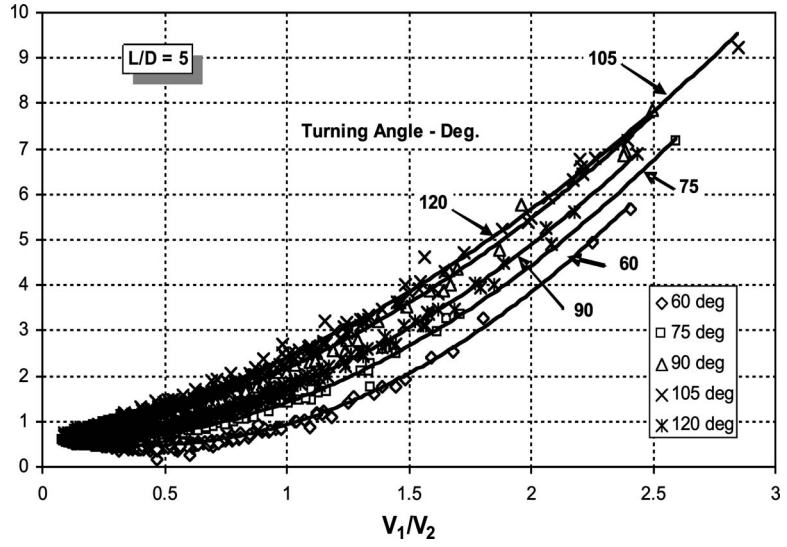

Fig. 11 Correlation of K_L for differing velocity ratio and turning angle

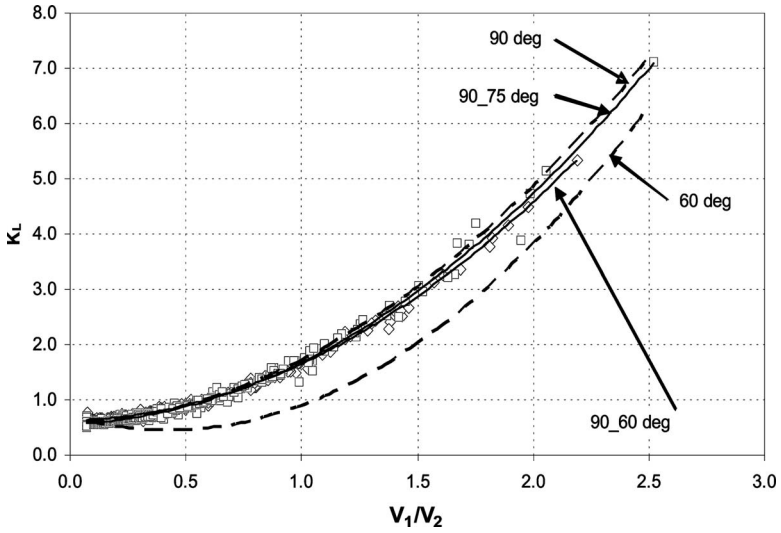

Fig. 12 Velocity ratio impact on K_L for compound angle orifices

this velocity would be expected to be small. Note that the R^2, root mean square error, is less than 1% for all angles.

4.2.2 Compound Angle Direction Feed. Impact of Orifice Variables on K_L. The head loss coefficient, K_L, for the compound angle direction feed data was also determined as a function of the manifold-to-orifice velocity ratio. The results are plotted in Fig. 12 and compared with the 60 deg and 90 deg single direction results. As for the cavitation data the turbulent noncavitation data also plot on a single curve for both the 60_90 and 75_90 orifices. However, for the noncavitation regime the comparison suggests that while the 90 deg turning angle appears to have the largest impact on head loss the orifice turning angle impacts cannot be ignored.

4.2.3 Comparison With Other Studies. There are several comparisons that can be made to illustrate the differences and similarities between well established correlations and this study. The results from this study are compared with (1) the loss coefficient as a function of velocity ratio between in-line [8] and the cross velocity configuration used in this study for various L/D, (2) existing constant area pipe bending losses as a function of the bending angle, and (3) the correlation presented by Idelchik [9] for merging and division of flow streams.

Comparison of In-Line Orifice and Cross Flow Configuration Loss Coefficient. In the cross velocity configuration only a portion of the input manifold flow is emitted through the orifice (the remainder exits through the manifold exit) after negotiating a 90 deg turn. The manifold provides a means of both varying the cross flow velocity and the velocity ratio. For in-line orifice configurations all of the flow enters the manifold and directly flows axially into the orifice. Consequently, the velocity ratio for the cross flow configuration is not equivalent to the area ratio as in the in-line orifice configuration. Therefore, the data are compared in Fig. 13 in terms of the velocity ratio rather than the area ratio. The cross flow configuration data tend to converge at a value of K_L around 0.74 at zero cross flow velocity ($V_1/V_2=0$). Comparison of the in-line configuration where the manifold provides ~0 velocities with the cross flow configuration suggests that even at near zero manifold cross velocity the turning increases the loss coefficient by about 15%.

As expected this impact increases as the velocity ratio increases. This is the result from the impact of the acceleration in turning the flow on both the contraction and expansion processes.

Comparison of Pipe Bending Losses With Manifold Turning

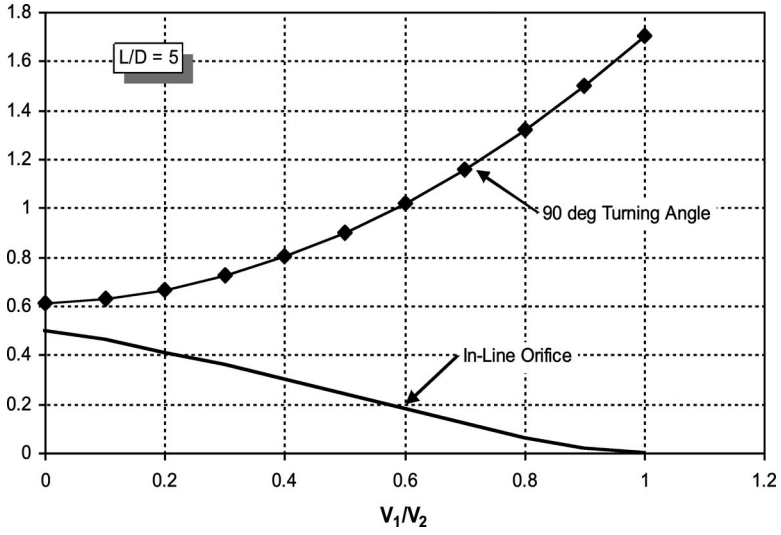

Fig. 13 Comparison of K_L for in-line [8] and cross velocity configuration

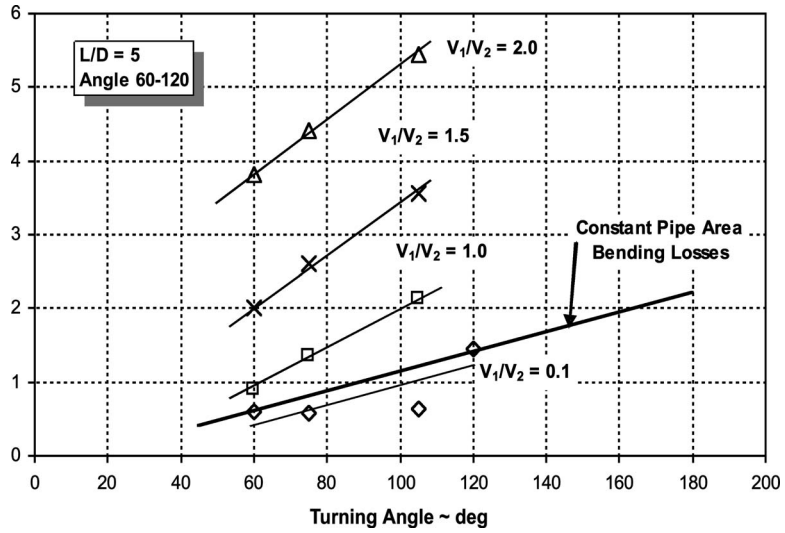

Fig. 14 Comparison of K_L between this study and constant area bending

Losses. The results from this study were also compared with pipe bending loss coefficients typically published in fluid dynamic tests [10] and handbooks [11]. Typical examples are

45 deg K_L

90 deg $K_L = 0.90$ rounded bend and 1.1 for $R/D = 0$

180 deg $K_L = 2.2$

It is assumed that for constant area bends the bending loss is independent of Reynolds number. In fact, no discussion is found to suggest that K_L is not a constant. Since for our study K_L varies not only with bending angle but also with manifold-to-orifice velocity ratio, the results cannot be directly compared. The comparison that was made was to compare the value of K_L for various V_1/V_2 ratios. This was accomplished by application of the correlations provided in Table 4 at constant velocity ratio. The results are plotted in Fig. 14. In addition, the constant area pipe bending loss coefficient for various turning bends is also plotted. Note that as the velocity ratio is lowered the value of K_L approaches that of the constant area bending loss coefficient. It would be expected that as the contraction and expansion losses are reduced the loss coefficient should approach that of a constant area bending value [11].

Comparison With Idelchik Loss Coefficient. The original translation of the Handbook of Hydraulic Resistance [9] was published in 1966. This handbook contains extensive Russian hydraulic data for a multitude of configurations. Of interest to this study are the correlations provided for merging and division of flow streams of design identical to our cross flow configuration. The Russian study included turning angles from 15 deg to 90 deg and their correlation is

$$K_L = \frac{H_L}{(\rho V_1^2/2)} \tag{15}$$

The difference between Idelchik and this study is the reference manifold inlet velocity.

The relationship for the loss coefficient defined by Idelchik is

$$K_L = A'\left(1 + \left(\frac{V_2}{V_1}\right)^2 - 2\left(\frac{V_2}{V_1}\right)\cos\alpha\right) \tag{16}$$

Note that the loss coefficient is defined as a function of both the velocity ratio and turning angle in addition to A'. A' is a variable defined by Idelchik that is a function of the volumetric flow rate ratio (equivalent to the flow rate ratio for constant density) and area ratio. Although the derivation of this variable is not discussed it seems to be a variable correction factor to Eq. (16). Idelchik provided a table for determination of K_L (Table 7-4, p. 418, Ref. [9]) as a function of the turning angle.

A comparison of the loss coefficient using the table values given by Idelchik with our data (converted to V_1 reference) is made in Figs. 15 and 16 for both 60 deg and 90 deg turning angles.

The comparison between the Idelchik correlation and the results of this study is similar in that, as the velocity ratio increases, they both asymptote at the same value. There is, however, significant difference in the actual value of resistance in the 0.25 to about 1 velocity ratio range. The characteristic sharp increase at lower values of the velocity ratio is dictated by the loss resistance, approaching infinity as V_1 approaches 0. Nevertheless, the comparison between both studies is considered to support the hypothesis made in this study that the loss coefficient (K_L) is a function of both the turning angle and velocity ratio.

5 Conclusions

The results from this study demonstrate that the simple linear relationship between C_d and $K_{\text{cav}}^{1/2}$ as well as H_L and K_L is valid for nonaxial orifices with cross flow as well as in-line orifices where the cross velocity is 0. Also, the correlations provided should aid designers in determining where cavitation will occur and define the C_c in addition to the head loss in the noncavitation regime. Additional test efforts should be directed to extend the range of results to include L/D variation for all angles, inlet r/R, increased orifice angles for compound angles, and a larger range in orifice diameters as well as other fluids to define Reynolds number impacts. It is expected that the first order relationship will not be adequate for larger area ratios.

An attempt was made to reduce the individual equations for turning angle in both the cavitation and noncavitation regimes to a single equation. However, the nonlinear nature of the equations did not produce a correlation with an acceptable error. No attempt at this time was made to reformulate our equation to conform to the equation form of Idelchik. Based on the comparisons made, the differences in the lower values of V_1/V_2 will, as a minimum, result in different constants.

The significant limitation for this study is that the manifold-to-orifice area ratio was not varied sufficiently to determine its impact. Therefore, the resulting correlations are valid only for small area ratios.

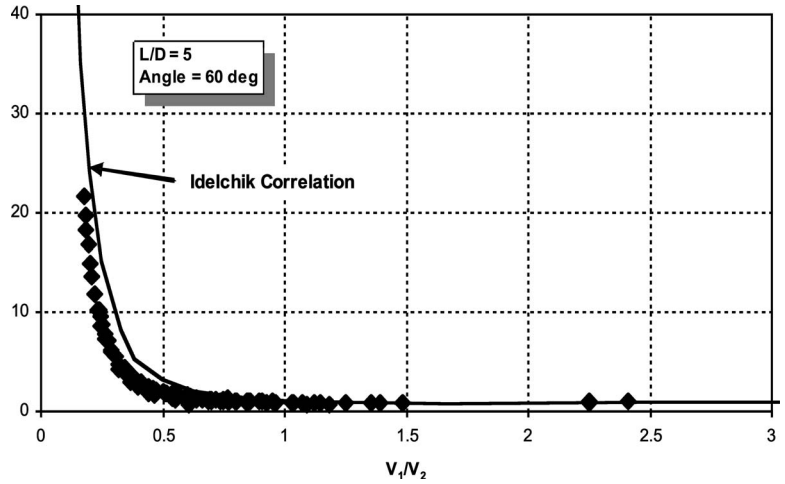

Fig. 15 Comparison of Idelchik with this study for 60 deg angle

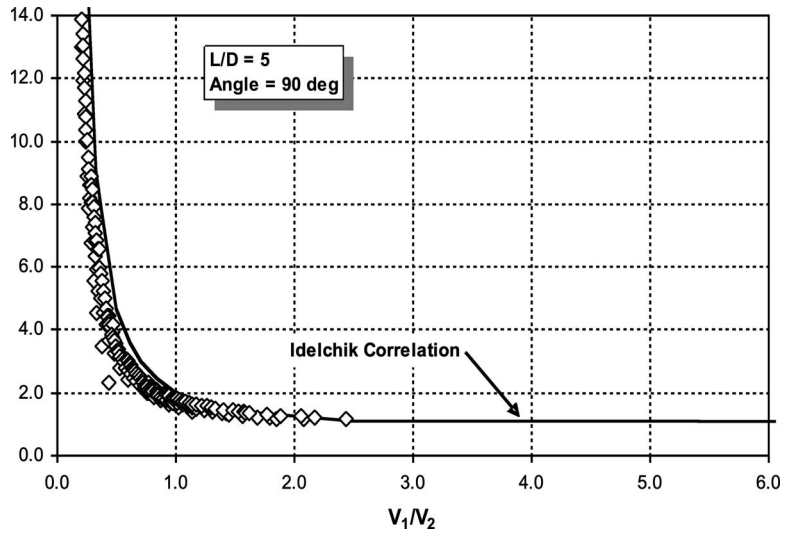

Fig. 16 Comparison of Idelchik with this study for 90 deg angle

The conclusions that can be drawn from the results presented are as follows.

5.1 Cavitation Regime.

- In the cavitation regime, C_c is controlled by the cavitation parameter for in-line flows.
- When only part of the flow enters the orifice (i.e., cross velocity flow) the contraction coefficient is governed by both the turning angle and the velocity ratio V_1/V_2.
- Inception of cavitation occurs at a K_{cav} of 1.8.
- Full cavitation occurs at a K_{cav} of $\sim$1.5–1.8.
- For the compound angle orifices C_c is more impacted by the initial 90 deg turning angle than the orifice turning angle.

5.2 Noncavitation Regime.

- The head loss coefficient K_L was found to be a function of both turning angle and velocity ratio V_1/V_c when only part of the manifold flow enters the orifice.
- For the compound angle orifices K_L is more impacted by the initial 90 deg turning angle than the orifice turning angle.

The application of our results to predict orifice C_d is rather straightforward. Obviously the first step is similar to that described above utilizing the design information to determine that it does not fall within the cavitation regime. Once this is determined then K_L is determined from Fig. 12 or the equation and constants provided in Table 4, and the head loss, H_L, is determined from Eq. (7). Lastly, C_d can then calculated from Eq. (2).

Nomenclature

A, B, C = constants defined in Eqs. (13) and (14) and Table 4
A' = Idelchik defined value used in Eq. (16)
A_1 = manifold area (m^2)
A_2 = orifice area (m^2)
A_2/A_1 = area ratio
A_c = vena-contracta area (m^2)
b = constant defined in Eq. (11)
C_c = contraction coefficient, A_2/A_c
C_d = discharge coefficient
D = orifice diameter (mm)
H_L = head loss (MPa)
K_{cav} = cavitation parameter
K_L = loss coefficient
L = orifice length (mm)
P_1 = manifold pressure (MPa)

P_2 = back pressure downstream of the orifice exit (MPa)
P_v = fluid vapor pressure (MPa)
Re = Reynolds number
V_1 = manifold entrance velocity (m/s)
V_2 = orifice velocity (m/s)
V_1/V_2 = velocity ratio
V_c = vena-contracta velocity (m/s)
V_{out} = manifold exit velocity (m/s)

Greek

ρ = liquid density (g/cm^3)
θ = turning angle (deg)

References

[1] Nurick, W. H., 1976, "Orifice Cavitation and Its Effect on Spray Mixing," ASME Trans. J. Fluids Eng., **98**(4), pp. 681–687.
[2] Nurick, W. H., Ohanian, T., Talley, D. and Strakey, P., 2008, "Impact of L/D on 90 Degree Sharp-Edge Orifice Flow With Manifold Passage Cross Flow," submitted.
[3] Martynov, S., Mason, D., and And Heikal, M., 2005, "Hydrodynamic Similarity of Cavitation Flows in Nozzles" *Proceedings of the Fifth International Symposium on Multiphase Flow, Heat Mass Transfer and Energy Conversion*, Xi'am, China.
[4] Mishra, C., and Peles, Y., 2005, "Size Scale Effects on Cavitating Flows Through Microorifices Entrenched in Rectangular Microchannels," J. Microelectromech. Syst., **14**(55), pp. 987–999.
[5] Heiniger, K. C., 2001, "Introduction to the Flow States in Water Jet Systems," WJM–2001, Krakow.
[6] Schmidt, D. P., Rutland, C. J., and Corradini, M. L., 1997, "A Numerical Study of Cavitating Flow Through Various Nozzle Shapes," SAE Paper No. 971597.
[7] Knapp, R. T., Daily, J. W., and Hammitt, F. G., 1970, *Cavitation*, McGraw-Hill, New York.
[8] Weisbach, J., 1885, *Die Experimental Hydraulik*.
[9] Idelchik, I. E., 2003, *Handbook of Hydraulic Resistance*, 3rd ed., Jaico, Mumbai.
[10] Vernard, J. K., 1954, *Elementary Fluid Dynamics*, 3rd ed., Wiley, New York.
[11] Perry, R. H., and Chilton, C. H., 1963, *Chemical Engineers Handbook*, 5th ed., McGraw-Hill, New York.

Numerically Investigating the Effects of Cross-Links in Scaled Microchannel Heat Sinks

Minh Dang

Ibrahim Hassan[1]
e-mail: ibrahimh@alcor.concordia.ca

Sung In Kim

Department of Mechanical and Industrial Engineering,
Concordia University,
Montreal, QC, H3G 1M8, Canada

Thermal management as a method of heightening performance in miniaturized electronic devices using microchannel heat sinks has recently become of interest to researchers and the industry. One of the current challenges is to design heat sinks with uniform flow distribution. A number of experimental studies have been conducted to seek appropriate designs for microchannel heat sinks. However, pursuing this goal experimentally can be an expensive endeavor. The present work investigates the effect of cross-links on adiabatic two-phase flow in an array of parallel channels. It is carried out using the three-dimensional mixture model from the computational fluid dynamics software, FLUENT 6.3*. A straight channel and two cross-linked channel models were simulated. The cross-links were located at 1/3 and 2/3 of the channel length, and their widths were one and two times larger than the channel width. All test models had 45 parallel rectangular channels, with a hydraulic diameter of 1.59 mm. The results showed that the trend of flow distribution agrees with experimental results. A new design, with cross-links incorporated, was proposed and the results showed a significant improvement of up to 55% on flow distribution compared with the standard straight channel configuration without a penalty in the pressure drop. Further discussion about the effect of cross-links on flow distribution, flow structure, and pressure drop was also documented.* [DOI: 10.1115/1.3001093]

Keywords: two-phase flow, cross-links, CFD, flow distribution, pressure drop, microchannel heat sinks

1 Introduction

In the past decades, heat sinks have emerged as a cooling approach to improve thermal management for high performance miniaturized electronics devices. Since the pioneering work of Tuckerman and Pease [1], various studies have been conducted to investigate heat transfer characteristics, such as flow distribution and flow pattern, in microchannel heat sinks. In this research area, poor cooling performance from the nonuniform temperature distribution on the surfaces of heat sinks requires a solution as it causes maldistribution in an array of multiple channels. A number of experimental studies have been conducted to improve flow distribution through header modifications such as the works of Samson et al. [2], and Hrnjak [3], or through modification of the channel core using cross-links [4–6]. However, in the search for appropriate designs with uniform flow distribution for microchannel heat sinks, experimental analysis can be prohibitively expensive. Taking advantage of computer hardware and software available today, computational fluid dynamics (CFD) studies can be a favorable approach to pursue the same goal.

Literature on the investigations of two-phase flows in multiple channels contains ample experimental data but lacks available results from numerical studies. A number of studies have been carried out for two-phase flow in a single channel, tubes, tube bends, and *T*-junctions by using different methods such as the volume of fluid (VOF), mixture, and Eulerian.

Qian and Lawal [7] studied slug Taylor flow at a T-junction in a single microchannel using the VOF method in FLUENT. They compared the slug length to those in other experiments and showed agreement. Correlations were also made to predict the gas and liquid slug lengths. Yang et al. [8] studied bubbly two-phase flow in a narrow channel, using the Lattice–Boltzmann method. Their results showed that the average film thickness of the liquid fluid between the Taylor bubble and the channel wall agreed with the classical analytical correlation developed by Bretherton [9].

Other studies used two fluids other than gas and liquid to study the blocking length in the pipe when fluid and solid were incorporated into the two-phase pipe flow [10]. Shepel and Smith [11] used a new level set method for modeling two-phase incompressible flows with moving boundaries, and the method was implemented in the CFX-4 code. Aliabadi et al. [12] used the Eulerian method to study three-dimensional two-phase flow in pipe bends. The results showed that the model can accurately predict the experimental pressure drop for single phase. However, it could not predict the experimental data for two-phase pressure drop in their studied range.

Further numerical results can be found in works on single-phase flow to optimize the geometrical design of parallel multichannel configurations of heat sinks [13,14]. Unlike the single-phase flow, the two-phase flow behavior in an array of parallel channels is very complex. Thus, the simulation of two-phase flow in multiple channels should be expected to cause some issues because of time consumption for convergence or insufficient memory of available computer resources. Due to such potential challenges, computational domains as well as simulation methods should be carefully considered. Moreover, since a universal two-phase model is not yet available, various two-phase models are still being developed.

The present work attempts a numerical study on the effect of cross-links incorporated in the channel core of scaled microchannel heat sinks. The results will be compared with experimental data obtained from the previous work [6], which investigated the effects of cross-links in six different configurations of scaled microchannel heat sinks, as summarized in Table 1. The experimental setup is shown in Fig. 1. Water is collected from the four selected channels in a graduated cylinder while the elapsed time is

[1]Corresponding author.

Contributed by the Fluids Engineering Division of ASME for publication in the JOURNAL OF FLUIDS ENGINEERING. Manuscript received July 14, 2007; final manuscript received July 3, 2008; published online October 23, 2008. Assoc. Editor: Rajat Mittal.

Table 1 Summary of experimental test section geometries

Test sections	No. of channels	Channel width (mm)	Channel length (mm)	No. of cross-links	Width of cross-links (mm)	Positions of cross-links respected to channel length
STR	45	1.5875 (1/16 in.)	131.3	—	—	—
CR-2	45	1.5875 (1/16 in.)	131.3	2	1.5875 (1/16 in.)	1/3 and 2/3s
CR-2A	45	1.5875 (1/16 in.)	131.3	2	3.175 (2/16 in.)	1/3 and 2/3s
CR-2B	45	1.5875 (1/16 in.)	131.3	2	4.7625 (3/16 in.)	1/3 and 2/3s
CR-4	45	1.5875 (1/16 in.)	131.3	4	1.5875 (1/16 in.)	1/5, 2/5s, 3/5s, and 4/5s
CR-6	45	1.5875 (1/16 in.)	131.3	6	1.5875 (1/16 in.)	1/7, 2/7s, 3/7s, 4/7s, 5/7s, and 6/7s

recorded (Fig. 2). This procedure is repeated for each of the four selected channels for flow measurements. From uncertainties in the measurement instrumentation including the timer, flow meters, and metering cylinders, an uncertainty of less than 5% is estimated for flow measurements. Uncertainty in pressure drop measurement is estimated at 0.45 kPa (0.065 psi) based on instrument specification. Three sets of 400 data points were taken in periods of 2 s to measure pressure drop for a particular flow condition. The mean of these three measuring sets was calculated for the pressure drop of the system, including the tube connected to the test section. The same procedure was then repeated for the tube only. The pressure drops for the test section are then differences of the means of the above pressure drop measurements.

Their results showed that there was a significant impact on flow distribution due to the effect of cross-links incorporated to the channel core. However, they suggested that more investigation of the effects of cross-links is needed since the effect of cross-links cannot overcome maldistribution due to the entrance effect. There are several approaches suggested in their work, for example, an increased number of cross-links with widths twice that of the channel, as well as inclined angles between cross-links. These approaches are suggested based on the results that flow could be easily shared along the cross-links from high flow channels to low flow channels. This demonstrates that numerical work can allow researchers a preliminary search for appropriate designs before continuing with further experiments.

In developing cross-linked heat sinks, a number of unknown parameters exist including the cross-link width and the number of cross-link paths. The role these parameters play on the two-phase flow characteristics and heat transfer is not clear. Ideally, heat transfer investigations could be carried out on each of the possible configurations to-scale. The present work numerically simulated models of the scaled microchannel heat sinks under adiabatic conditions. The aim is to develop and validate the models of a two-phase flow in microchannel heat sinks by using CFD software FLUENT, and then to compare with experimental results. This study

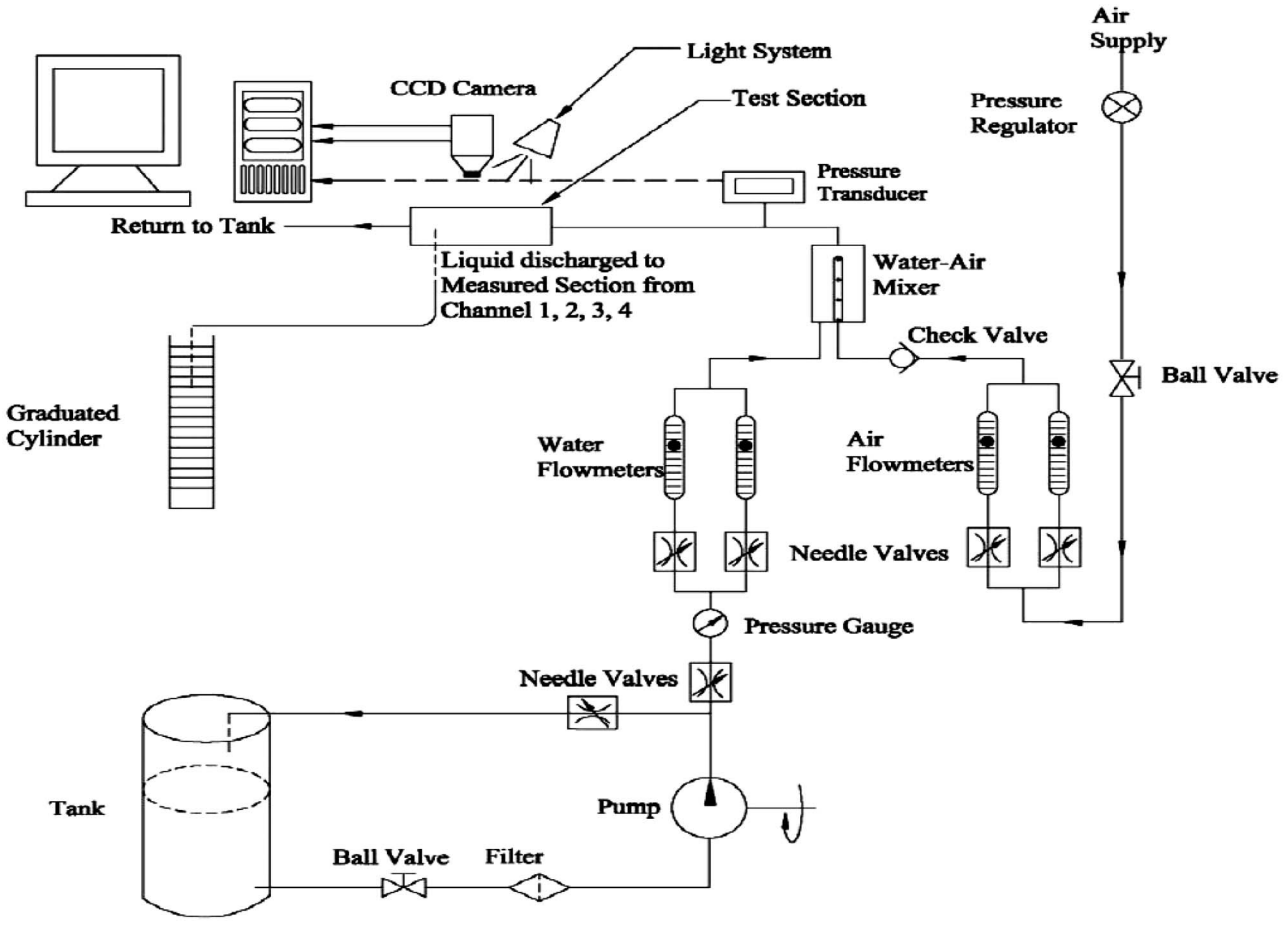

Fig. 1 Schematic of the experimental setup

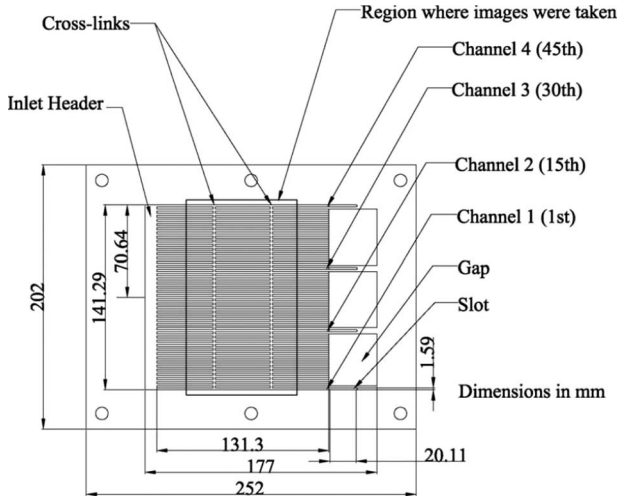

Fig. 2 Experimental cross-linked channel plate

is also conducted to look for better designs for two-phase flow distributions in multiple channels heat sinks. This is part of a larger research program whereby the knowledge gained will be helpful in identifying promising designs to be investigated under to-scale conditions with heat transfer.

1.1 Methods of Modeling the Experiments. Three test models, having the same geometry of the test models in the work of Dang and Hassan [6], are simulated in the present work. The difference between the three test models is that the cross-links were introduced to the channel core of the standard straight channel model (STR). The cross-linked models, namely, CR-2 and CR-2A, consist of two cross-links that are located 1/3 and 2/3 of the channel length and have a width of one and two times larger than the channel width, respectively. The computational domain is shown in Fig. 3(*a*). The origin of the coordinate is located right below the center of the inlet hole on the bottom surface of the header. The computational results of three models are validated by comparing with experimental data. A new design is also proposed and simulated in the present paper, as illustrated in Fig. 3(*b*). The proposed design has cross-links inclined with angles from high flow channels to low flow channels.

The commercial CFD code FLUENT 6.3 is used to simulate the 3D two-phase flow with the same experimental flow conditions [6] (see Table 2). For a three-dimensional two-phase flow, there are several available models in FLUENT, such as VOF, discrete phase, mixture, and Eulerian. However, each model can be used depending on the particular interest of researchers. For example, VOF, a free surface flow model, is used most often to simulate two-phase flow pattern. However, this model cannot allow two-phase flows to be interpenetrated. It is therefore used for particular flow patterns, for example, plug, bubble flow, without dispersed phases.

The mixture model is a simplified multiphase flow model, and it is less computationally expensive. It allows phases to interpenetrate and to move with different velocities. It is also used as a homogeneous two-phase model when phases move at the same velocity. The volume fractions of phases can vary from 0 to 1 for a control volume. The mixture model is therefore used as a suitable two-phase model to seek appropriate designs for microchannel heat sinks in terms of flow distribution. Water and air at room temperature are used for simulation while their properties are determined.

The two-phase flow is considered to be incompressible for a studied flow range. The steady state is also assumed in this study, while the standard k-ε turbulent model is taken into account. The cavitation model is not considered in this study. Moreover, since the hydraulic diameter of the channel is small, the effect of gravity can be neglected. The governing equations can be written as follows.

For the continuity equation,

$$\nabla \cdot (\mathbf{v}_m) = 0 \tag{1}$$

For the momentum equation,

$$\nabla \cdot (\rho_m \mathbf{v}_m \mathbf{v}_m) = -\nabla P + \nabla \cdot [\mu_m (\nabla \mathbf{v}_m + \nabla \mathbf{v}_m^T)] + \mathbf{F} + \nabla \cdot \left(\sum_{k=1}^{n} \beta_k \rho_k \mathbf{v}_{dk,k} \mathbf{v}_{dr,k} \right) \tag{2}$$

For the volume fraction equation,

$$\nabla \cdot (\mathbf{v}_m) = -\nabla \cdot (\mathbf{v}_{dr,k}) \tag{3}$$

where the mass average velocity $\mathbf{v}_m$ is

$$\mathbf{v}_m = \frac{\sum_{k=1}^{n} \beta_k \rho_k \mathbf{v}_k}{\rho_m} \text{ m/s} \tag{4}$$

where β_k is the volume fraction of phase k.

The drift velocity for secondary phase k $\mathbf{v}_{dr,k}$ is

$$\mathbf{v}_{dr,k} = \mathbf{v}_k - \mathbf{v}_m \tag{5}$$

The dynamic viscosity of the mixture μ_m is

$$\mu_m \sum_{k=1}^{n} \beta_k \mu_k \text{ N s/m}^2 \tag{6}$$

and the mixture density ρ_m is

$$\rho_m = \sum_{k=1}^{n} \beta_k \rho_k \text{ kg/m}^3 \tag{7}$$

1.2 Inlet and Outlet Boundary Conditions. For the inlet boundary condition, the two-phase flow mixture is assumed to be homogeneous. Moreover, the above assumptions lead to determining the volume fraction and the mixture velocity for the inlet flow boundary condition from Eqs. (8) and (9). The volume fraction is determined as the same as the volume quality, which is the ratio of the volume flow rates of a gas and a mixture (Eq. (8)). The boundary conditions at the channel outlets are set as a pressure outlet with ambient pressure. An adiabatic wall boundary condition with no-slip is imposed at all walls.

$$\beta_G = \frac{\boldsymbol{Q}_G}{\boldsymbol{Q}_m} \tag{8}$$

$$j_m = \frac{j_G}{\beta_G} \tag{9}$$

2 Results and Discussion

2.1 Mesh Independence and Validation. Mesh independence test is conducted for the STR model using four different mesh systems, namely, coarse mesh, base mesh, fine mesh, and finer mesh (Table 3). The hexahedral mesh is used for the header, the channels, and the cross-links, whereas the tetrahedral mesh is used for the inlet tube, as illustrated in Fig. 4. The V-velocity profiles along a cross line in the header (located at $Y=0.0023$, $Z=0.0007$) and at the channel outlets ($Z=0.0007$) are compared for mesh independence. The results show that almost the same velocity profiles are observed for the fine and finer mesh systems (Fig. 5). Moreover, using these mesh types, the V-velocity profiles at the corner of the header are reasonable. The flow gradually decreases near the end wall of the header and ends up at zero veloc-

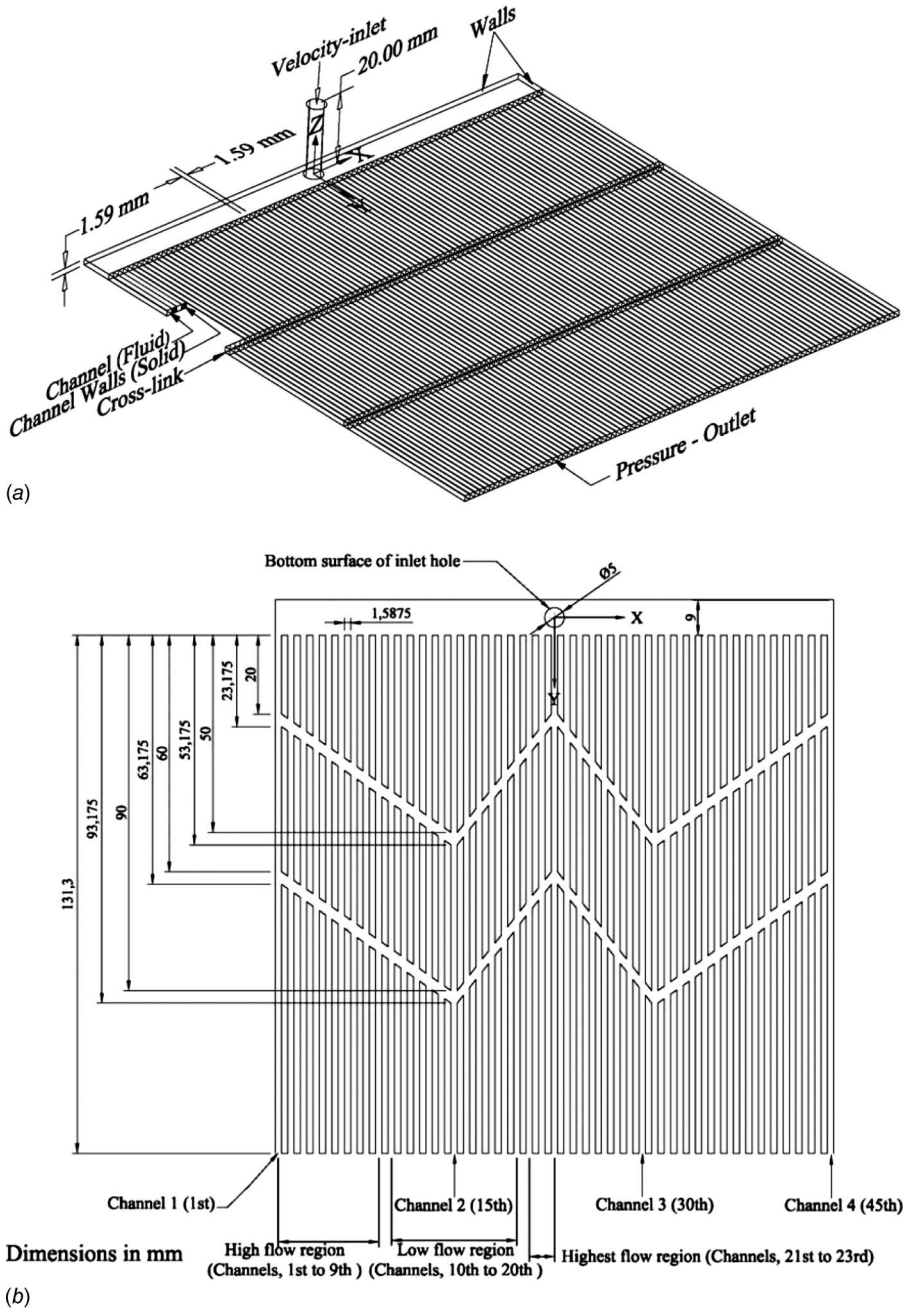

Fig. 3 Test module

ity when they reach the wall. This cannot be seen when using the coarse and base mesh types since their grid sizes are too large to resolve the flow near the wall (Fig. 4(*a*)). It is interesting to note that the finer mesh has almost double the number of cells compared with the fine mesh system. To conserve computational time, the fine mesh type is used in all cases. The results converge in a range of 3500–4500 iterations with 10^{-6} residuals.

To validate the present work, the mass flow rates of water in four selected channels, 1, 2, 3, and 4, corresponding to the 1st, the

Table 2 Flow conditions

Case	J_G (m/s)	J_L (m/s)	J_m (m/s)	β_{air}	x
1	0.142	4.828	4.970	0.029	3×10^{-5}
2	2.186	1.581	3.766	0.580	0.002
3	2.186	0.819	3.004	0.727	0.003
4	26.642	0.819	27.461	0.970	0.037

Table 3 Mesh information

Examined mesh	Total no. of cells
Coarse	419,235
Base	430,329
Fine	636,838
Finer	1,250,419

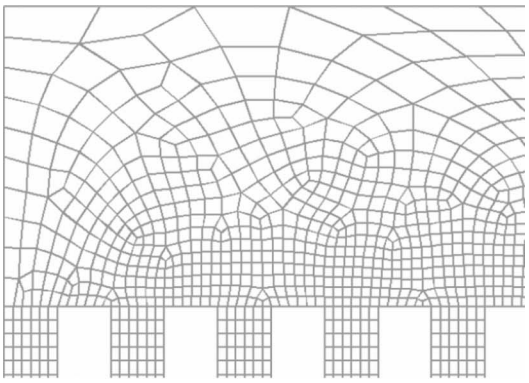

(*a*)

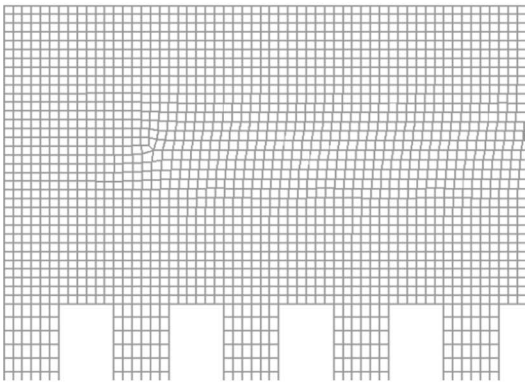

(*b*)

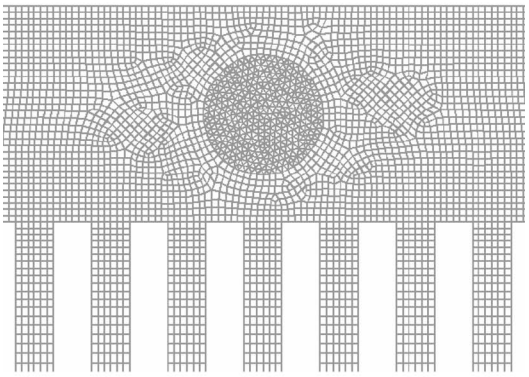

(*c*)

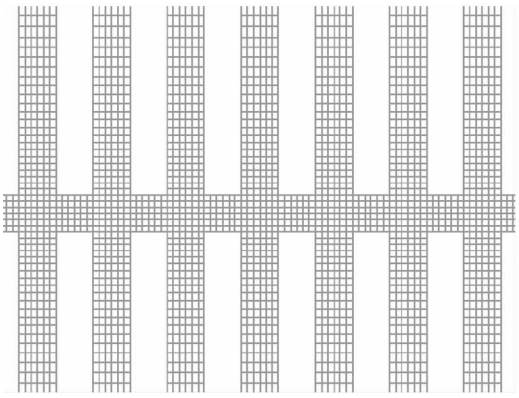

(*d*)

Fig. 4 Samples of chosen mesh

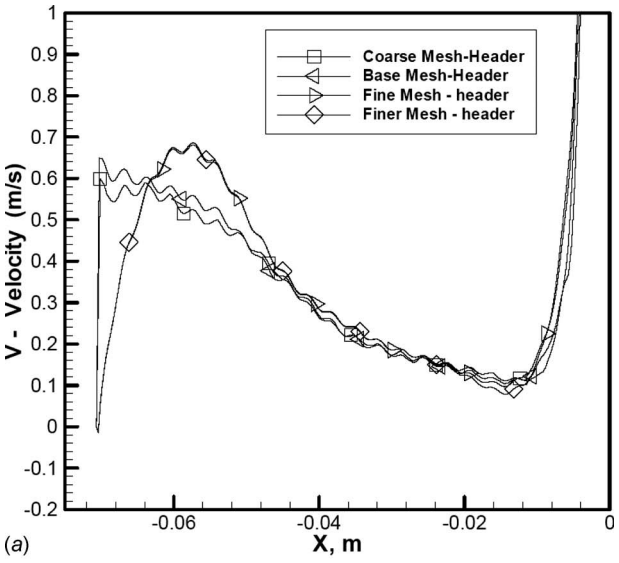

(*a*)

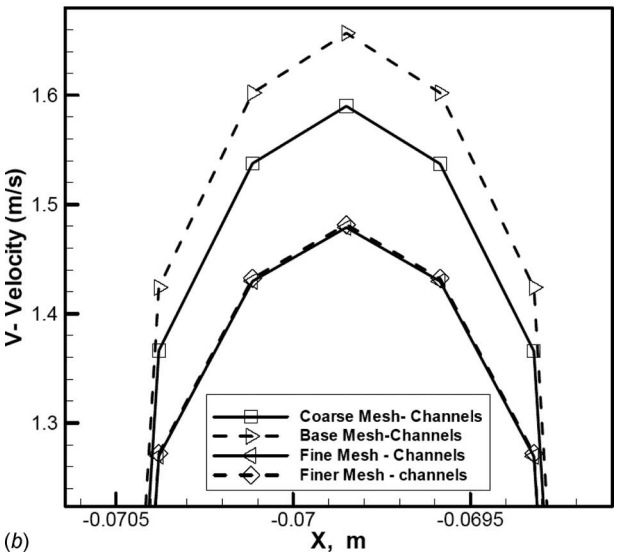

(*b*)

Fig. 5 Results of mesh independence test, taken from Case 1

15th, the 30th, and the 45th channels of the 45 channels (Fig. 3), are compared with the experimental data in Fig. 6. The results show that both numerical and experimental data have the same trend of flow distribution in the four selected channels. The numerical results, however, show that the present data underpredicts the experimental data for all cases. It is also observed that the flow distribution results are symmetrical to numerical results in this study but not to the experimental data. There are smaller differences between numerical and experimental data for channels 1 and 2 than for channels 3 and 4. Differences exist due to the CFD assumption as well as the experimental uncertainty.

2.2 Flow Distribution. The CFD study enables ease in gaining insight into flow distribution throughout 45 channels, whereas it is difficult to obtain from experiments. Figure 7 presents the channel outlets' flow distribution comparison between the test models for different flow conditions. The results of flow distribution show that a high water mass flow rate occurs at certain central channels and some outermost channels for all test models. The results show symmetric flow distributions throughout 45 channels for all test models. For simplification, a flow distribution profile can be divided into three regions with respect to the ideal uniform flow distribution. The highest flow rate region is from the 21st–

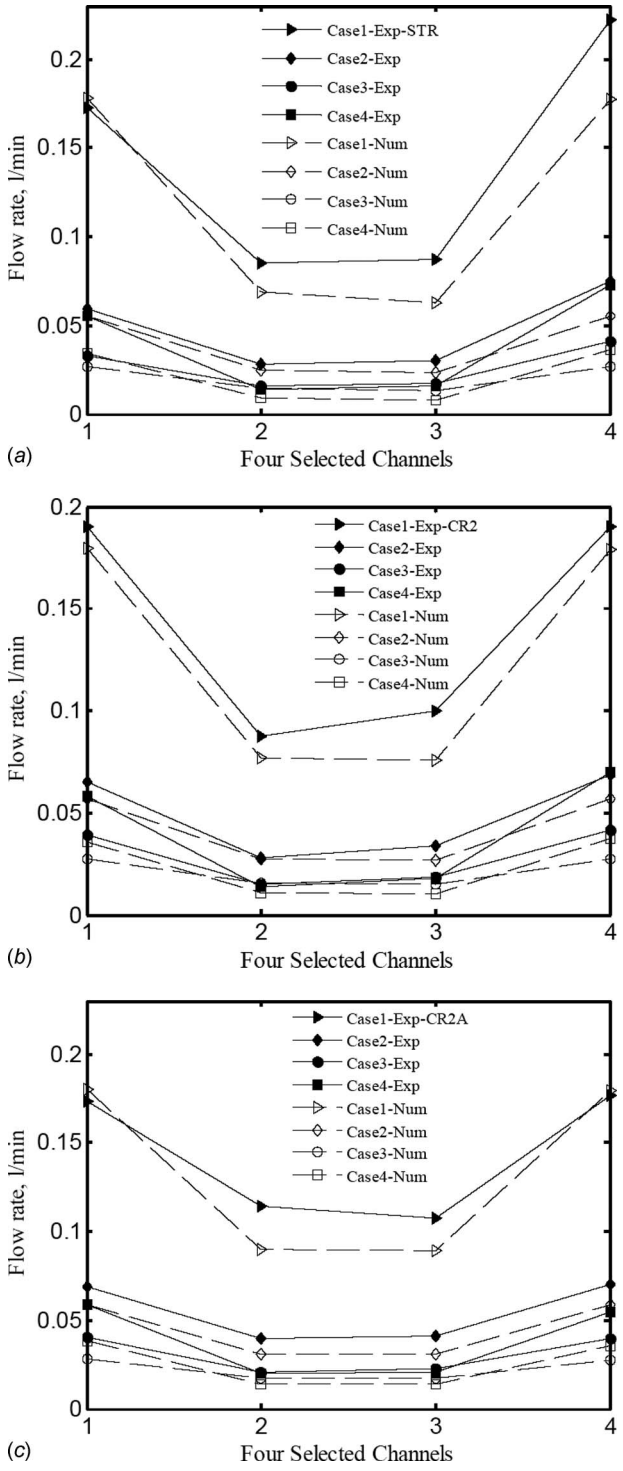

Fig. 6 Flow distributions compared with experimental results

23rd channels, the high flow rate region is from 1st–9th channels, and the low flow rate region is from 10th–20th channels (indicated in Fig. 3(*b*)). These flow regions can be considered for both sides, as per symmetric flow distribution. In the low flow rate region, mass flow rate is lower than ideal mass flow rate for all test models. However, the deviation between the measured flow rate and the ideal flow rate tends to decrease, close to ideal uniform line, when the cross-links are incorporated. These results are the same for other flow regions. Figure 7(*e*) presents the comparison of flow distribution between test models in terms of the standard deviation calculated from

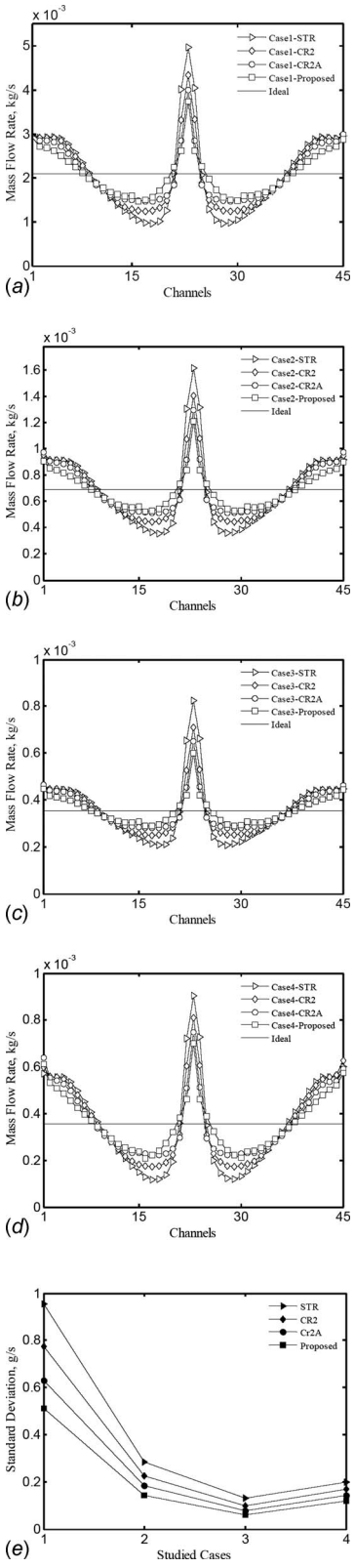

Fig. 7 Comparison of flow distributions for all test models

$$\mathrm{STDEV} = \sqrt{\frac{1}{N-1}\sum_{i=1}^{N}(x_i - \bar{x})^2} \tag{10}$$

The results show that the standard deviation decreases from Case 1 to Case 3 and it starts to increase at Case 4 for all test

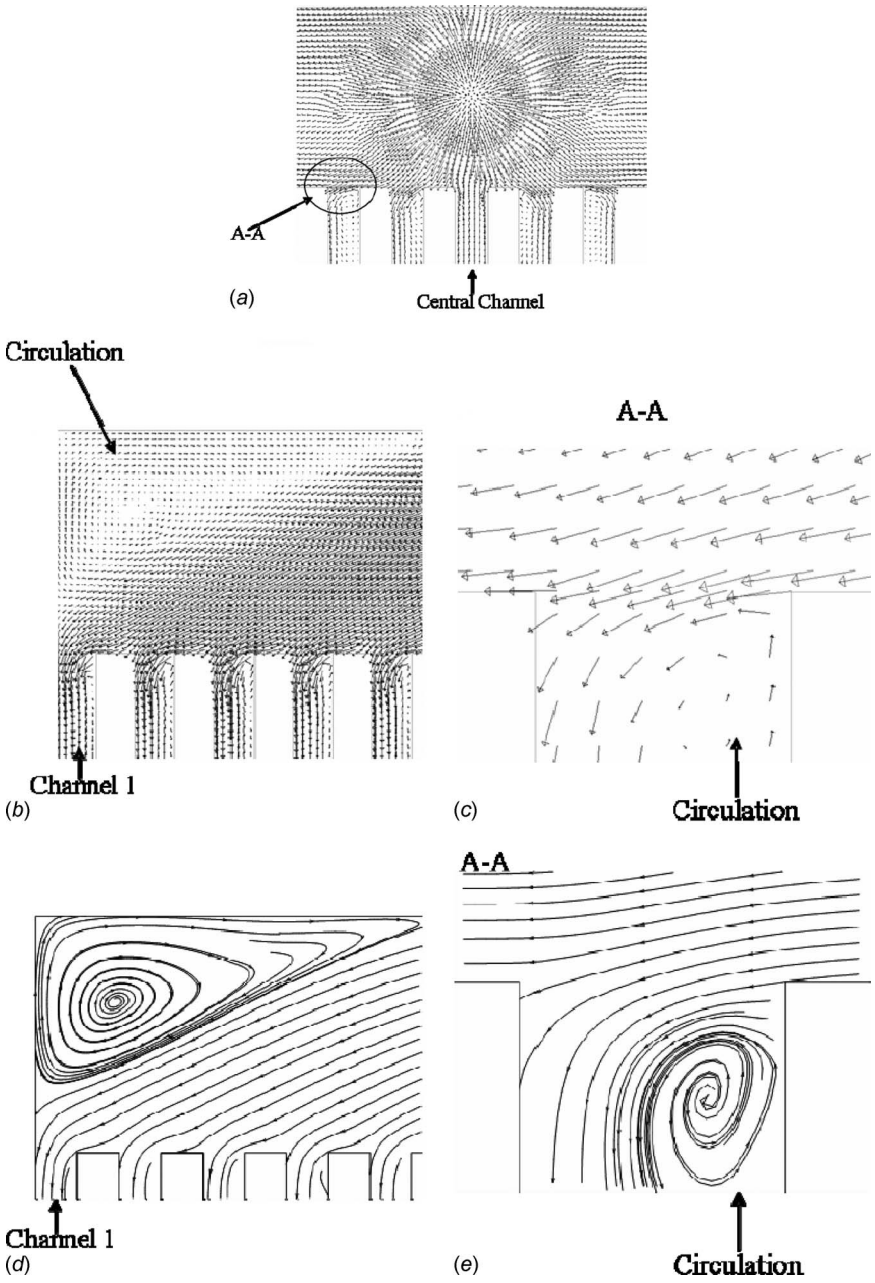

Fig. 8 Velocity vectors and streamlines in the header and channel entrance region (Case 1)

models. The lowest standard deviation is observed at Case 3. The lower standard deviation means better flow distribution. Notably, Dang and Hassan [6] observed intermittent flow patterns (plug and elongated bubble flow patterns) as dominant flow patterns in the straight and cross-linked models in this case. However, more data points between these studied cases should be investigated to see what flow conditions will result in uniform flow distribution. Compared with the standard STR model, the cross-linked and the proposed models have lower standard deviations, where the standard deviation improves from 39% to 55%, from 28% to 40%, and from 14% to 25% in a studied flow range for the proposed CR-2A and CR-2 models, respectively.

The flow distribution inside the header plays an important role in an array of parallel multiple channels. To understand the physical flow behavior inside the header, Fig. 8 presents a velocity vector of two-phase flow near the inlet tube of the header (Fig. 8(*a*)) and at the corner end of the header (Fig. 8(*b*)). From these figures, circulations are observed in some regions, especially at the corners of the header, due to the stagnation region. It is also observed that circulations occurred at the entrance regions of each channel. Small circulations are observed at the high and highest flow regions, whereas larger circulations are observed in the low flow region. In channels with large circulations, entrance flow is limited (Fig. 8(*e*)). Circulations at the channel entrances are due to the cross flow effects, such as a high momentum cross flow passing by the cavity, which is the entrance of channels in this case (Fig. 8(*c*)). The cross flow is pushed to the end wall of the header. Hence, a higher flow rate is observed at the outermost channels (1st and 45th in Fig. 7). No cross flow is observed at the inlet of 23rd, the central channel, which is in line with the flow inlet. As a result, the highest flow is observed in this channel for all studied cases. It is suggested that rounding the inlets of channels will lessen the cross flow effect at the channel entrances.

Introducing cross-links into the channel core allows flow shar-

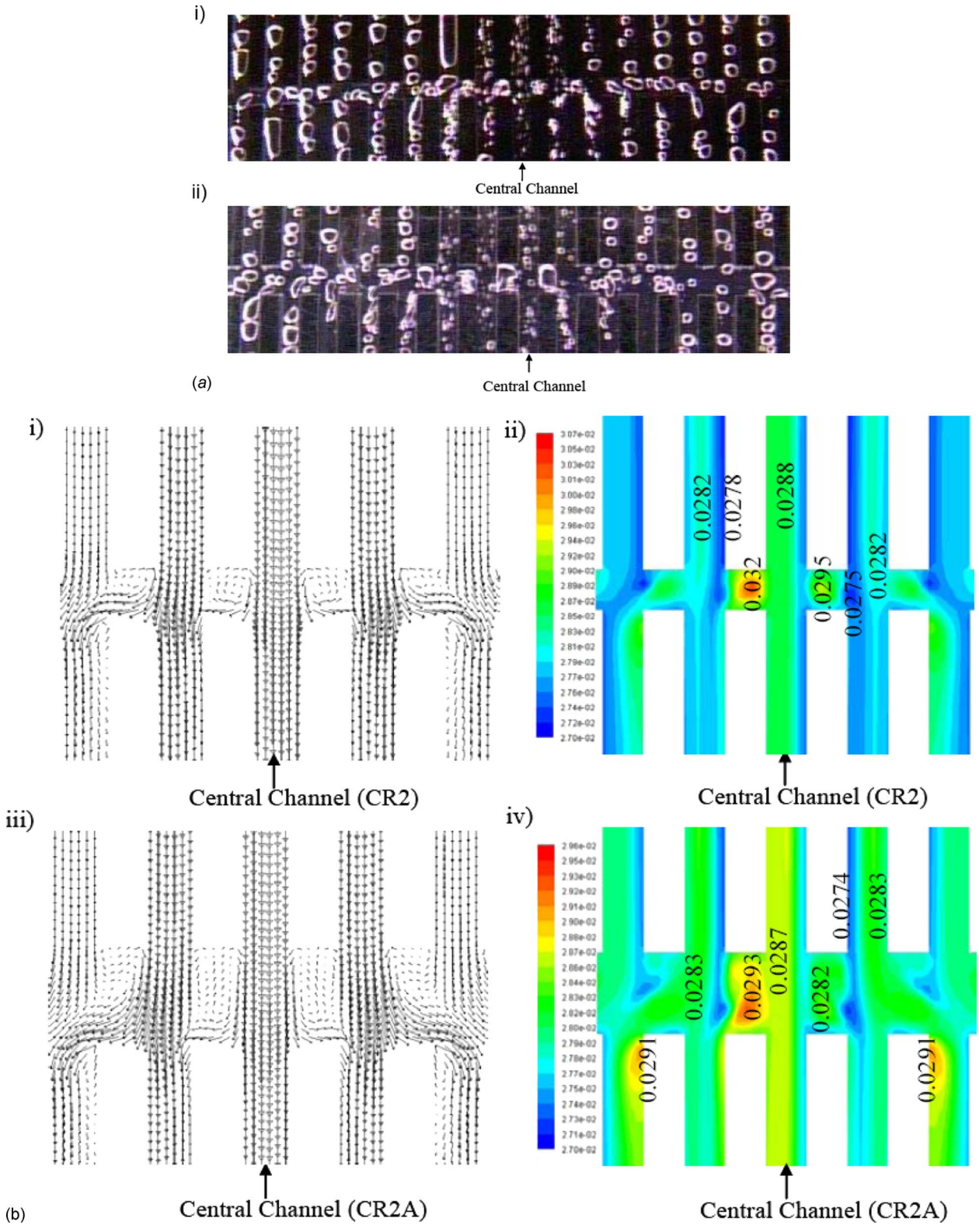

Fig. 9 Samples of flow sharing from cross-links (Case 1).

ing from high flow rate channels to low flow rate channels [6]. This can be seen in Fig. 9, which presents the velocity vector of flow field in cross-links at Case 1. The two-phase mixture velocities show that they traverse from high flow rate channels to low flow rate channels along the cross-links, as supported by the images in Fig. 9(*a*). Although the bubbles cannot be seen in the CFD results, it can be shown that the circulation is present in the cross-links and channels. It is observed that the larger cross-links permit more flow sharing compared with smaller cross-links (Fig. 9). The cross-links are considered as the additional inlets and exits along channels. Circulations are observed in the cross-links between channels, as well as in the channels after flow goes through the cross-links. This partially prevents flow sharing among channels through the cross-links. Figure 9(*b*) also presents the volume frac-

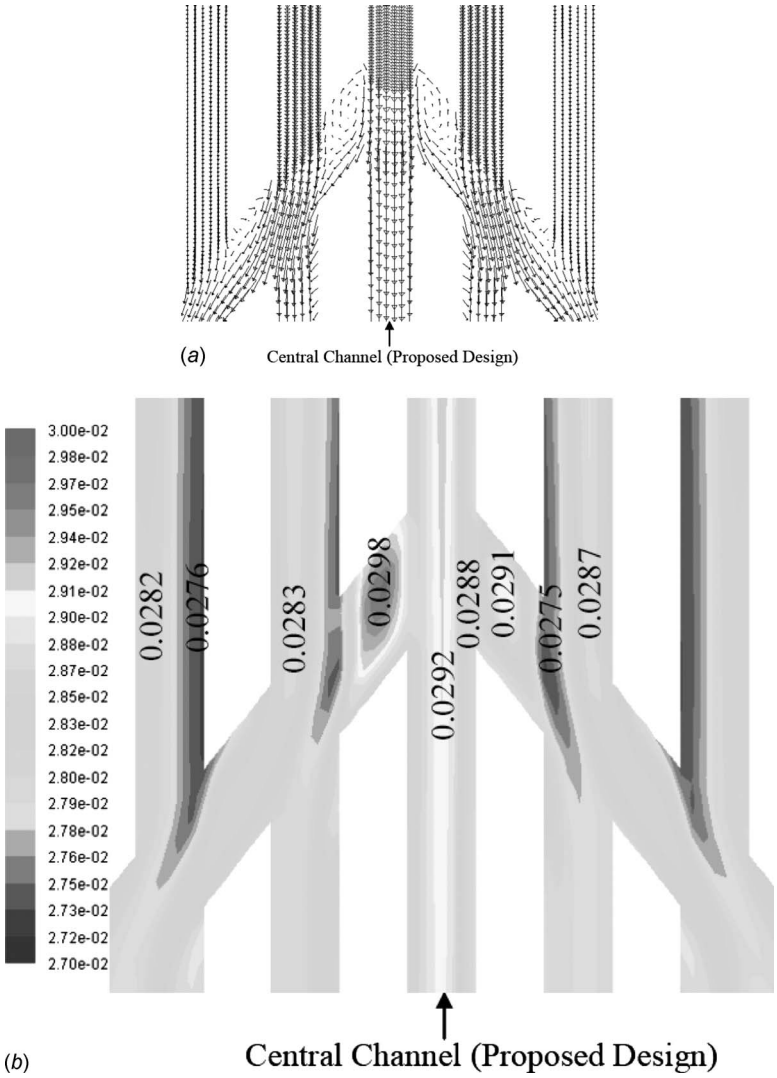

Fig. 10 Sample of flow sharing from cross-links for the proposed design (Case 1, β=0.0286)

tion of air in the channels and the cross-links at Case 1, with the volume fraction of 0.0286 for the inlet flow condition. This figure shows that some regions with a high volume fraction of air among the channels and the cross-links, for example, a value of 0.032, can mean the possibility of bubbles. Figures 10 and 11 show more two-phase flow mixture sharing between channels due to less circulation observed in the inclined cross-links. As a result, the proposed design improves flow sharing from high flow rate channels to low flow rate channels.

The effect of the cross-links on flow distribution will be more understood from flow analysis through Fig. 12, which presents the *V*-velocity distribution along the center lines of the 1st, 15th, and 23rd channels at Case 1. From this figure, two-phase flow velocity is disturbed at the entrance of the channels, especially from the 15th channel due to the effect of cross flow (Fig. 8(*c*)). The two-phase flow enters and develops along the channel. A fully developed flow is observed in the STR model results, whereas the developing flows are observed in the CR-2, the CR-2A, and in the proposed design results. Two-phase flow velocities are disturbed when flow goes through the cross-links. This is due to cross flow sharing between channels through the cross-links.

The velocity profiles can explain how flow distribution improves due to the effects of cross-links. Figure 12(*a*) shows that high velocity is observed at the exit of the 1st channel for the CR-2 and the CR-2A models, but low velocity is observed from the proposed design when compared with the straight model. The straight cross-links cannot be effective in this channel, whereas the inclined cross-links can be. The improvement is observed in the 15th channel (Fig. 12(*b*)). The *V*-velocity increases 38.4% for the proposed model compared with that for the STR model, whereas 13.6% and 30.8% for the CR-2 and the CR-2A models, respectively. The improvement is also observed in the 23rd channel, where the *V*-velocity in this channel decreases 24.4% for the proposed model and 12.6% and 19.3% for the CR-2 and the CR-2A models, respectively (Fig. 12(*c*)). Therefore, we can obtain more improved (uniform) flow distribution using the proposed model.

2.3 Pressure Drop. Two-phase pressure drop is calculated using the surface weight average at the bottom surface of the inlet hole (Fig. 3(*b*)). The results are compared between the test models in Fig. 13(*a*). The results show that no significant differences are observed between the test models. The average deviation percentage is presented to compare two-phase pressure drops. It is defined as the average of the two-phase pressure drop deviations in all studied cases, whereas the deviation is the difference of a two-phase pressure drop between two test models. In terms of the average deviation percentages, the pressure drop for the CR-2 and

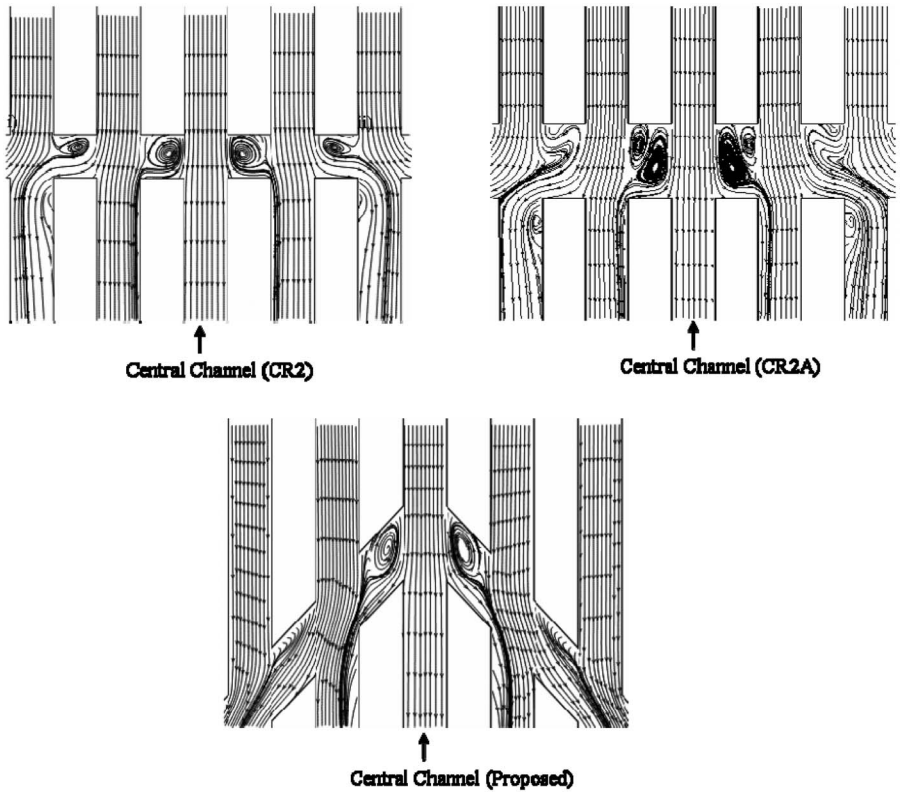

Fig. 11 Samples of streamline along the cross-links at Case 1

the CR-2A are 0.5% and 1.2% higher than that of the STR models respectively, whereas the proposed design has a lower percentage of 0.48%.

Figure 13(*b*) presents the comparison of the present data with experimental pressure drop measurements [6]. The results show that the present data overpredicts the experimental pressure drop at Case 1 and underpredicts from Cases 2–4 for all three test models, whereas the average deviations are 65.3%, 60.9%, and 42.3% compared with the experimental results for the STR, the CR-2, and the CR-2A models, respectively. However it is worthwhile to note that the present data has low deviation from Cases 2–4, at 39.9%, 46%, and 19.5% of the average deviation for the STR, CR-2, and CR-2A, respectively. As a result, it can predict the experimental pressure drop for the CR-2A model at Cases 2 and 4.

Since there are no appropriately experimental works to be compared with, the present data of a two-phase pressure drop of the straight test section is compared with those calculated from the homogeneous model, the models by Friedel [15], and the model by Chisholm [16], as seen in Fig. 13(*c*). The homogeneous model is one of the simplest models defined for the two-phase pressure drop calculation. This model considers the two phases as a single-phase and assumes that the two phases form a well-mixed mixture. The models [15,16] are separated flow models, assuming liquid and gas flow differently through conduits whose areas are proportional to void fraction. These two models use a two-phase multiplier (Φ_{LO}^2), as expressed in Table 4. The Chisholm model is suggested to be used for $\mu_l/\mu_g > 1000$, whereas the Friedel model is suggested to be used for $\mu_l/\mu_g \ll 1000$ [17]. The results show that the average deviation percentages from the present data to the three models are observed as 317.74%, 166.67%, and 441.58%, respectively. Similar to the previous comparison with experimental results, the present data overpredicts two-phase pressure drop from the three above models in Case 1. It is interesting to note that the present data fairly predicts the Friedel model from Case 2 to Case 4. In these cases, the average deviation of the present data are observed as 28.7%, 198.6%, and 350.5% compared with the Friedel, the homogeneous, and the Chisholm models, respectively. In this flow range, the Friedel model fairly predicts the experimental data [6]. However, more data points should be numerically investigated to further confirm this agreement.

3 Conclusions

Two-phase flow in scaled microchannel heat sinks is modeled and simulated in the present work under adiabatic condition. The mixture and standard k-ε turbulent flow models are used to simulate the three-dimensional two-phase flow in three test model geometries, namely, the STR, the CR-2, and the CR-2A.

- The results of flow distribution are validated with the experimental data and show both results have the same trend of two-phase flow distribution.
- The new design is proposed and simulated with the three test models in this work. The results show that the proposed design improves two-phase flow distribution up to 55% compared with the standard straight channel model.
- There are no significant differences between the test models when comparing the two-phase pressure drop. The CR-2 and the CR-2A test models produce a slightly higher pressure drop compared with the STR test model, whereas the lowest case is from the proposed design.
- The present two-phase pressure drop overpredicts the experimental data at Case 1. However, low deviation between the two results is observed from Cases 2 to 4. Moreover, the results from the CR-2A fairly predict the experimental results at Case 2 and Case 4.
- The Friedel model predicts the present data from Cases 2 to 4, while the homogeneous model and the Chisholm's model underpredict the present data for all studied cases.

Although the accuracy of the 3D simulation of the two-phase flow using the CFD code FLUENT needs further investigations, the

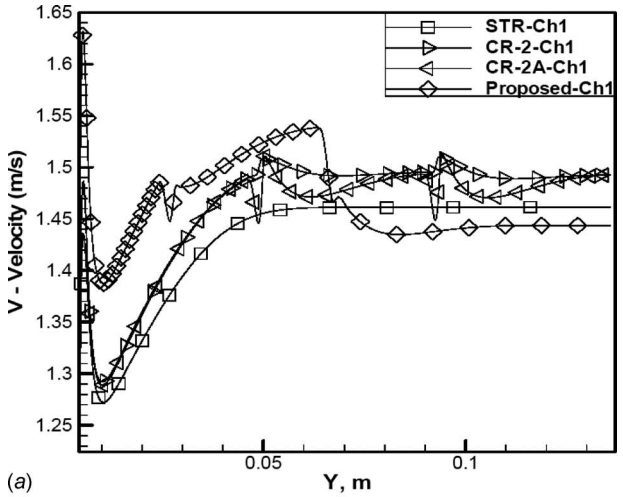

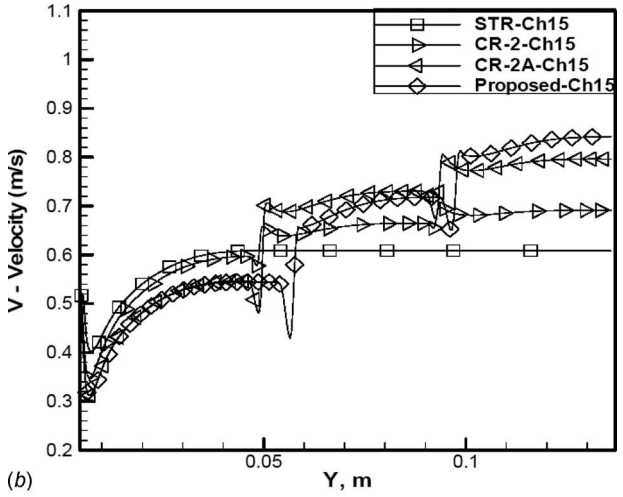

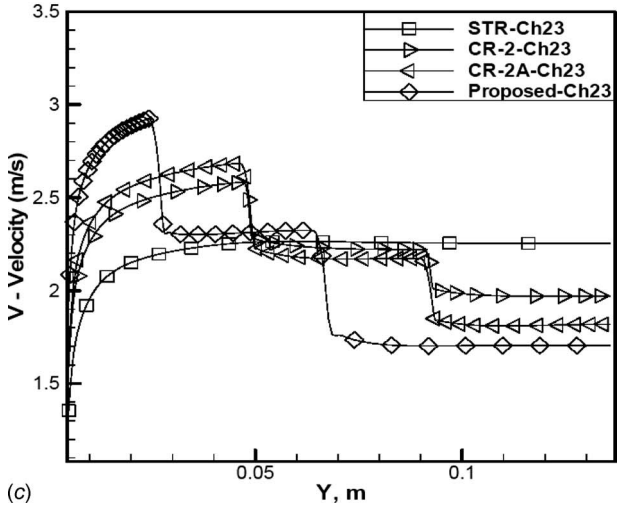

Fig. 12 Velocity profiles along a center line of the channels (Case 1)

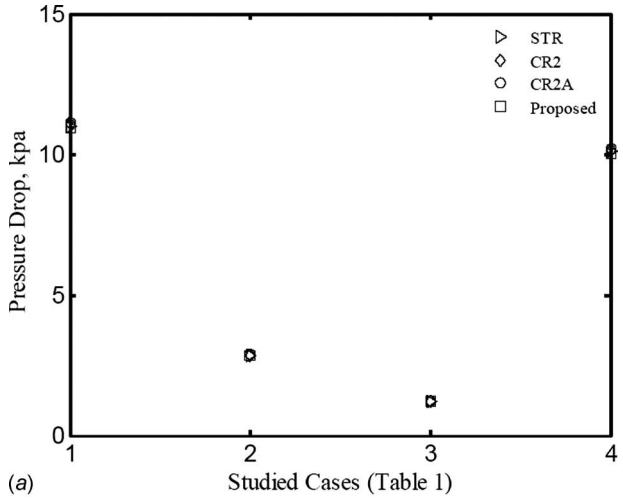

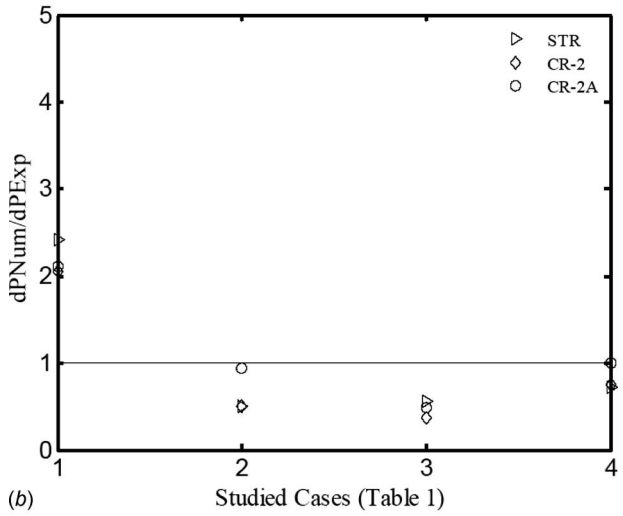

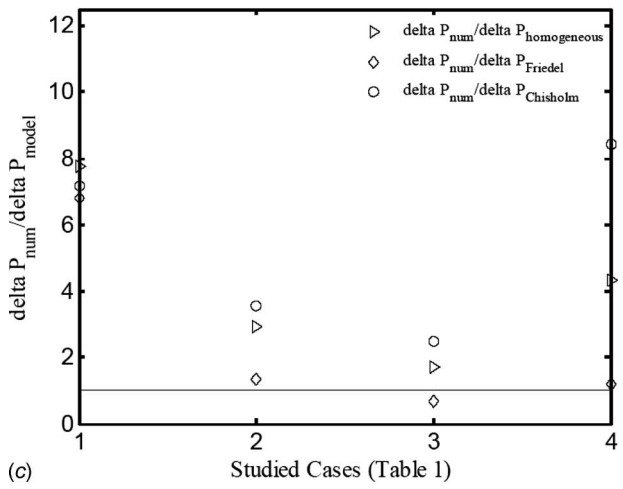

Fig. 13 Pressure drop comparison

results from the present works provide significant data for seeking appropriate designs of parallel multichannel heat sinks in terms of flow distribution.

The present work opens a new look on two-phase flow research by using CFD codes such as FLUENT, which can be a less expensive way to seek better designs for mini- and microchannel heat sinks, especially in terms of flow distribution. The present results direct future investigation of the effects of cross-links on flow distribution for microchannel heat sinks. For example, more cross-links, with same geometry of the proposed design in this work, should be investigated while rounding all sharp corners at the channel inlets to lessen the entrance effect. Moreover, various angles between the cross-links and the channels can be taken into account as well as locations of cross-links along the channels.

Table 4 Two-phase pressure drop correlations

Models	Frictional component ΔP_f
Homogeneous	$\Delta P_f = f_{TP}\frac{L}{D}\frac{\rho_{TP}U^2}{2}$, where $f_{TP}=57/\mathrm{Re}_{TP}$ (laminar), $f_{TP}=0.3164\,\mathrm{Re}_{TP}^{-0.25}$ (turbulent), $\mathrm{Re}_{TP}=\frac{\rho_{TP}UD}{\mu_{TP}}$, $\rho_{TP}=\left(\frac{x}{\rho_G}+\left(\frac{1-x}{\rho_L}\right)\right)^{-1}$, $\mu_{TP}=\left(\frac{x}{\mu_G}+\left(\frac{1-x}{\mu_L}\right)\right)^{-1}$
Friedel [15]	$\left(-\frac{dp}{dz}\right)_{f,TP}=\Phi_{LO}^2\left(-\frac{dp}{dz}\right)_{f,LO}$, where $\left(-\frac{dp}{dz}\right)_{f,LO}=\frac{2f_{LO}}{D}\frac{G^2}{2\rho_L}$, $\Phi_{LO}^2=A+3.24x^{0.78}(1-x)^{0.24}\left(\frac{\rho_L}{\rho_G}\right)^{0.91}\left(\frac{\mu_G}{\mu_L}\right)^{0.19}\left(1-\frac{\mu_G}{\mu_L}\right)^{0.7}\mathrm{Fr}^{-0.0454}\mathrm{We}_{TP}^{-0.035}$, $A=(1-x)^2+x^2\rho_L f_{GO}(\rho_G f_{LO})^{-1}$, $\mathrm{Fr}=\frac{G}{gD\rho_{TP}^2}$, $\mathrm{We}_{TP}=\frac{G^2D}{\rho_{TP}\sigma}$
Chisholm [16]	$\left(-\frac{dp}{dz}\right)_{f,TP}=\Phi_{LO}^2\left(-\frac{dP}{dz}\right)_{f,LO}$, where $\Phi_{LO}^2=1+\left(\frac{C}{K}\right)+\left(\frac{1}{K}\right)^2$, ($C=20$ for turbulent-turbulent, $C=12$ for laminar-turbulent, $C=10$ for turbulent-laminar, while $C=5$ for laminar-laminar), $K^2=\frac{\left(\frac{\Delta P}{\Delta L}\right)_L}{\left(\frac{\Delta P}{\Delta L}\right)_G}$, $\mathrm{Re}_L=\frac{G(1-x)D}{\mu_L}$, $\mathrm{Re}_G=\frac{G(x)D}{\mu_G}$, $\mathrm{Re}_{GO}=\frac{GD}{\mu_G}$, $\mathrm{Re}_{LO}=\frac{GD}{\mu_L}$

Further investigation should be done under to-scale conditions for microchannel heat sinks.

Nomenclature

A = cross-sectional area (m^2)
C = constant value ($5 \le C \le 20$)
D = diameter (m)
F = body force (N)
G = mass flux (kg/m^2)
j_G = superficial gas velocity (m/s)
j_L = superficial liquid velocity (m/s)
K = Martinelli parameter, $K^2=(\Delta P/\Delta L)_L/(\Delta P/\Delta L)_G$
L = channel length (m)
$\dot{m}$ = mass flow rate (kg/ s)
N = number of value x
n = number of phases
P = channel wetted perimeter (m)
Q = volume flow rate (m^3/s)
U = velocity (m/s)
V = velocity along the Y-direction (m/s)
$\mathbf{v}_{dr,k}$ = drift velocity for phase k, $\mathbf{v}_{dr,k}=\mathbf{v}_k-\mathbf{v}_m$ (m/s)
$\mathbf{v}_m$ = mass average velocity of the mixture, $\mathbf{v}_m=\Sigma_{k=1}^n\beta_k\rho_k\mathbf{v}_k/\rho_m$ (m/s)
x = flow quality, $x=\dot{m}_G/(\dot{m}_G+\dot{m}_L)$
x = one value in a set of data
$\bar{x}$ = mean of all values x
X = X-coordinate (m)
Y = Y-coordinate (m)
Z = Z-coordinate (m)
ΔP (or dp/dz) = pressure drop (Pa)
Re = Reynolds number, $\mathrm{Re}=\rho v d/\mu$
Φ^2 = two-phase multiplier
We = Weber number, $\mathrm{We}=G^2D_h/\rho_{TP}\sigma$
Fr = Froude number, $\mathrm{Fr}=G/gD\rho_{TP}^2$

Greek

f = friction factor
μ = dynamic viscosity ($N\,s/m^2$)
ρ = density (kg/m^3)
β = volume fraction
σ = surface tension (N/m)

Subscripts

dr, k = drift velocity for secondary phase k
f = frictional
FM = flow meter
G = gas
GC = graduated cylinder
GO = all gas flow only
h = hydraulic
k = phase k
L = liquid
LL = laminar-laminar
LO = all liquid flow only
LT = laminar-turbulent
m = mixture
TL = turbulent-laminar
TT = turbulent-turbulent
TP = two-phase

Superscripts

T = transpose

References

[1] Tuckerman, D. B., and Pease, R. F. W., 1981, "High-Performance Heat Sink-

ing for VLSI," IEEE Electron Device Lett., **EDL-2**, pp. 126–129.
[2] Samson, E. B., Stark, J. A., and Grote, M. G., 1987, "Two-Phase Flow Header Tests," *Proceedings of the 17th Intersociety Conference on Environmental Systems*, SAE Technical Paper No. 17p.
[3] Hrnjak, P., 2004, "Developing Adiabatic Two Phase Flow in Headers-Distribution Issue in Parallel Flow Microchannel Heat Exchangers," Heat Transfer Eng., **25**(3), pp. 61–68.
[4] Jiang, L., Koo, J. M., Wang, E., Bari, A., Cho, E. S., Ong, W., Prasher, R. S., Maveety, J., Kim, M. S., Kenny, T. W., Santiago, J. G., and Goodson, K. E., 2002, "Cross-Linked Microchannels for VLSI Hotspot Cooling," *Proceedings of the ASME International Mechanical Engineering Congress & Exposition*, pp. 13–17.
[5] Cho, E. S., Koo, J., Jiang, L., Prasher, R. S., Kim, M. S., Santiago, J. G., Kenny, T. W., and Goodson, K. E., 2003, "Experimental Study on Two-Phase Heat Transfer in Microchannel Heat Sinks With Hotspots," *Proceedings of the Annual IEEE Semiconductor Thermal Measurement and Management Symposium*, pp. 242–246.
[6] Dang, M., and Hassan, I., 2007, "The Effects of Cross Links on Adiabatic Two-Phase Flow Characteristics in Scaled Microchannel Heat Sinks," *Proceedings of the ASME Fifth International Conference on Nanochannels, Microchannels and Minichannels*.
[7] Qian, D., and Lawal, A., 2006, "Numerical Study on Gas and Liquid Slugs for Taylor Flow in a T-Junction Microchannel," Chem. Eng. Sci., **61**, pp. 7609–7625.
[8] Yang, Z. L., Palm, B., and Sehgal, B. R., 2002, "Numerical Simulation of Bubbly Two-Phase Flow in a Narrow Channel," Int. J. Heat Mass Transfer, **45**, pp. 631–639.
[9] Bretherton, F. P., 1961, "The Motion of Long Bubbles in Tubes," J. Fluid Mech., **10**, pp. 166–188.
[10] Conde, R., Parra, M. T., Castro, F., Villafruela, J. M., Rodriguez, M. A., and Méndez, C., 2004, "Numerical Model for Two-Phase Solidification Problem in a Pipe," Appl. Therm. Eng., **24**, pp. 2501–2509.
[11] Shepel, S. V., and Smith, B. L., 2006, "New Finite-Element/Finite-Volume Level Set Formulation for Modeling Two-Phase Incompressible Flows," J. Comput. Phys., **218**, pp. 497–494.
[12] Aliabadi, S., Johnson, A., Zellars, B., Abatan, A., and Berger, C., 2002, "Parallel Simulation of Flows in Open Channels," Future Gener. Comput. Syst., **18**, pp. 627–637.
[13] Tonomura, O., Tanaka, S., Noda, M., Kano, M., Hasebe, S., and Hashimoto, I., 2004, "CFD-Based Optimal Design of Manifold in Plate-Fin Microdevices," Chem. Eng. J., **101**, pp. 397–402.
[14] Lu, M. C., and Wang, C. C., 2006, "Effect of the Inlet Location on the Performance of Parallel-Channel Cold–Plate," IEEE Trans. Compon. Packag. Technol., **29**, pp. 30–38.
[15] Friedel, L., 1979, "Improved Friction Pressure Drop Correlations for Horizontal and Vertical Two-Phase Pipe Flow," *Proceedings of the European Two-Phase Group Meeting*, Ispra, Italy, Paper No. E2.
[16] Chisholm, D., 1967, "A Theoretical Basis for the Lockhart Martinelli Correlation for Two-Phase Flow," Int. J. Heat Mass Transfer, **10**, pp. 1767–1778.
[17] Whalley, P. B., 1987, *Boiling, Condensation and Gas–Liquid Flow*, Oxford University Press, New York.

Hydraulic Circuit Design Rules to Remove the Dependence of the Injected Fuel Amount on Dwell Time in Multijet CR Systems

Mirko Baratta

Andrea Emilio Catania

Alessandro Ferrari

IC Engines Advanced Laboratory,
Politecnico di Torino,
C.so Duca degli Abruzzi 24,
10129 Torino, Italy

In multijet common rail (CR) systems, the capability to manage multiple injections with full flexibility in the choice of the dwell time (DT) between consecutive solenoid current pulses is one of the most relevant design targets. Pressure oscillations triggered by the nozzle closure after each injection event induce disturbances in the amount of fuel injected during subsequent injections. This causes a remarkable dispersion in the mass of fuel injected when DT is varied. The effects of the hydraulic circuit layout of CR systems were investigated with the objective to provide design rules for reducing the dependence of the injected fuel amount on DT. A multijet CR of the latest solenoid-type generation was experimentally analyzed at different operating conditions on a high performance test bench. The considerable influence that the injector-supplying pipe dimensions can exert on the frequency and amplitude of the injection-induced pressure oscillations was widely investigated and a physical explanation of cause-effect relationships was found by energetics considerations, starting from experimental tests. A parametric study was performed to identify the best geometrical configurations of the injector-supplying pipe so as to minimize pressure oscillations. The analysis was carried out with the aid of a previously developed simple zero-dimensional model, allowing the evaluation of pressure-wave frequencies as functions of main system geometric data. Pipes of innovative aspect ratio and capable of halving the amplitude of injected-volume fluctuations versus DT were proposed. Purposely designed orifices were introduced into the rail-pipe connectors of a commercial automotive injection system, so as to damp pressure oscillations. Their effects on multiple-injection performance were experimentally determined as being sensible. The resulting reduction in the injector fueling capacity was quantified. It increased by lowering the orifice diameter. The application of the orifice to the injector inlet-pipe with innovative aspect ratio led to a hydraulic circuit solution, which coupled active and passive damping of the pressure waves and minimized the disturbances in injected fuel volumes. Finally, the influence of the rail capacity on pressure-wave dynamics was studied and the possibility of severely reducing the rail volume (up to one-fourth) was assessed. This can lead to a system not only with reduced overall sizes but also with a prompter dynamic response during engine transients. [DOI: 10.1115/1.2969443]

Introduction

In modern solenoid-type common rail (CR) systems, full flexibility in the management of the electronic dwell time (DT) between sequential injection shots is considerable in view of the development of new injection strategies, so as to optimize the trade off between raw emission levels, fuel consumption, and noise in the presence of relatively high exhaust gas recirculation (EGR) degrees [1–4]. The electronic DT is the time interval between the shutoff of the energizing electric current to the solenoid, for stopping the ongoing injection, and the rise of the electric pulse to start the subsequent injection [5].

Figure 1 shows the allowed DT regions between sequential injections for electroinjectors of the first and second solenoid generations. The light-color area on the left side (400–750 μs) is related to second-generation solenoid multijet injectors only for "after-injections," i.e., the last of five injection pulses.

Remarkable progresses have been made in the capability of approaching consecutive injection shots moving from the first to the second electroinjector generation. For injectors of the first generation, the impossibility of performing multiple injections with DT values lower than 1500 μs was basically due to the presence of a high electromagnetic inertia in the driving circuit of the pilot valve. Consequently, at the end of any current pulse, a minimum time interval of approximately 1500 μs was needed to extinguish the electromagnetic transients consequent to the solenoid energizing.

In electroinjectors of the second solenoid-type generation, the electromagnetics of the pilot-valve driving circuit is much faster so that the electronic control unit can apply much lower DTs, up to 100 μs, as experimentally verified. For these electroinjectors, main limits to the capacity of approaching sequential injections each other stem from hydrodynamic effects. When multiple injections are carried out, pressure oscillations, which are induced by the water hammer consequent to the injector-nozzle closure after each injection shot, affect the fuel injected amount during the subsequent injection [6]. For example, when pilot and main injections occur, the main fuel injected volume presents significant oscillations about a mean value as DT is varied [7]. The amplitude of such volume fluctuations increases with the pressure-wave amplitude and generally becomes larger when two consecutive current pulses are approached up to a DT close to the so-called injection fusion threshold [8]. Hence, a lower limit to DT (750 μs,

Contributed by the Fluids Engineering Division of ASME for publication in the JOURNAL OF FLUIDS ENGINEERING. Manuscript received July 30, 2007; final manuscript received June 10, 2008; published online October 27, 2008. Review conducted by Joseph Katz. Paper presented at the 2006 Spring Conference of the ASME Internal Combustion Engine Division (ICES2006), Aachen, Germany, May 7–10, 2006.

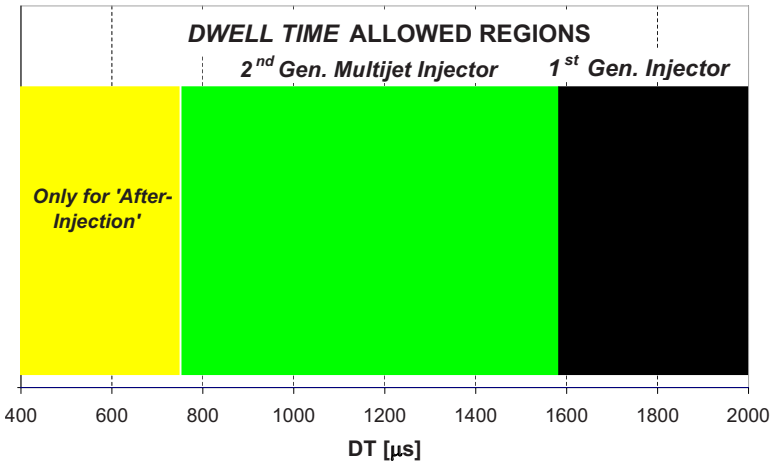

Fig. 1 Multiple-injection solenoid CR system evolution

in Fig. 1) is set in the electronic control unit maps of commercial systems. Nevertheless, even in the allowed range of DT, the fuel injected volume through the second of two consecutive injection shots can present significant oscillations around their nominal values, namely, up to 25% for pilot-main injection patterns [9]. Higher percentage deviations can be observed for "main-post-injection" distributions.

The occurrence of pressure waves with high amplitude and relatively low frequency represents one of the most important critical issues in multijet CR solenoid injectors for automotive applications. The present work aims at studying hydraulic layout solutions to minimize the disturbances that are caused in sequential injections by nozzle-closure triggered pressure oscillations. These solutions will lead to a better control of the fuel volume injected at each shot when DT is varied.

A remarkable attenuation of pressure oscillations can be achieved by modifying the injector inlet-pipe sizes in system design [9,10]. It has already been verified, within the range of commercial sizes for automotive applications, that shorter injector feeding pipes with larger diameters give rise to lower amplitude and higher frequency pressure waves [9–11].

In the present paper an original explanation of this phenomenon is provided on the basis of energetics considerations. Experimental tests were carried out, showing that the energy stored in pressure waves induced by injection events with the same energizing time (ET) and p_{rail} keeps almost the same when the geometrical quantities of the injector-supplying ducts are modified. Hence, owing to the fact that the energy stored in a sinusoidal pressure-wave train rises with the square of both its amplitude and frequency, hydraulic layout modifications leading to increased pressure-oscillation amplitudes should yield reduced frequencies of the same fluctuations and vice versa.

An analysis of injector-supplying pipe design, aimed at finding solutions to minimize disturbances induced in multiple injections, has been carried out, taking pipe length and internal diameter as parameters. Experimental tests were planned with the support of a simple zero-dimensional model, allowing for pressure-wave frequency evaluation as a function of system geometric data. Owing to the radial dimensions of the engine cylinders, there is obviously a lower limit to the length of the injector inlet-pipes if the actual rail geometrical shape has to be retained. On the other hand, no particular technical constraints are present for the possibility of increasing the internal diameter of the injector inlet-pipes.

Substantial reductions in the pressure-oscillation amplitude were observed by introducing specifically designed orifices into the rail connectors or at the injector inlet. Orifice effects on injection characteristics were experimentally investigated along with any perturbation induced by them on system performance. A hydraulic circuit solution applying both injector inlet-pipes with optimized dimensions and wave-damping orifice at the rail outlet was then tested, so as to assess the effective potential of the combined active and passive damping means in contrasting pressure-oscillation induced disturbances on multiple injections and their implications.

Finally the possibility of employing smaller rail volumes was explored in order to reduce overall sizes and system inertia during transients. Experiments with rail hydraulic capacities of 5 cm^3, 10 cm^3, and 15 cm^3 were performed to analyze the effects of a drastic rail volume reduction on pressure-wave dynamics.

Experimental Setup

The experimental investigation was carried out on the high performance Moehwald-Bosch MEP2000/CA4000 test bench [7] at the IC Engines Advanced Laboratory of Politecnico di Torino. This facility includes the following main instruments: the volumetric device EMI2, gauging the total injected volume of fuel and also capable of separately measuring the discharged volume during each shot in multiple injections; the injection-rate indicator EVI of the Bosch-type to take injection flow-rate traces by recording the pressure signal produced by each injection into a pipe loop, which the injector nozzle is connected with; piezoresistive sensors to monitor pressures in the rail and in the pipes at the electroinjector inlet as well as at the pump delivery.

Detailed descriptions of EMI2 and EVI devices, of their working principle and of the mathematical model, which was developed and applied to draw injected flow rates directly from measured EVI pressure data (p_{EVI}), can be found in Refs. [7,12].

Injector Inlet-Pipe Design

A set of experimental tests was carried out to further assess the effects of the injector inlet-pipe geometrical features on the system dynamics and multiple-injection performance. Figure 2 shows the CR layout (*a*) and the main internal features of the electroinjector (*b*). A rail of 20 cm^3 was connected to the rotary high-pressure pump, 0.657 cm^3/rev in displacement, and to only one injector, so as to remove fluid dynamic interaction between injectors [7]. Different combinations of length and diameter were considered for the injector-supplying duct, both inside and outside the range of production (commercial injector inlet-pipes for automotive application present a length range between 125 mm and 300 mm and internal diameters of 2.4 mm or 3.0 mm). For each duct configuration, in relation to a single injection with ET $=1000$ μs, $p_{rail}=1000$ bar, and $n=2000$ rpm, the following measured quantities are reported in Table 1: injected volume per cycle of the pump (V_{inj}); volume (V_{refl}) that flows back through the pilot

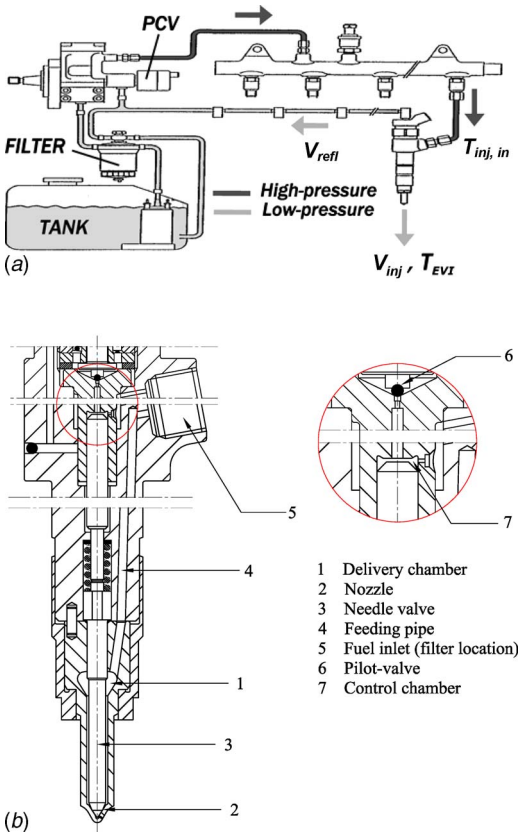

Fig. 2 Injection system layout (*a*) and electroinjector main internal features (*b*)

valve (Fig. 2(*a*)) for each pump cycle, and time-averaged temperature of the flow at the nozzle outlet (T_{EVI}) and at the injector inlet ($T_{inj,in}$). Besides, Fig. 3 reports the corresponding injected flow-rate time distributions in terms of pressure taken by the EVI instrument for a couple of inlet-pipe geometrical data that are reported in Table 1.

From the analysis of the obtained results, first of all one can conclude that the dimensions of the injector-supplying pipe do not sensibly influence the single-injection performance. With reference to the properties in some other hydraulic circuit components, the time-averaged temperatures in the rail and at the pump delivery resulted to be nearly independent of the pipe geometric data. Their values ranged from 38.8°C to 39.2°C and from 45.6°C to 46.4°C, respectively. Moreover, the mass drained by the pressure control valve (PCV) was equal to 0.44 l/min for all the pipe configurations, and the average mass flow rate of the fuel

Table 1 Single-injection performance for different injector inlet-pipes (ET_{main}=1000 μs, p_{rail}=1000 bar, and n=2000 rpm)

l (mm) d (mm)	V_{inj} (mm^3/rev)	V_{refl} (mm^3/rev)	T_{EVI} (°C)	$T_{inj,in}$ (°C)
80 3.5	59.7	23.4	76.4	43.29
80 4.0	60.1	23.3	76.4	42.8
200 2.4	60.5	23.3	76.3	43.4
300 2.4	59.5	23.3	76.4	42.7
125 2.4	59.9	23.3	76.8	43.6

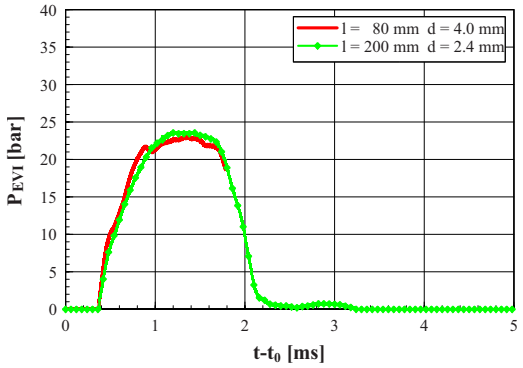

Fig. 3 Injected flow-rate time history (ET_{main}=1000 μs, p_{rail}=1000 bar, and n=2000 rpm)

delivered by the high-pressure pump was constant because both the pump-speed and nominal rail-pressure levels were fixed.

It is worth pointing out that the values of T_{EVI} and $T_{inj,in}$ reported in Table 1 as well as the abovementioned values of the time-averaged temperatures in the rail and at the pump delivery are lower than the real operating temperatures in an engine. However, this does not influence the outcomes of the present investigation that is aimed at analyzing the effects of the system hydraulic layout on injection performance.

Figure 4 shows the time histories of p_{rail} and $p_{inj,in}$ versus $t-t_0$, where t_0 is an arbitrary reference instant of time for the indicated inlet-pipe size and operating conditions. It can be inferred, from this figure, that the supplying pipe has a strong influence on the pressure oscillations, which arise at the end of injection. As stated before, both the amplitude and the period of pipe pressure fluctuations are substantially lower for the shorter and larger-diameter injector inlet duct. For the pipe dimensions of Fig. 4(*b*), the dependence of any subsequent injected volume on DT can be expected to be drastically reduced.

The explanation of such pipe behavior with regard to pressure oscillations can be drawn from energetics considerations. At each injection, the nozzle discharges the fuel feeding it. The macroscopic movement of the fuel toward the injector tip is the result of the perturbation induced by the electric input to the solenoid. The kinetic energy (E_c) that is related to such a fuel motion is comparable for the different geometrical data of the injector feeding pipe, as can be inferred from what follows. By applying the energy conservation law to the subsystem made up of the injector, its supplying pipe, the rail, and the pump to rail connection pipe in the time interval ($t_{start}-t_{end}$) between the start of the current signal and the end of injection, one obtains the following equation:

$$Q + E_{el} = \Delta U^o + \sum_j \int_{t_{start}}^{t_{end}} (\dot{H}^o_{out,j} - \dot{H}^o_{in,j})dt \qquad (1)$$

where Q is the heat transferred across the walls in the interval $t_{start}-t_{end}$, E_{el} is the electric energy to the solenoid, $\dot{H}^o_{in}$ and $\dot{H}^o_{out}$ are, respectively, the input and output total-enthalpy fluxes for the considered control volume, and ΔU^o is the average total internal energy variation of the system, that is,

$$\Delta U^o = \Delta U + \Delta E_c \qquad (2)$$

The amount of the electric energy input to the injector E_{el} depends only on the ET value and therefore it does not vary when the pipe geometric data change. In addition, because the average mass flow rates and thermodynamic conditions at the injector-nozzle holes, in the oil recirculation pipe from the pilot valve and at the pump outlet, keep almost the same values for different layouts, as has already been assessed, the time-averaged total-enthalpy fluxes of fuel going out and into the system are expected to be practically the same for the different layouts and conse-

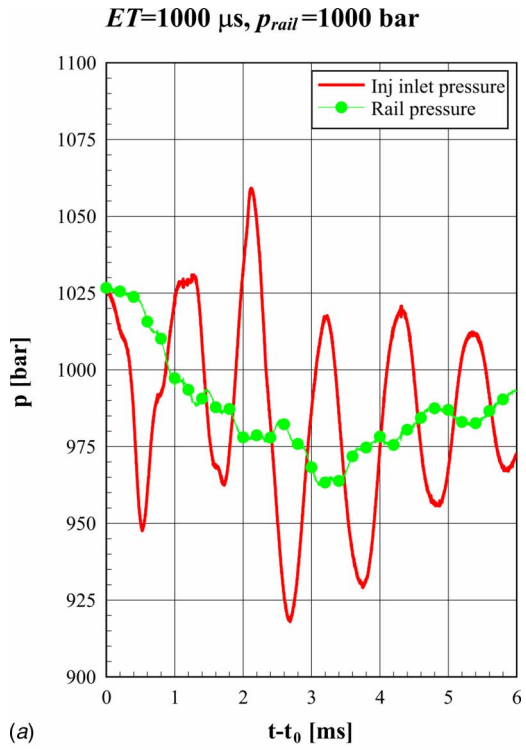

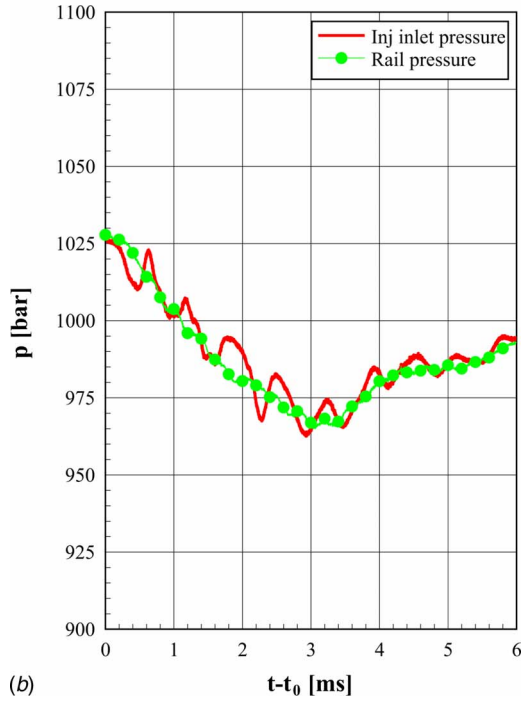

Fig. 4 Pressure time histories: (*a*) *l*=200 mm, *d*=2.4 mm and (*b*) *l*=80 mm, *d*=4 mm

quently the same can be taken for the heat transferred to the walls. Therefore, from Eq. (1), it can be drawn that the total internal energy variation with respect to time, ΔU^o, is the same for the various configurations. A polytropic-like thermodynamic evolution law has been shown to allow accurate modeling of the fuel flow in multijet CR systems in Refs. [13,14]. Under these premises, the fuel internal energy per unit mass u is a function of only one thermodynamic intensive property, namely, the pressure,

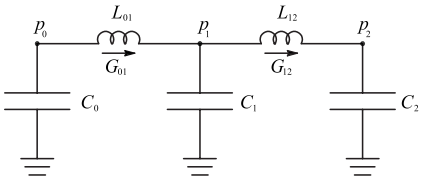

Fig. 5 LC model

that is, $u=u(p)$. Due to the fact that, during the time interval $t_{start}-t_{end}$, the rail pressure, which can be regarded as the system mean pressure, undergoes nearly the same change for the different injector inlet-pipe dimensions (Figs. 4(*a*) and 4(*b*)), it follows that the internal energy variation ΔU is the same for the different layouts. As a consequence, ΔE_c in Eq. (2) depends only on the working conditions and not on injector-supplying-pipe sizes.

As stated, the water hammer at the injection end is the cause of the pressure oscillations in the closed injection system. When the injection terminates, the fuel moving toward the nozzle is stopped and all its kinetic energy, i.e., ΔE_c, is stored into pressure waves, which travel forth and back through the supplying pipe and the electroinjector drilled passage. Thus, the energy feeding the pressure waves under fixed working conditions can be taken as comparable for the different injector inlet-pipe configurations. Hence, since the energy stored in pressure waves increases with their amplitude and frequency square product, higher frequencies should imply lower amplitudes when the sizes of the injector-supplying-duct change. Owing to this tight relationship between pressure-oscillation natural frequency and amplitude, the lumped parameter model that was developed in Ref. [7] can be very useful for hydraulic layout design and optimization because it allows the prediction of the natural frequency of the pressure waves with good accuracy when the system geometry is changed. In this model the rail, the injector inlet-pipe, and the electroinjector are simulated as being constituted of hydraulic capacitances, inductances, and resistances, though the effect of these latter can be neglected.

In particular, the subsystem lumped parameter model that is described in Ref. [7] corresponds to the experimental layout scheme of Fig. 5. In such a drawing, the rail capacitance C_0 is connected to the injector through the inlet-pipe (Fig. 2(*a*)) of inductance L_{01}, which is bounded by a capacitance that takes the valve control chamber (7 in Fig. 2(*b*)) as well as the filter (5 in Fig. 2(*b*)) volume effects into account. The capacitance that is equivalent to these volume effects is C_1. The feed pipe (4 in Fig. 2(*b*)) of inductance L_{12}, in turn, starts from this capacitance and ends at the delivery chamber volume (1 in Fig. 2(*b*)) of capacitance C_2 (in general one has $C=V/a^2$, $L=l/A$).

Figure 6 shows the influence of injector inlet-pipe internal diameter on the free fluctuation period T, taking the pipe length as

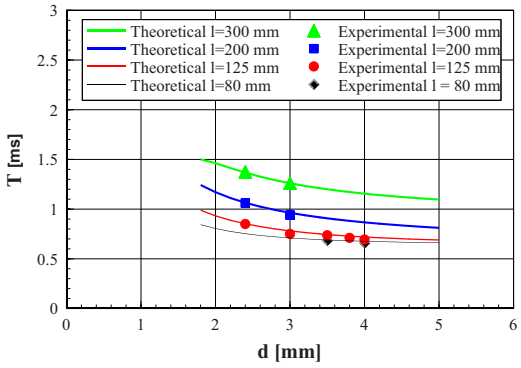

Fig. 6 Inlet-pipe diameter influence on natural period *T*

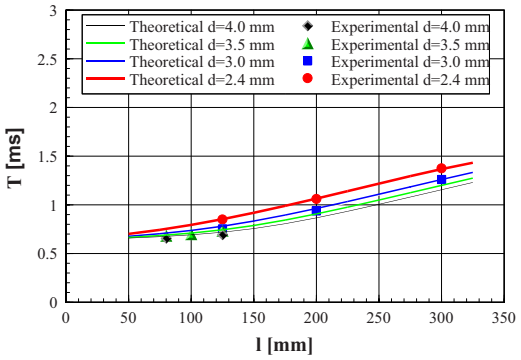

Fig. 7 Inlet-pipe length influence on natural period *T*

parameter, whereas the effect of the pipe length on the same quantity is illustrated in Fig. 7. In the plots, the solid lines refer to the theoretical results obtained by the model, and the symbols correspond to the experimental values in the range of the tested injector inlet-pipe configurations that are or can be employed in commercial CR systems for automotive applications.

The information illustrated by these graphs will support the design of injector inlet-pipes. The objective is to decrease the oscillation natural period. Figure 6 demonstrates that enlarging the internal diameter of the supplying ducts produces a sensible reduction on such a period. However, all the curves approach horizontal asymptotes at high diameters, so that, for a fixed pipe length, increasing the internal diameter over 4 mm does not seem to be convenient. On the other hand, Fig. 7 shows that, for a fixed internal diameter, shortening the length of the injector-supplying pipe is always effective in cutting down the pressure oscillations. Nevertheless, in Fig. 7 the curves that correspond to different diameters tend to become coincident for the lowest values of the injector feeding-pipe length. As a consequence, it does not seem to be convenient designing too short injector inlet-pipes when a significant diameter increase is operated at the same time. An additional useful indication for identifying the optimum pipe length comes from the graphs in Fig. 6, where the benefit of nearly the same percentage reduction in length is shown to be less effective for shorter pipes. In fact, in the diameter range between 2.4 mm and 3.0 mm, T reduces about 0.3 ms when the pipe length is changed from $l=300$ mm to $l=200$ mm. T reduces about 0.2 ms when the pipe length is varied from $l=200$ mm to $l=125$ mm.

The data in Figs. 6 and 7 can be used to build up a response surface [15], mapping T as a function of l and d. Such a surface would show that T monotonically decreases if l decreases or d increases. However, from the results of Figs. 6 and 7, it can be inferred that a suitable layout solution should be pursued in the range of 80 mm$\leqslant l\leqslant$125 mm and 3.5 mm$\leqslant d\leqslant$4.0 mm.

Table 2 reports the pipe geometric data that were selected for experimental tests from the lumped parameter analysis of the CR hydraulic layout, i.e., inlet-pipe lengths of 80 mm, 100 mm, and

Table 2 Experimental inlet-pipe dimensions

l (mm)	d (mm)
80	3,5 4,0
100	3,5 3,8
125	3,5 3,8 4,0

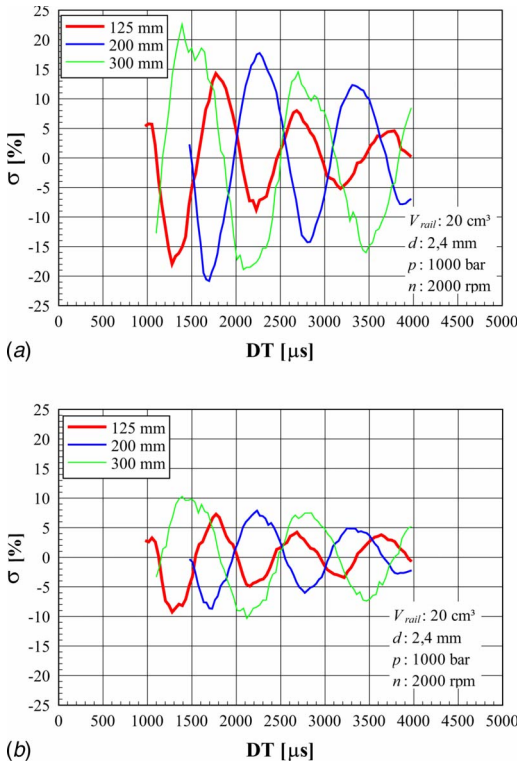

Fig. 8 Main injected-volume deviations for different pipe lengths (p_{rail}=1000 bar): (*a*) ET_{pil}=400 μs, ET_{main}=600 μs and (*b*) ET_{pil}=400 μs, ET_{main}=900 μs

125 mm and internal diameters of 3.5 mm, 3.8 mm, and 4.0 mm. It has to be pointed out that each pipe combination in Table 2 is out of the actual production range for automotive application.

Experimental Tests. Figure 8 shows the injected-volume pattern during the main injection, for three commercial inlet-pipe lengths, as a function of DT, ranging from 1000 μs to 4000 μs, between a pilot and a main injection at fixed energizing times: ET_{pil}=400 μs, ET_{main}=600 μs (Fig. 8(*a*)) and ET_{pil}=400 μs, ET_{main}=900 μs (Fig. 8(*b*)). An engine speed of 2000 rpm and a nominal rail pressure of 1000 bar were considered. The main injected volume is reported as percentage deviation from its mean value, that is,

$$\sigma = \frac{V_{main} - \bar{V}_{main}}{\bar{V}_{main}} \times 100 \tag{3}$$

where V_{main} is the main injected volume for a given DT and $\bar{V}_{main}$ is its mean value that is worked out as (DT_{min}=1000 μs, DT_{max}=4000 μs)

$$\bar{V}_{main} = \frac{1}{DT_{max} - DT_{min}} \int_{DT_{min}}^{DT_{max}} V_{main} dt \tag{4}$$

The deviation σ is significantly higher in Fig. 8(*a*) than in Fig. 8(*b*), that is, higher for shorter ET_{main}. In fact, the pressure fluctuations triggered by the pilot injection are the same for both ET_{main}, with the result of the same amplitude in main injected-volume fluctuations but of lower deviations for the higher ET_{main} due to the higher injected-volume mean values. Besides, higher main injected-volume deviations can be reached with lower p_{rail} nominal levels due to the reduced values of $\bar{V}_{main}$.

Figure 9 shows the main injected-volume fluctuations for an inlet-pipe length of 125 mm and the three diameters reported in Table 2 as a function of the dwell time between the pilot and main

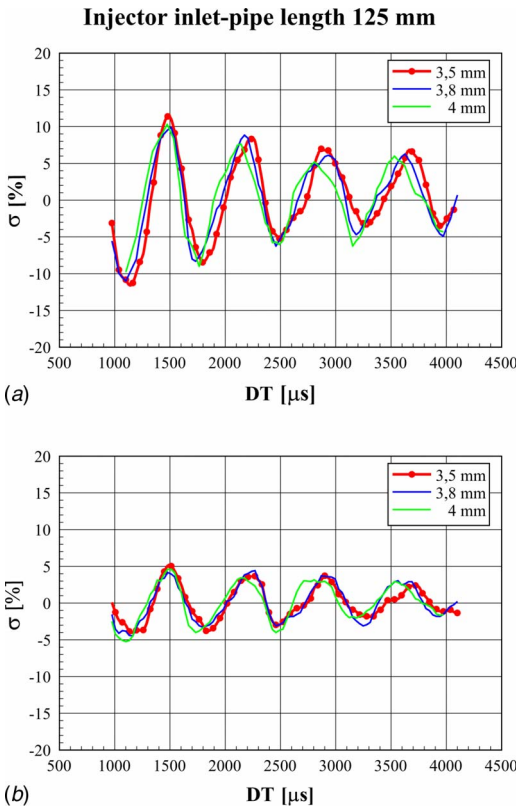

Fig. 9 Main injected-volume deviations for different pipe diameters (p_{rail}=1000 bar): (*a*) ET_{pil}=400 μs, ET_{main}=600 μs and (*b*) ET_{pil}=400 μs, ET_{main}=900 μs

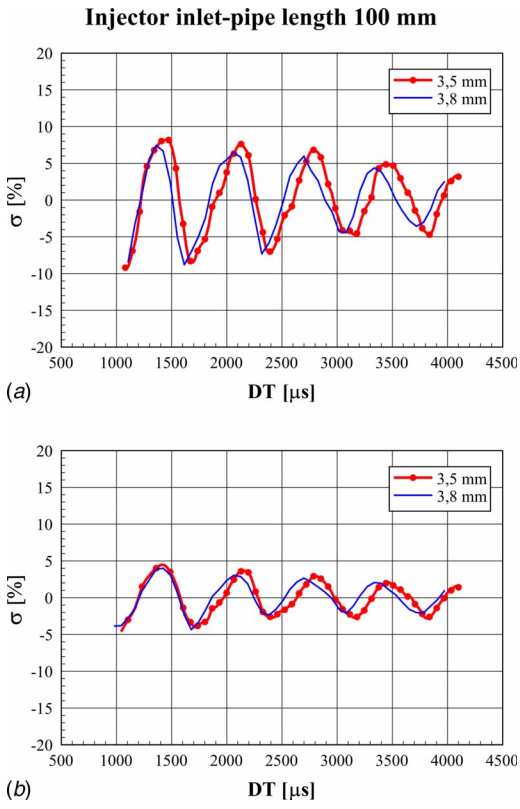

Fig. 10 Main injected-volume deviations for different pipe diameters (p_{rail}=1000 bar): (*a*) ET_{pil}=400 μs, ET_{main}=600 μs and (*b*) ET_{pil}=400 μs, ET_{main}=900 μs

injections, taking energizing times at two fixed value sets, i.e., ET_{pil}=400 μs, ET_{main}=600 μs (Fig. 9(*a*)) and ET_{pil}=400 μs, ET_{main}=900 μs (Fig. 9(*b*)). The engine speed of 2000 rpm and the nominal rail pressure of 1000 bar were also considered.

As can be inferred, for all the examined configurations, the main injected-volume oscillations are significantly reduced with respect to those at the same pipe length in Fig. 8. For lower DT values, better results in Fig. 9 are obtained with d=4 mm, the largest internal diameter. This is interesting especially in view of widening the DT range allowed for second-generation multijet electroinjectors. It is worth pointing out that in the present paper results on multiple injections with DT in the forbidden range, for the second generation of electroinjectors (Fig. 1), are not reported. The reason for this resides in the fact that the EMI2 accuracy in the measurement of the injected fuel amounts in sequential injection shot decays when DT is below a critical threshold. This latter is higher than the lower limit for electroinjectors of the second generation.

Figure 10 plots the main injected fuel-volume deviations versus DT under the same working conditions of Fig. 9 for two different inlet-pipes sharing the same length of 100 mm. The influence of the internal diameter on the oscillations of fuel volume is virtually the same as in Fig. 9. Thus, the fluctuation amplitude and period in Fig. 10 are slightly lower than those in Fig. 9 due to the shorter pipe length.

The sharp reduction in the maximum absolute values of σ observed in Figs. 9 and 10 with respect to Fig. 8 is only due to an efficient modulation of the pressure-wave energy and not to a $\bar{V}_{main}$ lessening. In fact, the system capability of injecting is not altered by changes in the injector inlet-pipe dimensions, as is shown in Table 1 for ET=1000 μs and p_{rail}=1000 bar. More evidence of this is given in Fig. 11, which reports the injection characteristics for three different geometric data combinations of the injector feeding pipes, under the condition p_{rail}=1000 bar. Such differences in pipe dimensions are substantial and thus significant. As can be observed for every ET value, the pipe dimensions have a rather negligible influence on the injected fuel volume. A comparison between results similar to those in Fig. 11, but obtained at different nominal rail pressure, that is, p_{rail}=750 bar, p_{rail}=1250 bar, and p_{rail}=1500 bar, led to the same conclusion.

Experimental tests with l=80 mm were also made. The results in terms of percentage deviation of the main injected volumes versus DT are reported in Fig. 12 for the same operating conditions as in Figs. 9 and 10. The effect of the pipe diameter on volume fluctuations, at the selected large d values, appears to be very small, mainly in Fig. 12(*b*). Besides, as can be observed, there are no sensible improvements in main volume fluctuations with respect to Fig. 10. This agrees with the general indications

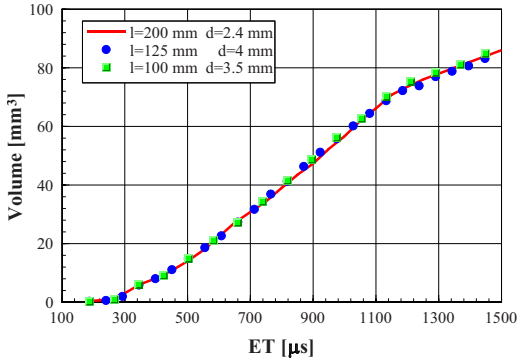

Fig. 11 Injector characteristics for different pipe sizes (p_{rail} =1000 bar)

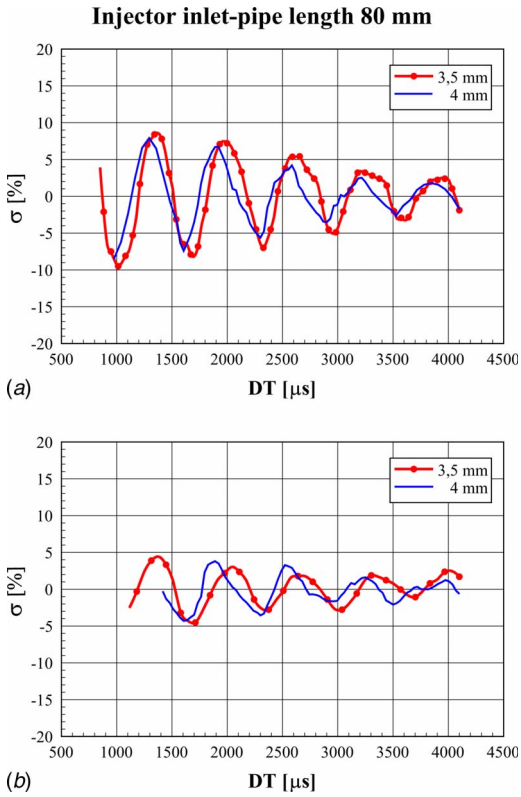

Fig. 12 Main injected-volume deviations for different pipe diameters (p_{rail}=1000 bar): (*a*) ET_{pil}=400 μs, ET_{main}=600 μs and (*b*) ET_{pil}=400 μs, ET_{main}=900 μs

provided by the lumped parameter model in Figs. 6 and 7.

Besides, the adoption of very short pipes (80 mm) would imply changes in the production rail shape (e.g., longer and narrower rails should be applied). Actually, the injector inlet ducts have to connect the rail with the electroinjectors, which are installed in the cylinder head, and thus commercial pipes cannot be too short.

The presented experimental results support the design rules that the reduction in the length to diameter ratio for commercial injector inlet-pipes is effective in minimizing the dependence of the injected fuel on DT for multiple injections. In particular, optimal results can be achieved by selecting a pipe with a length of 125 mm and an internal diameter of 4 mm. The advantages that can be obtained by means of further pipe-length reductions are quite small.

Application of Gauged Orifices

A commercial CR multijet system for passenger cars, with a rail volume of 20 cm^3 and injector inlet-pipes of l=125 mm, d=2,4 mm, was then equipped with a gauged orifice (0.8 mm in diameter) at the rail outlet to test its effectiveness in damping the pressure oscillations. The cross section of the applied orifice is shown in Fig. 13. In order to prevent oil leakages at high-pressure levels, it is fundamental that both the internal and the external component templates are made in a way to fit the oval shape of the extremity of the injector-supplying pipe as far as possible.

Figure 14 shows the main injected fuel-volume fluctuations as functions of DT at the working conditions of p_{rail}=1000 bar and ET values that are quoted in Figs. 14(*a*) and 14(*b*), respectively. In each plot, the solution applying the calibrated orifice is compared with the one without orifice. The most relevant effect produced by the orifice application to the hydraulic circuit is given by the attenuation of the fluctuation amplitude in the main injected fuel volume, the values of σ keeping always below 7%. The cutting down on the main injected-volume fluctuations was shown to become more significant as the dwell time reduced (with particular reference to Fig. 14(*b*)). This is quite effective because the amplitude of the main injected-volume oscillations increases when the dwell time reduces. The graphs related to the presence of the orifice show a periodic behavior versus DT with a fluctuation frequency that is lower than the one in the diagrams corresponding to the layout without orifice.

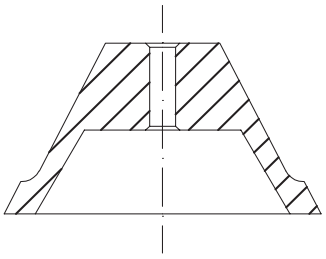

Fig. 13 Gauged orifice

Experiments were also carried out with the gauged orifice located at the injector inlet. In such a case, the upstream injector filter had to be shortened, through a grinder, in order to avoid its mechanical contact with the orifice, an event that would drastically reduce the system capability of injecting fuel. The marketability of the solution presenting the orifice at the injector inlet required technical changes in the injector filter design, which were not necessary for our purposes, because no further benefits could be obtained in terms of reduction in pressure-oscillation amplitude with respect to the orifice setup at the rail outlet. Therefore, the layout solution applying the calibrated orifice at the injector inlet was not taken into account.

The explanation of the experimental results in Fig. 14 resides in the time histories of the pressure waves triggered by the pilot

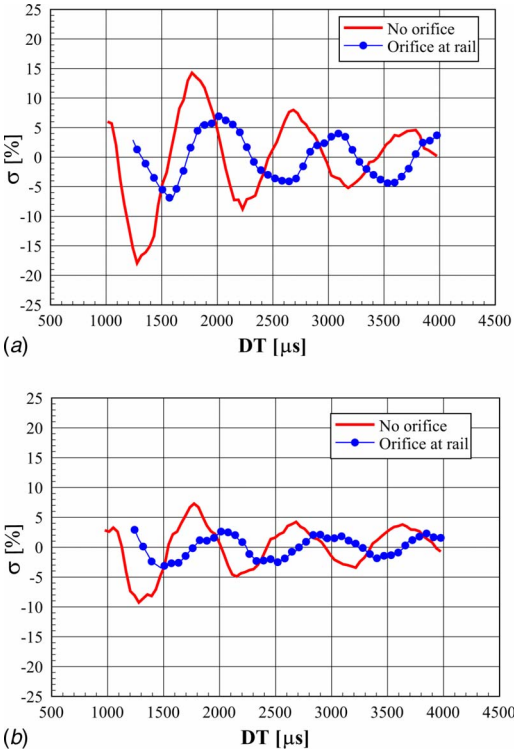

Fig. 14 Orifice effect on main injection volume deviations for pipe dimensions l=125 mm and d=2.4 mm (p_{rail}=1000 bar): (*a*) ET_{pil}=400 μs, ET_{main}=600 μs and (*b*) ET_{pil}=400 μs, ET_{main}=900 μs

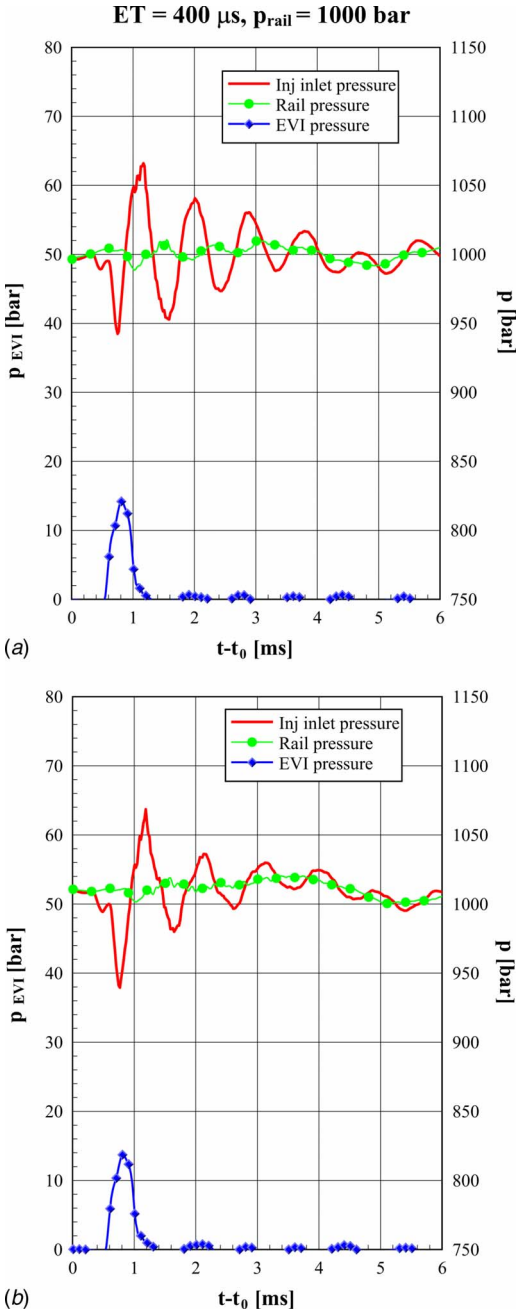

Fig. 15 Response of the system (*l*=125 mm and *d*=2.4 mm) to a pilot injection without (*a*) and with (*b*) the gauged orifice: (*a*) commercial layout and (*b*) layout with the orifice

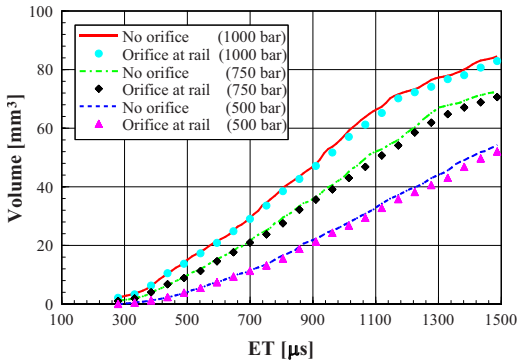

Fig. 16 Orifice effect on injector characteristics (*l*=125 mm, *d*=2.4 mm, and V_{rail}=20 cm^3)

injections for the two different layout configurations. Figure 15 reports the rail and the injector-inlet pressure, in addition to the injected flow-rate time histories, at p_{rail}=1000 bar for the case of a single injection having the same energizing time (i.e., 400 μs) of the pilot injections in Figs. 14(*a*) and 14(*b*). The nozzle closure causes a water hammer that is visible in Figs. 15(*a*) and 15(*b*) at $t \approx 1.2$ ms subsequent to the depression induced by the fuel expulsion from the nozzle during the injection. The pressure oscillations due to the water hammer at the end of the pilot injections are the cause of the fluctuations in the main injected fuel volume as the dwell time is changed. The amplitude of the main injected fuel-volume fluctuations increases with that of the pressure waves. In Fig. 15 the amplitude of the pressure waves is progressively damped by the friction distributed losses along the injector-supplying pipe. The dissipation of the pressure-wave kinetic energy in Fig. 15(*b*) is faster than the one in Fig. 15(*a*) because of the further action of the concentrated pressure loss at the orifice. This is in agreement with the fact that in Fig. 14 the main injected-volume fluctuations are further damped in the presence of the orifice.

Furthermore, the pressure drop at the orifice decreases with the fluid velocity through it, so that the damping action of the narrow passage is less effective as the time elapses from the nozzle-closure instant on because of the progressive pressure-wave kinetic energy dissipation due to the viscous loss effects. This motivates an increasing efficiency of the orifice in damping oscillations when DT is reduced (Fig. 14). Finally, because the calibrated orifice should be modeled as a resistance element, the system natural frequency, which is worked out by the lumped parameter model of the type described in Ref. [7], tends to decrease. Therefore, in Fig. 15(*b*) the pressure waves present a frequency that is slightly lower than the one in Fig. 15(*a*).

In Fig. 16, the influence of the orifice on the electroinjector characteristics is analyzed for different nominal pressure levels in the rail. The conclusion is that, in the presence of the orifice, the injected fuel volume for any ET and p_{rail} generally reduces. The percentage amount of reduction in the injected volume is variable. Nevertheless, in any case, the reduction in the injected fuel volume is under 8% for an orifice diameter of 0.8 mm.

At p_{rail}=1000 bar and ET=1200 m, Fig. 17 reports the time patterns of the injected flow rate as well as of the pressure at the injector inlet and in the rail for the system commercial layout without (Fig. 17(*a*)) and with (Fig. 17(*b*)) the gauged orifice. In the interval of time 1 ms$<t-t_0<$2 ms, the injected flow rate takes higher values in the absence of the orifice, according to the data in Fig. 16. The explanation of such an occurrence resides in the fact that the average value of the injector inlet-pressure over the injection duration in Fig. 17(*a*) is higher than the one in Fig. 17(*b*).

The expansion wave arising as a consequence of the nozzle opening is marked with 1 in Fig. 17 and propagates toward the rail and nozzle. This traveling depression wave draws the fuel from the injector inlet to the delivery chamber (i.e., 1 in Fig. 2(*b*)) and then to nozzle (2 in Fig. 2(*b*)). The needle-seat passage in the nozzle determines a flow restriction and thus the pressure in the delivery chamber stops lowering and begins to increase. This causes a compression wave to start from the nozzle and move upward. Such a wave is marked as 2 in Figs. 17(*a*) and 17(*b*). In Fig. 17(*a*), this compression wave at the injector inlet precedes another compression wave indicated with 3, which derives from the reflection at the rail of the depression wave related to the nozzle opening. However, in the presence of the calibrated orifice, this expansion wave due to the nozzle opening is reflected partially in front of the orifice as an expansion wave and partially in the rail as a compression wave. Because the wave reflection at the orifice front needs shorter time than the wave reflection in the

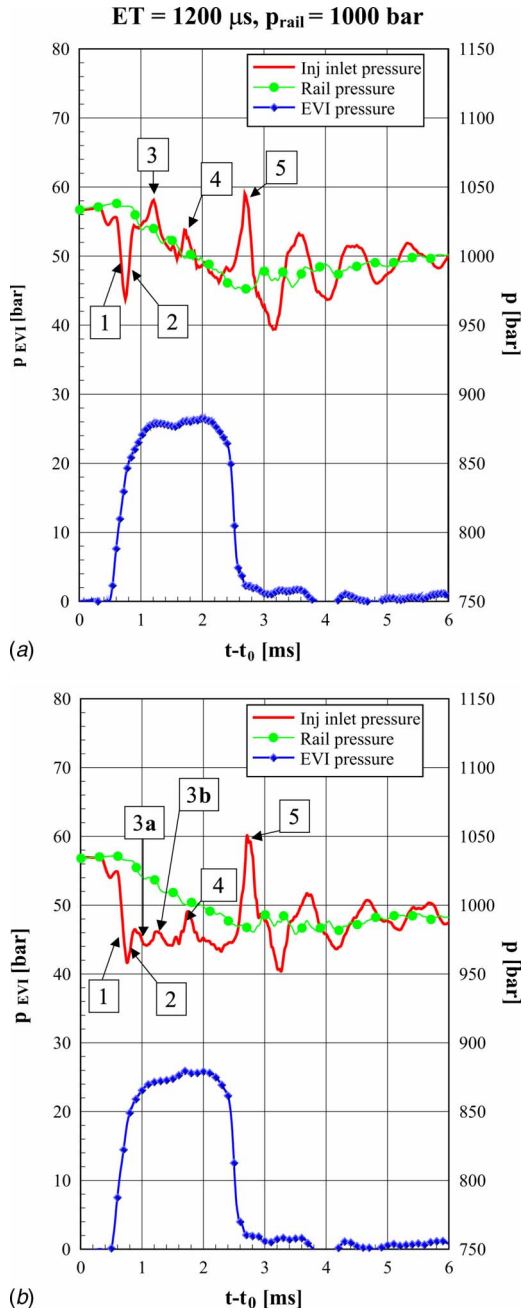

Fig. 17 Response of the system (*l*=125 mm and *d*=2.4 mm) to a main injection without (*a*) and with (*b*) the gauged orifice: (*a*) commercial layout and (*b*) layout with the orifice

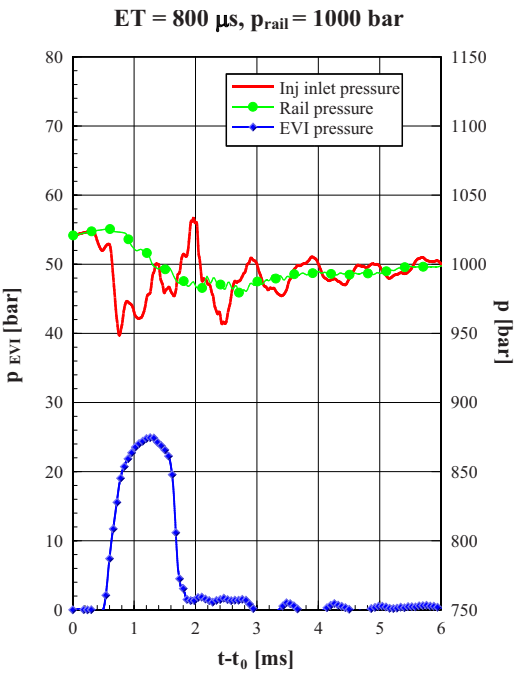

Fig. 18 Effect of the main injection duration on the response of the system (*l*=125 mm and *d*=2.4 mm) with the gauged orifice

accumulator, the reflected depression wave comes before the reflected compression wave in its motion toward the injector. Furthermore, as the ratio between the orifice and the injector inlet-pipe diameters is equal to 1/3, the reflected depression wave has an intensity that is stronger than the intensity of the reflected compression wave. In Fig. 17(*b*) the reflected depression wave (3a) is shown to be almost in phase, at the injector inlet, with the compression wave (2) coming from the nozzle so that they cancel each other, maintaining the pressure level close to the value resulting from the depression wave 1. The reflected compression wave is marked as 3b and is slightly delayed with respect to the analogous one in Fig. 17(*a*) due to the fact that the presence of the orifice increases the time period required by pressure waves to travel from the nozzle to the rail and back, as observed. The pressure peaks that are indicated by 4 in Figs. 17(*a*) and 17(*b*) are due to the closure of the pilot valve (6 in Fig. 2(*b*)) at the end of the solenoid energizing time, whereas the pressure peak, that is marked with 5, is determined by the water hammer at the nozzle closure.

Figure 18 plots the time histories of the same variables that are reported in Fig. 17(*b*) for p_{rail}=1000 bar and ET= 800 μs. The start of injection occurs at the same instant as in Fig. 17(*b*). However, since the energizing time in Fig. 18 is shorter than ET in the case of Fig. 17(*b*), the pressure peaks caused by the closure of the pilot valve and of the nozzle take place closer to the depression wave induced by the nozzle opening. In addition, the distance between these two pressure peaks in Fig. 18 is lower than the one in Fig. 17(*b*) because the nozzle-closure delay reduces with ET [8]. In particular, the compression peak, caused by the pilot-valve closure, results in phase with the compression wave coming from the rail (3b in Fig. 17(*b*)). For small ET values, the events marked with 2, 3a, 3b, 4, and 5 in Fig. 17(*b*) are almost in phase and the resulting pressure time distribution is close to the one corresponding to the case without any orifice at the same working conditions (Figs. 15(*a*) and 15(*b*)).

The orifice presence contributes to damp the pressure waves at the end of each injection shot, but introduces additional energy dissipation sources inside the system. Even though this generally leads to a worsening of the injection system efficiency, in any case, the application of the orifice to the rail outlet appears to be an effective solution for attenuating the pressure oscillations. The best results in terms of minimization of pressure fluctuation disturbances on multiple injections can be reached combining the use of the orifice with optimized dimensions of the injector-supplying-pipe. In the presence of the orifice and with reference to an injector inlet-pipe length and diameter equal to 125 mm and 4 mm, respectively, Fig. 19 reports, with square symbols, the volume-oscillation deviations for ET_{pil}=400 μs, ET_{main}=600 μs (Fig. 19(*a*)) and for ET_{pil}=400 μs, ET_{main}=900 μs (Fig. 19(*b*)). As can be deduced, the improvements that can be attained adopting this last solution are remarkable with respect to commercial layouts (Fig. 8), resulting in absolute values of σ always lower than 4% for DT values higher than 1000 μs (Fig. 19).

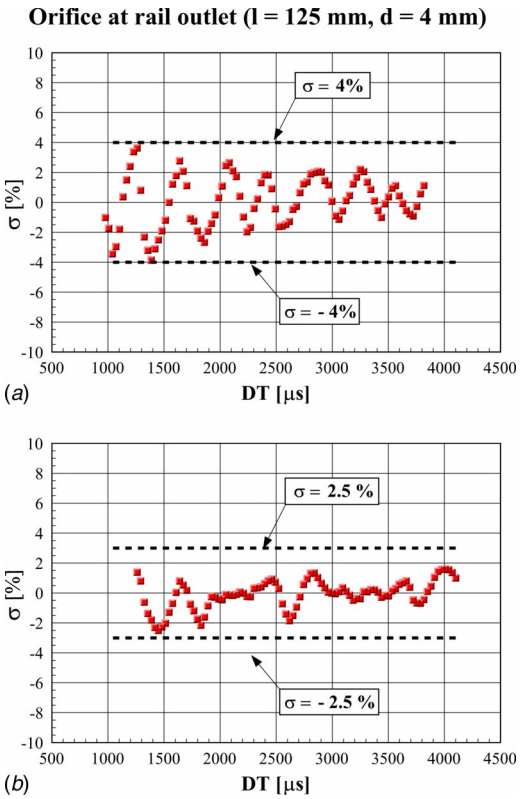

Fig. 19 Main injection volume deviations, p_{rail}=1000 bar: (*a*) ET_{pil}=400 μs, ET_{main}=600 μs and (*b*) ET_{pil}=400 μs, ET_{main}=900 μs

Rail Volume Design Rules

The rail volume should be large enough to give a stabilized pressure level inside the injection system during each operating condition. On the other hand, smaller rail sizes lead to prompter injection-system dynamic response during engine transients. The rail volumes in commercial automotive injection systems vary in the range of 20–40 cm^3.

The solid line in Fig. 20 reports the pressure-wave natural period, calculated by the lumped parameter model, as a function of the rail volume below 25 cm^3. This period seems to be scarcely influenced by the rail size, showing only a slight decrease when the accumulator volume is reduced. This seems to suggest that the dynamics of pressure oscillations is almost independent of rail hydraulic capacity. Based on these theoretical results, experimental tests were carried out to assess the possibility of condensing the rail in order to have a prompter system dynamic response

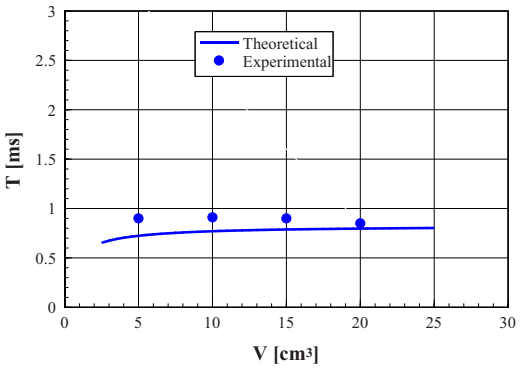

Fig. 20 Pressure-wave period versus rail volume

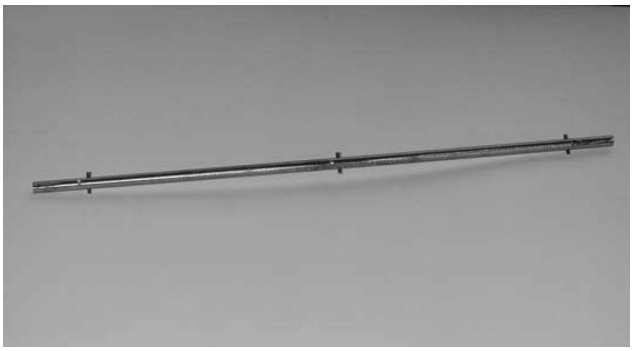

Fig. 21 Gauged cylinders for rail-volume reduction

without virtually any increase in the pressure-wave amplitude. Rails with a volume lower than 20 cm^3 were obtained by the introduction of a calibrated cylinder inside the accumulator of the commercial system under consideration. Figure 21 shows a photograph of one of these cylinders. Each of them presents nine staggered radial pins, which allow fixing it to the internal walls of the rail without introducing any flow restriction in this component, and thus do not affect the results of the investigation.

Figure 22 shows main injected-volume deviations σ when the accumulation volume is varied in the range of 5–20 cm^3. It is quite evident that no significant differences occur, neither in amplitude nor in frequency, in the oscillations of main injected volume when the accumulator size is reduced.

Figure 23 plots injector inlet (*a*) and rail (*b*) pressure distributions for different rail hydraulic capacities at p_{rail}=1000 bar and ET=1000 μs. The most striking difference between the presented data is in the starting pressure level when the injection event begins. As a matter of fact, the pressure control valve, which is

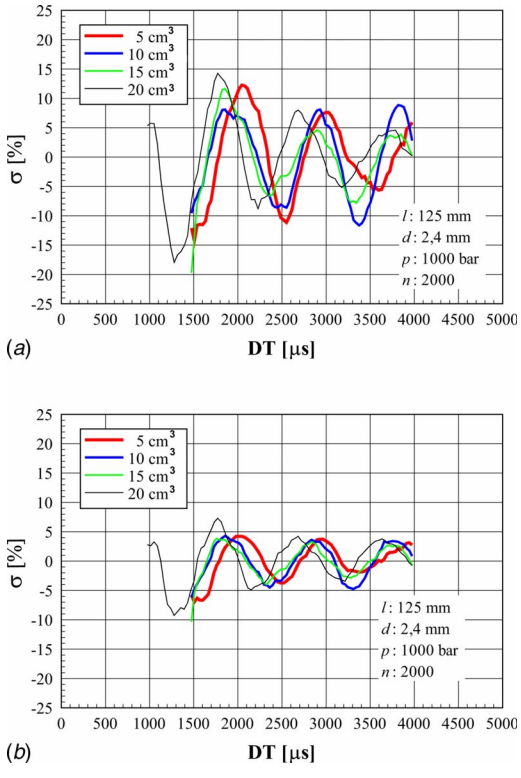

Fig. 22 Main injection volume deviations for different rail capacities: (*a*) ET_{pil}=400 μs, ET_{main}=600 μs and (*b*) ET_{pil}=400 μs, ET_{main}=900 μs

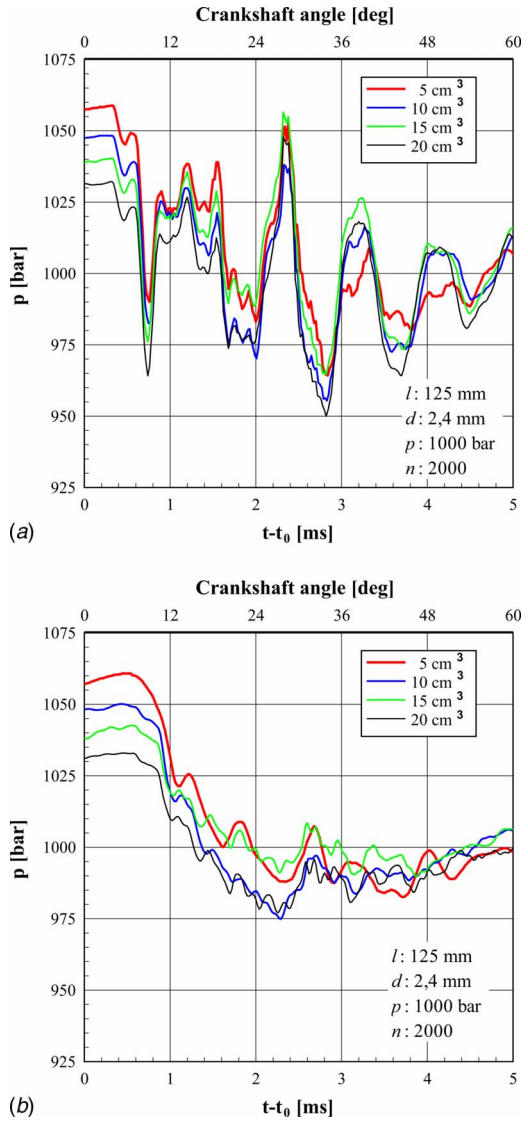

Fig. 23 Pressure distributions for different rail volumes: (*a*) injector inlet pressure, ET=1000 μs and (*b*) rail pressure, ET =1000 μs

managed by a pulse width modulation control strategy at the frequency of 1 kHz, operates in a way to compensate the different hydraulic capacities provided by the different rail internal volumes (lower volume involving lower capacity). Therefore, the pressure level at the start of injection is higher for lower accumulation volumes. In this way, the mean pressure is maintained at the desired value throughout the whole injection. It is interesting to observe that there is no other significant difference between the various system dynamic behaviors with different rail accumulation volumes. In CR systems the rail and the pressure control valve team up to maintain the rail-pressure level at its nominal value as far as possible, the dynamics of the pressure control valve being dependent on the rail size. If the rail accumulation volume is changed, the pressure control valve undergoes different working conditions; to give an example, when a rarefaction wave reaches the rail, the duty cycle of the pressure control valve is higher for the smaller rail due to its lower capacity. Thus, the pressure control valve can compensate for the rail accumulation volume reduction, which leads one to the conclusion that the rail volume does not play a major role in the response of the system to the injection events, as it might appear instead.

For three different rail accumulation volumes, namely, 20 cm^3, 10 cm^3, and 5 cm^3, Fig. 24 plots the injector characteristics obtained at distinct nominal rail pressures. Substantial modifications in the rail dimensions introduce only tiny changes in the dependence of the injected volume on ET.

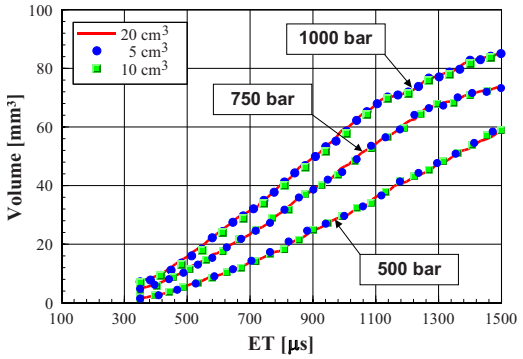

Fig. 24 Injector characteristics for different rail volumes

An additional important point to examine is the dependence of the so-called system saturation conditions on the rail capacity. When the injected fuel amount per engine cycle is particularly elevated, the rotary pump does not succeed in restoring the nominal pressure level in the rail before the next injection cycle starts. As a consequence, the system delivers the fuel with an injection pressure that is lower than the expected one, and thus the overall injected mass is lower than planned. In these situations the injection system is said to reach its saturation conditions. If the energizing times or the nominal rail pressure are further increased, the injection system will not be capable of reproducing the commands. The system saturation conditions are related to the maximum torque that can be developed by the engine. It would be interesting to verify if the values of ET and p_{rail} leading to injection system saturation conditions depend on the rail volume.

In the case of single injections and at a fixed engine speed (namely, 2000 rpm), Table 3 reports the ET_{crit} values (critical energizing times), which lead to saturation conditions for the different nominal rail pressures. These conditions are considered to occur when the time-averaged rail pressure over the overall pump cycle is more than 20 bar below the setup nominal rail pressure level. The data in the second column refer to a rail volume of 20 cm^3 (commercial configuration) and those in the third column refer to a rail accumulation volume of 10 cm^3. Each energizing critical time has been worked out as ensemble average over repeated tests. As can be inferred, the maximum amount of fuel that can be injected under a certain nominal rail pressure does not seem to be significantly affected by the rail size. In fact, the critical energizing times in the second and in the third column are almost similar for every p_{rail}. According to Fig. 23(*b*), when a certain quantity of fuel is injected, the pressure decrease in the rail tends to grow as the rail volume reduces. However, at the end of injection, during the subsequent action of the pressure control valve, smaller rail accumulation volumes are prompter in restoring the nominal pressure level inside the system due to their lower

Table 3 Saturation limits

P_{rail} (bar)	ET_{crit} (μs) 20 cm^3	ET_{crit} (μs) 10 cm^3
1250	1210	1220
1300	1135	1140
1350	1075	1085
1400	1020	1030
1450	945	950
1500	785	790

inertia. In other words, smaller rail volumes give rise to larger pressure drop in the rail during the injection phase but allow higher-pressure growth during the pump cycle phase subsequent to the injection event.

Therefore, it is well founded that saturation conditions in Table 3 are not modified by significant rail-capacity changes.

Conclusion

The design of the injector-supplying pipe is shown to be very important for minimizing the impact of pressure waves on the oscillations of fuel injected in multiple injections when DT is varied. Shorter-length and larger-diameter injector inlet-pipes give rise to smaller amplitude and higher frequency pressure oscillations that are triggered by the nozzle-closure induced water hammer at the end of each injection event. The experimentally gained evidence of this can be physically explained on the basis of energetics considerations. During injection the fuel inside the system flows to the nozzle and then is expelled. The kinetic energy related to such a fuel movement is shown to be the same for different aspect ratios of the injector inlet-pipe. When the injection terminates, the fuel moving toward the nozzle is arrested and all its kinetic energy is stored inside the pressure waves that travel forth and back along the feeding pipe and inside the electroinjector. Hence, the energy stored in the pressure waves under definite working conditions of ET, n, and p_{rail} is comparable for system layouts applying injector inlet-pipes with different dimensions. Since the energy stored in the pressure waves increases with both their amplitude and frequency, system configurations leading to higher amplitude of pressure waves imply lower frequencies and vice versa.

A theoretical-experimental study aimed at identifying injector inlet-pipe dimensions effective in minimizing pressure-wave perturbations of multiple-injection performance was carried out. Such an enhancement was found to be given by a suitable pipe pressure-wave energy modulation, according to an active strategy of oscillation damping. The experimental tests were designed with the aid of a simple zero-dimensional model, allowing the evaluation of the pressure-wave frequencies as functions of the system geometric features. One design rule that can be synthetically provided is that the reduction in the length to diameter ratio of commercial injector inlet-pipes is very useful for decreasing the dependence of the injected fuel amount on DT in multiple injections. On the other hand, the benefits that can be obtained by reducing the length below 100 mm or increasing the diameter beyond 4 mm are quite small. These results are general and can be applied to any injection system size.

In fuel injection systems for automotive application, good results can be obtained selecting injector inlet-pipes 100 mm in length and 3.8 mm in internal diameter. More specifically, for the case $p_{rail}=1000$ bar, $ET_{pil}=400$ μs, and $ET_{main}=600$ μs, the maximum value of $|\sigma|$, i.e., $|\sigma_{max}|$, for $DT \geq 1000$ μs changed from 20%, that is typical of a commercial layout, to 9%, and for $p_{rail}=1000$ bar, $ET_{pil}=400$ μs, and $ET_{main}=900$ μs $|\sigma_{max}|$ lowers from 10% to 5%. In general, the amplitude of the fluctuation volume versus DT halved using the injector inlet-pipes with the innovative aspect ratio.

Significant reduction in injected-volume dependence on DT was also obtained introducing a specifically designed orifice in the rail-pipe connection, so as to yield significant passive damping of pressure waves. A gauged orifice with a diameter of 0.8 mm was selected for automotive-application pipes with $l=125$ mm and $d=2.4$ mm. For the case $ET_{pil}=400$ μs and $ET_{main}=600$ μs, $|\sigma_{max}|$ reduced to 8%, whereas for the case $ET_{pil}=400$ μs and $ET_{main}=600$ μs, it decreased up to 4%. Owing to the fact that an additional energy dissipation source was thus introduced within the hydraulic circuit, modifications in injection characteristics were observed. The injected fuel volume, for any ET and p_{rail}, generally reduced with respect to hydraulic layout without orifice. The percentage reduction was variable, but in any case it kept under 8%. Although it generally led to a worsening in the injection system hydraulic efficiency, the application of the orifice to the rail outlet was shown to be an effective solution to contrast pressure oscillations.

The best result in terms of minimization in the pressure-wave induced disturbances of multiple injections was obtained when the calibrated orifice was combined with aspect ratios of the injector-supplying pipe suitable for reducing oscillations in the injected volume. In particular, by applying a 0.8 mm gauged orifice to an injector inlet-pipe with $l=125$ mm and $d=4$ mm $|\sigma_{max}|$ reduced to 4.0% for the case $p_{rail}=1000$ bar, $ET_{pil}=400$ μs, and $ET_{main}=600$ μs and to 2.5% for the case $p_{rail}=1000$ bar, $ET_{pil}=400$ μs, and $ET_{main}=900$. In general, a reduction to one-fourth was assessed for the injected-volume fluctuation amplitude with respect to the values that were measured in the standard layout ($l=125$ mm and $d=2.4$ mm) without orifice.

When the rail accumulation volume is reduced the variations in the injector characteristics take the same magnitude order of the EMI accuracy, and thus the single-injection performance results to be virtually independent of the rail size. This rule is of general validity. With reference to the considered automotive injection system, the rail volume was reduced from 20 cm^3 up to 5 cm^3, in the presence of the pressure-control valve, but without any worsening of the pressure-oscillation influence on multiple-injection performance. This resulted in a system with a prompter dynamic response during engine speed transients.

Each hydraulic-circuit layout modification suggested in the present work does not have any appreciable cost increase with respect to the commercial configurations. Furthermore, if the accumulator size is considerably reduced, the manufacturing costs of the rail decrease, at least owing to the savings in the employed material amounts.

Acknowledgment

Financial support to this research was provided by Fiat Research Center, FA-GM Powertrain, and Ministry of University and Research (MUR) under COFIN'04 and COFIN'06 Projects. The authors would like to thank S. Canale, G. Bonetto, F. Guglielmo, and E. Rigon of Fiat Research Center for their invaluable technical assistance.

Nomenclature

- C = hydraulic capacitance
- a = sound speed
- A = pipe cross section
- d = pipe diameter
- E = energy
- H = average system enthalpy
- l = pipe length
- L = hydraulic inductance
- n = engine speed
- p = pressure
- Q = heat transferred across the system walls
- t = time
- T = natural period; temperature
- u = average system internal energy per unit mass
- U = average system internal energy
- V = volume

Subscripts

- c = kinetic
- crit = critical (saturation conditions)
- el = electric
- end = injection end
- EVI = at injection-rate indicator
- inj = injected
- inj, in = injector inlet
- main = main injection

pil = pilot injection
PV = pilot valve
rail = rail chamber
refl = reflux
start = start of energizing current
0 = reference value

Superscripts

o = stagnation or total

References

[1] Nehmer, D. A., and Reitz, R. D., 1994, "Measurement of the Effect of Injection Rate and Split Injections on Diesel Engine Soot and NO_x Emissions," SAE Paper No. 940668.

[2] Tow, T. C., Pierpont, D. A., and Reitz, R. D., 1994, "Reducing Particulates and NO_x Emissions by Using Multiple Injections in a Heavy-Duty D. I. Diesel Engine," SAE Paper No. 940897.

[3] Pierpont, D. A., Montgomery, D. T., and Reitz, R. D., 1995, "Reducing Particulate and NO_x Using Multiple Injections and, EGR in a D.I. Diesel," SAE Paper No. 950217.

[4] Chen, S. K., 2000, "Simultaneous Reduction of NO_x and Particulate Emissions by Using Multiple Injections in a Small Diesel Engine," SAE Paper No. 2000-01-3084.

[5] Henein, N. A., Lai, M.-C., Singh, I. P., Zhong, L., and Han, J., 2002, "Characteristics of a Common Rail Diesel Injection System Under Pilot and Post Injection Modes," SAE Paper No. 2002-01-0218.

[6] Mulemane, A., Han, J.-S., Lu, P.-H., Yonn, S.-J., and Lai, M.-C., 2004, "Modeling Dynamic Behavior of Diesel Fuel Injection Systems," SAE Paper No. 2004-01-0536.

[7] Catania, A. E., Ferrari, A., Manno, M., and Spessa, E., 2005, "Experimental Investigation of Dynamics Effects on Multiple-Injection Common Rail System Performance," ASME ICED Spring Conference, and ASME J. Eng. Gas Turbines Power, **130**(3), p. 032806.

[8] Catania, A. E., Ferrari, A., and Spessa, E., 2006, "Numerical-Experimental Study and Solutions to Reduce the Dwell-Time Threshold for Fusion-Free Consecutive Injections in a Multijet Solenoid-Type CR System," ASME ICED Spring Conference, ICES2006 Best Paper Award, and ASME J. Eng. Gas Turbines Power, in press.

[9] Catania, A. E., Ferrari, A., and Manno, M., 2005, "Parametric Study of Hydraulic Layout Effects on Common-Rail Multiple Injections," presented at *2005 Fall Technical Conference of the ASME ICED*, Ottawa, Canada, Sept. 11–14, Paper No. ICEF 2005-1288.

[10] Bianchi, G. M., Falsari, S., Brusiani, F., Osbat, G., Parotto, M., and Pelloni, P., 2005, "Numerical Investigation of Critical Issues in Multiple-Injection Strategy Operated by a New C.R. Fast-Actuation Solenoid Injector," SAE Paper No. 2005-01-1236.

[11] Beierer, P., Huhtala, K., Lehto, E., and Vilenius, M., 2005, "Study of the Impact of System Characteristics on Pressure Oscillations in a Common Rail Diesel Fuel Injection System," SAE Paper No. 2005-01-0910.

[12] Bosch, W., 1966, "The Fuel Rate Indicator: A New Measuring Instrument for Display of the Characteristics of Individual Injection," SAE Paper No. 660749.

[13] Catania, A. E., Ferrari, A., and Manno, M., 2005, "Development and Application of a Complete Common Rail Injection System Mathematical Model for Layout Hydro-Dynamic Analysis," ASME ICED Spring Conference, and ASME J. Eng. Gas Turbines Power, **130**(6), p. 062809.

[14] Catalano, L. A., Tondolo, V. A., and Dadone, A., 2002, "Dynamic Rise of Pressure in the Common Rail Fuel Injection System," SAE Paper No. 2002-01-0210.

[15] Box, G. E. P., and Wilson, K. B., 1951, "On the Experimental Attainment of Optimum Conditions," J. R. Stat. Soc. Ser. B (Methodol.), **13**(1), pp. 1–45.

Mark Potter
Marko Bacic
Phil Ligrani[1]

Department of Engineering Science,
University of Oxford,
Parks Road,
Oxford OX1 3PJ, UK

Matthew Plackett
Hardware Engineering-Fleet Controls,
Rolls Royce PLC,
P.O. Box 31,
Derby DE24 8BJ, UK

Instabilities of Nonreturn Valves in Low-Speed Air Systems

Practical observations of the nonreturn valve wear in aero-engine cabin-bleed systems suggest that such valves are subject to unstable behavior. A theoretical model for the prediction of nonreturn valve instabilities in air systems is proposed and a nonlinear state-space model of the nonreturn valve and air volume interaction is derived from first principles. Experimental work is used to identify both the dynamic characteristics and the flow properties of the valve, which are used to identify the coefficients within the model. Through frequency analysis of valve oscillatory behavior, the levels of damping within the system are identified. Finally, using a local linearization of the state-space model an explicit mathematical prediction of valve stability is derived based on system parameters. These predictions are used to generate a map of the transition from stable to unstable system behavior for low-speed air flow, which is in excellent agreement with experimental data. [DOI: 10.1115/1.2969746]

1 Introduction

Nonreturn valves (NRVs) are used in a variety of thermofluid systems involving gas flow where there is a requirement to prevent reverse flow conditions. Nonreturn valve wear in the aero-engine cabin-bleed systems has been a recognized problem since the 1970s. Specifically nonreturn flapper valves, as shown in Fig. 1, have consistently failed to meet long-life specifications postulated by manufacturers. The most common failure is wear in the return spring that can lead to breakage and regular costly inspections. There have also been recorded instances of hinge wear and flap cracking. This combination of failure modes suggests that the valves experience a larger number of opening-closing cycles than expected. Related pressure control poppet valves are also known to experience unstable and irregular behavior, under certain flow conditions, due to an interaction of the valve with an up or downstream volume of fluid [1]. Results from the present study show that nonreturn valves experience similar phenomena.

There has been a significant amount of work conducted on the behavior of nonreturn valves, where the majority of this work focuses on the behaviour of the valve under a reversing flow condition in hydraulic applications. If the flow velocity through a nonreturn valve rapidly decelerates and then reverses, it is possible that the valve will close only after a reverse flow condition has been established. If this occurs, fluid momentum can cause a sudden increase in system pressure and valve differential pressure, leading to slamming of the nonreturn valve [2,3]. The large pressure spikes, and resultant valve slamming, caused by a flow reversal can cause damage to hydraulic systems. When designing such a system, it is therefore important to understand the key parameters affecting nonreturn valve behavior. Thorley [4,5] determined relevant parameters using nondimensional analysis and identified four key nondimensional terms, which relate flow characteristic to the dynamics of the valve. Valibouse and Verry [6] approached the problem of check valve slamming by deriving a second-order mathematical model of valve dynamics, which includes the hydrodynamic forces exerted on the flaps. This model is then used to investigate valve behavior under flow reversal, and good agreement is found between theoretical and experiment valve behavior.

These previous investigations show good understanding of valve dynamics under flow reversal, and the second-order mathematical models of the valve are in general agreement with experimental data. However, slamming behavior does not explain the high levels of wear that are seen on valves in the cabin bleed environment. Rahmeyer [7] suggested that valve flutter and motion under positive flow conditions, where the direction of flow acts to open the flaps, are the leading causes of wear in nonreturn valves. The author indicates that this flutter is caused by unsteady forces and unsteady separation of the flow within the valve. One proposed solution to this problem is to introduce a minimum flow velocity constraint into the system which ensures that the valve flaps are fully open [8]. By investigating a swing check valve, Rahmeyer [7] modeled the opening of the valve as a function of the mean steady-state flow velocity and used this model to derive the minimum flow requirement based on valve geometry. Botros et al. [9] further refined Rahmeyer's model for an NPS 4 swing check valve in air, improving the accuracy of the model's coefficients and response through experimental work. This work again focuses on the steady state behavior of nonreturn valves and does not consider transients or system stability. In order to understand transient behavior, as an aid to system design, Pandula and Halasz [10] derived a model of valve behavior under step changes in flow rate. By modeling the flow characteristics and frictional behavior in the valve bearing, an accurate model of the system is developed, which is validated using experimental data. This work highlights the need for accuracy when determining the levels of damping in the system in order to capture the true dynamic behavior of the system.

Despite generating this understanding of nonreturn valve dynamics, literature does not directly address the cause of valve stability and the possibility of fluid-valve interactions leading to flapping behavior. However, some studies consider such phenomena in poppet valves. Poppet valves are used in a variety of hydraulic system applications as pressure regulating valves. The poppet valve system consists of an upstream supply line, an upstream plenum chamber separated from the supply by an orifice, and a valve seat with a spring-loaded poppet. An interaction of the upstream volume of fluid with the poppet dynamics is known to cause self-excited oscillations. This can lead to excessive noise, spring breakage, or damage to the valve seat [1]. Stone [11] investigated poppet valve behavior by developing a steady-state model of the system, relating discharge coefficient, and reaction forces to poppet and seat geometry. Kasai [12,13] incorporated the dynamics of the up and downstream piping into a system model, which is then used to determine whether the valve is locally stable. Hayashi et al. [14–16] extended the idea of local stability

[1]Corresponding author.

Contributed by the Fluids Engineering Division of ASME for publication in the JOURNAL OF FLUIDS ENGINEERING. Manuscript received September 24, 2007; final manuscript received March 25, 2008; published online October 27, 2008. Assoc. Editor: James A. Liburdy.

Fig. 1 Spring-loaded twin flapper nonreturn valve

numerically, using a Routh–Hurwitz type criterion, to form a global stability map. This map plots the stability of the system as a function of the supply pressure and the lift of the valve head. The geometry of the upstream volume is kept constant during this theoretical analysis. Hyashi et al. [16] also investigated behavior of the poppet type valves, which is sometimes chaotic, using Lyapunov exponents and bifurcation diagrams.

Although poppet valves perform a very different function to nonreturn valves, this work suggests that, through an interaction with a volume of fluid, spring loaded valves can exhibit highly unstable behavior. In this paper, the importance of interactions between a nonreturn valve and a volume of air is confirmed. A lumped parameter mathematical model of a system containing a nonreturn valve and a partially restricted volume of air is developed. Experimental apparatus is used to identify the parameters within this model and to examine the nature of valve instabilities. Pandula and Halasz [10] demonstrated that an accurate knowledge of the damping within the valve system is essential in order for any model to accurately capture the behavior of the system. To address this problem here, frequency analysis methods are used to determine damping coefficients present in the model. By considering the phase lag between the pressure loading and the motion of the valve under experimental transient flow conditions, the level of viscous damping is calculated with a high degree of confidence. While previous system simulations mainly consider numerically solving nonlinear differential equations, this paper uses control engineering techniques to develop a linearized state-space model of the system. With the model in this form, the effects of system geometry and mass flow are investigated, and global stability criteria are derived that are based on local linearizations of the model at all operating points. These stability criterion predictions are validated and confirmed by experimental measurements, which show transition from stable to unstable behavior as mass flow and system geometry are altered.

While there are significant results on the stability of poppet valves [11–16] for hydraulic systems, very little information exists on instabilities of nonreturn valves for air systems. Here we show that nonreturn valve instabilities are related to valve and downstream volume interactions both through derivation of simple theoretical models and through their experimental validation. This paper thus presents a unique and different approach, compared to all known existing studies, for the understanding of the unstable behavior of nonreturn valve systems. Through the use of frequency and eigenvalue analysis within a state-space system model, the effects of both system mass flow and system geometry, specifically the interaction with a downstream volume, on valve behavior are determined theoretically and then validated experimentally.

2 Valve Configuration and Mathematical Models

The nonreturn valve under consideration is shown in Fig. 1. Figure 2 shows a schematic of the valve with different components labeled. The valve is of flapper type design with two spring-loaded independent flaps. The problem of valve interaction with a column of air, as schematically shown in Fig. 3, is considered. The variables within the system are P_2, the pressure within the downstream system, the angle of the valve flaps θ (assumed to be symmetric), and the volume V. Within the cabin-bleed system the downstream volume is isolated by a pressure regulating valve. When modeled, this valve is replaced by an outlet restrictor with discharge coefficient and area given by $(C_dA)_{\text{out}}$.

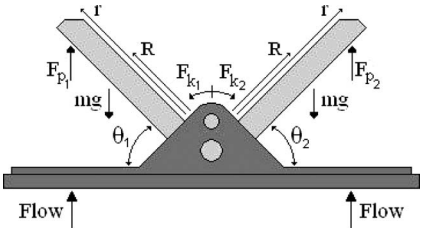

Fig. 2 Nonreturn valve geometry and loading

2.1 Valve Dynamics. For this analysis, it is assumed that the valve sits in a horizontal plane with respect to the gravity vector. The weight of the flaps, along with the spring, closes the valve when no flow is present, while during a forward flow condition a pressure loading acts to open the valve. The valve flap angle is measured from the closed horizontal position, and only one flap is considered due to valve symmetry by assuming equal pressure loading on each of the flaps. Note that if the valve sits immediately after an offset bend in the pipe, this assumption cannot be made, and separate equations of motion would be required for the motion of each flap.

Applying Newton's law of motion to each flap, one obtains

$$T_F = I\ddot{\theta} \tag{1}$$

where $\ddot{\theta}$ is the acceleration of the valve flap angle. The spring is pretensioned so that there is a force component at zero valve angle. This offset is denoted θ_0. Assuming that the spring constant, K, is linear, the spring torque applied to each flap is given by

$$T_K = K(\theta + \theta_0) \tag{2}$$

Assuming that each flap is a half disk of uniform thickness hinged along its straight edge, the center of mass for each flap is then given by

$$R_r = \frac{4r}{3\pi} \tag{3}$$

where r is the flap radius. The gravity induced torque on the valve flaps is therefore of the form

$$T_{mg} = R_r mg\cos(\theta) \tag{4}$$

where m is the mass of each flap. The mechanical damping for the system is assumed to be viscous damping proportional to flap velocity, which leads to the result given by

$$T_c = c\dot{\theta} \tag{5}$$

where c is the damping coefficient. Denoting the torque on the flaps due to pressure loading with T_p and considering a force balance leads to the equation having the form

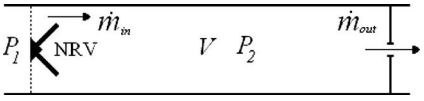

Fig. 3 Flow configuration, parameters, and arrangement

$$T_p = I\ddot{\theta} + c\dot{\theta} + K(\theta + \theta_0) + R_r mg\cos(\theta) \quad (6)$$

The equation of motion describing the valve flap dynamics is therefore a decoupled second-order system. Note that the cross coupling between the valve spring and hinge is neglected in this derivation.

2.2 Volume Dynamics. The nonreturn valve is modeled as a variable orifice plate in a low velocity flow. The mass flow rate into the volume, through the nonreturn valve, is therefore defined using

$$\dot{m}_{\text{in}} = C_{dv}A_v\sqrt{\frac{2(P_1 - P_2)P_1}{RT}} \quad (7)$$

where A_v is the area of the valve when fully open. C_{dv} is the discharge coefficient of the valve, defined as the ratio of the actual mass flow rate of fluid $\dot{m}_{\text{in}}$ to the theoretical or ideal mass flow rate. As the flaps open, the effective area of the valve increases, and so does the discharge coefficient. As a result, C_{dv} is a function of the valve opening angle θ. In order to model the system mass flows accurately, this function is determined experimentally, which is discussed later in this paper.

The mass flow rate out of the control volume $\dot{m}_{\text{out}}$ is regulated using an outlet restrictor across which the ratio of upstream to downstream pressure is sufficiently high to ensure approximately choked flow. The mass flow rate is therefore given by

$$\dot{m}_{\text{out}} = P_2\sqrt{\frac{\gamma}{RT}}\left(\frac{\gamma+1}{2}\right)^{-(\gamma+1)/2(\gamma-1)}(C_dA)_{\text{out}} \quad (8)$$

where $(C_dA)_{\text{out}}$ is the product of area and discharge coefficient of the outlet restrictor defined by the outlet geometry. Eq. (8) is used to relate $\dot{m}_{\text{out}}$, $(C_dA)_{\text{out}}$, and P_2 later in the analysis. The rate of change of the mass of air in the chamber between the nonreturn valve and the gate valve, which acts as a restrictor, is denoted $\dot{m}_2$ and is given by

$$\dot{m}_2 = \dot{m}_{\text{in}} - \dot{m}_{\text{out}} \quad (9)$$

Note that $\dot{m}_2 = 0$ with steady flow conditions. From the ideal gas equation with constant temperature, the time derivative of static pressure is determined using

$$\dot{P} = \frac{\dot{m}RT}{V}$$

and thus, Eq. (9) can be rewritten as

$$\dot{P}_2 = \frac{C_{dv}A}{V}P_1\sqrt{2RT(1 - P_2/P_1)} - \frac{P_2}{V}\sqrt{\gamma RT}\left(\frac{\gamma+1}{2}\right)^{-(\gamma+1)/2(\gamma-1)} \times (C_dA)_{\text{out}} \quad (10)$$

Solving for P_2 in the above equation requires knowledge of C_{dv}, which depends on the valve flap angle θ.

2.3 System Dynamics. To combine Eqs. (1)–(10) requires the knowledge of aerodynamic torques T_P in terms of pressures and angles. It is suggested by Tarnopolsky et al. [17] that if a sprung plate is subjected to a steady stream of the fluid, the aerodynamic force acting on that plate is related to the drag coefficient C_θ using

$$T_p = \tfrac{1}{2}C_\theta\rho D^3u^2 \quad (11)$$

Substituting Eq. (11) into Eq. (6) then yields

$$I\ddot{\theta} + c\dot{\theta} + K(\theta + \theta_0) + R_r mg\cos(\theta) = \tfrac{1}{2}C_\theta\rho D^3u^2 \quad (12)$$

Using $\dot{m} = \rho Au$, the equation for the discharge coefficient can be rearranged into the form

$$u = \frac{C_{dv}\sqrt{2(P_1 - P_2)\rho}}{\rho} \quad (13)$$

Then, by combining Eqs. (12) and (13), one obtains

$$I\ddot{\theta} + c\dot{\theta} + K(\theta + \theta_0) + R_r mg\cos(\theta) = C_\theta C_{dv}^2D^3(P_1 - P_2) \quad (14)$$

The valve dynamics can now be written in terms of the pressures within the system using

$$I\ddot{\theta} + c\dot{\theta} + K(\theta + \theta_0) + R_r mg\cos(\theta) = f_\theta(P_1 - P_2) \quad (15)$$

where $f_\theta = C_\theta C_{dv}^2D^3$. Equation (15) is used to determine valve/flow stability and instability behaviors at particular mass flow rates and air volumes. Note that the valve pressure loading coefficient f_θ is assumed to be dependent only on the valve flap angle θ since it is a product of valve discharge and aerodynamic drag coefficients. Note that steady-state f_θ values are employed for the unsteady stability analysis. In reality, however, f_θ is a time-varying quantity and depends on past values of θ and P_2. Nevertheless, the unsteady component of f_θ is assumed to play a minor role as individual local stability conditions are considered.

3 Theoretical Analysis of Valve Instabilities

From Eq. (15), $f_\theta(P_1 - P_2)$ acts as implicit nonlinear feedback on the system, and as such, can affect both global and local stabilities. To investigate the effect that $f_\theta(P_1 - P_2)$ has on the stability of the system, consider governing valve Eq. (15). Rewriting Eq. (10) then gives

$$\dot{P}_2 = \dot{P}_{\text{in}} - \dot{P}_{\text{out}} \quad (16)$$

where

$$\dot{P}_{\text{in}} = \frac{C_{dv}A}{V}P_1\sqrt{2RT}\sqrt{(1 - P_2/P_1)} \quad (17)$$

and

$$\dot{P}_{\text{out}} = \frac{P_2}{V}\sqrt{\gamma RT}\left(\frac{\gamma+1}{2}\right)^{-(\gamma+1)/2(\gamma-1)}(C_dA)_{\text{out}} \quad (18)$$

To characterize the local stability of the valve, consider first the steady-state condition, where $\ddot{\theta} = \dot{\theta} = 0$ and the valve flaps sit at an angle θ with volume pressure P_2. Then from Eqs. (10) and (15), the following equations are obtained:

$$(P_1 - P_2) = \frac{K(\theta + \theta_0) + Rmg\cos(\theta)}{f_\theta} \quad (19)$$

$$(C_dA)_{\text{out}} = \frac{C_dAP_1\sqrt{2(1 - P_2/P_1)}}{P_2\sqrt{\gamma}\left(\frac{\gamma+1}{2}\right)^{-(\gamma+1)/2(\gamma-1)}} \quad (20)$$

By defining θ' as the valve angle measured from the steady-state angle and P_2' as the gauge pressure measured from the steady-state condition, Eqs. (16)–(18) are linearized to become

$$\dot{P}_2 = \left(\frac{\partial\dot{P}_{\text{in}}}{\partial\theta}\right)\theta' + \left(\frac{\partial\dot{P}_{\text{in}}}{\partial P_2}\right)P_2' - \left(\frac{\partial\dot{P}_{\text{out}}}{\partial P_2}\right)P_2' \quad (21)$$

$$I\ddot{\theta}' + c\dot{\theta}' + K\theta' - R_r mg\sin(\theta)\theta' = \frac{\partial f_\theta}{\partial\theta}P_1\theta' - \frac{\partial f_\theta}{\partial\theta}P_2\theta' - f_\theta P_2' \quad (22)$$

where

$$\left(\frac{\partial\dot{P}_{\text{in}}}{\partial\theta}\right) = \frac{\partial(C_dA)}{\partial\theta}\frac{P_1}{V}\sqrt{2RT}\sqrt{(1 - P_2/P_1)} \quad (23)$$

$$\left(\frac{\partial\dot{P}_{\text{in}}}{\partial P_2}\right) = \frac{(C_dA)}{V}P_1\sqrt{2RT}\frac{-1}{2\sqrt{(1 - P_2/P_1)}P_1} \quad (24)$$

$$\left(\frac{\partial \dot{P}_{\text{out}}}{\partial P_2}\right) = \frac{1}{V}\sqrt{\gamma RT}\left(\frac{\gamma+1}{2}\right)^{-(\gamma+1)/2(\gamma-1)} (C_d A)_{\text{out}} \tag{25}$$

Note that Eq. (22) is a second-order ordinary differential equation and can be converted into two first-order equations. This allows Eqs. (21) and (22) to be written as three first-order ordinary differential equations in a vector-matrix, which is expressed using

$$\begin{bmatrix} \dot{\theta}' \\ \ddot{\theta}' \\ P_2' \end{bmatrix} = \begin{bmatrix} 0 & 1 & 0 \\ X_1 & X_2 & X_3 \\ X_4 & 0 & X_5 \end{bmatrix} \begin{bmatrix} \theta' \\ \dot{\theta}' \\ P_2' \end{bmatrix} \tag{26}$$

where

$$X_1 = \frac{1}{I}\left[\frac{\partial f_\theta}{\partial \theta}P_1 - \frac{\partial f_\theta}{\partial \theta}P_2 + R_r mg \sin(\theta) - K\right] \tag{27}$$

$$X_2 = \frac{1}{I}[-c] \tag{28}$$

$$X_3 = \frac{1}{I}[f_\theta] \tag{29}$$

$$X_4 = \left(\frac{\partial \dot{P}_{\text{in}}}{\partial \theta}\right) \tag{30}$$

$$X_5 = \left(\frac{\partial \dot{P}_{\text{in}}}{\partial P_2}\right) - \left(\frac{\partial \dot{P}_{\text{out}}}{\partial P_2}\right) \tag{31}$$

Equation (26) is the local linearization of the system dynamics at a steady-state condition (θ, P_2) for a given mass flow. To ensure the local stability of the system, the eigenvalues of the matrix λ given by

$$S = \begin{bmatrix} 0 & 1 & 0 \\ X_1 & X_2 & X_3 \\ X_4 & 0 & X_5 \end{bmatrix} \tag{32}$$

must have all negative real parts. By substituting Eqs. (21)–(31) into the matrix (32), it is possible to determine the eigenvalues of the system by solving the equation of the form

$$\det(S - \lambda I) = 0 \tag{33}$$

for a given upstream volume and inlet mass flow. By considering the signs of the real parts of the eigenvalues, system stability characteristics are determined. To confirm the validity of this analysis, experiments are used to demonstrate a good agreement between theoretical and experimental stabilities.

4 Experimental Apparatus and Procedures

4.1 Valve Instrumentation. To record the position of the valve flaps under positive flow conditions an optical position sensor is developed especially for this purpose. An optical system is chosen to avoid the need for a physical connection to the flaps, preventing damage to sensitive hardware in the case of high flap velocities and flap impacts. It is also employed to minimize disruptions to the air flow through the valve. By shining light across the valve housing into a detector on the other side, a line of sight path is created through which the valve flap passes while opening. As the flap angle increases, more light is obscured from the detector and the output signal reduces. Using one detector in this way greatly reduces the complexity of the supporting electronics and means that the output signal is continuous. The system is calibrated by measuring the output of the photodiodes for a range of known angles, while the system is detached from the rig. A polynomial equation is then fitted to these data. A bank of rectangular red light emitting diodes (LEDs) provides the light source and a General Semiconductor Industries 10530CAW internally amplified photodiode is used to detect the flap signal. Internal amplification within this photodiode is essential in producing a signal with acceptably low levels of random noise.

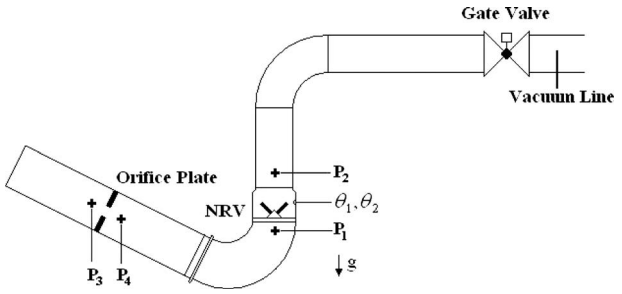

Fig. 4 Schematic of experimental setup and transducers

4.2 Experimental Facility. To validate the numerical analysis results, a low-pressure experimental facility is used, which is operated by a low-pressure vacuum line, and developed and constructed especially for this purpose. Figure 4 shows the rig layout. The flow development lengths on the upstream and downstream sides of the standard orifice plate are 2.0 m and 2.5 m, respectively. This plate is located within a section of piping that is fitted with upstream and downstream static pressure tappings, which are connected to a SensorTechnics BSDX ±0–100 mbar amplified differential pressure transducer, used to measure pressure drop for determination of the mass flow rate. Following this is the inlet elbow and the nonreturn valve. Static tappings on either side of the valve, connected to a second SensorTechnics differential pressure transducer, are used to determine the static pressure drop across the valve. The mass flow through the orifice plate is determined using the pressure drop across the plate $(P_3 - P_4)$, which is employed within the orifice flow equation. According to the British Standard Document No. BS1042, this equation is given as

$$\dot{m}_{\text{in}} = \frac{C}{\sqrt{1-\beta^4}}\frac{\pi}{4}d^2\sqrt{2(P_3 - P_4)\rho_1} \tag{34}$$

The ratio of the orifice diameter to the pipe diameter β is chosen to be equal to 0.5 so that all system mass flow values are measured with maximum accuracy. The flow discharge coefficient C is determined by orifice plate geometry and the Reynolds number of the incoming flow. For the selected β and system mass flows, the British Standard Document No. BS1042 gives $C = 0.6$.

All pressures are measured using SensorTechnics BSDX ±0–100 mbar amplified differential pressure transducers. These transducers are zeroed at the beginning of each data acquisition sequence at a zero mass flow rate condition. Each transducer is calibrated using a dead weight pressure testing apparatus. Signals from all instrumentation are sampled and acquired at a frequency of 1 kHz using a National Instruments NI6035E card. MATLAB/SIMULINK software is then employed in conjunction with an OpalRT RT-LAB and QNX operating system to ensure hard real-time operation.

4.3 Experimental Uncertainty Magnitudes of Measured Quantities. Experimental uncertainty magnitudes are determined based on 95% confidence levels using single-sample uncertainty analysis procedures. The associated uncertainty of differential pressure used to determine mass flow rate is ±1.2%. The experimental uncertainties of differential pressure across the nonreturn valve, the valve mass flow rate, and the valve flap angle are ±5.1%, ±0.61%, and ±1.0%, respectively.

5 Experimental and Analytical Results

5.1 Valve Parameters. To evaluate the stability matrix, as expressed by Eq. (32), and to determine the dynamic behavior of

Table 1 Nonreturn valve dynamic parameters

Flap radius	72×10^{-3} m
Flap inertia	6.2×10^{-4} kg m^2
Flap mass	0.47 kg
Spring constant	1.178×10^{-3} N m rad s^{-1}
θ_0	2.05 rad

the nonreturn valve, dynamic parameters of the valve and the flow characteristics of the system are required. The dynamic parameters are measured directly from the valve, while the flow characteristics are calculated from steady flow experimental data. To determine the spring coefficient K, the mass of the flaps m, and the spring offset angle θ_0, the valve alone is considered. With the valve flaps stationary, $\ddot{\theta}=\dot{\theta}=0$, Eq. (6) reduces to the form

$$T^0 = K(\theta^0 + \theta_0) + R_r mg\cos(\theta^0) \tag{35}$$

where T^0 and θ^0 are baseline values determined with this stationary arrangement. Using a spring balance to apply a torque to flap one at various flap angles, and solving this set of simultaneous equations, gives values for the coefficients K, m, and θ_0. The moment of inertia of each of the flaps is assumed to be that of a half disk of uniform thickness. The resulting valve dynamic parameters, determined through this procedure, are given in Table 1.

5.2 Steady Mass Flow Experiments. To accurately model the mass flow through the nonreturn valve and determine the effects of pressure loading on the valve flaps, the valve discharge coefficient and valve pressure loading coefficient must be known. To determine these parameters, a range of different system mass flow rates is considered, as the valve flap angle and the differential valve pressure are recorded. When these data are obtained, the valve is initially stabilized by starting the test at the maximum achievable mass flow. The system mass flow is then reduced in small increments to maintain valve stability. Figure 5 shows the variation of flap angle θ with the system mass flow rate. From this figure, it is evident that as the mass flow rate through the system increases, θ becomes larger as the valve opens in response. It is also evident that the dependence of θ on $\dot{m}$ is nonlinear. Figure 6 shows the variation of dimensional differential pressure across the nonreturn valve P_1-P_2 with the mass flow rate. This pressure drop increases as the system mass flow increases in a nonlinear fashion.

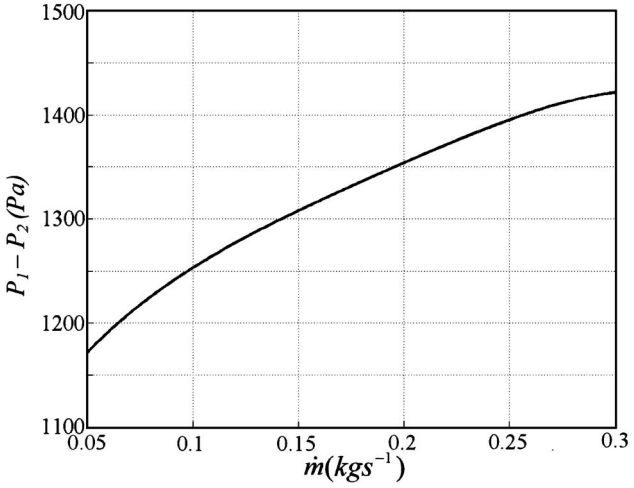

Fig. 6 Variation of differential pressure across the valve with system mass flow rate under stable operating conditions for all downstream volumes at different mass flow rates

The relationship between the steady flow discharge coefficient for the nonreturn valve C_{dv} and the valve flap angle θ is derived by rearranging Eq. (7) into the form

$$C_{dv} = \frac{\dot{m}_{\text{in}}}{A_v\sqrt{2(\Delta P)P_1/RT}} \tag{36}$$

With this equation, and with knowledge of the relationship between system mass flow rate and flap angle, and the relationship between system mass flow rate and differential valve pressure (given in Figs. 5 and 6), the variation of discharge coefficient C_{dv} with valve flap angle θ can be determined. The resulting nonlinear function is shown in Fig. 7. These data show that as the valve opens, the effective area of the valve increases, giving higher mass flow rate for a given differential pressure.

Tarnopolsky et al. [17] suggested that if a sprung plate is subjected to a steady stream of fluid, then the aerodynamic force acting on that plate is proportional to h_v, the dynamic head of the flow, with the loading coefficient C_θ as the constant of proportionality. This proportionality quantity is shown as it varies with flap angle θ in Fig. 8(*a*). To show that C_θ is not affected by flow

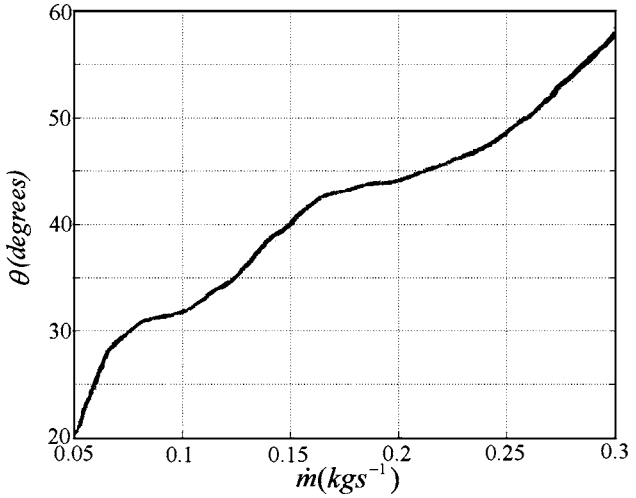

Fig. 5 Variation of the valve flap angle with system mass flow rate under stable operating conditions for all downstream volumes at different mass flow rates

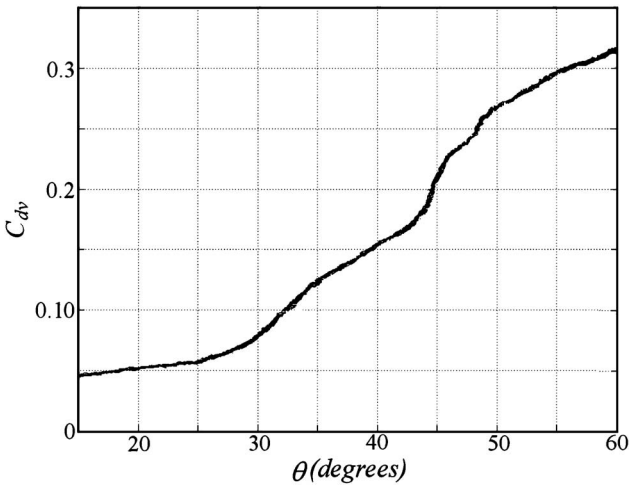

Fig. 7 Variation of the static discharge coefficient with the valve flap angle under stable operating conditions for all downstream volumes at different mass flow rates

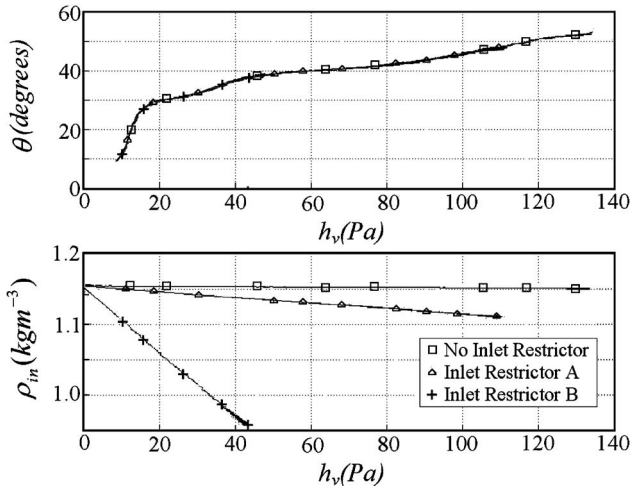

Fig. 8 Variation of dynamic head with the valve flap angle (*a*) for a range of inlet densities (*b*) under stable operating conditions for all downstream volumes at different mass flow rates

density, this inlet density is altered by changing the inlet restrictor. Three arrangements are used: No restrictor, restrictor A (where the ratio of the restrictor diameter to the pipe diameter is 0.50), and restrictor B (where the ratio of the restrictor diameter to the pipe diameter is 0.25). The resulting ρ_{in} density variations with h_v are shown in Fig. 8(*b*). The application of sequential restrictors thus reduces the inlet density ρ_{in}. With this in mind, Fig. 8(*a*) shows that the relationship between dynamic head and angular position is independent of flow density.

Using results in Figs. 5, 6, and 7, the valve pressure loading coefficient $f_\theta = C_\theta C_{dv}^2 D^3$ can be determined. This is needed in regard to the terms on the right-hand side of Eq. (14). The resulting f_θ function as it varies with valve flap angle θ is shown in Fig. 9. Recall that $f_\theta(P_1 - P_2)$ is the pressure loading on the nonreturn valve. From these data, it is evident that as the valve opens, less torque is present on the valve flaps for a given pressure difference.

5.3 Unsteady Flow Experiments. Pandula and Halasz [10] showed that accurate measurement of valve damping is essential to model the unsteady system behavior. In the stability analysis of the present nonreturn valve, the mechanical damping is assumed

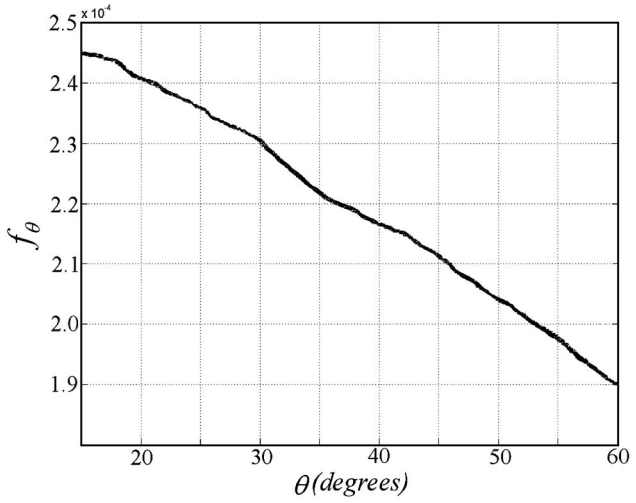

Fig. 9 Variation in the valve pressure loading coefficient with the valve flap angle under stable operating conditions for all downstream volumes at different mass flow rates

to be viscous damping, which is proportional to flap velocity, and characterized by a valve damping coefficient. The damping torque is equal to this valve damping coefficient c times the first derivative of the valve flap angle, as given in Eq. (5). To determine magnitudes of the valve damping coefficient c accurately, unsteady experiments, when the valve flaps, are employed. When the valve is subject to such unsteadiness, the valve flaps effectively oscillate sinusoidally, driven by a sinusoidal pressure loading force, given by $F = f_\theta(P_1 - P_2)$. Experimental data indicate the presence of a time lag between the loading force, F, and the flap response, θ. By considering the dynamics of the valve, this time lag can be related directly to the damping coefficient, c. By determining experimentally the level of time lag present in the system, it is possible to calculate the damping coefficient, c. To establish the relationship between the system time lag and the damping coefficient, the transfer function, $G(s)$, between the loading force, F, and the flap angle, θ, is required. $G(s)$ is determined by taking the Laplace transform of Eq. (22), the linearized valve position equation, which gives

$$G(s) = \frac{\theta'}{F} = \frac{1}{Is^2 + cs + K - R_r mg \sin(\theta)} \tag{37}$$

Any dynamic system will have a time lag between the input function and the output system response, which is given by

$$t_L = \frac{\arg(G(jw))}{w} \tag{38}$$

where $\arg(G(jw))$ is the argument of the transfer function evaluated at the driven frequency and w is the driven frequency. For the nonreturn valve system, the argument of the transfer function is then given by

$$\arg(G(jw)) = \arctan\left(\frac{wc}{K - Rmg \sin(\theta) - w^2 I}\right) \tag{39}$$

Equations (38) and (39) can be rewritten in terms of the damping coefficient, c, as

$$c = \frac{1}{w} \tan(wt_L)(K - R_r mg \sin(\theta) - w^2 I) \tag{40}$$

The time lag, t_L, between the pressure force F and the flap response θ is determined experimentally by considering the phase shift between the pressure variation across the valve and the valve flap position at the resonant frequency of the system and by employing the Blackman–Tukey approach [18]. The Blackman–Tukey approach can be used to compute the phase between the input and the output of a system, at a given frequency, by evaluating the argument of the ratio of the output-input cross-spectrum, $\Phi_{F\theta}$, and the input-input cross-spectrum, Φ_{FF}, at the driven frequency. The cross-spectra are determined by recording the pressure loading force F and the valve position θ for 25 s at a sample rate of 1000 Hz during unstable valve behavior. These data are then windowed using a Hanning window of the same length. The input-input cross-spectrum Φ_{FF} is calculated by correlating the windowed input signal with itself before taking the Fourier transform. The output-input cross-spectrum $\Phi_{F\theta}$ is similarly determined by correlating the windowed input signal with the windowed output signal before taking the Fourier transform. Using this approach, the time lag between the system input and output is given by

$$t_L = \frac{1}{w} \arg\left(\frac{\Phi_{F\theta}}{\Phi_{FF}}\right)_{w=w_n} \tag{41}$$

The damping coefficient is then calculated from t_L using Eq. (40) and is equal to $c = 0.0097$.

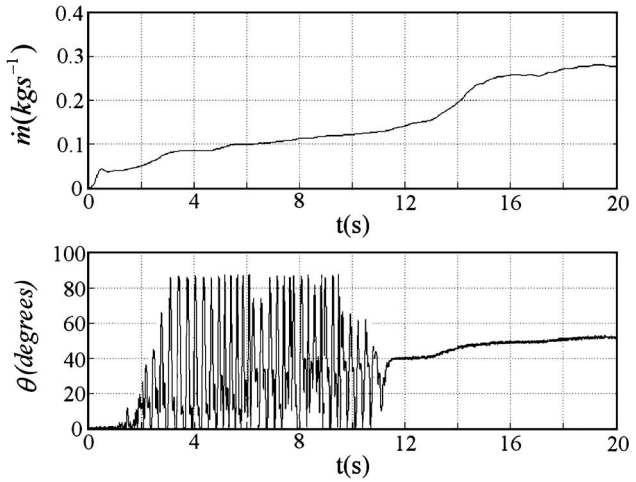

Fig. 10 Example of the valve instability as mass flow rate varies with time (top) and as the valve flap angle varies with time (bottom) for a downstream volume of 0.034 m^3

5.4 Stability Map and Comparisons Between Experimental and Analytic Results. Variations of the valve flap position and system mass flow rate with time, which illustrate the unstable valve behavior, are shown in Fig. 10. From these data, it is evident that as the system mass flow rate increases slowly, the system becomes unstable. This is apparent as the valve flaps begin to swing rapidly between fully closed and fully open, with violent impacts occurring at both locations. This behavior is self-exciting and continues indefinitely, unless the system mass flow is increased above a threshold level. For these experimental conditions and configuration, this threshold is present at approximately 0.15 kg/s.

For a given downstream volume, this threshold can be predicted using eigenvalue stability criteria and a linear state-space model of the system. For a given mass flow rate, the steady-state flap position θ and system pressure P_2 are calculated using Eqs. (19) and (20). These values are then used to evaluate the state-space matrix values within Eq. (32), which are the eigenvalues that determine whether the system is locally stable or unstable. By repeating this analysis for different mass flow rates and downstream volumes, the boundary between stable to unstable valve behavior is determined. This stability boundary is denoted in Fig. 11 by a black line, where the mass flow rate is given as it depends on the dimensional volume downstream of the valve V. The unstable region lies below this line. For the range of volumes considered, this stability boundary is approximately linear, with the threshold mass flow rate increasing with size of the downstream volume. Note that the influence of the downstream volume on the valve behavior is negligible when stable conditions are present.

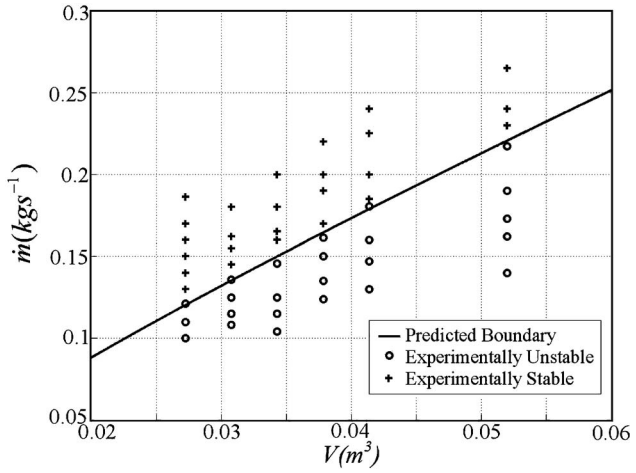

Fig. 11 Theoretically predicted transition from stable to unstable behavior (line) along with experimentally measured stable data points (o) and unstable data points (+)

Experimental data, obtained using the low-pressure test facility shown in Fig. 4, are used to validate this theoretical analysis. These data are first obtained for stable conditions using relatively high mass flow rates. For a given downstream volume, the mass flow rate is then reduced to sequentially lower values. This is done slowly to ensure that the stable valve behavior is maintained. For each mass flow rate, a disturbance is introduced by applying a restrictor plate of a fixed size to the inlet, which is then removed. This introduces a small step disturbance in the valve position. If the system is stable at this operating point, the valve flaps return to the initial position that existed prior to the perturbation. If the system is locally unstable, the flaps of the nonreturn valve rapidly and violently oscillate. This procedure is repeated at different mass flow rates to determine the experimental conditions that correspond to the change from locally stable to locally unstable behavior. The use of a fixed restrictor in generating the input disturbance ensures that the test is repeatable. The input flap angle step disturbance varies with the mass flow conditions and is approximately 2 deg for the lowest mass flow of 0.1 kg/s and approximately 3.5 deg for the highest mass flow of 0.27 kg/s. Such a step disturbance results in a local perturbation on the system, and as such, is suitable for validation of the locally linearized model. The size of the downstream volume is also varied by changing the duct length. The resulting measured points of stability and instability are shown in Fig. 11. Crosses indicate experimental conditions corresponding to stable valve behavior, while circles indicate experimental conditions corresponding to unstable behavior. It is clear from Fig. 11 that the experimental results and theoretical predictions are in excellent agreement.

The generally accepted solution to the problem of the nonreturn motion is to ensure that the valve is held fully open for all possible flow conditions [8]. This is achieved by placing a restriction on the minimum flow velocity in the system. Although this method is broadly successful, the condition that the valve is fully open is overly restrictive. The present stability map data are thus useful because they allow relaxation of this constraint on minimum flow velocity (for a particular downstream volume), which provides a definitive means to maintain the stable valve behavior when the valve is not fully open.

6 Summary and Conclusions

The performance of nonreturn valves in air systems is investigated and it is shown that, when the downstream ducting is confined by a restrictor, sprung nonreturn valves can exhibit unstable behavior. This behavior is a result of an interaction between the dynamics of the downstream volume and the dynamics of the nonreturn valve. In order to investigate this unstable interaction, a nonlinear state-space model of the nonreturn valve and air volume system is derived from first principles. Working with this model, it is shown that the local stability of the system is dependent on the volume of the downstream ducting and upon the mass flow rate through the system. By linearizing the state-space model and using control engineering techniques, the stability of the system is determined analytically, allowing a stability map to be produced.

Experiments on the valve are performed using a highly accurate valve flap position sensor in conjunction with a low-pressure flow facility to determine the flow performance characteristics of the valve. The variation of discharge coefficient and loading coefficient with valve flap angle is determined from the resulting experimental measurements. A novel frequency analysis method is also used to determine the damping coefficient of the valve from experimental data. A step disturbance in the valve position is in-

troduced to perturb the system behavior for a range of mass flow rates to determine the stable-to-unstable boundary for different downstream volumes. The resulting experimental stability boundary shows excellent agreement with the theoretical predictions, validating both the model and the stability criteria employed.

Nomenclature

A = valve area
c = damping coefficient
C_d = discharge coefficient for the gate valve
C_{dv} = discharge coefficient for the nonreturn valve
C_θ = loading coefficient
D = valve diameter
f_θ = valve pressure loading coefficient
h_v = inlet dynamic head
I = flap moment of inertia
K = spring angle
L = transducer pipe length
m = flap mass
$\dot{m}_{\text{in}}$ = mass flow into volume
$\dot{m}_{\text{out}}$ = mass flow out of volume
P_1 = nonreturn valve upstream pressure
P_2 = nonreturn valve downstream pressure
P_3 = orifice plate upstream pressure
P_4 = orifice plate downstream pressure
P' = pressure variation
r = flap radius
R = gas constant for air
R_r = center of pressure radius
t_L = time lag between pressure loading and nonreturn valve flap position
T = flow temperature
T_F = flap applied torque
T_{mg} = gravity induced torque
T_c = damping induced torque
T_P = pressure induced torque
u = flow velocity
U_∞ = spatially-averaged flow velocity
V = system volume

Greek Symbols

β = ratio of orifice to pipe diameter
γ = ratio of specific heats
θ = nonreturn valve flap angle
$\dot{\theta}$ = nonreturn valve flap angular velocity
$\ddot{\theta}$ = nonreturn valve flap angular acceleration
θ_0 = spring offset angle
θ' = theta variation
ρ = flow density
ρ_1 = flow density
ΔP = nonreturn valve pressure drop
$\Phi_{\theta\theta}$ = power spectrum density of nonreturn valve flap position
$\Phi_{F\theta}$ = power spectrum density of nonreturn valve flap pressure loading
ω = fundamental system frequency

Superscripts

$\dot{}$ = first time derivative
$\ddot{}$ = second time derivative

References

[1] Funk, J. E., 1964, "Poppet Valve Stability," ASME J. Basic Eng., **86**, pp. 207–212.
[2] Provoost, G. A., 1980, "The Dynamic Behaviour of Non-Return Valves," *Third International Conference on Pressure Surges*, BHRA, Canterbury, England, Paper No. J1, pp. 415–428.
[3] Provoost, G. A., 1983, "A Critical Analysis to Determine Dynamic Characteristic of Non-Return Valves," *Fourth International Conference on Pressure Surges*, Bath, England, pp. 275–286.
[4] Thorley, A. R. D., 1989, "Check Valve Behaviour Under Transient Flow Conditions: A State-of-the-Art Review," ASME J. Fluids Eng., **111**, pp. 178–183.
[5] Thorley, D., 1984, "Dynamic Response of Check Valves," Chem. Eng. (Rugby, U.K.), **402**, pp. 12–15.
[6] Valibouse, B. S., and Verry, H., 1983, "Modelling Check Valve Slamming," *Fourth International Conference on Pressure Surges*, Bath, England, pp. 263–273.
[7] Rahmeyer, W. J., 1983, "The effect of Upstream Piping on Swing Check Valves," J. Am. Water Works Assoc., pp. 553–555.
[8] Rahmeyer, W. J., 1993, "Sizing Swing Check Valves for Stability and Minimum Velocity Limits," ASME J. Pressure Vessel Technol., **115**(4), pp. 406–410.
[9] Botros, K. K., Jones, B. J., and Roorda, O., 1997, "Effects of Compressibility on Flow Characteristics and Dynamics of Swing Check Valves—Part 1," ASME J. Pressure Vessel Technol., **119**(2), pp. 192–198.
[10] Pandula, Z., and Halasz G., 2002, "Dynamic Model for Simulation of Check Valves in Pipe Systems," Period. Polytech., Mech. Eng.-Masinostr., **46**(2), pp. 91–100.
[11] Stone, J. A., 1960, "Discharge Coefficients and Steady State Flow Forces for Hydraulic Poppet Valves," ASME J. Basic Eng., **82**, pp. 144–154.
[12] Kasai, K., 1968, "On the Stability of a Poppet Valve With an Elastic Support, 1st Report, Considering the Effect of the Inlet Piping System," Japan Soc, Mech. Eng., **11–48**, pp. 1068–1083.
[13] Kasai, K., 1968, "On the Stability of a Poppet Valve With an Elastic Support, 2st Report, Considering the Effect of the Outlet Piping System," Japan Soc, Mech. Eng., **12–53**, pp. 1091–1098.
[14] Hayashi, S., and Ohi, K., 1993, "Global Stability of a Poppet Valve Circuit," J. Fluid Control, **21**, pp. 48–63.
[15] Hayashi, S., 1995, "Instability of Poppet Valve Circuit," JSME Int. J., Ser. C **38**, pp. 357–366.
[16] Hayashi, S., Hayase, T., and Kurahashi, T., 1997, "Chaos in a Hydraulic Control Valve," J. Fluids Struct. **11**, pp. 693–716.
[17] Tarnopolsky, A. Z., Lai, J. C. S., and Fletcher, N. H., 2002, "Aerodynamic Damping of Randomly Excited Plates in Stationary and Moving Air," J. Sound Vib., **253**(4), pp. 795–805.
[18] Lennart, L., 1999, *System Identification: Theory for the User*, 2nd ed., Prentice-Hall, New York.

Experimental Study on the Amplitude of a Free Surface Fluctuation

Ho-Yun Nam[1]
e-mail: hynam@kaeri.re.kr

Byoung-Hae Choi

Jong-Man Kim

Byung-Ho Kim

Fluid Engineering Division,
Korea Atomic Energy Research Institute,
150 Deokjin-dong, Yuseong-gu,
Daejeon, 305-353, Korea

An experimental study was performed to measure the fluctuation phenomena of a free surface in a vessel with or without an internal structure. A flow enters from the bottom and flows out of the side wall nozzles. Characteristics of the free surface fluctuation are investigated in terms of the geometry factors of the vessel and the flow rate. A modified Froude number is proposed to describe the amplitude of a free surface fluctuation. The fluctuation amplitude increases stably with an increase in the ratio of the vessel diameter to the water level in a vessel without an internal structure. When the ratio is greater than about 2, the fluctuation decreases suddenly with an increase in the ratio and it becomes unstable. The fluctuation amplitude is linearly proportional to the square of the Froude number. The amplitude of a free surface fluctuation increases with an increase in the height of an internal structure, but this increasing ratio is reduced when the height becomes higher. Two correlations were developed in terms of the Froude number and geometry factors to predict the amplitude of the free surface fluctuation in a vessel with or without an internal structure. [DOI: 10.1115/1.3001071]

1 Introduction

In a fast reactor using sodium as a coolant, there exists a free surface in the upper plenum of the reactor vessel where hot coolant contacts with a cold cover gas. A fluctuation of this free surface causes two important phenomena in the reactor; the induction of a thermal stress on the reactor vessel due to a free surface fluctuation of sodium and a cover gas entrainment at the free surface. If a significant amount of gas is entrained by the sodium fluctuation, the entrained gas causes a change in the reactivity and it also reduces the heat removal capability of the coolant in the core. Since the thermal stress on the wall and the breaking of a surface wave are strongly dependent on the amplitude and frequency of the free surface fluctuations, studies on the amplitudes and frequencies of these should receive more attention in the design of a fast reactor. In such a reactor, a flow enters from the reactor core and forms a free surface, and then it is discharged to the side wall nozzles. Some experimental studies on free surface fluctuations have been reported [1–7]. However, most of them have focused on the gas entrainment phenomena and only a few works were concerned with the basic characteristics of free surface fluctuations.

In this study, we performed experiments on free surface fluctuations in order to investigate the basic characteristics of these fluctuations. Since the hydraulic property of sodium is similar to that of water, water was used as a working fluid instead of sodium. Two kinds of experiments were carried out for two reasons in this work. One is to establish the effects of vessel size and nozzle size on the characteristic of a free surface fluctuation, and the other is to establish the effect of an internal structure installed in a vessel on a surface fluctuation, which simulates the upper internal structure (UIS) of a reactor.

Dimensionless numbers including the Froude number were studied to present the characteristics of a free surface fluctuation in a vessel by using experimental data, and to search for the effect of a vessel geometry on a free surface fluctuation. A correlation was developed by using a modified Froude number for the amplitude of a surface fluctuation. And then the effect of the geometry of an UIS was studied by using the experimental data obtained by varying the diameter and the height of the UIS. And also a correlation for the amplitude of a surface fluctuation in a vessel with an internal structure was developed by using the modified Froude number and the geometry factor.

2 Experiment

2.1 Experimental Apparatus. Since the fluctuation of a free surface is considerably affected by the flow conditions at the inlet and outlet nozzles of a test section, the experimental apparatus was made in such a way as to reduce fluctuation and rippling of the flow. The free surface fluctuation was measured by using water as a working fluid in the experimental apparatus shown in Fig. 1. The volume of the storage tank is about 4 m^3, and the temperature of the water in the storage tank was controlled automatically by a heater and a cooler of a refrigerator type to within $20 \pm 0.5\,^{\circ}C$. The water in the storage tank passes to the damper, filled with nitrogen as a cover gas, by a three stage centrifugal pump, where the pressure of the gas reduces a rippling of the flow. The flow rate was measured by three turbine flow meters (76.2 mm, 63.5 mm, and 25.4 mm in diameter) installed in parallel. The flow rate was controlled mainly by the inverter of the pump and partially by the valve at the bypass pipe. And the water was injected into the test section through a pipe 127 mm in diameter and 7 m in length. The water ejected from the test section passes the water level control valve and falls freely into the gas eliminator, which removes the air entrained in the flow, and returns it to the storage tank at a lower level than the free surface of the storage tank.

The experimental parameters and the dimensions are described in Table 1. Figure 2 shows the test section for the experiment. In the experiment without an UIS, the experimental parameters were the vessel diameter, the inlet nozzle diameter, the water level, and the flow rate. The water was injected at the bottom of the vessel and formed a free surface and then it flowed out at the side nozzles whose level was much lower than the level of the free surface. The test section was made of a transparent acryl for a visual observation of a free surface fluctuation. Five different in-

[1]Corresponding author. Present address: SFR Development Division, Korea Atomic Energy Research Institute, 150 Deokjin-dong, Yuseong-gu, Daejeon, 305-353, Korea.

Contributed by the Fluids Engineering Division of ASME for publication in the JOURNAL OF FLUIDS ENGINEERING. Manuscript received January 31, 2007; final manuscript received July 10, 2008; published online October 28, 2008. Assoc. Editor: Hamid Johari.

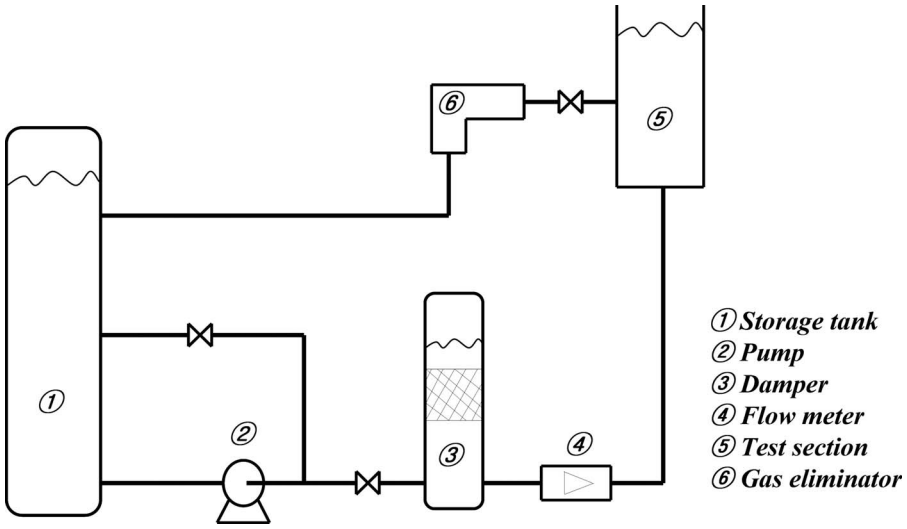

Fig. 1 Schematic of the experimental apparatus

ner diameters (d_V) of a vessel and five types of inlet nozzles (d_N) were used. The free surface level (H) from the inlet nozzle was varied for four cases to within ± 10 mm in a level set. The flow rate was controlled for 4–7 times in each experimental condition from a very low flow rate to a flow state where one or two air bubbles are entrained into the water from the free surface. The overall range of the flow rate was 1×10^{-3}–16×10^{-3} m^3/s in the experiment without an UIS. Four outlet nozzles were located at a 0.74 m elevation (H_o) from the bottom with a 90 deg interval, whose diameter was 0.046 m.

In order to study the effect of an UIS, two types of tests were carried out in the experiment. One (Test-1) is to measure the free surface fluctuation in terms of the diameter of an UIS and the height of an UIS from the inlet nozzle with a fixed diameter of 0.1 m. The other (Test-2) is only to measure the coupled effect of a nozzle diameter and that of an UIS on a surface fluctuation. The inner diameter of the vessel was fixed at 0.78 m and four outlet nozzles were located at a 0.46 m elevation in the experiment with an UIS. Four types of an UIS with different diameters (d_U), 0.1 m, 0.2 m, 0.35 m, and 0.6 m, were prepared. The height (S) of an UIS was varied at five locations, and the mean water level was varied four times. The flow rate was controlled five times in each experiment with a fixed geometrical condition, and the overall range of the flow rate was 5×10^{-3}–37×10^{-3} m^3/s. In Test-2, five types of inlet nozzles with different diameters and two types of an UIS with different diameters were used.

2.2 Measurement of a Free Surface Fluctuation. Since the range of the estimated maximum frequency is about 5 Hz in this experiment, an impedance type wire sensor supplied with ac power with a 1 kHz frequency was used as a level sensor in order to obtain an accurate enough response. When two electrodes are immersed in the water, the impedance is composed of the resistance of the water, which is the capacitance caused by a polarization of the water and the capacitance caused by a dielectric property of the water [8]. But the characteristics of this type of level sensor have not been reported in the literature so far. Owing to this reason, an experiment was carried out to establish the characteristics of the level sensor before the experiment for the free surface fluctuation measurement [9]. In this study, the ratio of a real amplitude to an experimental amplitude decreases exponentially with an increase in the oscillating frequency. But it is not

Table 1 Experimental parameters and dimensions for the experiment

Experiment	Vessel diameter (m)	Inlet nozzle diameter (m)	UIS diameter (m)	Height of UIS (m)	Mean water level (m)	Range of flow rate (m^3/s)	Step of flow rate change
Experiment without UIS	0.38 0.48 0.68 0.78 1.00	0.038 0.048 0.058 0.078 0.10	-	-	0.87 1.07 1.27 1.47	0.001–0.016	4–7
Experiment with UIS: Test-1	0.78	0.10	0.10 0.20 0.35 0.60	0.10 0.17 0.25 0.33 0.40	0.70 0.85 1.00 1.20	0.005–0.037	5
Experiment with UIS: Test-2	0.78	0.038 0.048 0.058 0.078 0.100	0.20 0.35	0.33 0.40	1.00	0.005–0.027	5

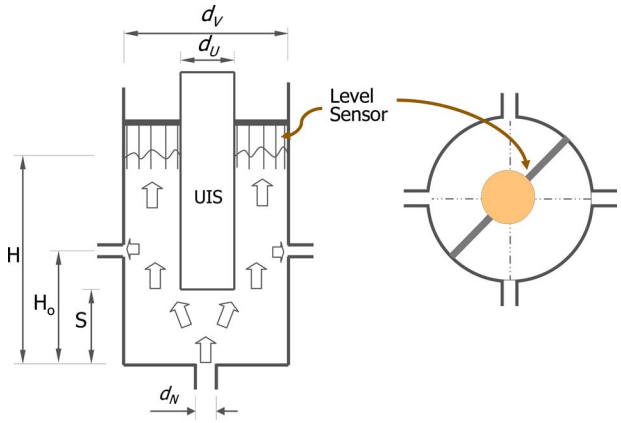

Fig. 2 Test section for the experiment with an internal structure

affected by the diameter of a wire sensor and the sensor type in the experimental range of this study. Also an experimental correlation for the ratio of a real amplitude to an experimental amplitude was developed in this study. The response of a wire sensor can be calibrated by a correlation.

The free surface fluctuation was measured by a wire level sensor at ten different locations in the radial direction. The calibrations of that were performed before and after an experiment in a practical condition. A wire level sensor was made by a nickel wire with 0.025 mm in diameter for an anode, and by a stainless steel rod 2 mm in diameter for the cathode. The results of the calibrations performed before and after an experiment were sometimes different owing to an elongation of the wire during the experiment. The data are eliminated from the analysis results in the case when the difference is greater than 3%. By this reason a wire level sensor made with a stainless steel wire with a 1 mm diameter and a 3 mm central distance in parallel was used in the experiment with an UIS.

The experimental data were collected by using the HP1413C data acquisition system. In the preoperation test, the data were collected with a 200 Hz sampling rate, but there was no significant signal greater than 5 Hz during a fluctuation beside a very low level signal due to surface tension. For this reason, the data were collected with a 25–33 Hz sampling rate during about 180 s.

2.3 Experimental Error. Most of the errors for the measurement of a free surface fluctuation originated from the measurements of the flow rate and the water level. There were three kinds of error for the measurement of the flow rate. One is an accuracy of 0.5% of a reading in the turbine flow meter itself. The second error coming from the calibration of the flow meter, and the noise of the acquisition system is less than 2% for a lower flow rate and less than 1% for a higher flow rate. The third error originated from the phenomenon that a flow rate was linked with a surface fluctuation at the test section. And it is about 1.5% at a minimum flow rate and about 0.5% at a maximum flow rate. Therefore, the total error for measuring the flow rate is less than 2.5% at a minimum flow rate and less than 1.2% at a maximum flow rate in order to obtain a 95% confidence level.

The errors in measuring the water level are composed of an electrical noise, a calibration error, and an error from the correlation of the amplitude according to the fluctuating frequency. The electrical noise is reduced to below ± 0.2 mm by an isolated high quality electrical earth system, but this error is dominant at a low fluctuation region. The error coming from the calibration of a wire level sensor is less than 4% although there is a deformation of a wire. The error coming from the correction of the amplitude is less than 4%. Therefore, the error for measuring the free surface level is 0.2 mm for a base error and less than 6% for a reading. In addition to these, the total amount of the other errors from measuring the dimensions of the devices is less than 1%. Therefore, the total measuring error of the data used in the development of a correlation is less than 22% at a minimum fluctuation region, and the error is less than 6.5% at a maximum fluctuation region.

3 Results and Discussions

3.1 Experimental Results Without an Internal Structure. Figure 3 shows a typical signal of a free surface fluctuation at the center location in the experiment. Figure 4 shows the frequency spectrum of the level signal. The frequencies of the experimental

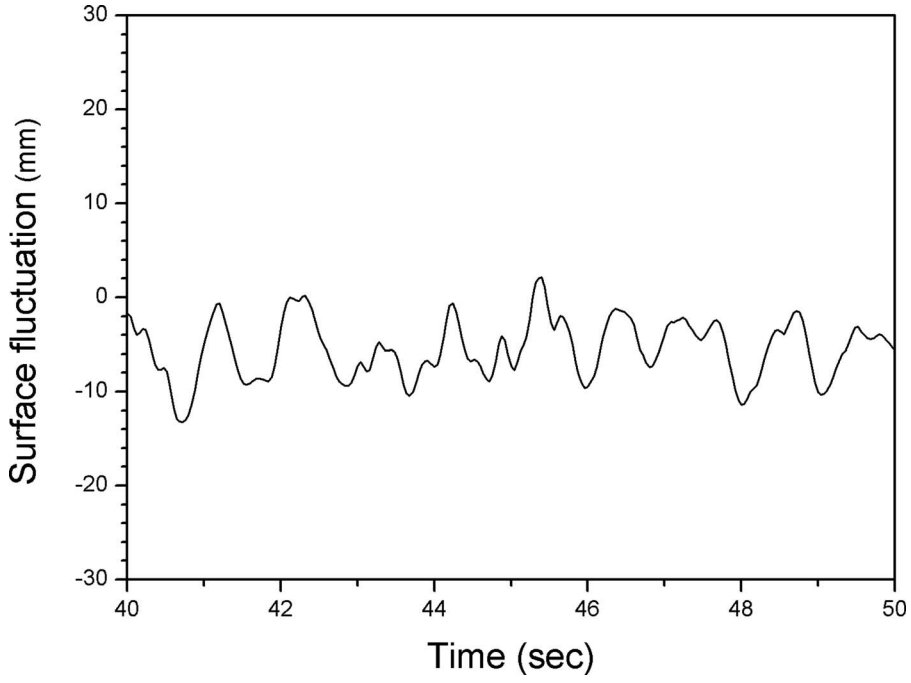

Fig. 3 Typical signal of a free surface fluctuation in the experiment

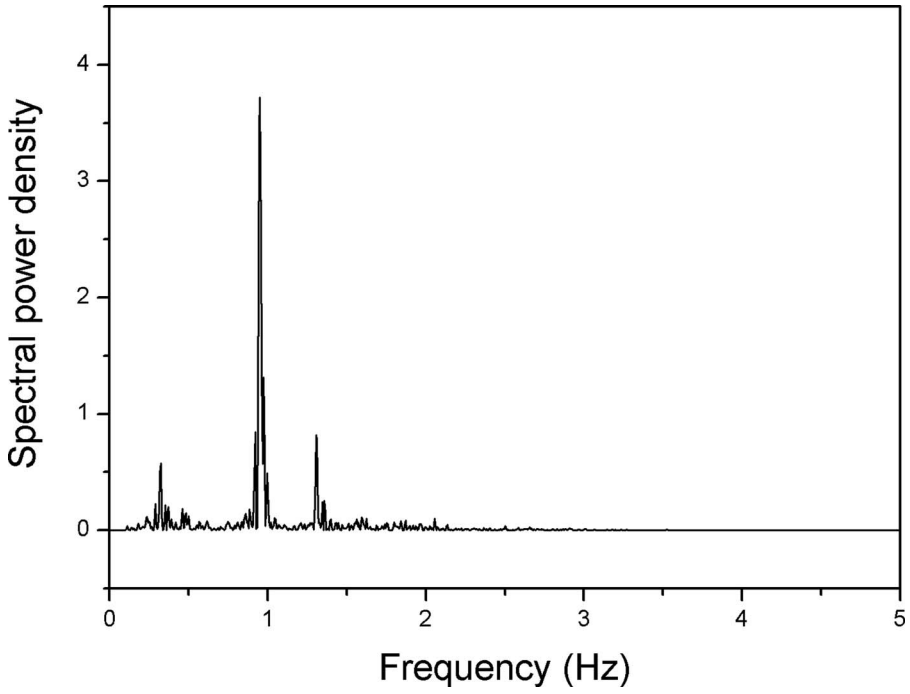

Fig. 4 Spectral power density of typical level fluctuation in the experiment

data are analyzed by using the fast Fourier transform (FFT) method. There are two dominant frequency regions. One is a standing wave related to the vessel diameter, and the other is generated by a jet related to the flow and geometry conditions. A dominant frequency in the range of 0.2–1.5 Hz appears regularly, and it appears irregularly at a very low frequency. Since a fluctuation with a low frequency is not a proper fluctuation caused by a system oscillation, a 0.05 Hz high pass filter is applied to cut off the dc bias and system frequency noise.

The standard deviation (σ) of a surface fluctuation was defined as follows:

$$\sigma = \sqrt{\sum_{i=1}^{N} (H_i - H)^2/(N-1)} \tag{1}$$

where H_i is the water level of the i step of a measurement, H is a mean free surface level, and N is the number of data. In the statistical analysis of this study, the maximum and minimum values were excluded from among the ten data sets obtained at ten positions. Then σ_{avg} was obtained by an averaging of the other eight data, and $\sigma_{\max}$ and $\sigma_{\min}$ are their maximum and minimum values, respectively.

In the case of analyzing a free surface fluctuation, the Froude number (Fr_o) is the most adequate dimensionless number, which is generally formulated by a velocity scale and a length scale as follows:

$$\text{Fr}_o = \frac{V}{\sqrt{g\lambda}} \tag{2}$$

where g is the gravitational acceleration, V is the velocity scale, and λ is the length scale described by a mean level or a vessel diameter in the analysis of a free surface. Figure 5 shows the $\sigma_{\max}$ versus the Froude number based on the water level and the velocity (V_N) at the nozzle. Also the degrees of a dispersion of $\sigma_{\max}$ are examined by the Froude numbers based on a vessel diameter and an inlet nozzle diameter instead of a water level. In the three cases, the degree of a dispersion of the data is similar, but that of the Froude number based on the water level is slightly more homogeneous than that of the other. From the figure, the Froude number defined by Eq. (2) is not proper to describe a surface fluctuation because of the wide dispersion of the experimental data.

In order to overcome this problem, we assumed that a surface fluctuation is proportional to the central velocity (V_S) of a circular jet instead of the velocity at a nozzle. Then the relation is defined as follows:

$$\sigma \sim V_S \tag{3}$$

The central velocity of a circular jet at distance H from an inlet nozzle is described by an analytical study [10] as follows:

$$V_S \sim \frac{1}{H}\sqrt{\frac{J}{\rho}} \tag{4}$$

where J is the momentum of a circular jet and it is simply defined by $J = \pi\rho d_N^2 V_N^2/4$, and d_N is an inlet nozzle diameter. From Eqs. (3) and (4), the following relation can be constructed as a dimensionless form with length scales λ_1 and λ_2:

$$\frac{\sigma}{\lambda_1} \sim \sqrt{\frac{d_N}{H}}\sqrt{\frac{d_N}{\lambda_2}}\frac{V_N}{\sqrt{gH}} \tag{5}$$

In order to study the effect of an inlet nozzle, the relation between σ/H and $d_N V_N$ is examined by the experimental data at a fixed larger vessel diameter and a lower water level. The result shows that σ is related to $d_N V_N$ for a fixed vessel and the σ/H is approximately proportional to $1/H^{3/2}$. Although $d_N V_N/H^{3/2}$ increases slightly with a decrease in the water level in order for an equal amplitude of a fluctuation to take place, the following relation can be described from Eq. (5):

$$\frac{\sigma}{H} \sim \sqrt{\frac{d_N}{H}}\sqrt{\frac{d_N}{H}}\frac{V_N}{\sqrt{gH}} \tag{6}$$

One can see that $\lambda_1 = \lambda_2 = H$ from a comparison between Eqs. (5) and (6). In the same manner, the dimensionless standard deviation (σ/d_V) based on a vessel diameter is examined by using data at a fixed water level, and the result shows that it is proportional to $1/d_V^{1/2}$. Also the dimensionless standard deviation (σ/d_N)

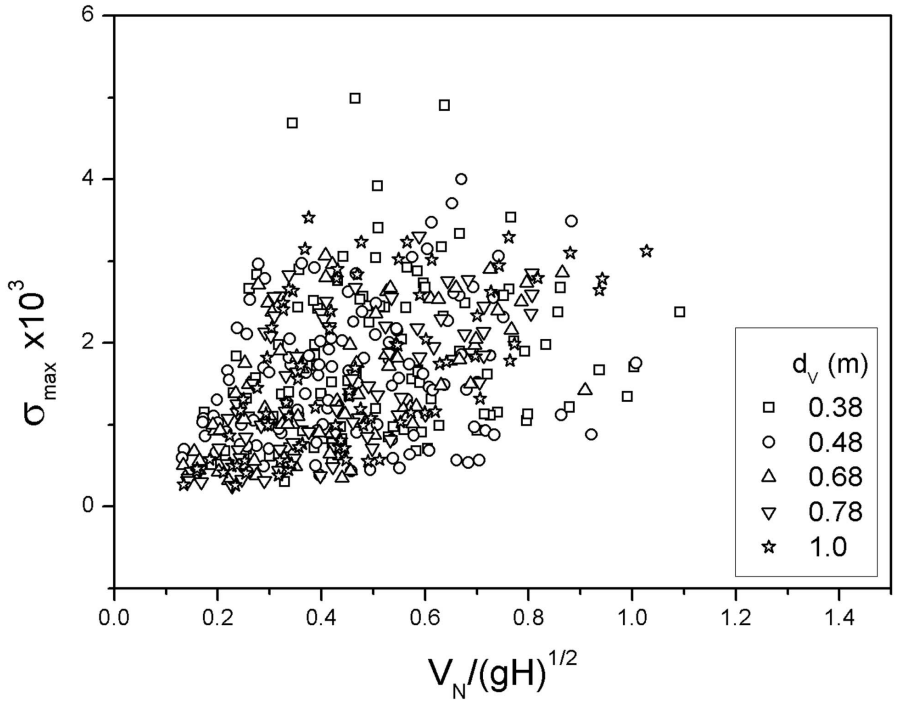

Fig. 5 Standard deviation of the free surface fluctuation versus the Froude number based on a water level and a velocity at an inlet nozzle

based on an inlet nozzle is examined in order to establish the effect of an inlet nozzle diameter. It is proportional to the right side of Eq. (5) when λ_2 is equal to d_N at a fixed water level.

Comparing Eq. (5) with Eq. (6) and the above analogies, λ_1 is equal to λ_2, and can be given a length scale λ. One can define a new modified Froude number related to the central velocity of a circular jet as follows:

$$\mathrm{Fr}_\lambda \equiv \sqrt{\frac{d_N}{H}}\sqrt{\frac{d_N}{\lambda}}\frac{V_N}{\sqrt{gH}} \tag{7}$$

Since the length scale in the left side of Eq. (5) appears in the form of a root square in the right side of the equation, a dimensionless standard deviation of a surface fluctuation is linearly pro-

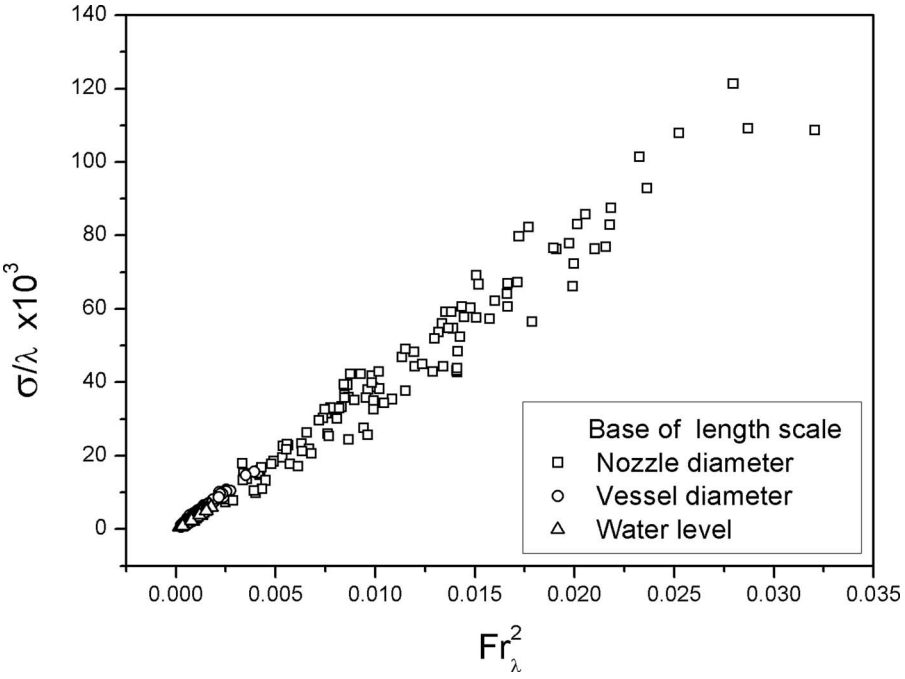

Fig. 6 Standard deviation with a different length scales versus the square of a Froude number at a fixed water level of 0.87 m

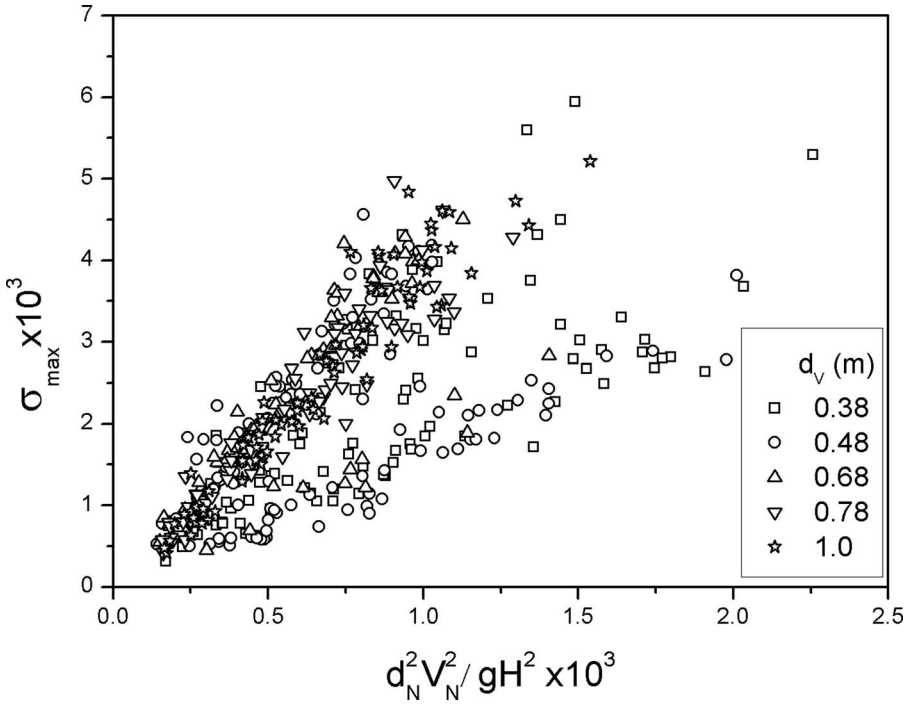

Fig. 7 Standard deviation of a free surface fluctuation versus $d_V^2 V_N^2 / gH^2$

portional to the square of the right side of the equation. Figure 6 shows the standard deviation at a fixed lower water level according to three length scales, namely, based on the nozzle diameter, the vessel diameter, and the water level. There is a linearity of the standard deviation of a free surface fluctuation versus the square of the Froude number, and three values with a different length scale are on the same line. It also can be described as follows using a new dimensionless number:

$$\frac{g\sigma H^2}{d_N^2 V_N^2} = \mathrm{Sn} \tag{8}$$

where Sn is a proportional constant dependent on a geometrical condition. Since the denominator in the left side of Eq. (8) is the momentum of an initial jet entering a tank, the numerator in the left side of Eq. (8) is considered as the momentum of a surface fluctuation at height H.

Figure 7 shows that the standard deviation of the surface fluctuation for all of the data by using $d_N^2 V_N^2 / gH^2$ appeared in the right side of Eq. (8). Data in the right lower part of this figure, which belong to the case of a high water level at a small vessel diameter, are scattered. However, data in the left upper part, which was measured at a low water level and at a large vessel diameter, are described well by the value. However, looking into this part in more detail, the inclinations are a significant difference according to the vessel diameter and the water level. In order to obtain the geometrical effect in more detail on the inclination, the tendency of the geometrical factor f_g for each condition is examined, where $f_g \equiv c/\mathrm{Sn}$ and c are constant.

Figure 8 shows the distribution of f_g obtained from the average standard deviations in all the conditions of the vessel diameter and the water level, where f_g is scaled to meet $f_g = 1$ at P_4 in Fig. 9, and an error band is the difference between the maximum and minimum of a f_g according to the flow rate at a geometry condition. In Fig. 8, when H/d_V is smaller than 2, f_g decreases with an increase in the value. This means that a surface fluctuation increases with an increase in H/d_V by the effect of a vessel wall. When H/d_V is greater than 2, f_g suddenly increases with an increase in the value, and the degree of a dispersion of the data also increases. After the transient region, the increment of f_g reduces when H/d_V is greater than about 2.6. It is suggested that the characteristics of a flow are changed from a jet flow to a pipe flow. Since stable data at P_1, which is the case of 0.38 m in vessel diameter and 0.87 m in water level, appears after the unstable data at $P_2(H=1.07\ \mathrm{m})$ and $P_3(H=1.47\ \mathrm{m})$, the value of H/d_V is not enough to properly separate the regions.

It is difficult to describe the effect of the elevation (H_o) of an outlet nozzle due to the lack of experimental data. When the other conditions are fixed in the experiment, the data are measured in a more convergent manner with shorter distance from the outlet nozzle to water surface. A compound variable is proper to separate the regions instead of H/d_V for the analysis of the present data. The dimensionless variable (H^*) is defined as follows:

$$H^* = \sqrt{\frac{1}{4}\frac{H}{d_V} + \frac{3}{4}\frac{H - H_o}{d_V}} \tag{9}$$

Figure 9 shows the geometry factor for all of the present data, where f_P is a factor, which means the effect of the radial distance on a fluctuation. Transient region is defined well with H^* in the range of $1.1 \le H^* \le 1.2$. In the steady state region ($H^* \le 1.1$) the lines of the three inclinations of f_g come together at one point (at P_4), which is considered as an ideal critical value. In other words, f_g becomes 1 at the center of jet when the boundary of vessel is very large. A geometry factor increases suddenly with an increase in H^* in the transient region, but it increases slowly with an increase in this at $H^* > 1.2$. When the position factors are considered, three lines match at one line in the each region, and the position factor of the maximum fluctuation is equal to 1. Therefore, the geometry factors of a vessel without an UIS are described as follows:

$$f_g = \frac{(2.57 - 0.95H^*)^2}{0.95 f_p (1.65 - H^*) + 1} \quad \text{at } H^* < 1.1 \tag{10}$$

$$f_g = 46.5\sqrt{d_V/H}[(H^* - 1.1) + 1.55]/f_p \quad \text{at } 1.1 \le H^* \le 1.2 \tag{11}$$

$$f_g = 3.75\sqrt{d_V/H}[(H^* - 1.2) + 6.2]/f_p \quad \text{at } H^* > 1.2 \tag{12}$$

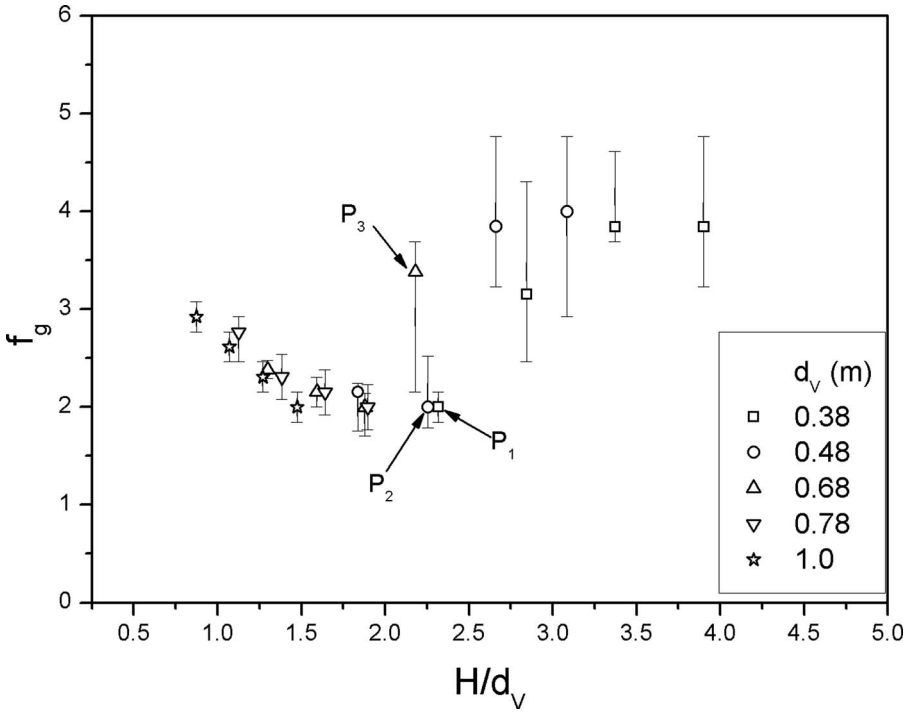

Fig. 8 Geometry factor versus H/d_V in σ_{avg}

It is very difficult to present the distribution of a standard deviation according to the radial distance because of its conditional complexity. When $H^* < 1.1$, the standard deviation decreases exponentially with an increase in the radial distance. Also the standard deviation of the vessel with a small diameter is flattened more than that of the vessel with a large diameter. A position factor f_P in the stable region is proposed for Eq. (10) by taking into account the experimental data, and it can be described as follows:

$$f_P = (1 + 82R^{*2})^{1/4} \tag{13}$$

where R^* is the ratio of the radius of a vessel to the distance from the center of a vessel.

The distribution of the standard deviation of a surface fluctuation in an unstable region is very different when compared with a stable region. A fluctuation at the position of $R^*=0.5$ is a little higher than that of a center position, and the fluctuation is flattened more than that of the stable region. It is suggested that this

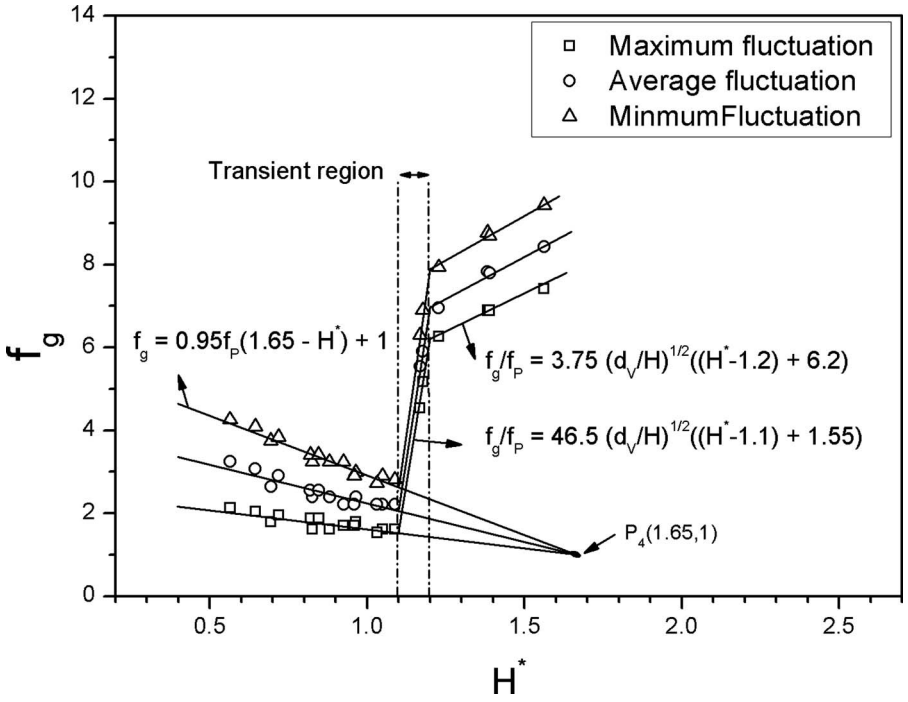

Fig. 9 Geometry factor f_g versus H^* in the experiment

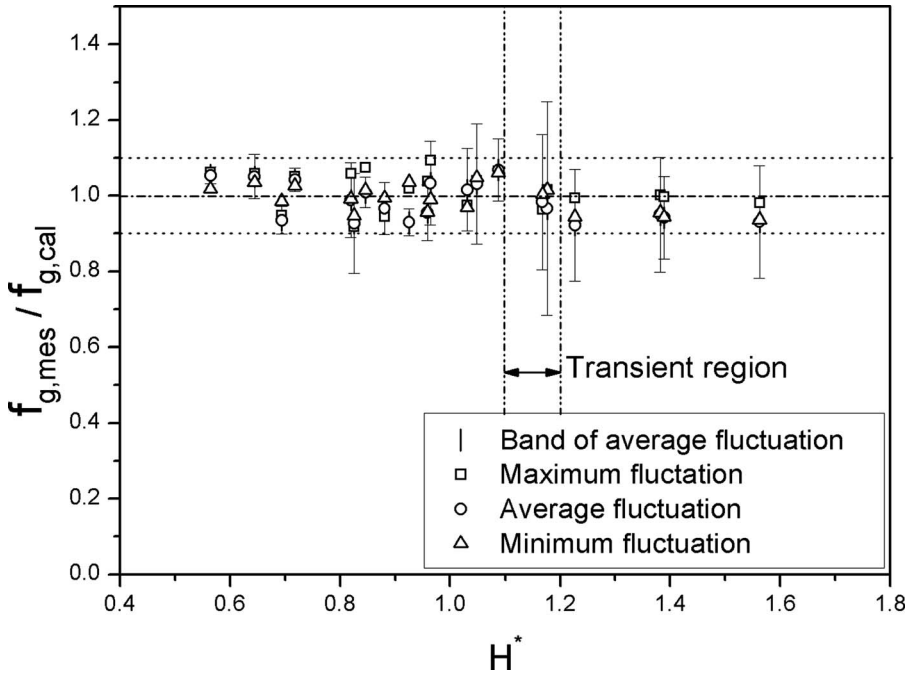

Fig. 10 Comparison of the calculated geometry factor with measured geometry factor

phenomenon is due to a mixture of the flows between a central jet flow and a vicinal jet flow accelerated by a wall according to a limited growth of a jet's width. Based on the experimental data, a position factor for Eqs. (11) and (12) in an unstable region is proposed as follows:

$$f_P = \frac{1}{1 - 0.45|R^* - 0.5|} \tag{14}$$

Using Eqs. (10)–(12), the proposed geometry factor is compared with the experimental geometry factor, as shown in Fig. 10. The averaged data are fitted well by the calculated geometry factor to within $\pm 10\%$, but the scattered data in the unstable region exceed the error range, where the error bands come from the maximum scattering of f_g for each experimental condition.

A correlation for a free surface fluctuation in a vessel is developed with the Froude number and the geometry factor, as shown in Fig. 11. The λ is an arbitrary length scale, which can be replaced by either a water level, vessel diameter, or nozzle diameter. The scattered data come from the unstable region, namely, $H^* > 1.1$ in this figure. And the correlation can be described by

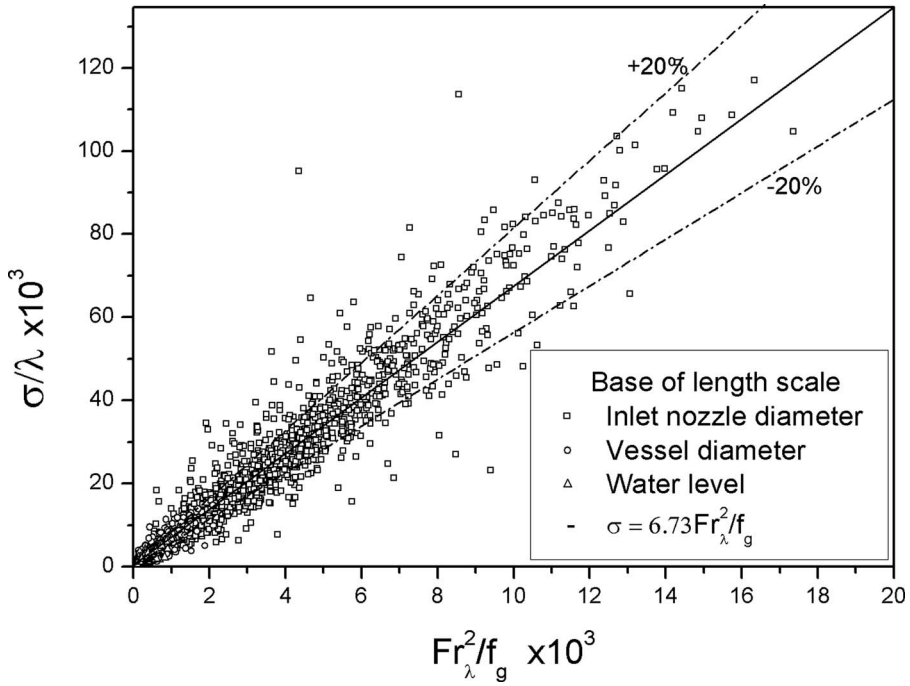

Fig. 11 Comparison of the three correlations with a different length scale for λ in the experiment without an UIS

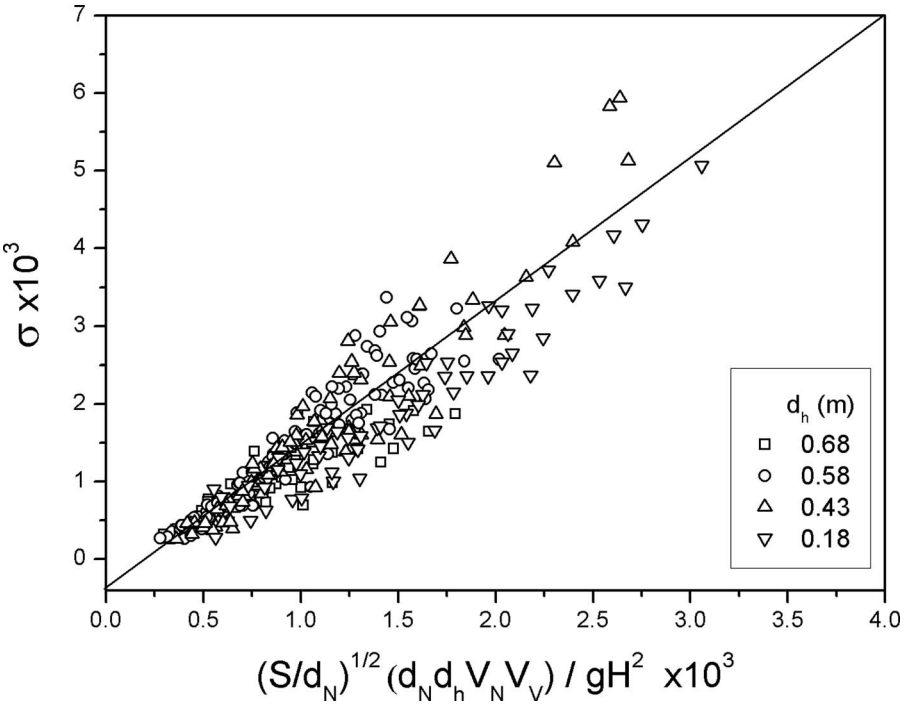

Fig. 12 Standard deviation of the surface defined in Eq. (17)

$$\frac{\sigma}{\lambda} = \frac{6.73}{f_g}\mathrm{Fr}_\lambda^2 \tag{15}$$

The estimated standard deviation error is ±1.6% to obtain a 95% reliability according to the ASME error analysis, and the error of the data used in developing the correlation is 6.5% at the maximum fluctuation region and 22% at the minimum fluctuation region.

3.2 Experimental Results With an Internal Structure. The free surface fluctuation in a vessel with an UIS is more complicated than that without an UIS due to the geometry effects of an UIS. According to the analysis of the experimental data, the standard deviation of a surface fluctuation is nearly uniformly distributed, but there is a maximum at $R/d_h=0.75$ for some degrees except for the case of a small hydraulic diameter (d_h), where R is the distance measured from the wall of an UIS to the wall of the vessel. By this reason, one should use an averaged standard deviation obtained by an averaging of the other eight data by excluding the maximum and minimum statistical values from among the ten data sets in the analysis.

There are many length scales and velocity scales applied to Eq. (2) in a vessel with an UIS. Several combined scales are applied to Eq. (2) to compare the tendencies of a surface fluctuation. According to the analysis of the data, the Froude numbers defined in Eq. (2) are not proper to describe a free surface fluctuation in a vessel with UIS such as the case without an UIS. When one uses the modified Froude number based on the central velocity of a free jet, the data correlate better with the Froude number than with that defined in Eq. (2), however, it is slightly scattered at a high Froude number region due to the effect of an UIS.

Since the shape of the test section is annular, the hydraulic diameter and the velocity for an annular space are considered as the important parameters. When the tendency of a fluctuation is examined by replacing $d_N V_N$ with $d_h V_V$ in Eq. (8), the data are scattered due to the effects of an inlet nozzle at a low value region, and it is also scattered due to the effect of an UIS at a high value region. When $d_N^2 V_N^2$ is replaced with $d_N V_N d_h V_V$, which is a mixed geometrical condition, the degree of dispersion of the data is similar to the two cases above, but the tendency is more homogeneous than those of the others. Since the three Froude numbers based on a different geometrical condition can be altered by the mass conservation relation, it is possible to use any relation from among the three relations. But one should use a Froude number based on a mixed geometrical condition to avoid a complexity in developing a geometry factor due to the fact that it contains both the nozzle effect and the vessel effect for the analysis, and it can be described as follows:

$$\mathrm{Fr}_\lambda \equiv \sqrt{\frac{d_N}{H}}\sqrt{\frac{d_h}{\lambda}}\sqrt{\frac{V_N V_V}{gH}} \tag{16}$$

The data are scattered according to the geometries of an UIS when the above equation is used. The amplitude of a free surface fluctuation increases with an increase in the height of an internal structure for the analysis of the experimental data, but this increasing ratio is reduced when the height becomes higher. And the standard deviation of a surface fluctuation is roughly proportional to $\sqrt{S/d_h}$, as shown in Fig. 12 in the experimental condition, and f_g is $\sqrt{d_N/S}$. The standard deviation of a surface fluctuation can be described simply by the following relation, and the estimated standard deviation error of the relation is less than 4% in order to obtain a 95% confidence level

$$\frac{g\sigma H^2}{d_N d_h V_N V_V} = 1.85\sqrt{\frac{S}{d_N}} \tag{17}$$

In order to investigate the effect of the geometries of a vessel and an UIS in detail, one should examine the inclination (c/f_g) of the data for all of the geometric conditions, as shown in Fig. 13, where f_g is not scaled. In the figure, the fluctuation amplitude increases with an increase in the height of an UIS, and it increases with a decrease of the water level except for the case of $S=0.1$ m at $d_U=0.6$ m. When the height of an UIS is higher than 0.25 m, f_g is nearly the same. But when the height is small, f_g increases with an increase in the diameter of an UIS.

Geometry factor f_g in a vessel with an internal structure is developed using Fig. 13 to best fit the experimental data, and it is expressed as follows:

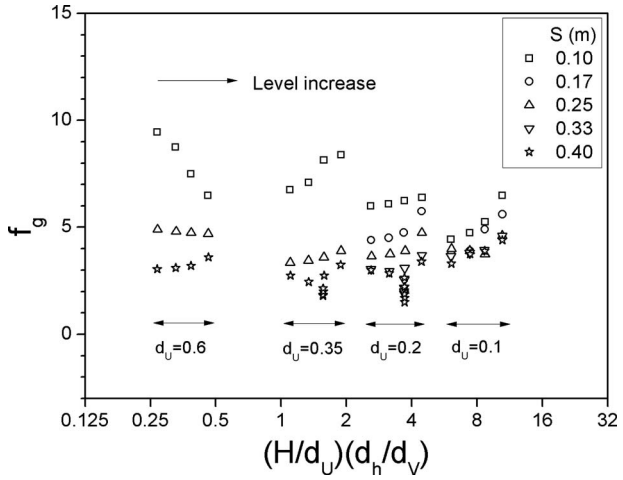

Fig. 13 Distribution of a fixed Froude number versus $(H/d_U) \times (d_h/d_V)$

$$f_g = \left(\frac{H}{d_V}\right)^{1/2}\left(\frac{d_N}{d_U}\right)^{1/2}\left(\frac{H}{S}\right)^{1/5} G^* \tag{18}$$

where

$$G^* = \mathrm{Exp}\left(\frac{1.6}{(S/d_U)^{1/3}(H/d_V)^{1/2}+0.1} - 1.3\right) \tag{19}$$

When the height of an UIS was small and the diameter of an UIS was large, the geometry factor was reduced rapidly, but it was reduced slowly for the other cases. G^* becomes 1 when the boundary of vessel becomes large. A correlation for the amplitude of a free surface fluctuation with an internal structure is developed by Eqs. (16) and (18), as shown in Fig. 14. The correlation line is not fitted at the zero point in the figure. Since the friction factor for a momentum loss is inversely proportional to a velocity at a laminar flow region, the momentum loss by an UIS at a low velocity is not proportional to $V_N V_V$. Therefore, it is considered that the surface fluctuation is not proportional to the square of a Froude number at a low velocity region. However, the fluctuation increases smoothly from zero to a low level of the present data measured at a low velocity, which is excluded from the analysis owing to a high error level. This relation can be described as follows:

$$\frac{\sigma + c}{\lambda} = \frac{2.3}{f_g}\mathrm{Fr}_\lambda^2 \tag{20}$$

where λ is an arbitrary length scale, and c is obtained as 4×10^{-4} m from the figure. The estimated standard deviation error of the relation is 2.4% by the scattering of the data in order to obtain a 95% confidence level and 349 data points were used to develop the correlation. The error originates from the data with a large diameter and small height of an UIS for the calculation of the geometry factor.

4 Conclusions

An experimental study was performed to measure the amplitude of a free surface fluctuation. It is difficult to explain the data by a general Froude number defined by Eq. (2). A new Froude number was proposed based on an arbitrary length scale and the central velocity of a jet. The standard deviation of a free surface fluctuation is linearly proportional to the square of a new Froude number.

The fluctuation of a free surface increases with an increase in the vessel diameter to the water level ratio, and the ratio exceeds 2, strictly speaking, when H^* is greater than 1.1, the fluctuation becomes scattered and suddenly falls into the transient region. The amplitude of a free surface fluctuation increases with an increase in the height of an internal structure, but this increasing ratio is reduced when the height becomes higher. When the height of an UIS is small and the diameter of an UIS is large, the geometry factor reduces rapidly, but it reduces slowly in the other cases.

Two correlations for the amplitude of a free surface fluctuation in a vessel with or without an internal structure were developed. The estimated standard deviation error of the correlation for the

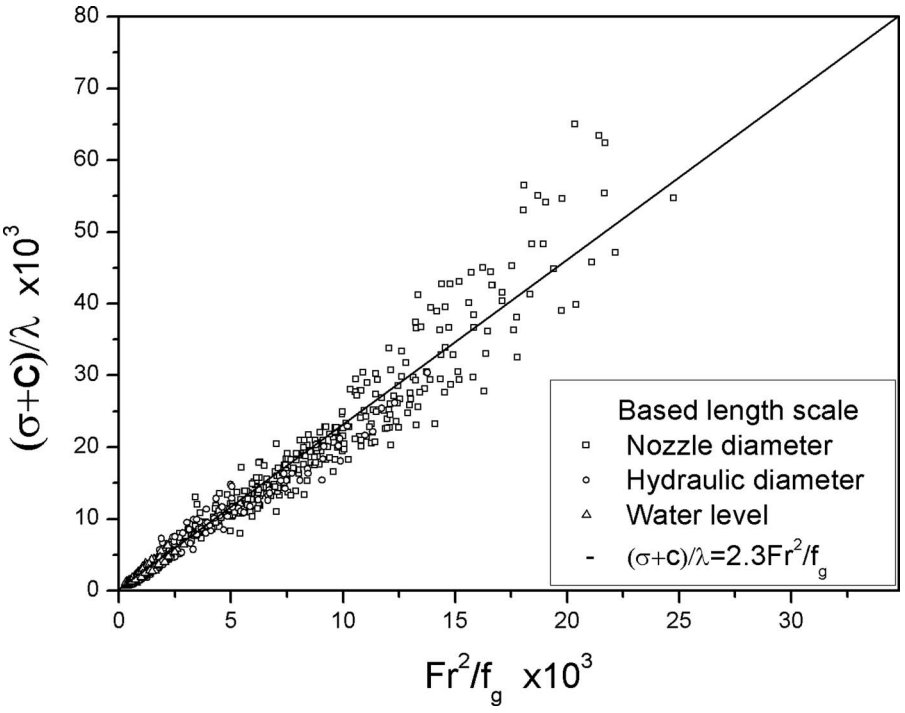

Fig. 14 Comparison of the three correlations with a different length scale in the experiment with an UIS

surface fluctuation in a vessel without an UIS was $\pm 1.6\%$ and that for the vessel with an UIS was $\pm 2.4\%$, in order to obtain a 95% confidence level. The error of the data used in developing the correlation was less than 6.5% at the maximum fluctuation region, and it was less than 22% at the minimum fluctuation region.

Acknowledgment

This study was carried out under the Nuclear Research and Development Program by the Ministry of Science and Technology of Korea.

Nomenclature

c = experimental constant
d_h = hydraulic diameter ($\equiv 4$ flow area/perimeter $= d_V - d_U$) (m)
d_N = diameter of the inlet nozzle (m)
d_U = diameter of the UIS (m)
d_V = diameter of the vessel (m)
Fr = Froude number
Fr_λ = Froude number based on λ
Fr_o = original Froude number
f_g = geometry factor
f_P = position factor
g = gravitational constant ($\mathrm{m/s^2}$)
H = height of the water free surface (m)
H_o = height of the outlet nozzle (m)
H^* = dimensionless value defined by Eq. (9)
J = momentum of the jet flow ($\mathrm{kg\ m/s^2}$)
N = number of data
R = radial distance from the center or wall of UIS (m)
R_o = radius of the vessel (m)
R^* = dimensionless radius (R/R_o)
S = height of UIS (m)
V_N = flow velocity at the inlet nozzle (m/s)
V_S = jet velocity at the free surface (m/s)
V_V = flow velocity at the vessel (m/s)

Greek

λ = length scale (m)
ρ = density ($\mathrm{kg/m^3}$)
σ = standard deviation of a surface fluctuation (m)

Subscript

Avg = average value
cal = calculated value
fix = fixed value
max = maximum value
mes = measured value
min = minimum value

References

[1] Baum, M. R., and Cook, M. E., 1975, "Gas Entrainment at the Free Surface of a Liquid: Entrainment Inception at a Vortex With an Unstable Gas Core," Nucl. Eng. Des., **32**, pp. 239–245.
[2] Takahashi, M., Inoue, A., Aritomi, M., Takennaka, Y., and Suzuki, K., 1988, "Gas Entrainment at Free Surface of Liquid," J. Nucl. Sci. Technol., **25**, pp. 131–142.
[3] Madarame, H., and Chiba, T., 1990, "Gas Entrainment Inception at the Border of a Flow-Swollen Liquid Surface," Nucl. Eng. Des., **120**, pp. 193–201.
[4] Kimura, N., Ezure, T., Tobita, A., and Kamide, H., 2006, "Empirical Study on Gas Entrainment at Free Surface in Reactor Vessel for a Compact Sodium Cooled Fast Reactor," NTHAS5 Symposium, Jeju, Korea, pp. 391–397.
[5] Nam, H. Y., Kim, M.-J., Kim, J. M., Choi, S. K., and Park, J. H., 2001, "Experimental Study on Amplitude and Frequency of Free Surface," *Proceedings of the ASME PVP Meeting*, Atlanta, GA, Vol. 421, pp. 223–230.
[6] Eguchi, Y., Yamamoto, K., Funada, T., Tanaka, N., Moriya, S., Tanimoto, K., Ogura, K., Suziki, T., and Maekawa, I., 1994, "Gas Entrainment in the IHX Vessel of Top-Entry Loop-Type LMFBR," Nucl. Eng. Des., **146**, pp. 373–381.
[7] Govindaraj, G., Raju, C., Kale, R. D., and Vaidyanathan, G., 1993, "Gas Entrainment in Surge Tank of a Liquid Metal Fast Reactors," J. Nucl. Sci. Technol., **30**(7), pp. 712–716.
[8] Jeong, M. K., Song, C. H., Won, S. Y., and Kim, B. D., 1994, "Development of the Impedance Void Meter," Report No. KAERI/TR-446/94.
[9] Nam, H. Y., Choi, B. H., Kim, J. M., and Kim, B. H., 2006, "Effect of the Type and Wire Diameter of a Wire Level Sensor in the Measurement of a Free Surface Fluctuation," *Proceedings of the KNS Spring Meeting*, Chuncheon, Korea.
[10] Schlichting, H., 1979, *Boundary Layer Theory*, 7th ed., McGraw-Hill, New York, pp. 733–749.

Computational Dynamics of a Thermally Decomposable Viscoelastic Lubricant Under Shear

T. Chinyoka[1]
Center for Advanced Studies in Mathematics,
Lahore University of Management Sciences,
54792 Lahore, Pakistan
e-mail: tchinyok@vt.edu

The effect of viscoelasticity on the thermodynamic performance of a thermally decomposable lubricant subjected to shear and Arrhenius kinetics is investigated with direct numerical simulations. A numerical algorithm based on the finite difference method is implemented in time and space with the Oldroyd-B constitutive equation as the model for the viscoelastic liquids. We report enhanced efficiency in the case of a polymeric lubricant as compared with the purely viscous lubricant. In particular, it is demonstrated that the use of polymeric liquids helps to delay the onset of thermal runaway as compared with progressively Newtonian liquids. [DOI: 10.1115/1.2978993]

Keywords: chemical kinetics, viscoelastic fluids, Oldroyd-B liquid, lubricant

1 Introduction

Supplied with sufficient activation energy, say, in the form of heat, the majority of liquid lubricants used in engineering processes would become reactive (i.e., undergo thermal decomposition) according to, say, Arrhenius kinetics [1–3]. The efficiency of lubricants in general is largely premised on their resistance to such thermal decomposition. To this end mechanisms that promote significant heat transfer to such a lubricant system (inevitably raising the corresponding temperatures within the liquid lubricant) would therefore decrease the performance of the fluid as a lubricant. Lubricants, in most engineering systems, separate solid sliding boundaries from coming into physical contact. The sliding motion of such solid boundaries clearly leads to shearing of the fluid enclosed in-between. In this work, we model this physical setup via a Couette type flow between parallel plates sliding in opposite directions. Whenever a fluid is subjected to shearing forces, some of the work done would necessarily be dissipated as heat [4]. Thus fluid shear is one such process, alluded to above, which would lead to temperature increases in the fluid system. It is the aim of this work to demonstrate that such temperature increases would not be as large when using viscoelastic liquid lubricants as the temperatures obtained in the case of purely viscous lubricants. By their physical definition, lubricants are generally very thin liquid films that occupy a very narrow region separating two solid boundaries. We will henceforth assume that the concentration/composition of the fluid remains constant in time. This assumption is also commonly referred to as negligible reactant consumption [2,3] and helps make the physics more tractable.

The need to understand such phenomena as thermal runaway, where, say, the liquid lubricant temperature blows up in finite-time, provides the impetus for investigations like the one considered in this work. In fact, the question of whether solutions of partial differential equations, which govern problems of industrial and engineering importance, exist globally in time or develop singularities in finite time has been a focus of attention in the scientific community. For a comprehensive overview of the typical examples where finite-time blowup, or at least very rapid growth, occurs in mechanical systems and, in particular, those of thermal-fluid mechanics refer to Ref. [5]. Experimental investigations and evidence of the thermal runaway problem are provided, for example, in Ref. [6].

In Sec. 2 we present the model problem and its governing equations and then proceed to develop the numerical algorithm that will be used to solve the set of equations. Section 3 is a validation of the current algorithm against physical intuition and we also furnish the purely viscous (Newtonian) results here. In Sec. 3 we provide and discuss the main results for the full viscoelastic problem with variable viscosity and relaxation. Concluding remarks follow in Sec. 5.

2 Mathematical Modeling

Figure 1 is a sketch of the model problem. The boundary conditions are that the walls at $y=-L^*,L^*$ move with speeds U_B^* and U_T^*, respectively, and are maintained at the same constant temperature T_B^*. The initial conditions we use for temperature, velocities, and the extra stresses are a uniform temperature, $T^*=T_B^*>0$, and either (i) a uniform shear flow and corresponding uniform stresses that would prevail under such a flow in isothermal conditions or (ii) zero velocity and stresses. The superscript * will be used for dimensional variables.

The specific heat capacity, density, and thermal conductivity of the fluid will be taken as constant and denoted by c_p^*, ρ^*, and κ^*, respectively. Viscosities and relaxation times tend to be more susceptible to temperature variations and so these will be assumed temperature dependent. The relaxation time is $\lambda(T)^*$, solvent viscosity is $\eta_s(T)^*$, polymer viscosity is $\eta_p(T)^*$, and we will denote the total viscosity, $\eta_s(T)^*+\eta_p(T)^*$, by $\eta(T)^*$. The plate separation (and hence L^*) is taken small enough so that the assumption of negligible fluid consumption holds.

The fluid system is governed by the continuity, momentum, and energy equations for incompressible fluids:

$$\nabla^* \cdot \mathbf{u}^* = 0 \tag{1}$$

$$\rho^* \frac{D}{Dt^*}\mathbf{u}^* = \nabla^* \cdot \underline{\underline{\sigma}}^* \tag{2}$$

[1]Also at Center for Research in Computational and Applied Mechanics, University of Cape Town, Rondebosch 7701, South Africa.

Contributed by the Fluids Engineering Division of ASME for publication in the JOURNAL OF FLUIDS ENGINEERING. Manuscript received November 20, 2006; final manuscript received September 11, 2007; published online October 23, 2008. Assoc. Editor: Dennis Siginer.

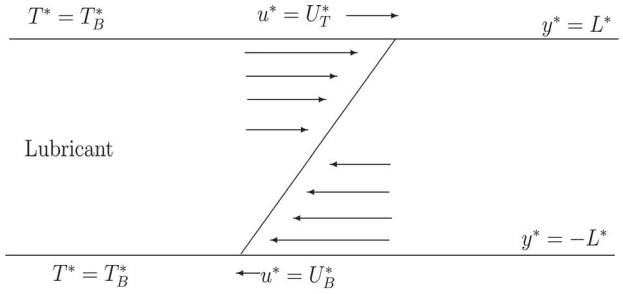

Fig. 1 Schematics of the model problem

$$\rho^* c_p^* \frac{D}{Dt^*} T^* = Q_D^* - \nabla^* \cdot \Phi_q^* + Q^* A^* C^* \exp\left(-\frac{E^*}{R^* T^*}\right) \tag{3}$$

where the notation $D/Dt^* := \partial/\partial t^* + \mathbf{u}^* \cdot \nabla^*$ represents the material derivative and $\nabla^* := \partial/\partial x^* + \partial/\partial y^*$ is the gradient operator. The total stress tensor is $\underline{\underline{S}}^* = \underline{\underline{\tau}}^* + \eta_s^* \underline{\underline{S}}^*$, where the extra stress tensor, $\underline{\underline{\tau}}^*$, is the polymer contribution and the remaining purely viscous component of the stress contains the deformation rate tensor $\underline{\underline{S}}^* = [\nabla^* \mathbf{u}^* + (\nabla^* \mathbf{u}^*)^T]$. The term $Q_D^* = \gamma \underline{\underline{\tau}}^* : \underline{\underline{S}}^* + (1-\gamma)\eta_s^* \underline{\underline{S}}^* : \underline{\underline{S}}^*$ represents the internal heat production consisting of an irreversible part $\eta_s^* \underline{\underline{S}}^* : \underline{\underline{S}}^*$ called the mechanical dissipation and a reversible part $\underline{\underline{\tau}}^* : \underline{\underline{S}}^*$ due to the orientation of polymer molecules. The constant γ is a weighting factor for the dissipative terms such that $0 \le \gamma \le 1$ and (:) denotes the double dot product of two tensors. Φ_q^* is the heat flux, Q^* is the heat release due to the exothermic reaction [2,7], A^* is the Arrhenius prefactor, C^* is the residue concentration, E^* is the activation energy, and R^* is the gas constant [3,8].

The heat flux is given by Fourier's law $\Phi_q^* = -\kappa^* \nabla^* T^*$, and the extra stress tensor, $\underline{\underline{\tau}}^*$, is modeled via the nonisothermal Oldroyd-B equation [9–13]

$$\underline{\underline{\tau}}^* + \lambda^* \left(\overset{\nabla}{\underline{\underline{\tau}}}^* - \underline{\underline{\tau}}^* \frac{D}{Dt^*} (\ln T^*/T_B^*) \right) = \eta_p(T)^* \underline{\underline{S}}^* \tag{4}$$

The upper convected time derivative $\overset{\nabla}{\underline{\underline{\tau}}}^*$ is defined as

$$\overset{\nabla}{\underline{\underline{\tau}}}^* = \frac{\partial \underline{\underline{\tau}}^*}{\partial t^*} + (\mathbf{u}^* \cdot \nabla^*)\underline{\underline{\tau}}^* - (\nabla^* \mathbf{u}^*)\underline{\underline{\tau}}^* - \underline{\underline{\tau}}^* (\nabla^* \mathbf{u}^*)^T \tag{5}$$

To model the temperature dependence of the viscosities and relaxation times, we use a Nahme-type law:

$$\lambda^* = \lambda_B^* \bar{\lambda}(T)^*, \quad \eta_s^* = \eta_{s_B}^* \mu(T)^*, \quad \eta_p^* = \eta_{p_B}^* \mu(T)^* \tag{6}$$

where

$$\bar{\lambda}(T)^* = (1 - \delta_\lambda) + \delta_\lambda \frac{T_B^*}{T^*} \exp(-\varepsilon_\lambda \Theta), \quad \mu(T)^* = \exp(-\varepsilon_\eta \Theta)$$

with $\Theta = (T^* - T_B^*)/T_B^*$. The constants λ_B^*, $\eta_{s_B}^*$, $\eta_{p_B}^*$, ε_λ, and ε_η are reference quantities and δ_λ is the delta function such that

$$\delta_\lambda = \begin{cases} 0 & \text{if } \varepsilon_\lambda = 0 \\ 1 & \text{otherwise} \end{cases}$$

If we assume a flow that is predominantly in the longitudinal direction (which would be justified since the plate separation is very small) then we have a one dimensional flow $\mathbf{u}^* = (u^*(t^*, y^*), 0, 0)$. Also $\partial/\partial x^* = \partial/\partial z^* = 0$ and hence all variables are functions of time t^* and the transverse variable y^*. If we denote

$$U_0^* = \begin{cases} (U_T^* - U_B^*)/2, & U_B^* < 0 \\ U_T^*, & U_B^* = 0 \end{cases}$$

then the dimensionless parameters for the problem are as follows:

$$\mathrm{Re} = \frac{\rho^* U_0^* L^*}{\eta_B^*}, \quad \mathrm{De} = \frac{\lambda_B^* U_0^*}{L^*}, \quad \mathrm{Pr} = \frac{c p^* \eta_B^*}{\kappa^*}, \quad \alpha = \frac{R^* T_B^*}{E^*}, \quad \beta = \frac{\eta_{p_B}^*}{\eta_B^*}$$

$$\delta_1 = \frac{Q^* A^* E^* C^* L^{*2}}{\kappa^* R^* T_B^{*2}} \exp\left(-\frac{1}{\alpha^*}\right), \quad \delta_2 = \frac{\eta_B^* U_0^{*2}}{Q^* A^* C^* L^{*2}} \exp\left(\frac{1}{\alpha^*}\right) \tag{7}$$

Here Re, De, and Pr are, respectively, the Reynolds, Deborah, and Prandtl numbers. α is an activation energy parameter and β is the ratio of the polymer to the total viscosity. The reaction parameter, δ_1, is called the Frank–Kamenetskii parameter and is described, say, in Refs. [1–3]. For a comprehensive discussion of the Frank–Kamenetskii parameter, see Ref. [14]. δ_2 is a viscous heating parameter. We introduce the following dimensionless variables:

$$t = \frac{U_0^*}{L^*} t^*, \quad y = \frac{y^*}{L^*}, \quad u = \frac{u^*}{U_0^*}, \quad \bar{\lambda}(T) = \frac{\lambda(T)^*}{\lambda_B^*}, \quad \mu(T) = \frac{\eta(T)^*}{\eta_B^*}$$

$$T = \frac{(T^* - T_B^*)}{\alpha^* T_B^*}, \quad \underline{\underline{\tau}} = \frac{L^*}{\eta_B^* U_0^*} \underline{\underline{\tau}}^*, \quad \underline{\underline{S}} = \frac{L^*}{U_0^*} \underline{\underline{S}}^*, \quad \nabla = L^* \nabla^* \tag{8}$$

The dimensionless governing equations for the longitudinal velocity u, temperature T, and extra stress components τ_{11}, τ_{12}, and τ_{22} are then

$$\frac{\partial u}{\partial t} = \frac{1}{\mathrm{Re}} \left(\frac{\partial}{\partial y} [\mu(T)\tau_{12}] + \frac{\partial}{\partial y} \left((1-\beta)\mu(T) \frac{\partial u}{\partial y} \right) \right) \tag{9}$$

$$\frac{\partial T}{\partial t} = \frac{\delta_1}{\mathrm{Re\,Pr}} \left(\exp\left(\frac{T}{1+\alpha T}\right) + 2\gamma\delta_2 \mu \tau_{12} \frac{\partial u}{\partial y} + 2\delta_2 (1-\gamma)(1-\beta)\mu \left(\frac{\partial u}{\partial y}\right)^2 \right) + \frac{1}{\mathrm{Re\,Pr}} \frac{\partial^2 T}{\partial y^2} \tag{10}$$

$$\tau_{11} + \mathrm{De} \frac{\bar{\lambda}}{\mu} \left(\frac{\partial}{\partial t} [\mu \tau_{11}] - \tau_{11} \frac{\partial}{\partial t} \ln[1+\alpha T] - 2\tau_{12} \frac{\partial u}{\partial y} \right) = 0 \tag{11}$$

$$\tau_{12} + \mathrm{De} \frac{\bar{\lambda}}{\mu} \left(\frac{\partial}{\partial t} [\mu \tau_{12}] - \tau_{12} \frac{\partial}{\partial t} \ln[1+\alpha T] - \tau_{22} \frac{\partial u}{\partial y} \right) = \beta \frac{\partial u}{\partial y} \tag{12}$$

$$\tau_{22} + \mathrm{De} \frac{\bar{\lambda}}{\mu} \left(\frac{\partial}{\partial t} [\mu \tau_{22}] - \tau_{22} \frac{\partial}{\partial t} \ln[1+\alpha T] \right) = 0 \tag{13}$$

The dimensionless viscosity and relaxation times, respectively, reduce to

$$\mu(T) = \exp(-\varepsilon_\eta \alpha T), \quad \bar{\lambda}(T) = (1 - \delta_\lambda) + \delta_\lambda \frac{1}{1+\alpha T} \exp(-\varepsilon_\lambda \alpha T)$$

In this work, we consider either the symmetric flow (i) $U_B = -U_T$ confined to $-1 \le y \le 1$ or (ii) limit our attention only to the upper half plane $0 \le y \le 1$ with $U_B = 0$. In either case, we have $U_0 = U_T$ and our boundary conditions reduce to

$$T(0) = T(1) = 0, \quad u(1) = 1, \quad \begin{cases} u(-1) = -1 & \text{case (i)} \\ u(0) = 0 & \text{case (ii)} \end{cases} \tag{14}$$

The lower boundary condition for $u(t, y)$ in the graphical results should clearly indicate which of the two choices we are using.

2.1 Numerical Algorithm. Our numerical algorithm is based on the semi-implicit finite difference scheme given in Refs. [15–17] for the isothermal viscoelastic case. We modify it here to instead take the implicit terms at the intermediate time level $(n+1/2)$ and also extend the algorithm to the temperature equation. The discretization of the governing equations is based on a linear

Cartesian mesh and uniform grid on which finite-differences are taken. We approximate both the second and first spatial derivatives with second-order central differences. The equations corresponding to the first and last grid point are modified to incorporate the boundary conditions. The semi-implicit scheme for the velocity component reads as follows:

$$\frac{u^{(n+1)}-u^{(n)}}{\Delta t}=\frac{1}{\mathrm{Re}}\left[\frac{\partial}{\partial y}(\mu^{(n)}\tau_{12}^{(n)})+\hat{\mu}^{(n)}(u_{yy}^{(n+1/2)}-\varepsilon_{\eta}\alpha u_{y}^{(n)}T_{y}^{(n)})\right] \tag{15}$$

Here $\hat{\mu}^{(n)}=(1-\beta)\mu^{(n)}$ and as in the Crank–Nicolson scheme, terms given at $(n+1/2)$ are taken as the averages of the corresponding terms at $(n+1)$ and n. The equation for $u^{(n+1)}$ then becomes

$$-r\,\hat{\mathrm{Re}}\,\mu^{(n)}[u_{j-1}^{(n+1)}+u_{j+1}^{(n+1)}]+2(1+r\,\hat{\mathrm{Re}}\,\mu^{(n)})u_{j}^{(n+1)}=\text{explicit terms} \tag{16}$$

where $\hat{\mathrm{Re}}=(1-\beta)/\mathrm{Re}$ and $r=\Delta t/(\Delta y)^2$. The solution procedure for $u^{(n+1)}$ thus reduces to inversion of tridiagonal matrices, which is an advantage over a full implicit scheme. The semi-implicit integration scheme for the temperature equation is similar to that for the velocity component. Unmixed second partial derivatives of the temperature are treated implicitly:

$$\frac{T^{(n+1)}-u^{(n)}}{\Delta t}=\frac{1}{\mathrm{Re\,Pr}}T_{yy}^{(n+1/2)}+\frac{\delta_1}{\mathrm{Re\,Pr}}\left(\exp\left(\frac{T}{1+\alpha T}\right)+2\gamma\delta_2\mu\tau_{12}\frac{\partial u}{\partial y}+2\delta_2(1-\gamma)(1-\beta)\mu\left(\frac{\partial u}{\partial y}\right)^2\right)^{(n)} \tag{17}$$

The equation for $T^{(n+1)}$ thus becomes

$$-\frac{r}{\mathrm{Re\,Pr}}T_{j-1}^{(n+1)}+2\left(1+\frac{r}{\mathrm{Re\,Pr}}\right)T_{j}^{(n+1)}-\frac{r}{\mathrm{Re\,Pr}}T_{j+1}^{(n+1)}=\text{explicit terms} \tag{18}$$

and the solution procedure also reduces to inversion of a constant tridiagonal matrix. The constitutive equation (4) is treated with an analogous semi-implicit integration scheme. The terms, which involve spatial derivatives of the extra stress tensor (which, however, identically vanish in this 1D case), are taken implicitly, as is the linear term in $\underline{\underline{\tau}}$:

$$\mathrm{De}\,\bar{\lambda}^{(n)}\left[\frac{(\mu\underline{\underline{\tau}})^{(n+1)}-(\mu\underline{\underline{\tau}})^{(n)}}{\Delta t}\right]+[\mu\underline{\underline{\tau}}]^{(n+1/2)}$$

The equations for the stresses $\tau_{11}^{(n+1)}$, $\tau_{12}^{(n+1)}$, and $\tau_{22}^{(n+1)}$ are thus of the form

$$(2\,\mathrm{De}\,\bar{\lambda}^{(n)}+\Delta t)[\mu\underline{\underline{\tau}}]^{(n+1)}=\text{explicit terms} \tag{19}$$

The solution procedure is even simpler as it simply entails the direct calculation of the explicit terms. Schemes (16), (18), and (19) were checked for consistency and it was shown that Eqs. (16) and (18) are second-order accurate in both space and time. On the other hand, Eq. (19) is only first-order accurate in time but still second order in space. Thus the algorithm applied to the full viscoelastic problem would be first-order accurate in time and second order in space whereas the corresponding Newtonian problem would be second order in both space and time. A linearized von Neumann stability analysis leads to the stability conditions $\Delta t/\Delta y\leq\mathrm{Re}$ from Eq. (16) and $r\leq\mathrm{De}/2$ for Eq. (19).

3 Code Validation

3.1 Purely Viscous Liquids. By taking $\beta=\gamma=\mathrm{De}=0$ we recover the case of a purely viscous Newtonian fluid, albeit for variable viscosity:

$$\frac{\partial u}{\partial t}=\frac{1}{\mathrm{Re}}\frac{\partial}{\partial y}\left(\mu(T)\frac{\partial u}{\partial y}\right) \tag{20}$$

$$\frac{\partial T}{\partial t}=\frac{\delta_1}{\mathrm{Re\,Pr}}\left(\exp\left(\frac{T}{1+\alpha T}\right)+2\delta_2\mu\left(\frac{\partial u}{\partial y}\right)^2\right)+\frac{1}{\mathrm{Re\,Pr}}\frac{\partial^2 T}{\partial y^2} \tag{21}$$

In this case all viscoelastic variables identically vanish, hence the absence of the equations for the extra stresses. The only remaining nontrivial quantities are the fluid velocity and temperature, which are the solutions to the coupled equations (Eqs. (20) and (21)). These equations are, however, still intractable to analytical treatment and this is attributable to their transient nature, the variable viscosity, and the presence of the nonlinear source terms in Eq. (21). We can, however, make reasonable predictions as to the qualitative behavior of these reduced equations by looking, say, at the steady state case with constant viscosity. Under such assumptions, Eq. (20) with boundary conditions (14) immediately yields the classical linear velocity profile $u(y)=y$. With this velocity profile, the dissipation terms in Eq. (21) become constant. If we further assume constant reaction source terms then, with the help of the boundary conditions (14), we obtain a classical parabolic temperature profile opening downward with a maximum along the centerline of the channel.

Figure 2 shows the variation of the fluid temperature, velocity, normal stress difference ($N_1=\tau_{11}-\tau_{22}$), and extra stress components with y for the full transient and variable viscosity model given by Eqs. (9)–(13). The parameter values used in Fig. 2 are $\beta=\gamma=\mathrm{De}=0$, $t=2.5$, $\delta_1=\delta_2=1$, $\alpha=0.001$, $\varepsilon_{\lambda}=0$, $\varepsilon_{\eta}=20$, $\mathrm{Re}=\mathrm{Pr}=1$, $\Delta y=0.05$, and $\Delta t=0.0005$. We recover the predicted linear velocity profile and parabolic temperature field. At the given parameter values, the maximum temperature is $T_{\max}=0.4280$. The corresponding problem with constant viscosity ($\varepsilon_{\eta}=0$) slightly increases the maximum temperature to $T_{\max}=0.4292$.

As noted, the above results were obtained at $t=2.5$ using the time step $\Delta t=0.0005$ and on a mesh width of $\Delta y=0.05$. In fact, the maximum temperature converges to $T_{\max}=0.4280$ for any $t\geq 1$. On a refined mesh, $\Delta y=0.02$, the maximum temperature converges to the same value $T_{\max}=0.4280$ for $t\geq 7$. An even finer mesh $\Delta y=0.01$ similarly gives $T_{\max}=0.4280$ for $t\geq 22.5$. The physical computational times are of the order of a few seconds, even for very fine meshes, on a standard personal computer.

3.2 Parameter Sensitivity. From the structure of the governing equations, it should be clear that the maximum temperature would increase with increasing reaction parameter δ_1 and/or viscous heating parameter δ_2 (at least initially with respect to δ_1). This is due to the fact that any such increases in these two parameters would correspondingly increase the magnitude source terms in the temperature equation. Similarly, decreasing α has the same effect of increasing the source terms and hence should also expectedly increase the maximum temperature. We use this analysis to perform a simple validation of our code, see Fig. 3.

Figure 3 is given at $t=0.5$, $\beta=\gamma=0.5$, $\varepsilon_{\lambda}=60$, $\varepsilon_{\eta}=20$, $\mathrm{Re}=\mathrm{Pr}=\mathrm{De}=1$, $\Delta y=0.05$, and $\Delta t=0.0005$, and unless it is the independent variable we also used $\delta_1=\delta_2=1$ and $\alpha=0.001$. The results are in line with our intuition.

4 Viscoelastic Effects

We extend the analysis just given to investigate the sensitivity of the model to viscoelastic parameters, γ, β, and De. Figure 4 is given at $t=0.5$, with $\delta_1=\delta_2=1$, $\alpha=0.001$, $\varepsilon_{\lambda}=60$, $\varepsilon_{\eta}=20$, $\mathrm{Re}=\mathrm{Pr}=1$, $\Delta y=0.05$, and $\Delta t=0.0005$ and unless it is the independent variable we also employed $\beta=\gamma=0.5$ and $\mathrm{De}=1$. We notice that an increase in the viscoelastic parameters correspondingly decreases the attainable maximum temperatures. Here we used $\mathrm{De}\,b=(\log_{10}\mathrm{De})/2$ so as to apply the same domain as for β and γ.

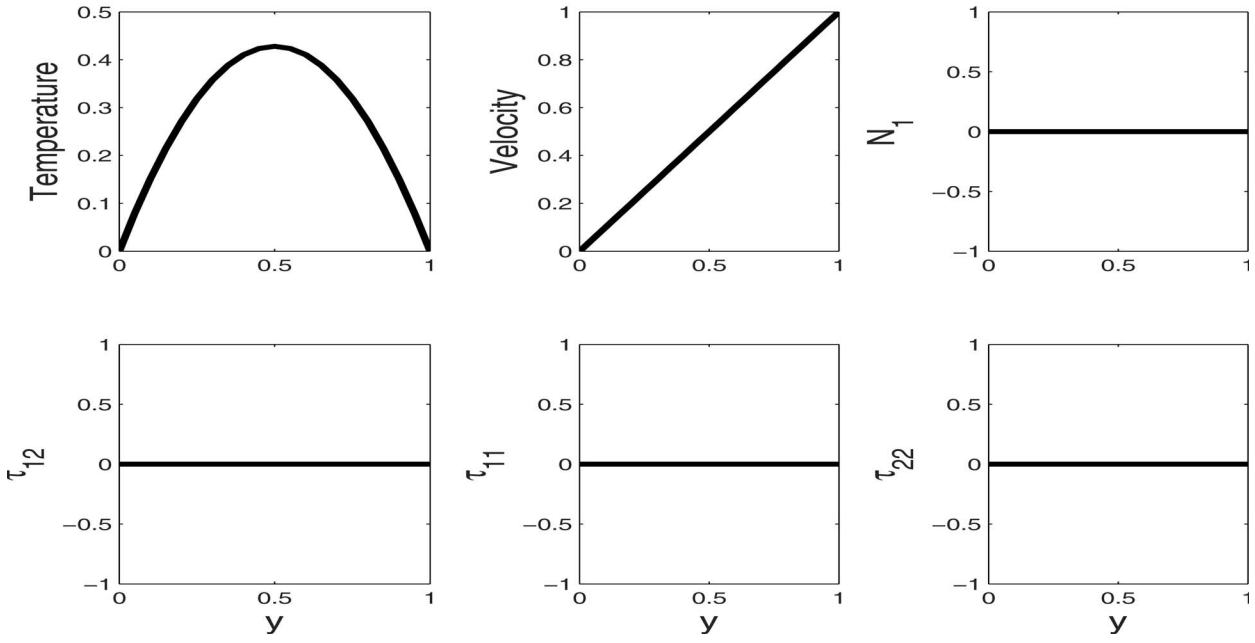

Fig. 2 Setting $\beta=\gamma=\mathrm{De}=0$ in our full model

As shown in Fig. 3, the long-term behavior of the fluid maximum temperature with respect to higher values of δ_1 is not directly obvious. There could be bifurcations or blowup of the solution if δ_1 exceeds certain threshold values as is demonstrated, say, in Refs. [2,3] and in related works cited therein. Our numerical algorithm captures the primary solutions for the fluid maximum temperature up to point that corresponds to the critical values of δ_1. At this point the fluid maximum temperature suddenly blows up and this manifests as sharp discontinuities in our solutions, see Fig. 5. Our numerical algorithm, however, does not capture any secondary solution branches beyond the critical values of δ_1, as illustrated in Fig. 6. Figures 5 and 6 were obtained at $t=0.5$ using the common parameter values as follows: $\delta_2=1$, $\alpha=0.001$, $\varepsilon_\lambda=60$, $\varepsilon_\eta=20$, $\mathrm{Re}=\mathrm{Pr}=1$, $\Delta y=0.05$, and $\Delta t=0.0005$. The remaining viscoelastic parameters were varied as follows: $\gamma=\beta=\mathrm{De}=0$ (dash circle); $\gamma=\beta=0.1$, $\mathrm{De}=1$ (dash dotted); $\gamma=\beta=0.3$, $\mathrm{De}=1$ (dash diamond); $\gamma=\beta=0.4$, $\mathrm{De}=1$ (dashed line); and $\gamma=\beta=0.8$, $\mathrm{De}=1$ (solid line).

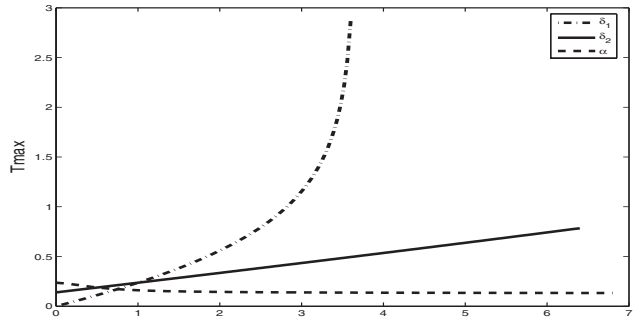

Fig. 3 Variation of maximum temperature with δ_1 (-·), δ_2 (–), and α (- -)

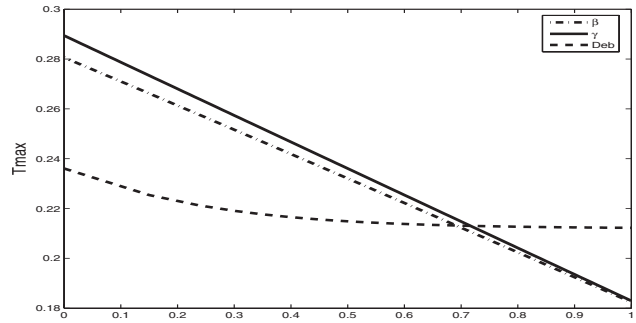

Fig. 4 Variation of maximum temperature with β (-·), γ (–), and De *b*(- -)

The sudden discontinuity or explosion of the physical temperature in finite time is commonly referred to as thermal runaway in chemical kinetics and tends to pose severe limitations on the performance of a liquid lubricant. As illustrated, the onset of thermal runaway is intricately connected with large increases in the Frank–Kamenetskii parameter, δ_1, beyond certain threshold values. Figures 5 and 6 clearly indicate that the threshold value of δ_1 is increased when we use increasingly polymeric liquids. Fluid viscoelasticity would thus delay the onset of thermal runaway this way. Figures 5 and 6 also show that for each given value of δ_1 progressively polymeric liquids have lower maximum temperatures compared with increasingly Newtonian liquids. Thus viscoelasticity tends to reduce the rate of growth of the fluid maximum temperature. This is also illustrated in both Figs. 4 and 7. Figure 7 is analogous to Fig. 2, except we now use nonzero viscoelastic parameters values: Fig. 7 is given at $t=2.5$, with $\delta_1=\delta_2=1$, $\alpha=0.001$, $\varepsilon_\lambda=60$, $\varepsilon_\eta=20$, $\mathrm{Re}=\mathrm{Pr}=1$, $\Delta y=0.05$, $\Delta t=0.0005$, $\beta=\gamma=0.8$, and $\mathrm{De}=50$. At these parameter values, the maximum temperature is decreased from the previous value of $T_{\max}=0.4280$ (for the Newtonian case) to the current value of $T_{\max}=0.1586$ under polymeric conditions.

We explain these results in terms of the polymer structure of our model problem. The deformation of a viscous fluid due to shear releases energy into the fluid system in the irreversible process of mechanical dissipation. On the other hand a similar shear induced deformation for polymeric fluids takes up or releases energy in a reversible process due to the orientation of the polymer chains. In particular, stretching of the polymer chains (say, due to fluid shear) takes up energy, which can in turn be released when these chains relax.

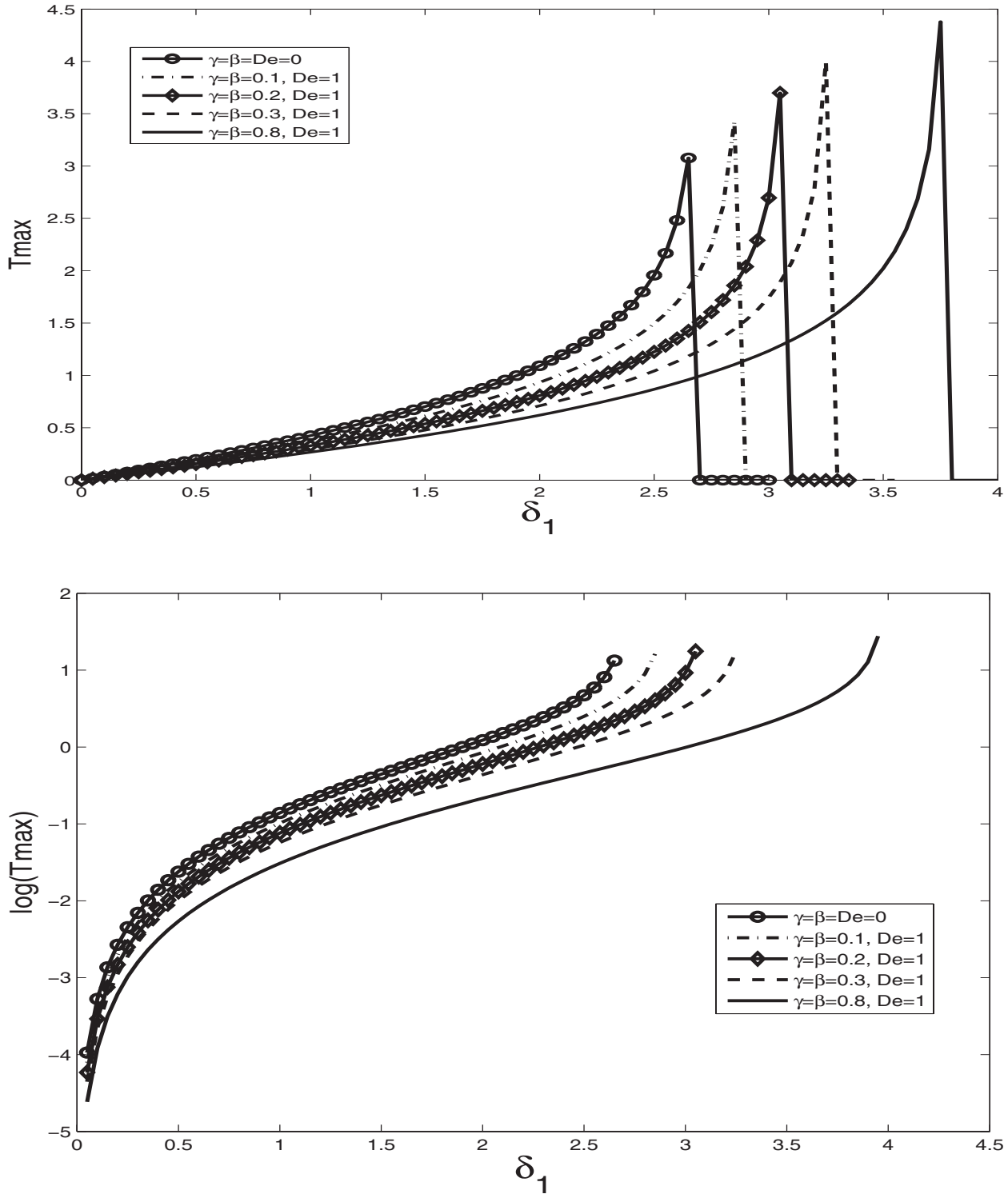

Fig. 5 Variation of maximum temperature with δ_1

As shown in Fig. 7, we notice that the normal stress difference N_1 is non-negative. In fact, N_1 is also non-negative under the parameters of Fig. 5. This means that the polymer chains in the viscoelastic liquid are in the stretched state and hence a significant portion of heat energy would be stored in the stretched polymer chains as explained earlier. Thus, for polymeric fluids, as long as the shear deformation of the fluid persists, the energy used in stretching the polymer chains would stay "locked up" in the stretched polymer molecules as opposed to being lost as direct fluid temperature. Since also higher polymeric conditions (in particular, high values of De) in turn imply high relaxation times, this means that the polymer chains in highly viscoelastic fluids would not relax as easily, explaining the lower fluid temperatures compared with increasingly Newtonian fluids. Also, for the Newtonian fluids the irreversible and exothermic mechanical dissipation is the dominant heat production process. This in turn means that the energy produced this way is directly integrated into the fluid system and chiefly manifests as direct fluid temperature. We note that

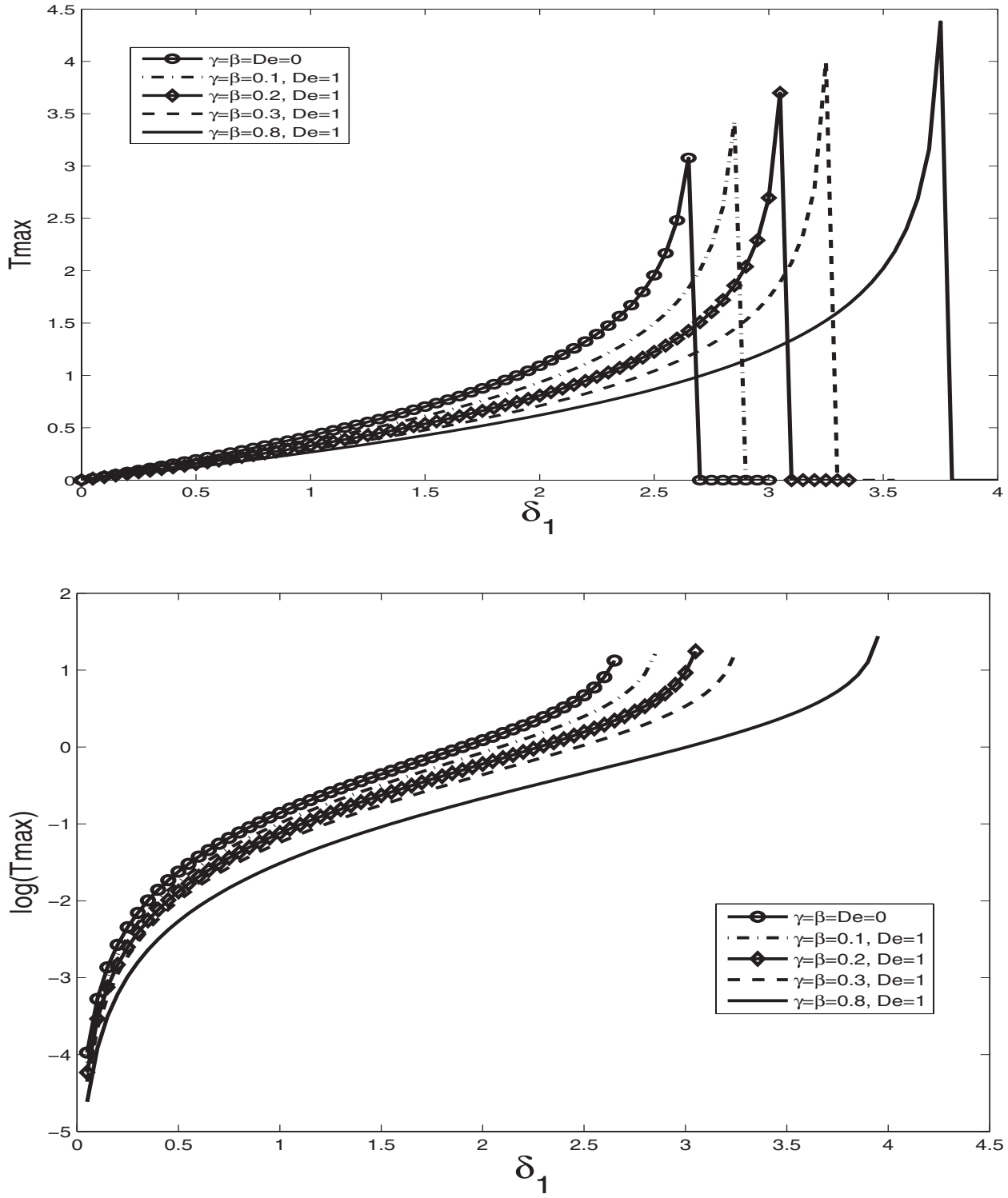

Fig. 6 Variation of the logarithm of maximum temperature with δ_1

increasing the polymeric parameter β damps out the mechanical dissipation term; thus viscoelasticity would decrease the attainable fluid temperatures this way.

All the preceding results are obtained using zero initial conditions for the velocity and stress components. The alternative initial condition given by a fully developed shear velocity profile and corresponding equilibrium stresses that would prevail under such an isothermal shear flow give similar results.

5 Conclusion

We investigate the effect of viscoelasticity on the temperature of a lubricant subjected to simple shear in one dimensional flow under Arrhenius kinetics. To this end, we demonstrate both (i) a decrease in attainable temperatures and (ii) a delay of the thermal runaway phenomenon (i.e., an increase in the threshold value of the Frank–Kamenetskii parameter). Both of these are directly at-

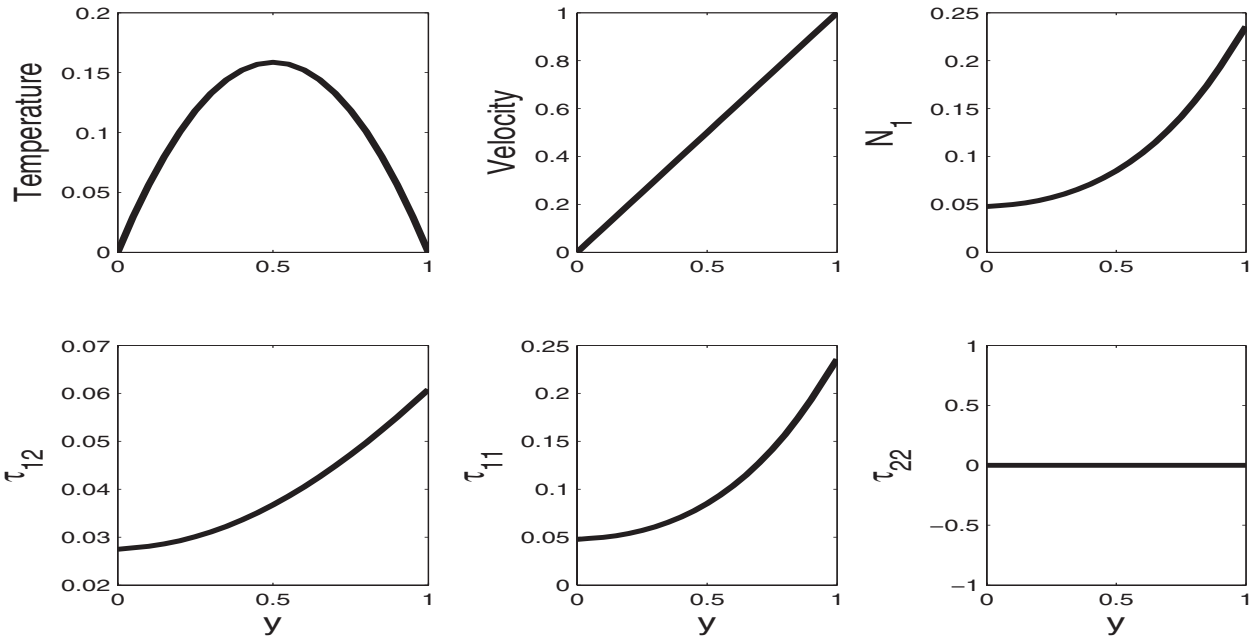

Fig. 7 Variation of fluid quantities in the viscoelastic case

tributable to increased polymeric effects. Hence we have effectively demonstrated the superiority of viscoelastic fluids (typified here by the Oldroyd-B liquid) over Newtonian fluids in lubrication processes that involve thermally reactive lubricants. We have also checked our code for both temporal and spatial convergences.

Acknowledgment

This research was carried out under a postdoctoral research grant from the Center for Advanced Studies in Mathematics (CASM) at Lahore University of Management Sciences (LUMS). The author would like to thank CASM for financial and material support. The author also thanks Professor Yuriko and Professor Michael Renardy (Virginia Tech) for discussions and the reviewers for insightful comments.

References

[1] Hutson, M. H., Hauger, S. A., and Edwards, G., 2002, "Thermal Diffusion and Chemical Kinetics in Laminar Biomaterial Due to Heating by a Free-Electron Laser," Phys. Rev. E, **65**, 061906.
[2] Adler, J., 1991, "Thermal Explosion Theory With Arrhenius Kinetics: Homogeneous and Inhomogeneous Media," Proc. R. Soc. London, Ser. A, **433**, pp. 329–335.
[3] Boddington, T., Gray, P., and Wake, G. C., 1977, "Criteria for Thermal Explosions With and Without Reactant Consumption," Proc. R. Soc. London, Ser. A, **357**, pp. 403–422.
[4] Yesilata, B., 2006, "Viscous Heating Effects in Viscoelastic Flow Between Rotating Parallel-Disks," Turk. J. Eng. Environ. Sci., **26**, pp. 503–511.
[5] Straughan, B., 1998, *Explosive Instabilities in Mechanics*, Springer, New York.
[6] Bair, S., Qureshi, F., and Khonsari, M., 1994, "Adiabatic Shear Localization in a Liquid Lubricant Under Pressure," ASME J. Tribol., **116**, pp. 705–709.
[7] Liebman, J. F., Afeefy, H. Y., and Slayden, S. W., 2000, *The Amide Linkage*, Wiley, New York, Chap. V.
[8] Lim, J. J., and Shamos, M. H., 1974, Biopolymers, **13**, pp. 1791.
[9] Dressler, M., Edwards, B. J., and Öttinger, H. C., 1999, "Macroscopic Thermodynamics of Flowing Polymeric Liquids," Rheol. Acta, **38**, pp. 117–136.
[10] Olagunju, D. O., 2005, "Secondary Flow in Non-Isothermal Viscoelastic Parallel-Plate Flow," J. Eng. Math., **51**, pp. 325–338.
[11] Olagunju, D. O., Cook, L. P., and McKinley, G. H., 2002, "Effect of Viscous Heating on Linear Stability of Viscoelastic Cone-and-Plate Flow: Axisymmetric Case," J. Non-Newtonian Fluid Mech., **102**(2), pp. 321–342.
[12] Al-Mubaiyedh, U. A., Sureshkumar, R., and Khomami, B., 1999, "Influence of Energetics on the Stability of Viscoelastic Taylor–Couette Flow," Phys. Fluids, **11**(11), pp. 3217–3226.
[13] Wapperom, P., Hulsen, M. A., and van der Zanden, J. P. P. M., 1998, "A Numerical Method for Steady and Nonisothermal Viscoelastic Fluid Flow for High Deborah and Péclet Numbers," Rheol. Acta, **37**, pp. 73–88.
[14] Frank-Kamenetskii, D. A., 1969, *Diffusion and Heat Transfer in Chemical Kinetics*, 2nd ed., Plenum, New York.
[15] Chinyoka, T., Renardy, Y. Y., Renardy, M., and Khismatullin, D. B., 2005, "Two-Dimensional Study of Drop Deformation Under Simple Shear for Oldroyd-B Liquids," J. Non-Newtonian Fluid Mech., **130**, pp. 45–56.
[16] Renardy, Y. M., Chinyoka, T., Khismatullin, D. B., and Li, J., 2004, "A Viscoelastic VOF-PROST Code for the Study of Drop Deformation," *Proceedings of the ASME Heat Transfer/Fluids Engineering Summer Conference*, Charlotte, NC, July 11–15, HTFED CDROM Track 5.
[17] Chinyoka, T., 2004, "Numerical Simulation of Stratified Flows and Droplet Deformation in 2D Shear Flow of Newtonian and Viscoelastic Fluids," Ph.D. thesis, Virginia Polytechnic Institute and State University, Blacksburg, VA.

Experiments and Models of the Magneto Rheological Behavior of High Weight Percent Suspensions of Carbonyl Iron Particles in Silicone Oil

Farzad Ahmadkhanlou
Monon Mahboob
Stephen Bechtel
Gregory Washington

Department of Mechanical Engineering,
The Ohio State University,
Columbus, OH 43210

Flow properties of magnetorheological (MR) fluids are greatly altered by the application of a magnetic field. The design, optimization, and control of novel devices that exploit MR fluid behavior in multidegree of freedom applications require three dimensional models characterizing the coupling of magnetic behavior to mechanical behavior in MR fluids. The authors have derived 3D MR fluid models based on multiscale kinetic theory. The underlying bases of the models are summarized, with phenomenological empiricism distinguished from multiscale first principles, and the models' ability to capture the experimentally measured mechanical response of a MR fluid-based damper to specified magnetic fields is assessed. The results of this comparison are that the kinetic theory-based models both relate macroscale MR fluid behavior to a first-principles description of magnetomechanical coupling at the microscale and possess the flexibility to best match the measured behavior of a particular MR fluid device observed in our experiments.
[DOI: 10.1115/1.2979001]

Keywords: magnetorheological fluid, multiscale model, kinetic theory, constitutive equation

1 Introduction

"Smart" materials are materials that exhibit physical changes in response to their environment. Magnetorheological (MR) fluids are a special class of smart materials consisting of micron- and/or nanometer-sized ferrous particles suspended in a carrier fluid, typically a mineral or silicone oil. Application of a magnetic field causes magnetization and alignment of the ferrous particles, altering the rheological properties of the composite particle/oil system.

In particular, MR fluids exhibit a controllable yield stresslike behavior in shear, whereby the application of a magnetic field transverse to the flow creates a resistance to flow, which increases with magnetic field magnitude. One degree of freedom pistonlike devices exploiting this controllable variation of resistance in simple shear have been under development since Rabinow [1] in the late 1940s. Practical devices incorporating MR fluids at present include vibration dampers [2–8], transmission-clutches [9–13], and brakes [14]. For these one degree of freedom devices, 1D macroscale phenomenological MR fluid models such as the Bingham and Herschel–Buckley models are sufficient. The Bingham model relates the total shear stress τ in simple shear to the shear rate $\dot{\gamma}$ and magnitude H of a transverse applied magnetic field according to the equation

$$\tau = [\tau_y(H) + \eta|\dot{\gamma}|]\mathrm{sgn}(\dot{\gamma}) \tag{1}$$

where $\tau_y(H)$ is a yield stress, assumed to be a function of the magnitude of the magnetic field, and the constant η is the effective bulk viscosity of the composite system. The Herschel-Buckley model generalizes the Bingham model to accommodate the shearing thinning observed in MR fluids,

$$\tau = [\tau_y(H) + K|\dot{\gamma}|^{1/m}]\mathrm{sgn}(\dot{\gamma}) \tag{2}$$

where m and K are the constants. We note that both models describe fluids that exhibit a strict yield stress $\tau_y(H)$ in shear where there is no flow (i.e., $\dot{\gamma}$ identically zero) until τ exceeds $\tau_y(H)$.

Novel MR fluid devices, currently being developed, extend beyond rectilinear motion, as evidenced by linear dampers, to full three dimensional applications. Figure 1 shows a MR fluid-based device being developed by the authors for force feedback in such applications as remote, minimally invasive surgery, and "drive by wire" automobile steering systems [15–17], in which the magnetic field/MR fluid interaction is controlled so as to mimic the resistance encountered by a remote robot in any direction in the plane [17–23].

For multidegree of freedom applications such as shown in Fig. 1, the Bingham, Herschel–Buckley, and similar models [24–28] are lacking in three aspects: (i) The models are *macroscale* (treating the fluid as single continuum rather than a composite system) and *phenomenological* (fitting the coefficients m and K and function $\tau_y(H)$ in an assumed form to experimental measurements of bulk properties rather than deducing the model from fundamental physics). The magnetomechanical coupling that is the cause of the macroscale properties of MR fluids takes place at the particle level and is governed by fundamental first principles (conservation of momentum, Maxwell equations, etc.) at that level. The empirical macroscale Bingham/Herschel–Buckley-type models have no particle level, are incapable differentiating between the particles and carrier fluid, and have no explicit connection to fundamental first principles. The use of empirical macroscale modeling for the design and control of MR fluid-based devices limits fidelity to a

Contributed by the Fluids Engineering Division of ASME for publication in the JOURNAL OF FLUIDS ENGINEERING. Manuscript received September 6, 2007; final manuscript received July 24, 2008; published online October 24, 2008. Assoc. Editor: Dennis Siginer. Paper presented at the 2007 ASME International Mechanical Engineering Congress (IMECE2007), Seattle WA, November 10–16, 2007.

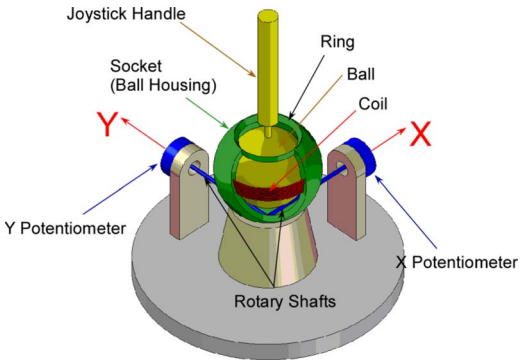

Fig. 1 2D force feedback device using a MR fluid (using MR fluid in the gap between steel ball and socket)

narrow range of applicability in the vicinity of the conditions used in the fit of the coefficients m and K and function $\tau_y(H)$ to experimental measurements. (ii) They only model 1D simple shear flow with a transverse applied magnetic field. The MR fluids in multidegree of freedom devices are subjected to flow and magnetic fields in all directions so that the models employed must be fully 3D. (iii) Because the Bingham plastic/Herschel–Buckley-type models, with their notion of a strict yield stress, idealize what actually are small nonzero flows at low values of shear stress to be identically zero, they are inaccurate at low values of stress. These low values of stress are important in force feedback systems for low levels of touch.

Instead of Bingham plastic/Herschel–Buckley-type models, what is needed to design and control advanced multidegree of freedom MR fluid-based devices are models of MR fluids, which (i) are microstructure-based and derived from first principles, resulting in fidelity beyond the vicinity of current practice, (ii) are applicable to general 3D motions, and (iii) remove the idealization of a strict yield stress so as to recognize that there is flow (albeit small) below large-scale yielding.

The authors have derived such 3D multiscale models for MR fluids, employing first principles at the microscale and kinetic theory to characterize the full 3D magnetorheological response of ferrous particle/viscous solvent composite systems to mechanical and magnetic inputs in terms of primitive measurements of the solvent properties and microstructural characterization of the metallic particles [29]. In this paper, we summarize these kinetic theory-based models and their derivation. The kinetic theory-based models connect macroscale behavior to the underlying microscale magnetomechanical coupling, ensuring physical relevance. They also possess the flexibility to best match experimental measurements.

2 Preparation and Characterization of the Magnetorheological Fluids

The MR fluid used by Rabinow in his seminal investigation [30] consisted of nine parts, by weight, of carbonyl iron to one part of silicone oil; we investigated MR fluids with a range of particle sizes, carrier fluids, and weight ratios to measure the dynamic range (the ratio of maximum viscosity in on-state to minimum viscosity in off-state) as a function of the MR fluid ingredients.

In this paper, we report our investigation of 30 different MR fluids, consisting of carbonyl iron powder in two different particle size ranges ($2-5$ μm and $4-7$ μm) mixed with five silicone oils of differing density and rheology. The steady shear rheology of these silicone oils is measured with an MCR300 rheometer fitted with Couette geometry. From these measurements, it is seen that all the silicone oils exhibit Newtonian behavior except the most viscous one, which exhibits non-Newtonian behavior especially at shear rates higher than 300/s. Weight ratios of carbonyl iron powder to silicone oil ranged from 2% to 6%.

These MR fluid samples were utilized in a linear damper designed and constructed by the authors [31,32]. Conventional MR fluid-based dampers have a reservoir of MR fluid sealed by an o-ring or gasket; these mechanical seals create sizable off-state (no applied magnetic field) shear resistance. The research in this paper employs a damper where the MR fluid is saturated in an open-celled polyurethane sponge, confining the fluid and eliminating the need for seals, thereby reducing the off-state shear resistance.

Figure 2 is the schematic of the piston and sleeve. A copper coil (350 turns of 24 AWG with 3.2 Ω of resistance) circles the shaft of the piston, so that in the sponge-filled gap the applied magnetic field is in the radial direction and hence transverse to the fluid flow of the MR fluid in the gap. The damper is designed to exert a resistive axial force of up to 100 N in response to the applied current.

The damper was used to characterize the MR fluid behavior: The solenoid was subjected to a controlled current ranging from 0 A to 4 A, generating a transverse magnetic field across the foam saturated with MR fluid. A tensile testing machine was used to control the axial motion of the damper and measure the required axial force.

Among the 30 different samples, 12 produced from silicone oils with viscosities of 1000 cS and 12,500 cS were too viscous to

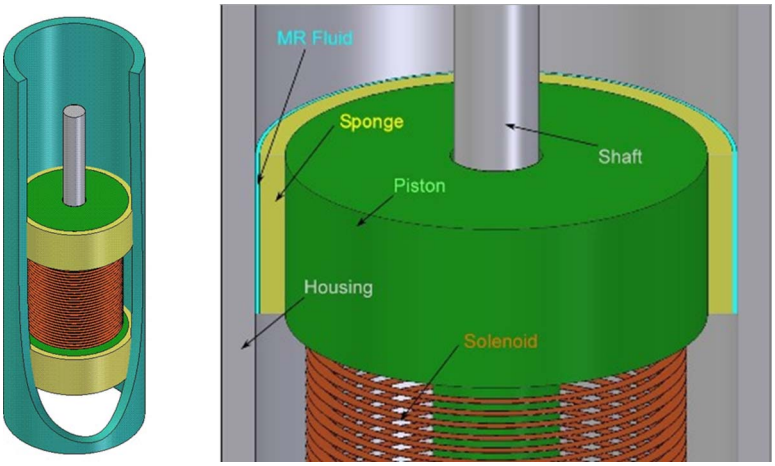

Fig. 2 Sections of the rectilinear foam-based damper

Table 1 MRF sample ingredients

Sample	Carbonyl iron powder	Silicone oil (carrier fluid)		Weight ratio of iron powder to oil
	Particle size (μm)	Density (kg/m^3)	Viscosity (Pa s)	
1	2–5	907	0.01	4
2	2–5	907	0.01	5
3	2–5	907	0.01	6
4	4–7	907	0.01	4
5	4–7	907	0.01	5
6	4–7	907	0.01	6
7	2–5	921	0.0192	4
8	2–5	921	0.0192	5
9	2–5	921	0.0192	6
10	4–7	921	0.0192	4
11	4–7	921	0.0192	5
12	4–7	921	0.0192	6
13	2–5	955	0.334	3
14	2–5	955	0.334	4
15	2–5	955	0.334	5
16	4–7	955	0.334	3
17	4–7	955	0.334	4
18	4–7	955	0.334	5

saturate the foam. Because of the very low magnetic permeability of free space ($\mu_0 = 4\pi \times 10^{-7}$ H/m), the air gap in the unsaturated foam increases the reluctance of the magnetic system dramatically, thereby decreasing the magnetic flux density. As there is no accurate way of measuring the magnetic flux density in a MR fluid during the experiment, the unsaturated foams with high viscous silicone oils were not investigated further, leaving 18 MR fluid samples (Table 1).

The tensile testing machine was used to measure the force for a controlled displacement. The different reference inputs that were applied to the system included ramp, sinusoidal, and tapered ramp. The resulting force versus time measurements of the damper for varieties of MR fluids were used to characterize the behavior of each MR fluid/damper system.

3 Kinetic Theory-Based 3D Model for MR Fluids

In our kinetic theory-based model, we consider the iron particles as dumbbells: two beads each of mass $m/2$ with position vectors $\mathbf{r}_1$ and $\mathbf{r}_2$, respectively, joined by a connector $\mathbf{q}=\mathbf{r}_2-\mathbf{r}_1$. The mass center of the bead-spring pair is $\mathbf{x}=(\mathbf{r}_1+\mathbf{r}_2)/2$. This connector $\mathbf{q}$ between two beads represents the orientation and length of the iron particle in the carrier fluid. The kinetic (or Smoluchowski) equation that describes the rate of change of the orientation vector $\mathbf{q}$ with time is

$$\dot{q}_i = \underbrace{(L_{ij} - \mu D_{ij})q_j}_{\text{effect of carrier fluid flow}} + \underbrace{a_{ij}\frac{2kT}{\psi}\frac{\partial}{\partial q_k}(\xi_{kj}^{-1}\psi)}_{\text{effect of Brownian motion}} + \underbrace{2a_{ij}f_j^{(\text{int})}}_{\text{effect of intraparticle force}} + \underbrace{a_{ij}(f_{1j}^{(\text{ext})} - f_{2j}^{(\text{ext})})}_{\text{effect of external force}} \tag{3}$$

The left hand side of Eq. (3) is the Lagrangian time derivative of particle orientation, and the terms on the right hand side arise from four physical effects that contribute to this change of orientation. The first term models the effect of carrier fluid to change particle orientation. $L_{ij}=(\partial/\partial x_j)v_i$ is the velocity gradient tensor, with symmetric part $D_{ij}=\frac{1}{2}(L_{ij}+L_{ji})$, where $v_i=v_i(\mathbf{x},t)$ is the velocity of the carrier fluid at location $\mathbf{x}$ and time t. The scalar parameter μ measures the magnitude of the nonaffine motion of the dumbbell. The second term $a_{ij}(2kT/\psi)(\partial/\partial q_k)(\xi_{kj}^{-1}\psi)$ is the effect of the Brownian motion caused by thermal fluctuation; k is the Boltzmann constant, T is the absolute temperature, $\psi(\mathbf{q},\mathbf{x},t)$ is the probability distribution function (PDF) of the particle orientation, ξ_{ij} is the anisotropic tensor responsible for the anisotropic Brownian motion, and a_{ij} is given by

$$a_{ij} = -(\delta_{im} - \varsigma_{in}\Omega_{nm})\varsigma_{mj}^{-1} \tag{4}$$

with ς_{ij} defined as the friction tensor. The Oseen–Burgers tensor Ω_{ij} accounting for the hydrodynamic interaction is

$$\Omega_{ij} = \frac{1}{8\psi\eta_s|\mathbf{q}|}\left[\delta_{ij} + \frac{1}{|\mathbf{q}|^2}q_iq_j\right] \tag{5}$$

where η_s is the solvent viscosity. The probability distribution function $\psi(\mathbf{q},\mathbf{x},t)$ is the probability of the particle at place $\mathbf{x}$ and time t having a specific orientation $\mathbf{q}$. It assigns to every interval of the real numbers a probability, so that the probability axioms are satisfied. The probability distribution function (PDF) is governed by the evolution equation

$$\frac{\partial}{\partial t}\psi = -\frac{\partial(\psi\dot{\mathbf{q}})}{\partial\mathbf{q}} = -\frac{\partial(\dot{q}_i\psi)}{\partial q_i} \tag{6}$$

Brownian motion contribution is retained in the model to make it applicable to full range of particle sizes with its effect becoming more important as the size decreases.

The third term $2a_{ij}f_j^{(\text{int})}$ is the effect of intraparticle forces, such as elasticity, on the particle orientation, with $f_j^{(\text{int})}$ the force in the connector. The fourth term $a_{ij}(f_{1j}^{(\text{ext})}-f_{2j}^{(\text{ext})})$ is the effect of external forces (the magnetic field in this paper); $\mathbf{f}_1^{(\text{ext})}$ is the magnetic force on bead 1 and $\mathbf{f}_2^{(\text{ext})}$ is the magnetic force on bead 2.

The second order orientation tensor $\langle\mathbf{q}\otimes\mathbf{q}\rangle$ with components $\langle q_iq_j\rangle$, defined as the dyadic product of $\mathbf{q}$ averaged over orientation space

$$\langle q_iq_j\rangle \equiv \int q_iq_j\psi(\mathbf{q},\mathbf{x},t)dq_1dq_2dq_3 \tag{7}$$

provides a concise interpretation of the mesoscale orientation state, namely, the orientation of the particles averaged over a suitably large region, and is the measure of orientation that influences the stress in the material. To obtain the governing evolution equation of the orientation tensor $\langle\mathbf{q}\otimes\mathbf{q}\rangle$, we multiply Eq. (7) by q_iq_j, integrate over space $\mathbb{R}^3$ (using the divergence theorem and $\psi\to 0$ as $|\mathbf{q}|\to\infty$), and insert Eq. (3):

$$\frac{D}{Dt}\langle q_i q_j\rangle = 2kT\left\langle \frac{\partial}{\partial q_k}\{[(\delta_{im}-\zeta_{in}\Omega_{nm})\zeta_{ml}^{-1}]q_j + q_i[(\delta_{jm} - \zeta_{jn}\Omega_{\mathrm{nm}})\zeta_{ml}^{-1}]\}\xi_{kl}^{-1}\right\rangle - \langle q_i[(\delta_{ij}-\zeta_{jm}\Omega_{mk})\zeta_{kl}^{-1}(2f_l^{(\mathrm{mech})} + f_{1l}^{(\mathrm{mag})} - f_{2l}^{(\mathrm{mag})})] + [(\delta_{ik}-\zeta_{im}\Omega_{mk})\zeta_{kl}^{-1}(2f_l^{(\mathrm{mech})} + f_{1l}^{(\mathrm{mag})} - f_{2l}^{(\mathrm{mag})})]q_j\rangle \tag{8}$$

where the Gordon–Schowalter derivative is defined by

$$\frac{D}{Dt}\langle q_i q_j\rangle = \frac{d}{dt}\langle q_i q_j\rangle - W_{ik}\langle q_k q_j\rangle + \langle q_i q_k\rangle W_{kj} - a[D_{ik}\langle q_k q_j\rangle + \langle q_i q_k\rangle D_{kj}] \tag{9}$$

with $(d/dt)\langle q_i q_j\rangle(x,t) = (\partial/\partial t)\langle q_i q_j\rangle(x,t) + (\partial/\partial x_k)\langle q_i q_j\rangle \dot{x}_k$, W_{ij} the skew part of the velocity gradient $(\partial v_i/\partial x_j)$, and $a = 1-\mu$; $a = 1, 0, -1$ correspond to the upper convected, corotational, and lower convected derivative, respectively.

In this paper, we investigate the kinetic theory-based models with the constitutive assumption that anisotropic effects in the Brownian motion and hydrodynamic interaction are negligible (i.e., $\xi_{ij} = \delta_{ij}$ and $\Omega_{ij} = 0$), and the friction is isotropic (i.e., $\zeta_{ij} = \zeta\delta_{ij}$). With these specializations, the evolution Eq. (8) of the orientation tensor simplifies to

$$\frac{D}{Dt}\langle q_i q_j\rangle = \frac{4kT}{\zeta}\delta_{ij} - \frac{2}{\zeta}\{\langle q_i f_j^{(\mathrm{int})} + f_i^{(\mathrm{int})} q_j\rangle\} - \frac{1}{\zeta}\{\langle q_i (f_{1j}^{(\mathrm{ext})} - f_{2j}^{(\mathrm{ext})}) + (f_{1i}^{(\mathrm{ext})} - f_{2i}^{(\mathrm{ext})})q_j\rangle\} \tag{10}$$

We assume that the total stress tensor τ_{ij} of the composite system is given by the sum of the constraint pressure p maintaining incompressibility, the viscous stress $2\eta_s D_{ij}$ due to the solvent, a mechanical stress $\tau_{ij}^{\mathrm{mech}}$, and, for the MR fluid, the stress τ_{ij}^{mag} due to the magnetic field:

$$\tau_{ij} = -p\delta_{ij} + 2\eta_s D_{ij} + \tau_{ij}^{\mathrm{mech}} + \tau_{ij}^{\mathrm{mag}} \tag{11}$$

The mechanical stress $\tau_{ij}^{\mathrm{mech}}$ consists of contributions from the intraparticle mechanical force f^{int} and the bead motion:

$$\tau_{ij}^{\mathrm{mech}} = \frac{n}{2}\langle q_i f_j^{(\mathrm{int})} + f_i^{(\mathrm{int})} q_j\rangle - nm\sum_{\nu=1}^{2}[\![(\dot{r}_\nu - v)(\dot{r}_\nu - v)]\!] + nkT\delta_{ij} \tag{12}$$

where n is the particle number density, m is the mass of each particle, $\dot{r}_\nu$ denotes the velocity of the bead $(\nu = 1, 2)$, and $\mathbf{v}$ is the velocity of the solvent particle at $\mathbf{x}$. With a Maxwellian velocity distribution, the mechanical stress $\tau_{ij}^{\mathrm{mech}}$ simplifies to

$$\tau_{ij}^{\mathrm{mech}} = \frac{n}{2}\langle q_i f_j^{(\mathrm{int})} + f_i^{(\mathrm{int})} q_j\rangle - nkT\delta_{ij} \tag{13}$$

The magnetic stress τ_{ij}^{mag} is related to magnetic forces in Eq. (3) through

$$\tau_{ij}^{\mathrm{mag}} = \frac{1}{2}n\langle q_i (f_{1j}^{(\mathrm{ext})} - f_{2j}^{(\mathrm{ext})})\rangle \tag{14}$$

To complete the MR fluid model, there remains to specify the dependence of the intraparticle force $\mathbf{f}^{(\mathrm{int})}$ and magnetic force $\mathbf{f}_1^{(\mathrm{ext})} - \mathbf{f}_2^{(\mathrm{ext})} z$ appearing in Eqs. (13) and (14).

We consider the ferrous particles to be deformable and linearly elastic, so that the two beads in the dumbbell idealization of each particle is a linear finite length unstretched spring with spring constant β,

$$f_i^{(\mathrm{int})} = \beta q_i. \tag{15}$$

The expression (13) for mechanical stress $\tau_{ij}^{\mathrm{mech}}$ incorporating the elastic constitutive assumption (15) simplifies to

$$\tau_{ij}^{\mathrm{mech}} = n\beta\langle q_i q_j\rangle - nkT\delta_{ij} \tag{16}$$

We introduce the magnetic force as

$$f_{1j}^{(\mathrm{ext})} - f_{2j}^{(\mathrm{ext})} = \frac{c\dot{\gamma}}{(1+\chi)|\mathbf{H}|}q_j \tag{17}$$

where χ is the magnetic susceptibility of the particle corresponding to magnetic field $\mathbf{H}$ and c is a material constant. Substituting the constitutive equations (15) and (17) into Eqs. (10) and (11) gives

$$\frac{D}{Dt}\langle q_i q_j\rangle = \frac{4kT}{\zeta}\delta_{ij} - \frac{4\beta}{\zeta}\langle q_i q_j\rangle - \frac{c\dot{\gamma}}{\zeta(1+\chi)|\mathbf{H}|}[\langle q_k q_j\rangle + \langle q_i q_k\rangle] \tag{18}$$

$$\tau_{ij} = -p\delta_{ij} + 2\eta_s D_{ij} + n\beta\langle q_i q_j\rangle + \frac{c\dot{\gamma}n}{2(1+\chi)|\mathbf{H}|}\langle q_i q_k\rangle - nkT\delta_{ij} \tag{19}$$

This kinetic theory-based model for MR fluids is now complete. It consists of the evolution equation (18) for the orientation tensor $\langle q_i q_j\rangle$, constitutive equation (19) for Cauchy stress tensor τ_{ij}, and the balance of momentum.

4 Modeling and Experimental Results of MR Fluid-Based Damper

As mentioned earlier, the sponge used in the linear damper for characterization of MR fluid is an open-celled polyurethane foam. The sponge is stretched and then glued to the piston using heat-resistant epoxy. There is a gap of approximately 0.1 mm between the stretched sponge and the inner housing. After attaching the sponge to the piston, the sponge is saturated with one of the aforementioned MR fluids that were developed in the laboratory. The 0.1 mm gap is then filled with MR fluid. The reason for having this gap between the sponge and the housing is to reduce the off-state viscosity/shear stress. A copper coil (350 turns of 24 AWG with 3.2 Ω of resistance) is used that can carry a maximum current of 6 A (during the experimental tests the maximum applied current was kept below 4 A to prevent the coil from heating up).

The shear stress versus shear rate curves are plotted based on $\dot{\gamma} = v/\alpha h$, where v is the velocity of the linear damper, h is the thickness of the open-celled polyurethane sponge saturated with MR fluid sample, and $\alpha \geq 1$ is a coefficient that takes into account the shear strain of the MR fluid sponge and determined to be $\alpha = 1.08$ (Fig. 3).

The velocity v is calculated by filtering the displacement signal using a low-pass filter for displacement and then taking a numerical derivative with respect to time. To find the value of α, several tests were conducted in the absence of magnetic field $(H = 0)$ using the tensile testing machine and a rheometer with and without sponge.

The magnetic field H versus shear stress τ curves are plotted based on the following procedure: Using a dc power supply, the current I is applied to the damper solenoid and the magnetic flux ϕ is calculated by $\phi = I(N/R_T)$, where R_T is the sum of reluctance elements within circuit and N is the number of turns in the solenoid. Then the magnetic induction is given by $B = \phi/A$, where $A = 2(2\pi RL)$. Finally, the magnetic field intensity is calculated by $H = B/\mu$, where μ is the magnetic permeability of MR fluid and is calculated based on Frohlisch–Kennelly law in which the magnetization is calculated by $M = M_s\chi_i H/M_s + \chi_i H$, where $\chi_i = 131$ is the initial susceptibility and $M_s = 1990$ kAmp/m is the saturation magnetization, and the permeability is computed by $\mu = 1 + \chi = 1 + (dM/dH)$.

The measurements in the modeling were produced by experimental tests on a linear MR damper under a tensile testing machine. The tensile testing machine used in this research is a

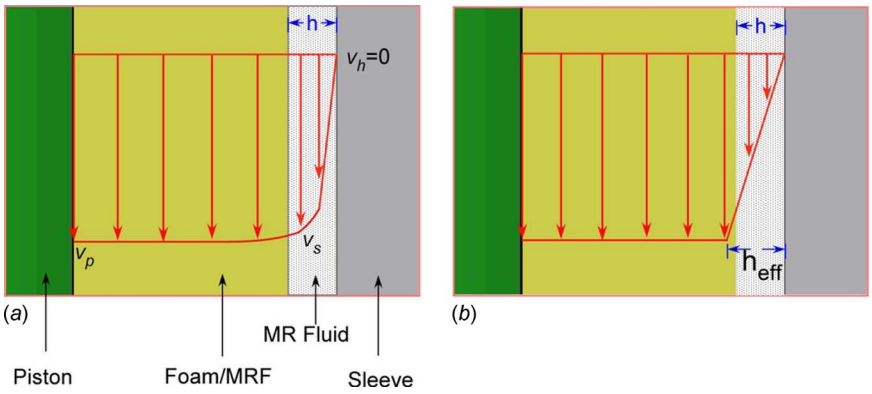

Fig. 3 (*a*) **Hypothesized velocity profile of the MR fluid in the foam and gap;** (*b*) **effective simple shear flow**

MTS® machine, which has three components: SilentFlo™ hydraulic power unit, 858 Table Top System load frame, and a TestStar™ IIs control unit. The input is current to the solenoid, which is controlled. The magnetic field strength H is calculated analytically based on the material and geometry specifications of the damper and solenoid. Also the magnetic field is measured directly using a Gaussmeter. The applied force on the damper is measured by the tensile testing machine and the shear stress is calculated based on the measured force and geometry of the damper and the area wetted by the MR fluid.

To testify how the tensile testing machine test characteristic such as type of reference input, speed, frequency, and amplitude will affect the maximum shear stress of MR fluid samples, four experiments with identical MR fluid sample but different reference inputs and frequencies were performed. The results show that regardless of the shape of the reference input the maximum shear stress is almost the same. Also for smaller amplitudes, the graphs show a more continuous behavior without any sharp point. The high frequency test results in the interference of the dynamics of the tensile testing machine and consequently not well behaved graphs. The very low frequency test, on the other hand, shows a very noisy result. The sinusoidal reference input seems to be the best choice. The yield stress is obtained by extrapolation at zero shear rate.

The MR fluid suitable for a haptic device should have the following characteristics: very low off-state viscosity, large dynamic range, and low particle settlement. The MR fluid sample made of five parts by weight of 4–7 μm carbonyl iron powder to one part of 10 cS silicone oil was determined to be the one most appropriate to be used in the MR fluid-based haptic system in Sec. 5. Figures 4–7 are done on this MR fluid sample.

The experimental tests shown in Fig. 4 were done for an applied current within range 0 A to 4 A. Within the result curves, five are selected for further investigations (I=0 A, 1 A, 2 A, 3 A, and 4 A), which are presented in Fig. 5.

Figure 6 displays the steady state experimental measurements of shear stress versus shear rate in magnetic fields of five different magnitudes; Fig. 7 displays the same measurements as shear stress versus magnetic field. To investigate the accuracy of the 3D models, the 1D form of each model is computed. These models are then compared with experimental results obtained from tensile testing machine test. For this purpose, the shear stress versus shear rate and shear stress versus magnetic field curves were studied. The details are presented in the following section.

5 Reduced 1D Models for Simple Shear

We specialize the 3D theory to the 1D application of steady simple shear in the presence of a transverse magnetic field by inserting the special velocity and magnetic fields

$$\mathbf{V} = \begin{bmatrix} \dot{\gamma} x_2 \\ 0 \\ 0 \end{bmatrix}, \quad \mathbf{H} = \begin{bmatrix} 0 \\ H \\ 0 \end{bmatrix} \tag{20}$$

with $\dot{\gamma}$ and H positive constants. In the steady state, $(\partial/\partial t)\langle q_i q_j \rangle = 0$, $(\partial/\partial x_1)\langle q_i q_j \rangle = 0$, and $(\partial/\partial x_3)\langle q_i q_j \rangle = 0$, and for simplicity we assume the viscous carrier fluid is Newtonian (so that η_s is a constant). From the evolution equation (8), we solve for $\langle q_1 q_2 \rangle$ (i=1 and j=2), substitute the solution into the equation for the total stress tensor (19), and compute the 1D shear stress.

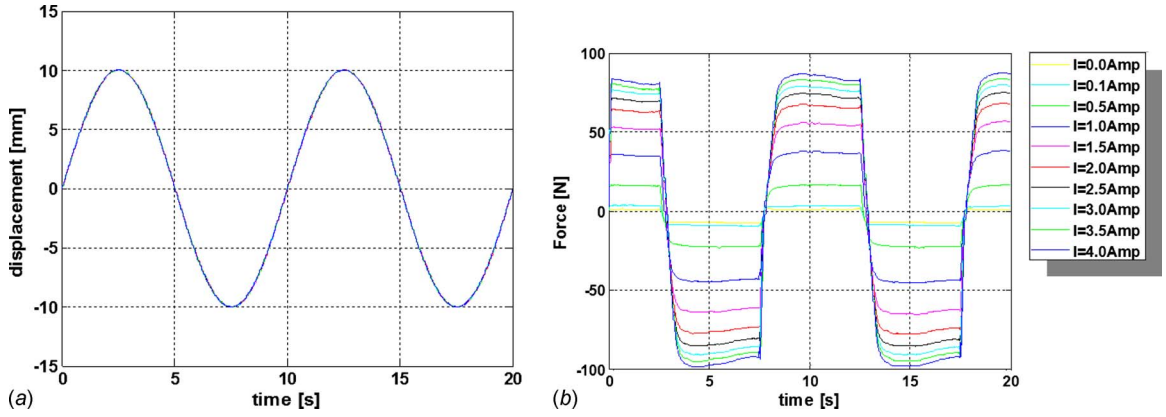

Fig. 4 Tensile testing machine test results for sinusoidal input

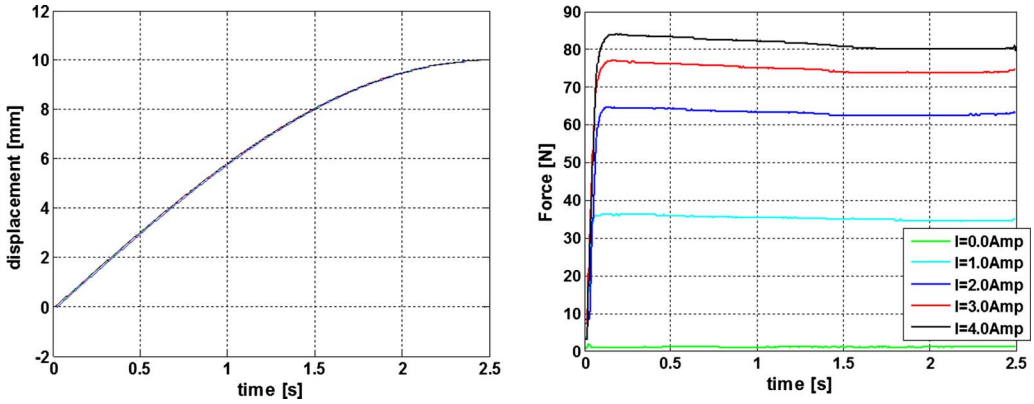

Fig. 5 Tensile test results for a sinusoidal input

$$\tau_{12} = \eta_s \dot{\gamma} + \frac{nkT\zeta\dot{\gamma}}{4\left(\beta + \frac{c\dot{\gamma}}{2(1+\chi)|\mathbf{H}|}\right)} \tag{21}$$

This equation is in proper agreement with the experimental results.

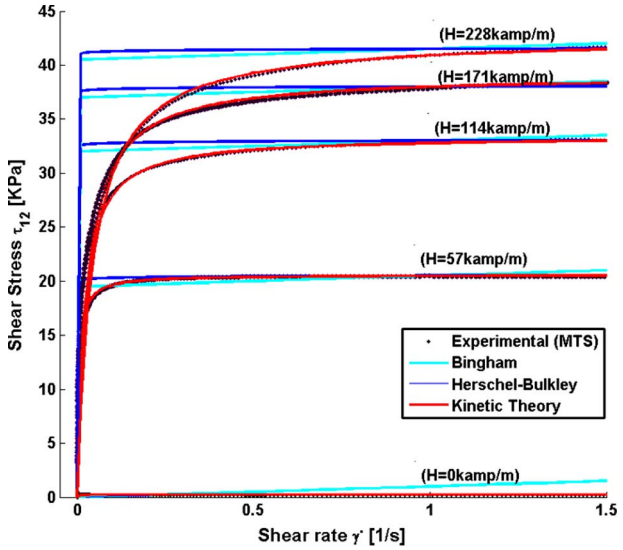

Fig. 6 Experimental measurements tensile testing machine: shear stress as a function of shear rate and magnetic field strength

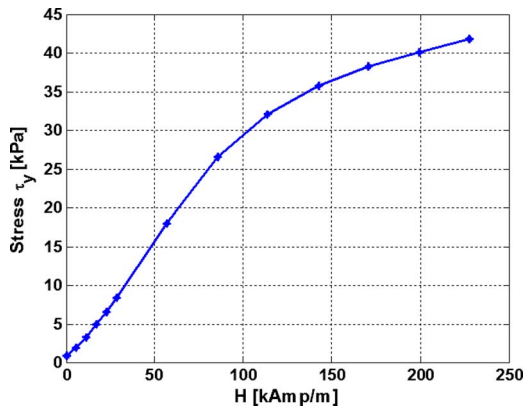

Fig. 7 The same experimental measurements as Fig. 6 but expressed as yield shear stress versus magnetic field

The sum of squared errors (SSE) for Bingham plastic model, Herschel–Buckley model, and our kinetic-based model are presented in Table 2. The SSE is calculated by

$$\sum_{i=1}^{n} ((\tau_{12})_i - (\hat{\tau}_{12})_i)^2 \tag{22}$$

where τ_{12} is the shear stress measured using the MTS machine and $\hat{\tau}_{12}$ is the one predicted by model.

6 Conclusions

Referring to Eq. (3), change of nanostructure in our kinetic theory model is due to four additive effects. These effects are modular in the sense that the model for one effect can be modified without interfering the other effects. Three modules are obtained via straightforward assumptions on the first physical principles. The first principal content of the magnetic force component of the external force module is weak relative to the other modules. In our study, however, we observed that the first-principles content structure in the model as the whole together with the flexibility afforded by the empirical constants in the magnetic term allows for the modeling successes we report, at least in the deformation regime of this paper.

In Fig. 6, the behavior predicted by our expression (21) is plotted against experimental measurements and the predictions of the Bingham plastic and Herschel–Buckley models (1) and (2). We observe that expression (21) replaces the strict yield stress of the Bingham/Herschel–Buckley-type viscoplastic models (i.e., absolutely no flow until the shear stress reaches a specified value) with a steep gradient, which is in better agreement with experimental observation.

Importantly, we emphasize that while we have reduced the general equations (10) and (11) to a 1D form similar to the Bingham plastic model, we now have a clear path for incorporating 3D flow and magnetic field conditions, when velocity and magnetic fields other than those of Eq. (20) are investigated.

We have developed a methodology for deriving generalized 3D tensorial expressions relating forces, flow, and applied magnetic

Table 2 Sum of squared errors

H (kAmp/m)	Sum of squared errors		
	Bingham	Herschel–Buckley	Our kinetic model
0	18	19	6
57	8132	7296	849
114	33273	31331	1069
171	48280	46040	2423
228	51442	49188	1696

field in a MR fluid. We note that in the special case of simple shear the dependence of τ_{12} on **H** presented by Eq. (21) is in agreement with observed behavior.

The new model we have developed has been successfully employed in a couple of novel haptic systems that we have designed and tested [17,19–23]. Our model is superior to the existing models especially at low values of shear rates [18].

References

[1] Rabinow, J., 1948, "The Magnetic Fluid Clutch," Trans. Am. Inst. Electr. Eng., **67**, pp. 1308–1315.

[2] Carlson, J. D., Catanzarite, D. N., and St. Clair, K. A., 1996, "Commercial Magneto-Rheological Fluid Devices," *Proceedings of the Fifth International Conference on ER Fluids, MR Suspensions and Associated Technology*, World Scientifc, Singapore, pp. 20–28.

[3] Jolly, M. R., and Carlson, J. D., 1996, "A Controllable Squeeze Film Damper Using Magnetorheological Fluid," *Proceedings of Actuator 96*, Bremen, Germany, June 26–28, pp. 333–336.

[4] Kamath, G. M., Hurt, M. K., and Wereley, N. M., 1996, "Analysis and Testing of Bingham Plastic in Semi-Active Electrorheological Fluid Dampers," Smart Mater. Struct., **5**, pp. 576–590.

[5] Kamath, G. M., Wereley, N. M., and Jolly, M. R., 1996, "Analysis and Testing of a Model-Scale Magnetorheological Fluid Helicopter Lag Mode Damper," J. Am. Helicopter Soc., **44**, pp. 234–248.

[6] Spencer, B. F., Yang, G., Carlson, J. D., and Sain, M. K., 1998, "Smart Dampers for Seismic Protection of Structures: A Full-Scale Study," *Proceedings of the Second World Conference on Structural Control (2WCSC)*, Kyoto, Japan, June 28–July 1, pp. 417–426.

[7] Yang, G., 2001, "Large-Scale Magnetorheological Fluid Damper for Vibration Mitigation: Modeling, Testing and Control," University of Notre Dame.

[8] Yang, G., Jung, H. J., and Spencer, J. B. F., 2001, "Dynamic Modeling of Full-Scale MR Dampers for Civil Engineering Applications," *Proceedings of the US-Japan Workshop on Smart Structures for Improved Seismic Performance in Urban Region*, Seattle, WA, Aug. 14–16.

[9] Bansbach, E. E., 1998, "Torque Transfer Apparatus Using Magnetorheological Fluids."

[10] Gopalswamy, S., and Jones, G. L., 1998, "Magnetorheological Transmission Clutch."

[11] Kavlicoglu, B., Gordaninejad, F., Evrensel, C. A., Cobanoglu, N., Xin, M., Heine, C., Fuchs, A., and Korol, G., 2002, "A High-Torque Magneto-Rheological Fluid Clutch," *Proceedings of the SPIE Conference on Smart Materials and Structures*, San Diego, Nov. 14.

[12] Lampe, D., and Grundmann, R., 2000, "Transitional and Solid State Behavior of a Magnetorheological Clutch," *Proceedings of the Seventh International Conference on New Actuators*, Bremen, Germany, June 19–21.

[13] Lampe, D., Thess, A., and Dotzauer, C., 1998, "MRF-Clutch: Design Considerations and Performance," *Proceedings of the Sixth International Conference on New Actuators*, Bremen, Germany, June 17–19.

[14] Carlson, J. D., 2001, "Magnetorheological Brake With Integrated Flywheel."

[15] Doell, C., 2001, "Drive-By-Wire Technology," *Proceedings of the Vehicle Technologies Symposium: Intelligent Systems for the Objective Fleet*, May 29–31, sponsored by NDIA.

[16] Bajcinca, N., CortesZo, R., Hauschild, M., Bals, J., and Hirzinger, G., 2003, "Haptic Control for Steer-by-Wire Systems," *Proceedings of the 2003 IEEE/RSJ International Conference on Intelligent Robots and Systems*, Las Vegas, NV, Oct. 27–31.

[17] Ahmadkhanlou, F., Washington, G., Bechtel, S., and Wang, Y., 2006, "Magnetorheological Fluid Based Automotive Steer-By-Wire Systems," *Proceedings of the 13th SPIE International Symposium*, San Diego, CA, Feb. 26–Mar. 2.

[18] Ahmadkhanlou, F., Wang, Y., Bechtel, S. E., and Washington, G. N., "An Improved Model For Magnetorheological Fluid-Based Actuators and Sensors," Int. J. Eng. Sci., submitted.

[19] Ahmadkhanlou, F., Washington, G., and Bechtel, S., 2008, "The Development of a Five DOF Magnetorheological Fluid-Based Telerobotic Haptic System," *Proceedings of the 15th SPIE International Symposium*, San Diego, CA, Mar. 9–13.

[20] Ahmadkhanlou, F., Washington, G. N., and Bechtel, S., 2008, "Modeling and Control of Single and Two Degree of Freedom Magnetorheological Fluid-Based Haptic Systems for Telerobotic Surgery," J. Intell. Mater. Syst. Struct., accepted.

[21] Ahmadkhanlou, F., Washington, G. N., Wang, Y., and Bechtel, S. E., 2005, "The Development of Variably Compliant Haptic Systems Using Magnetorheological Fluids," *Proceedings of the 12th SPIE International Symposium*, San Diego, CA, Mar. 6–10.

[22] Ahmadkhanlou, F., Zite, J. L., Neelakantan, V. A., and Washington, G. N., 2006, "A Magnetorheological Fluid Based Orthopaedic Active Knee Brace," *Proceedings of the 13th SPIE International Symposium*, San Diego, CA.

[23] Ahmadkhanlou, F., Zite, J. L., and Washington, G. N., 2007, "A Magnetorheological Fluid Based Controllable Active Knee Brace," *Proceedings of the 14th SPIE International Symposium*, San Diego, CA, Dec. 10.

[24] Bingham, E. C., 1922, *Fluidity and Plasticity*, McGraw-Hill, New York.

[25] Genç, S., 2002, "Synthesis and Properties of Magnetorheological (MR) Fluids," University of Pittsburgh.

[26] Genç, S., and Phule, P., 2002, "Rheological Properties of Magnetorheological Fluids," Smart Mater. Struct., **11**, pp. 140–146.

[27] Herschel, W. H., and Bulkley, R., 1926, "Model for Time Dependent Behavior of Fluids," *Proceedings of the American Society of Testing Materials*, Philadelphia, Vol. 26, p. 621.

[28] Promislow, J. H. E., and Gast, A. P., 1997, "Low-Energy Suspension Structure of a Magnetorheological Fluid," Phys. Rev. E, **56**, pp. 642–651.

[29] Bechtel, S., Washington, G., Ahmadkhanlou, F., and Wang, Y., 2004, "Microstructural Analysis and Control of Magnetorheological Fluid," ASME International Mechanical Engineering Congress and Exposition, Anaheim, CA, Nov. 13–19, pp. 509–518.

[30] Carlson, J. D., 2001, "What Makes a Good MR Fluid?," *Proceedings of the Eighth International Conference on Electrorheological (ER) Fluids and Magneto-Rheological (MR) Suspensions*, Nice, France, July 9–13, pp. 63–69.

[31] Neelakantan, V. A., Washington, G. N., and Wolfe, R., 2002, "Force Feedback System Using Magneto Rheological Fluids for Telerobotic Surgery," *Proceedings of the SPIE International Conference on Smart Structures and Materials: Industrial and Commercial Applications of Smart Materials*, San Diego, CA, Nov. 14.

[32] Neelakantan, V. A., 2003, "Modeling, Design, Testing, Control and Applications of Magnetorheological Fluid Devices," Ohio State University.

A Three-Equation Eddy-Viscosity Model for Reynolds-Averaged Navier–Stokes Simulations of Transitional Flow

D. Keith Walters
Department of Mechanical Engineering,
Mississippi State University,
HPC2 SimCenter,
P.O. Box ME,
Mississippi State, MS 39762
e-mail: walters@me.msstate.edu

Davor Cokljat
Ansys, Inc.,
Fluent Europe Ltd.,
Sheffield Business Park,
6 Europa View,
Sheffield S9 1XH, UK
e-mail: davor.cokljat@ansys.com

An eddy-viscosity turbulence model employing three additional transport equations is presented and applied to a number of transitional flow test cases. The model is based on the k-ω framework and represents a substantial refinement to a transition-sensitive model that has been previously documented in the open literature. The third transport equation is included to predict the magnitude of low-frequency velocity fluctuations in the pretransitional boundary layer that have been identified as the precursors to transition. The closure of model terms is based on a phenomenological (i.e., physics-based) rather than a purely empirical approach and the rationale for the forms of these terms is discussed. The model has been implemented into a commercial computational fluid dynamics code and applied to a number of relevant test cases, including flat plate boundary layers with and without applied pressure gradients, as well as a variety of airfoil test cases with different geometries, Reynolds numbers, freestream turbulence conditions, and angles of attack. The test cases demonstrate the ability of the model to successfully reproduce transitional flow behavior with a reasonable degree of accuracy, particularly in comparison with commonly used models that exhibit no capability of predicting laminar-to-turbulent boundary layer development. While it is impossible to resolve all of the complex features of transitional and turbulent flows with a relatively simple Reynolds-averaged modeling approach, the results shown here demonstrate that the new model can provide a useful and practical tool for engineers addressing the simulation and prediction of transitional flow behavior in fluid systems. [DOI: 10.1115/1.2979230]

Introduction

The ability to accurately predict transitional fluid flow behavior is important to the design of engineering systems in a wide variety of applications including aerospace, automotive, biomedical, heating and cooling, power generation, marine systems, and chemical processing. Methods for addressing boundary layer transition in computational fluid dynamics (CFD) simulations can range from highly empirical approaches based on "engineering insight"—for example, selecting an appropriate transition location and applying a turbulence model only downstream of this location—to direct numerical simulation (DNS) [1]. From a design standpoint, Reynolds-averaged Navier–Stokes (RANS)-based CFD represents a reasonable compromise between accuracy and expense, and a number of researchers have developed prediction methodologies for boundary layer transition. The simplest RANS-based approach is unmodified low Reynolds number eddy-viscosity turbulence models, which have been used for prediction of transitional flows with some degree of success [2–5]. A critical examination of several such model forms recently suggested that their ability to simulate transition is, in fact, an accidental artifact of the models rather than a reflection of any true predictive capability [6], but they remain useful options, especially for "engineering" simulations of transitional flow.

More recent research efforts for RANS-based CFD have focused on models specifically developed to predict transitional behavior. Two common approaches are the coupling of fully turbulent models with empirical transition correlations and the addition of transport equations to the turbulence model equations in order to include the effects of transitional flow. The former adopts appropriate correlations based on available experimental databases from relatively simple geometries and flow conditions. Several well-known correlations for transition initiation prediction have been employed [7–10], and new versions are yet being developed [11]. The empirical correlation is coupled with the turbulence model either by assuming "instantaneous transition" at the predicted onset location [11] or by incorporating some form of transition zone into the simulation, usually based on the universal intermittency profile of Dhawan and Narasimha [12]. This approach presents some difficulty in implementation, particularly for complex 3D geometries. In general, the correlations are based on downstream distance (x) or boundary layer momentum thickness (θ), and the determination of either requires the use of nonlocal or integral quantities in the simulation, in contrast to single-point models typically used for fully turbulent flows. The development of techniques for calculating such nonlocal quantities is a current area of research effort [13,14], but the use of these methods remains problematic for complex three-dimensional geometries.

The more general approaches make use of additional transport equations and/or model terms in order to include the effects of transition on the flowfield prediction. Examples include either phenomenological models [15–17] or correlation-based models [18–20]. Within each category, most models still require nonlocal or integral information to be included in the model terms, making them less easily incorporated into general-purpose CFD codes. Several recent efforts have focused on the use of single-point models, including the phenomenological model of Wang and Perot [16], the phenomenological model of Walters and Leylek [17] that is currently used in the commercial CFD code FLUENT (Ansys, Inc., Canonsburg, PA), and the correlation-based model of Menter et al. [20] that is currently used in the commercial code

Contributed by the Fluids Engineering Division of ASME for publication in the JOURNAL OF FLUIDS ENGINEERING. Manuscript received November 16, 2007; final manuscript received July 24, 2008; published online October 24, 2008. Assoc. Editor Paul Durbin.

CFX (Ansys, Inc., Canonsburg, PA)Single-point modeling represents the most versatile and easily implemented approach for the CFD prediction of laminar, transitional, and turbulent flow. To date, the proposed models have used modified forms of a two-equation eddy-viscosity model coupled with additional transport equations. These include equations for turbulence potential terms [16], intermittency and transition Reynolds number terms [20], or laminar kinetic energy to represent the pretransitional fluctuations in laminar attached or separated boundary layers [17]. Each of these different approaches shares the same goal: to provide CFD end users with a relatively simple, single-point, RANS-based model for prediction of laminar-to-turbulent transition that is accurate, efficient, and robust. It remains unlikely that any one of these approaches will become a "magic bullet" for predicting transition, but their availability provides designers and applications engineers with useful new tools for analysis of complex flow systems.

One of the primary difficulties with implementing phenomenological modeling approaches—and one reason they are less prevalent than empirical models—is that the physics of transition is still not entirely understood and indeed is an active area of research in itself. Because of this, some authors have argued that correlation-based models are more appropriate candidates for consistent RANS-based transition prediction than their physics-based counterparts [21]. However, recent analytical, numerical, and experimental investigations have helped to highlight some of the relevant underlying physical mechanisms as well as the universal characteristics of boundary layer flows, both transitional and turbulent. Knowledge of the relevant scaling mechanisms may allow reasonably accurate model forms without recourse to a purely empirical-based approach.

The current work presents a new version of a single-point model that was previously developed based on the universal physics of transitional and turbulent flows [17]. Subsequent studies have demonstrated the ability of the model to resolve transition in a number of complex flows [22–24]. However, the model was shown to be less successful in predicting some complex flow conditions [25] and for attached boundary layer transition to display a nonphysical sensitivity to freestream turbulence length scale [26]. The physical basis of the modeling approach is extended in the current work to substantially improve the accuracy for a wide array of demonstration test cases.

New Model Development and Implementation

Background. The new model presented here follows the conceptual description first proposed by Walters and Leylek [17]. The model addresses laminar, transitional, and fully turbulent flows entirely within the framework of Reynolds averaging, in which the influence of unsteady velocity fluctuations on the mean flow is represented by the appearance of Reynolds stress terms in the time-averaged governing equations. The Reynolds stress is typically interpreted as the "turbulent stress," although it is important to note that the Reynolds stress arises as a consequence of the averaging process and is nonzero for any time varying velocity field, even if velocity fluctuations are not due to "turbulence" in the strict sense. In theory, transitional as well as turbulent fluctuations may be modeled through the Reynolds stress tensor, a point recently stressed by Wang and Perot [16]. Steady laminar flow is effectively "modeled" when the Reynolds stress components are assigned values that are negligibly small.

The simplest RANS models assume a linear relationship between the Reynolds stresses and the strain rate tensor, the so-called Boussinesq hypothesis:

$$\overline{\rho u_i u_j} - \frac{1}{3}\overline{\rho u_k u_k}\delta_{ij} = -2\mu_T S_{ij} \tag{1}$$

where μ_T is the turbulent, or eddy, viscosity. Currently, this is the most common method of RANS-based CFD. The primary advantage is its simplicity, but a major challenge lies in the fact that all of the relevant effects of the fluctuating velocity field must be modeled by a single parameter—the eddy-viscosity. For the new model presented here, this includes the physics of laminar-to-turbulent transition.

For so-called two-equation models, two additional transport equations are solved to obtain the turbulence quantities used to compute the eddy-viscosity. For example, a k-ω model form, which forms the basis for the present work, solves equations for the turbulent kinetic energy k and for the inverse time-scale ω (also interpreted as the specific dissipation rate). In the current work, an additional transport equation is included in order to represent pretransitional (i.e., nonturbulent) velocity fluctuations, and this concept is discussed in more details below.

Transition-Sensitive Modeling Concept. The pretransitional boundary layer is effectively laminar in terms of the mean velocity profile. For freestream turbulence intensities less than about 1%, the development of low amplitude pretransitional velocity fluctuations is dominated by self-sustained instability mechanisms, most famously Tollmien–Schlichting waves [27]. As freestream turbulence intensity (Tu_∞) increases, the mean velocity in the pretransitional boundary layer becomes noticeably distorted from the typical Blasius profile, with an increase in momentum in the inner region and a decrease in the outer, even for Tu_∞ as low as about 1% [28]. This shift in mean velocity profile is accompanied by the development of relatively high-amplitude streamwise fluctuations, which can reach intensities several times the freestream level [29]. This process results in an augmentation of skin friction and heat transfer in the pretransitional region, and eventually leads to transition through the breakdown of the streamwise fluctuations. This process is known as bypass transition. The pretransitional fluctuations leading to bypass transition are due to the presence of low-frequency/low amplitude streamwise vortices in the boundary layer, and appear as "streaky structures" in flow visualizations, direct numerical simulations [30], and large-eddy simulations [31].

It is important to note that these streamwise fluctuations represent Klebanoff modes [29] and are not turbulence in the usual sense of that word. This distinction was made for modeling purposes by Mayle and Schulz [32], who developed the laminar kinetic energy concept to describe the development of pretransitional fluctuations leading to bypass transition. They proposed the adoption of a second kinetic energy equation to govern these fluctuations, and this approach was used in Ref. 17. Other authors have adopted a similar modeling approach for the pretransitional region [33,34]. Following Ref. 32, the energy of the fluctuations is referred to here as laminar kinetic energy k_L.

The dynamics of laminar kinetic energy production are not entirely understood at present, but a number of researchers have shed light on the subject. Two aspects are critical: selectivity of the boundary layer to certain freestream eddy scales and amplification of low-frequency disturbances in the boundary layer by the mean shear. The growth of k_L has been shown experimentally [35] and analytically [36] to correlate with low-frequency normal (v') fluctuations of the freestream turbulence. This selectivity of the boundary layer was also demonstrated by Johnson and Ercan [37], who compared the amplification of six different frequency bands in a pretransitional boundary layer. Because of this selectivity, the frequency content of k_L has been found to be relatively independent of the forcing spectrum, provided that the forcing is broadband [30,38]. The dynamics of k_L growth have been found to be quite universal. Energy grows linearly with Re_x for flat plate boundary layers, where the linearity constant depends on the level of freestream turbulence [28,39]. These observations suggest that a modeling approach based on appropriate scaling parameters may be capable of representing the fluctuation growth of Klebanoff modes in the pretransitional region.

The original model of Mayle and Schulz [32] proposed that the

growth of laminar kinetic energy was due to the transport of energy from the freestream into the boundary layer due to the pressure diffusion term in the kinetic energy budget. The model form adopted in Ref. 17 used an alternative description in which production of k_L is assumed to be due to the interaction of the Reynolds stresses associated with pretransitional (i.e., nonturbulent) velocity fluctuations and the mean shear. The change induced in the mean velocity profile by the presence of pretransitional fluctuations represents a loss of mean flow kinetic energy, suggesting that the more traditional strain-based production mechanism is appropriate. Recent large-eddy simulations of the transitional boundary layer [31] appear to confirm that this description of k_L production is more physically correct than the transport based description.

The transition process itself is represented in the new model by a transfer of energy from the laminar kinetic energy k_L to the turbulent kinetic energy k_T. Conceptually, the variable k_T is assumed to represent the magnitude of fluctuations that display the characteristics of fully turbulent flow, such as strong three-dimensionality, multiple length and time-scales, energy cascading, and significant viscous dissipation. The initiation of the transition process in the model is based on local (single-point) flow conditions. In contrast to Ref. 17, the new model presented here adopts an approach for transition initiation based on the concept of shear-sheltering and consideration of relevant time-scales for nonlinear disturbance amplification and dissipation. It is expected that this modification will yield more accurate prediction of the effect of freestream turbulence length scale on the transition process.

"Shear-sheltering" refers to the damping of turbulence dynamics that occurs in thin regions of high vorticity [40]. Its effect is to inhibit nonlinear turbulence breakdown mechanisms. This occurs, for example, in the pretransitional boundary layer. Once transition initiates, the effects of shear-sheltering are restricted to the viscous sublayer in the turbulent boundary layer. It is proposed here that in a Reynolds-averaged sense, transition may be interpreted as a growth of the pressure-strain terms in the Reynolds stress equations. The rapid and slow pressure-strain terms tend to return the fluctuations to isotropy and represent the growth in strength of three-dimensional turbulence fluctuations during the transition process, and a corresponding reduction in magnitude of the more highly anisotropic Klebanoff modes. In the model presented here, this action of the pressure-strain terms is represented as an energy transfer from the laminar kinetic energy, which models the Klebanoff modes, to the turbulent kinetic energy, which models the highly three-dimensional fluctuations of fully turbulent flow. Since the total fluctuation energy in the model is comprised of the sum of k_L and k_T, the transfer of energy from one to another is appropriately interpreted as energy redistribution (via the pressure-strain mechanism) rather than production (due to interaction with the mean flow) or dissipation (due to viscous mechanisms).

In the new model, shear-sheltering is incorporated through a production damping term, while transition initiation is included through transfer terms in the k_L and k_T equations. It is proposed that the relevant dimensionless quantity responsible for transition inception is the ratio between the turbulent production time-scale and the molecular diffusion time-scale. Conceptually, entrained disturbances in the developing boundary layer undergo nonlinear breakdown and amplification when the time-scale associated with turbulence production dynamics is sufficiently short relative to the time-scale associated with molecular diffusion. The onset of transition is therefore assumed to occur when the time-scale ratio reaches a critical value. Similarly, the viscous sublayer in a turbulent boundary layer suppresses turbulence production in part because the time-scale ratio is below the critical value for disturbance amplification. This conceptual description of bypass transition was also proposed by Praisner and Clark [11], who used it to develop an empirical correlation for transition start location. In the current study, this analysis is extended to include natural transition, by assuming that disturbances associated with Tollmien–Schlichting waves are characterized by a time-scale proportional to the inverse of the vorticity within the pretransitional boundary layer. The natural transition criterion is therefore a function of the ratio of the Tollmien–Schlichting time-scale to the molecular diffusion time-scale. These two dimensionless parameters are used to develop the transition-sensitive damping functions for the turbulence production term in the model equations.

Downstream of either bypass or natural transition, the model should correctly predict a fully turbulent boundary layer. In this region, the production damping functions discussed above assume a value of unity, except within the viscous sublayer. The viscous and inviscid wall effects on the eddy-viscosity are included through turbulent damping functions with similar form to other commonly used two-equation models. A complete presentation of the model equations is given in the following subsection.

Model Equations. This section summarizes the governing equations for the new model. For simplicity, we focus on incompressible single-phase flow with no body forces, governed by the steady Reynolds-averaged continuity and momentum equations, and a linear eddy-viscosity model is adopted for the Reynolds stresses (Eq. (1)).

Three additional model transport equations are solved for the turbulent kinetic energy (k_T), the laminar kinetic energy (k_L), and the scale-determining variable (ω), defined here as $\omega=\varepsilon/k_T$, where ε is the isotropic dissipation. The transport equations are

$$\frac{Dk_T}{Dt} = P_{k_T} + R_{\mathrm{BP}} + R_{\mathrm{NAT}} - \omega k_T - D_T + \frac{\partial}{\partial x_j}\left[\left(\nu + \frac{\alpha_T}{\sigma_k}\right)\frac{\partial k_T}{\partial x_j}\right] \quad (2)$$

$$\frac{Dk_L}{Dt} = P_{k_L} - R_{\mathrm{BP}} - R_{\mathrm{NAT}} - D_L + \frac{\partial}{\partial x_j}\left[\nu\frac{\partial k_L}{\partial x_j}\right] \quad (3)$$

$$\frac{D\omega}{Dt} = C_{\omega 1}\frac{\omega}{k_T}P_{k_T} + \left(\frac{C_{\omega R}}{f_W} - 1\right)\frac{\omega}{k_T}(R_{\mathrm{BP}} + R_{\mathrm{NAT}}) - C_{\omega 2}\omega^2 + C_{\omega 3}f_\omega \alpha_T f_W^2 \frac{\sqrt{k_T}}{d^3} + \frac{\partial}{\partial x_j}\left[\left(\nu + \frac{\alpha_T}{\sigma_\omega}\right)\frac{\partial \omega}{\partial x_j}\right] \quad (4)$$

The various terms in the model equations represent production, destruction, and transport mechanisms. Note that the new model uses inverse turbulent time-scale (ω) rather than the dissipation rate (ε), in contrast to the original version of Walters and Leylek [17]. It has been noted previously that this form yields improved accuracy in the transition region [22]. In the ω equation, the fully turbulent production, destruction, and gradient transport terms (first, third, and fifth terms on the right-hand side of Eq. (4)) are analogous to the similar terms in the k_T and k_L equations and are similar to terms that appear in other k-ω model forms. The transition production term (second term on right-hand side) is intended to produce a reduction in turbulence length scale during the transition breakdown process. A similar term was included in the ε equation of the original model [17]. The fourth term on the right-hand side was included in order to decrease the length scale in the outer region of the turbulent boundary layer, which is necessary to ensure correct prediction of the boundary layer wake region [22].

The total fluctuation kinetic energy is $k_{\mathrm{TOT}}=k_T+k_L$. The production of turbulent and laminar kinetic energy by mean strain is modeled as:

$$P_{k_T} = \nu_{T,s}S^2 \quad (5)$$

$$P_{k_L} = \nu_{T,\mathrm{l}}S^2 \quad (6)$$

The "small-scale" eddy-viscosity concept follows Ref. 17, and is defined as

$$\nu_{T,s} = f_w f_{\mathrm{INT}} C_\mu \sqrt{k_{T,s}} \lambda_{\mathrm{eff}} \tag{7}$$

where $k_{T,s}$ is the effective small-scale turbulence.

$$k_{T,s} = f_{\mathrm{SS}} f_W k_T \tag{8}$$

The kinematic wall effect is included through an effective (wall-limited) turbulence length scale λ_{eff} and damping function f_W [17].

$$\lambda_{\mathrm{eff}} = \min(C_\lambda d, \lambda_T) \tag{9}$$

$$\lambda_T = \frac{\sqrt{k_T}}{\omega} \tag{10}$$

$$f_W = \left(\frac{\lambda_{\mathrm{eff}}}{\lambda_T}\right) \tag{11}$$

The viscous wall effect is incorporated through the viscous damping function, which is computed in terms of the effective turbulence Reynolds number.

$$f_\nu = 1 - \exp\left(-\frac{\sqrt{\mathrm{Re}_T}}{A_\nu}\right) \tag{12}$$

$$\mathrm{Re}_T = \frac{f_W^2 k_T}{\nu\omega} \tag{13}$$

The shear-sheltering effect discussed in the previous subsection is included in the damping function f_{SS}.

$$f_{\mathrm{SS}} = \exp\left[-\left(\frac{C_{\mathrm{SS}}\nu\Omega}{k_T}\right)^2\right] \tag{14}$$

The turbulent viscosity coefficient C_μ is defined to satisfy the realizability constraint following Shih et al. [41]:

$$C_\mu = \frac{1}{A_0 + A_s\left(\frac{S}{\omega}\right)} \tag{15}$$

The effect of intermittency on the turbulence production is included through an empirical intermittency damping function.

$$f_{\mathrm{INT}} = \min\left(\frac{k_L}{C_{\mathrm{INT}} k_{\mathrm{TOT}}}, 1\right) \tag{16}$$

The production of laminar kinetic energy (k_L) is assumed to be governed by the large-scale near-wall turbulent fluctuations [17], based on the correlation of pretransitional fluctuation growth with freestream low-frequency wall-normal turbulent fluctuations [35,36]. The large-scale turbulence contribution is

$$k_{T,\mathrm{l}} = k_T - k_{T,s} \tag{17}$$

where the small-scale contribution is defined by Eq. (8). The production term is

$$P_{k_L} = \nu_{T,\mathrm{l}} S^2 \tag{18}$$

where

$$\nu_{T,\mathrm{l}} = \min\left\{ f_{\tau,\mathrm{l}} C_{\mathrm{l}1}\left(\frac{\Omega\lambda_{\mathrm{eff}}^2}{\nu}\right)\sqrt{k_{T,\mathrm{l}}}\lambda_{\mathrm{eff}} + \beta_{\mathrm{TS}} C_{\mathrm{l}2}\,\mathrm{Re}_\Omega\, d^2\Omega, \frac{0.5\cdot(k_L + k_{T,\mathrm{l}})}{S}\right\} \tag{19}$$

The limit is applied to ensure satisfaction of the realizability constraint for the total Reynolds stress contribution. The production term is comprised of two parts—the first addresses the development of Klebanoff modes and the second addresses self-excited (i.e., natural) modes. This term is identical to the form proposed in Ref. [17], with

$$\mathrm{Re}_\Omega = \frac{d^2\Omega}{\nu} \tag{20}$$

$$\beta_{\mathrm{TS}} = 1 - \exp\left(-\frac{\max(\mathrm{Re}_\Omega - C_{\mathrm{TS,crit}}, 0)^2}{A_{\mathrm{TS}}}\right) \tag{21}$$

$$f_{\tau,\mathrm{l}} = 1 - \exp\left[-C_{\tau,\mathrm{l}}\frac{k_{T,\mathrm{l}}}{\lambda_{\mathrm{eff}}^2\Omega^2}\right] \tag{22}$$

The anisotropic (near-wall) dissipation terms for k_T and k_L take a common form.

$$D_T = \nu\frac{\partial\sqrt{k_T}}{\partial x_j}\frac{\partial\sqrt{k_T}}{\partial x_j} \tag{23}$$

$$D_L = \nu\frac{\partial\sqrt{k_L}}{\partial x_j}\frac{\partial\sqrt{k_L}}{\partial x_j} \tag{24}$$

The turbulent transport terms in the k_T and ω equations include an effective diffusivity α_T defined as

$$\alpha_T = f_\nu C_{\mu,\mathrm{std}}\sqrt{k_{T,s}}\lambda_{\mathrm{eff}} \tag{25}$$

The boundary layer production term (intended to reproduce proper behavior of the boundary layer wake region) includes a kinematic damping function of the form

$$f_\omega = 1 - \exp\left[-0.41 * \left(\frac{\lambda_{\mathrm{eff}}}{\lambda_T}\right)^4\right] \tag{26}$$

The remaining terms in the transport equations are related to the laminar-to-turbulent transition mechanism in the model. As mentioned above, transition occurs as a transfer of energy from k_L to k_T, with a concurrent reduction in turbulence length scale from the freestream value to the value found in an equilibrium turbulent boundary layer. The model terms R_{BP} and R_{NAT} appear with opposite signs in the k_T and k_L equations and represent bypass and natural transition, respectively. The model forms are

$$R_{\mathrm{BP}} = C_R\beta_{\mathrm{BP}}k_L\omega/f_W \tag{27}$$

$$R_{\mathrm{NAT}} = C_{R,\mathrm{NAT}}\beta_{\mathrm{NAT}}k_L\Omega \tag{28}$$

Transition initiation is governed by the threshold functions β_{BP} and β_{NAT}. As discussed in the previous section, transition in both cases is assumed to initiate when the characteristic time-scale for turbulence production is smaller than the viscous diffusion time-scale of the pretransitional fluctuations. The forms used are

$$\beta_{\mathrm{BP}} = 1 - \exp\left(-\frac{\phi_{\mathrm{BP}}}{A_{\mathrm{BP}}}\right) \tag{29}$$

$$\phi_{\mathrm{BP}} = \max\left[\left(\frac{k_T}{\nu\Omega} - C_{\mathrm{BP,crit}}\right), 0\right] \tag{30}$$

$$\beta_{\mathrm{NAT}} = 1 - \exp\left(-\frac{\phi_{\mathrm{NAT}}}{A_{\mathrm{NAT}}}\right) \tag{31}$$

$$\phi_{\mathrm{NAT}} = \max[(\mathrm{Re}_\Omega - C_{\mathrm{NAT,crit}}/f_{\mathrm{NAT,crit}}), 0] \tag{32}$$

$$f_{\mathrm{NAT,crit}} = 1 - \exp\left(-C_{\mathrm{NC}}\frac{\sqrt{k_L}d}{\nu}\right) \tag{33}$$

Note that the function $f_{\mathrm{NAT,crit}}$ is included so that the amplitude of the pretransitional fluctuations influences the initiation of natural transition in an appropriate manner.

The turbulent viscosity used in the momentum equations is the sum of the small-scale and large-scale contributions defined above.

Table 1 Summary of model constants

A_0=4.04	C_{INT}=0.75	$C_{\omega 1}$=0.44
A_s=2.12	$C_{\mathrm{TS,crit}}$=1000	$C_{\omega 2}$=0.92
A_ν=6.75	$C_{R,\mathrm{NAT}}$=0.02	$C_{\omega 3}$=0.3
A_{BP}=0.6	C_{l1}=3.4*10^{-6}	$C_{\omega R}$=1.5
A_{NAT}=200	C_{l2}=1.0*10^{-10}	C_λ=2.495
A_{TS}=200	C_R=0.12	$C_{\mu,\mathrm{std}}$=0.09
$C_{\mathrm{BP,crit}}$=1.2	$C_{\alpha,\theta}$=0.035	Pr_θ=0.85
C_{NC}=0.1	C_{SS}=1.5	σ_k=1
$C_{\mathrm{NAT,crit}}$=1250	$C_{\tau,\mathrm{l}}$=4360	σ_ω=1.17

$$\nu_T = \nu_{T,s} + \nu_{T,\mathrm{l}} \tag{34}$$

When including heat transfer effects, the turbulent heat flux vector can be modeled using a turbulent thermal diffusivity α_θ.

$$-\overline{u_i T} = \alpha_\theta \frac{\partial T}{\partial x_i} \tag{35}$$

$$\alpha_\theta = f_W\left(\frac{k_T}{k_{\mathrm{TOT}}}\right)\frac{\nu_{T,s}}{\mathrm{Pr}_\theta} + (1-f_W)C_{\alpha,\theta}\sqrt{k_T}\lambda_{\mathrm{eff}} \tag{36}$$

Model constants are listed in Table 1.

Boundary Conditions. The boundary conditions for the three-equation model are similar to those for more commonly used k-ε and k-ω models. At solid boundaries, the no-slip condition enforces

$$k_T = k_L = 0 \tag{37}$$

A zero-normal-gradient condition is used for ω:

$$\frac{\partial \omega}{\partial \eta} = 0 \tag{38}$$

where η is the wall-normal coordinate direction. Note that the wall boundary condition (Eq. (38)) is substantially different from that commonly used in other k-ω model forms. The reason for this is that, in most other models, the value of ω must increase in the viscous sublayer to model the increased level of dissipation near the wall and to ensure asymptotically correct behavior of the model in the near-wall region. The current model adopts an alternative approach similar to many low-Re k-ε models, in which the increased viscous dissipation in the sublayer is incorporated into the k_L and k_T equations through a viscous wall destruction term (Eqs. (23) and (24)). The product ωk_T therefore represents a scalar isotropic dissipation [22], which approaches zero with $\mathrm{O}(\eta^2)$ as the wall distance approaches zero. Viscous destruction in the k_T and k_L equations near the wall is therefore dominated by the wall destruction terms. This behavior has been verified by testing an alternative Dirichlet wall boundary condition (ω=0). Interestingly, this alternative boundary condition was found to yield almost identical results as the zero-flux condition in Eq. (38).

At flow inlets, the values of k_T and ω are prescribed exactly analogous to other two-equation models. The turbulent kinetic energy is often determined based on the inlet turbulence intensity Tu_∞, assuming isotropic freestream turbulence:

$$\mathrm{Tu}_\infty = \frac{\sqrt{\frac{2}{3}k_T}}{U_\infty} \tag{39}$$

The value of the specific dissipation is chosen to coincide with the available freestream information. For example, if the turbulent length scale or the decay rate is known, ω may be chosen to reproduce the appropriate freestream conditions.

For velocity inlets sufficiently far from solid walls, the inlet flow may be considered to be completely outside the boundary layer. In that case, the laminar kinetic energy associated with pre-transitional fluctuations is zero. The appropriate inlet boundary condition is therefore k_L=0, and this condition was used for all of the test cases presented here.

Compressible Flow Formulation. For application to compressible flow, the mass-weighted average form of the continuity, momentum, and energy equations can be adopted, and the model equations outlined above can be implemented using compressible forms of the Boussinesq approximation of the turbulent stress tensor.

$$\overline{\rho u_i u_j} = \frac{1}{3}\left(\overline{\rho u_k u_k} + 2\mu_T \frac{\partial U_k}{\partial x_k}\right)\delta_{ij} - 2\mu_T S_{ij} \tag{40}$$

and the conservative forms of the transport equations are as follows:

$$\frac{D(\rho k_T)}{Dt} = \rho(P_{k_T} + R_{\mathrm{BP}} + R_{\mathrm{NAT}} - \omega k_T - D_T) + \frac{\partial}{\partial x_j}\left[\left(\mu + \frac{\rho\alpha_T}{\sigma_k}\right)\frac{\partial k_T}{\partial x_j}\right] \tag{41}$$

$$\frac{D(\rho k_L)}{Dt} = \rho(P_{k_L} - R_{\mathrm{BP}} - R_{\mathrm{NAT}} - D_L) + \frac{\partial}{\partial x_j}\left[\mu\frac{\partial k_L}{\partial x_j}\right] \tag{42}$$

$$\frac{D(\rho\omega)}{Dt} = \rho\left[C_{\omega 1}\frac{\omega}{k_T}P_{k_T} + \left(\frac{C_{\omega R}}{f_W} - 1\right)\frac{\omega}{k_T}(R_{\mathrm{BP}} + R_{\mathrm{NAT}}) - C_{\omega 2}\omega^2 + C_{\omega 3}f_\omega\alpha_T f_W^2\frac{\sqrt{k_T}}{d^3}\right] + \frac{\partial}{\partial x_j}\left[\left(\mu + \frac{\rho\alpha_T}{\sigma_\omega}\right)\frac{\partial\omega}{\partial x_j}\right] \tag{43}$$

Here the mean velocity (U_i) and the turbulent statistical quantities (k_T, k_L, and ω) represent mass-weighted (Favre) averaged values rather than ensemble or time-averaged values. All other model terms remain unchanged. The compressible form of the equations was used for the VKI airfoil test cases in the following section, which included both compressible subsonic and transonic flow behaviors.

Test Cases

The model described above was implemented directly into the commercial CFD solver FLUENT (Ansys, Inc., Canonsburg, PA) and applied to a number of simple and complex test cases, which were chosen to highlight the performance of the model for the prediction of boundary layer skin friction and heat transfer in a number of relevant applications. Each of the test cases is presented individually below, including the problem description, simulation details, results, and discussion. The channel and flat plate tests, including all seven of the T3 cases, were used to calibrate the model coefficients listed in Table 1. Once calibrated, the model was applied to the remaining airfoil cases in order to validate its performance for more complex and realistic flow applications.

All of the simulations presented here were performed using the FLUENT solver, version 6.4. This solver is based on an unstructured control-volume method whereby the domain is subdivided into discrete control-volumes and the integration of the equations is performed on the individual control-volumes [42]. All results presented in this study used a second order upwind-based discretization scheme. The velocity components, pressure, and all scalars are calculated at the center of each control-volume (collocated approach). The pressure-velocity coupling is achieved via a coupled pressure based algorithm (see Ref. [43] for full details), which the authors find particularly advantageous over more traditional segregated schemes (e.g. SIMPLE, SIMPLEC, PISO etc.) for the type of simulations that require resolution of the boundary layer, as is the case in the present study.

For all test case geometries, an initial mesh was constructed with a first cell y^+ value of one or less, and a structured body fitted mesh in the boundary layer region. In order to confirm grid inde-

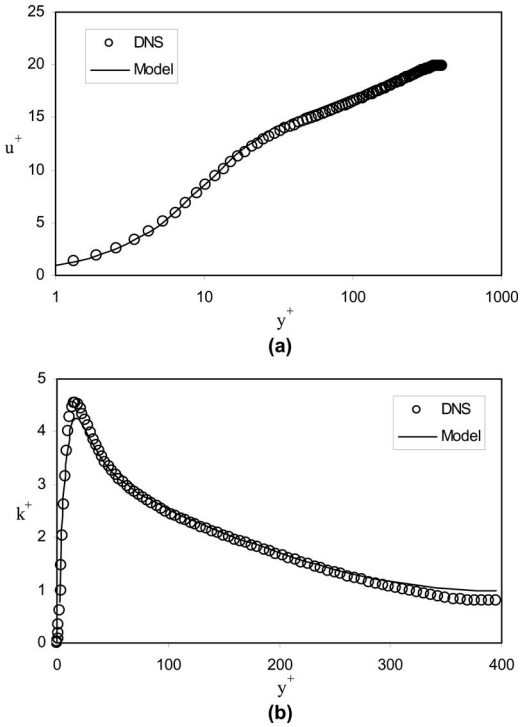

Fig. 1 Dimensionless velocity (*a*) and turbulent kinetic energy (*b*) profiles for fully developed turbulent channel flow at $Re_\tau = 395$

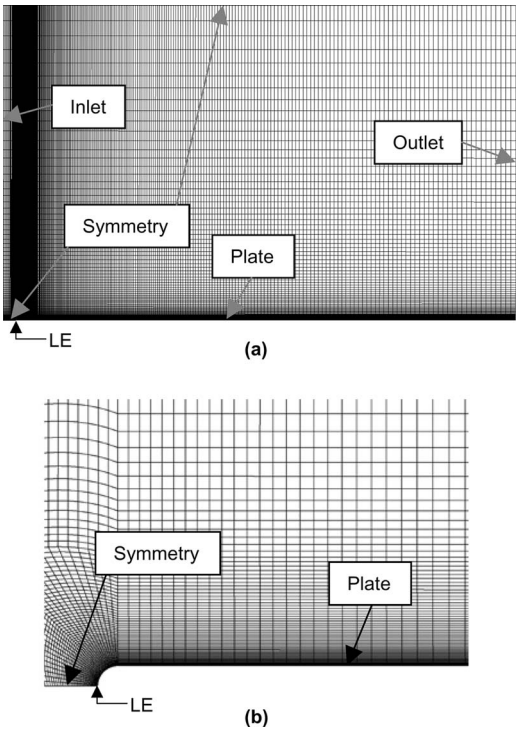

Fig. 2 Domain and computational meshes used for ZPG flat plate test cases: (*a*) overall mesh; and (*b*) close-up view of leading-edge region

pendence of the results, a second mesh with twice the resolution in the streamwise and wall-normal directions was constructed, and the results were compared to the original mesh. In all cases, the results showed negligible difference and were therefore judged to be mesh independent. All cases were run to full convergence, determined based on a drop in residuals of typically five orders of magnitude, as well as a flattening of all residuals indicating that machine accuracy had been reached.

Fully Developed Turbulent Channel Flow. The first test case is intended to verify the correct behavior of the new model in the fully-turbulent regime. The test case is a fully developed 2D channel flow with $Re_\tau = 395$, and the results are compared to the DNS simulations of Moser et al. [44]. The channel flow was modeled using a 2D domain with a periodic boundary condition in the streamwise direction. The Cartesian mesh consisted of 40 cells in the wall-normal direction, with grid stretching to ensure that the near-wall cell corresponded to $y^+ = 1$. The applied pressure gradient was chosen to ensure $Re_\tau = 395$ in terms of friction velocity and channel half-height. The flow was incompressible, and the viscosity was assumed constant.

Figure 1(*a*) shows the dimensionless velocity profile in the channel expressed in terms of inner scaling. The new model indicates good agreement with the DNS data, including a clear reproduction of the viscous sublayer, buffer zone, and inertial sublayer. Figure 1(*b*) shows the turbulent kinetic energy profile in the channel. The new model correctly reproduces the peak in turbulence near $y^+ = 15$, although the magnitude is underpredicted slightly. Throughout most of the channel extent, the model is in excellent agreement with the DNS data.

The channel flow results indicate that the model yields an appropriate response in fully-turbulent near-wall flow. Agreement with DNS data is as good as or better than a number of other fully-turbulent eddy-viscosity models recently published in the literature [45,46]. The remaining test cases assess the validity of the model for flows that exhibit laminar, transitional, and turbulent boundary layer behavior.

Zero-Pressure-Gradient Flat Plate. The transition behavior of the model was first tested for a simple zero-pressure-gradient (ZPG) flat plate, in order to assess the response to freestream turbulence, and to compare the prediction of transition start length with experimental data and available empirical correlations. The test cases chosen match the T3A, T3B, and T3A− validation cases from the European Research Consortium on Flow, Turbulence and Combustion (ERCOFTAC) database. The T3 test cases were developed specifically for validation of transition models and have become a recognized standard in the research community.

The computational domain was constructed to match as closely as possible the experimental geometry, including the rounded leading-edge of the flat plate. A symmetry condition was applied on the bottom surface upstream of the leading-edge, in order to allow a natural stagnation and boundary layer start. The left, right, and top boundaries were set as velocity inlet, pressure outlet, and symmetry planes, respectively. The placement of the symmetry plane was chosen to be far enough from the plate to ensure negligible acceleration of the freestream due to the finite plate thickness and boundary layer development. The results confirmed a freestream acceleration of less than 0.5%.

The mesh, shown in Fig. 2, consisted of block-structured quadrilaterals clustered in the near-wall and leading-edge regions. As discussed above, the first near-wall cell was placed so that the first-cell y^+ was less than one over the entire plate for each of the three cases. The total number of grid cells was 49,156.

Dimensionless freestream conditions for each of the three ZPG test cases are listed in Table 2 [47]. The turbulence intensity is defined in Eq. (39), and the (freestream) turbulent viscosity ratio is computed as

$$\mu_T = \rho C_{\mu,\text{std}} \frac{k_T}{\omega} \tag{44}$$

The values shown in Table 2 correspond to the freestream at the leading-edge location; the inlet values of k_T and ω were chosen in order to correctly reproduce the streamwise decay of freestream

Table 2 Leading-edge freestream conditions for T3 ZPG test cases

Case	Tu (%)	μ_T/μ
T3A−	0.874	8.73
T3A	3.3	12.0
T3B	6.5	100.0

turbulence reported in the experiments. An example of a typical agreement in the freestream is shown in Fig. 3.

The predicted skin friction coefficient is shown in Fig. 4 for cases T3A−, T3A, and T3B. The figure also indicates the limiting cases of laminar and turbulent flows on the flat plate. The model yields a good agreement between the experimental data for all three cases, although transition occurs slightly too quickly for the T3A test case. Most significantly, the model responds correctly to changes in freestream turbulence intensity—the location of transition moves upstream as turbulence intensity increases. The predictive capability is further underscored when considering the comparison between the transition-sensitive model presented here and the more typical linear eddy-viscosity models. Such models predict a turbulent boundary layer from the leading-edge onward and would closely match the limiting turbulent behavior shown in Fig. 4, with no resolution of laminar-to-turbulent transition.

The predicted behavior of the boundary layer before, during, and after transition is illustrated in Fig. 5. For case T3A, transition is predicted to begin at $\mathrm{Re}_x \approx 140{,}000$ and end at $\mathrm{Re}_x \approx 250{,}000$. Boundary layer profiles of velocity, total fluctuation energy (k_{TOT}), laminar kinetic energy (k_L) and turbulent kinetic energy (k_T), are shown at locations corresponding to $\mathrm{Re}_x = 1\times10^5$, 2×10^5, and 4×10^5. Shown for comparison purposes are the experimental data at the same locations. The corresponding shape factors for the mean velocity profile in the pretransitional, transitional, and turbulent regions are 2.39, 1.90, and 1.47, respectively, for the experimental data, and 2.51, 1.84, and 1.45, respectively, for the simulations.

In the pretransitional region, the velocity profile is approximately laminar, although the presence of the Klebanoff modes (indicated by the relatively large values of k_L) results in the small amount of momentum transport observed by Matsubara and Alfredsson [28]. In the transition region, laminar kinetic energy is transferred to turbulent kinetic energy, and the velocity profile begins to change as indicated. Downstream of transition, at $\mathrm{Re}_x = 4\times10^5$, the mean velocity and the turbulence kinetic energy profiles clearly indicate a turbulent boundary layer. There is also a residual level of laminar kinetic energy visible at this location. The magnitude of k_L is reduced as the boundary layer further develops in the streamwise direction; however, a small amount remains at all Reynolds numbers. In the fully-turbulent region, the peak level of k_L asymptotically decays to approximately 17% of the peak level of k_T.

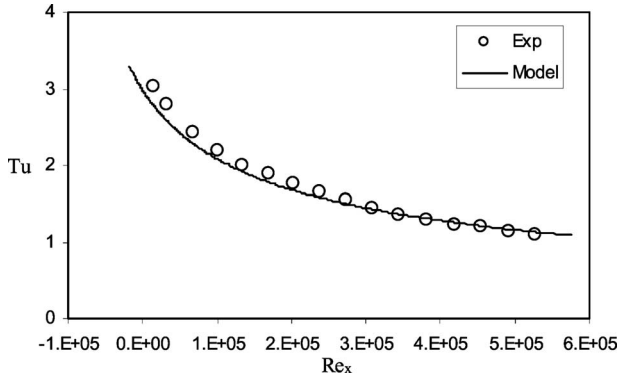

Fig. 3 Streamwise decay of freestream turbulence for test case T3A

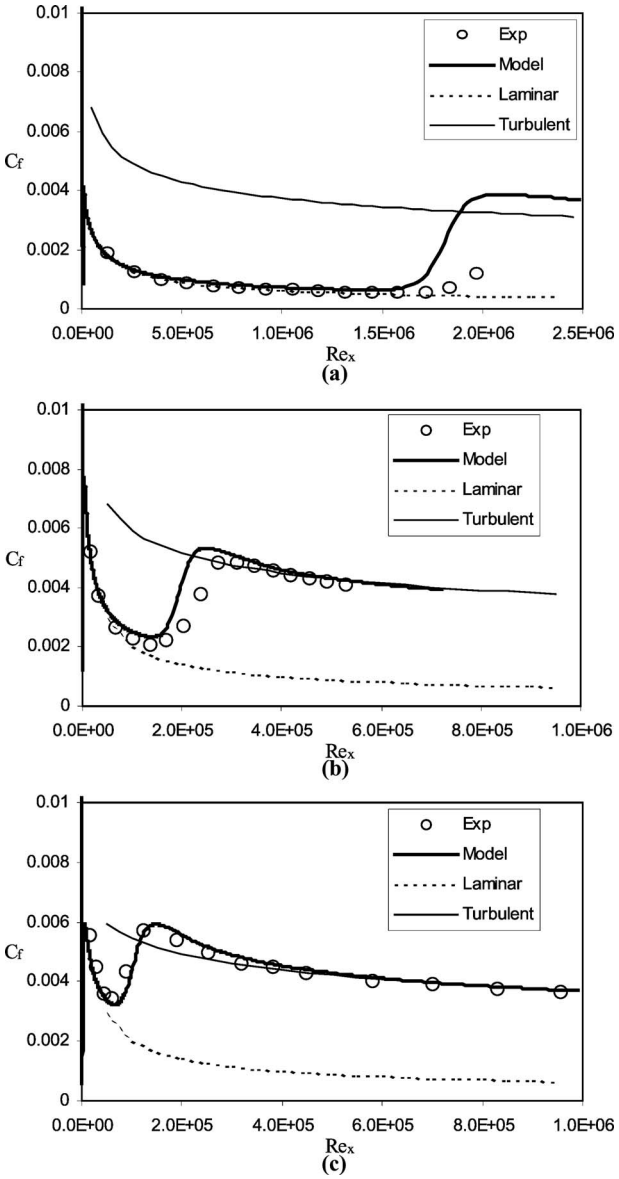

Fig. 4 Distribution of skin friction coefficient for ZPG flat plate cases: (*a*) T3A−, (*b*) T3A, and (*c*) T3B

The location of transition start was obtained based on the local minimum of shear stress in the skin friction distribution, and the momentum thickness Reynolds number (Re_θ) was computed at that location for each of the three cases. The values are plotted versus freestream turbulence intensity in Fig. 6. Shown for comparison is the transition start Reynolds number predicted by three empirical correlations available in the literature [8–10]. The results show that the new model prediction is quite similar to the transition start predicted by the correlations, although the model does not require computation of nonlocal parameters (such as momentum thickness) or coupling of an empirical model to the CFD simulation. By contrast, the use of a "typical" eddy-viscosity turbulence model would effectively yield transition at approximately $\mathrm{Re}_\theta = 0$ for all freestream turbulence levels.

Flat Plate With Pressure Gradient. The effect of streamwise pressure gradient was assessed using the T3C set of test cases from the ERCOFTAC database [48]. The geometry consisted of a

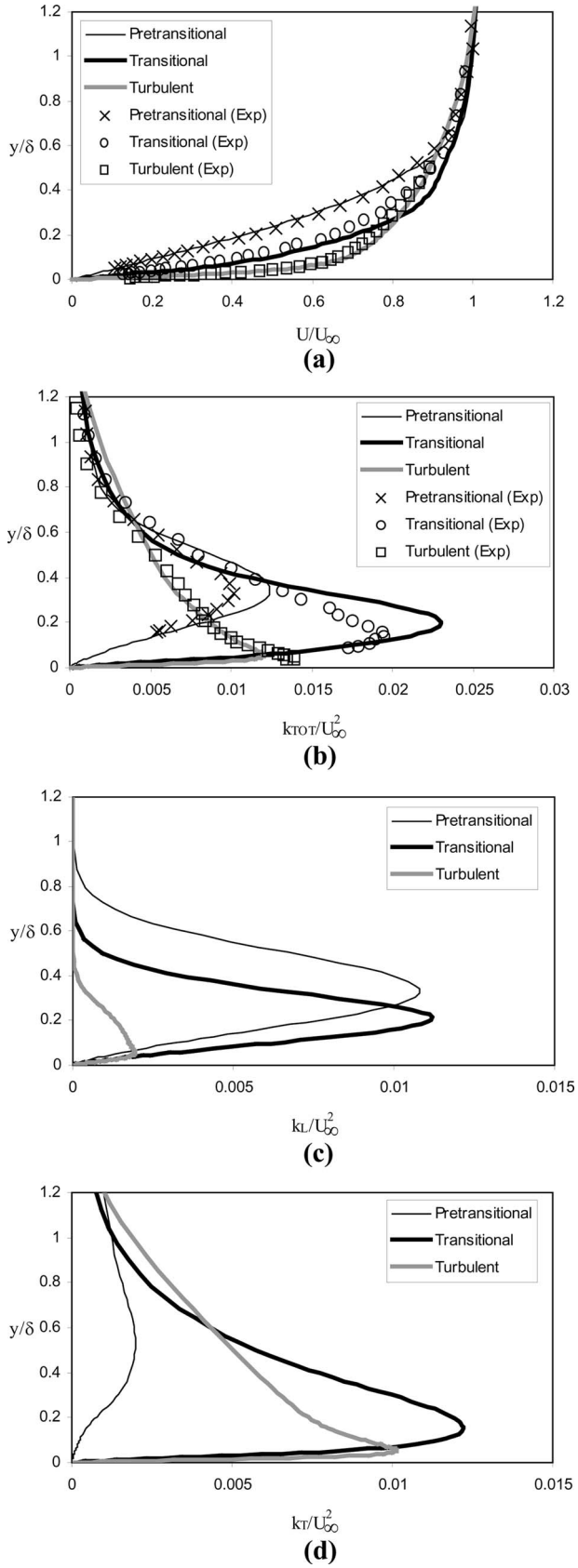

Fig. 5 Boundary layer profiles of mean velocity (*a*), total fluctuation kinetic energy (*b*), laminar kinetic energy (*c*), and turbulent kinetic energy (*d*), showing development from pretransitional to fully-turbulent regions in T3A flat plate case

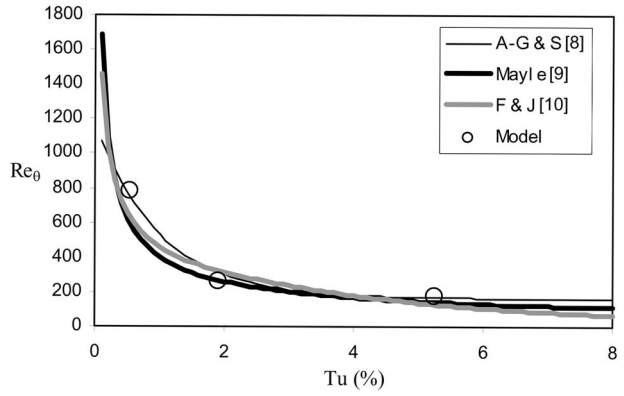

Fig. 6 Comparison between model and empirical correlations for transition start versus freestream turbulence intensity, in cases T3A–, T3A, and T3B.

flat plate, similar to the previous section, with the top wall of the wind tunnel test section contoured in order to produce a varying (favorable and adverse) streamwise flow acceleration. The computational domain was similarly constructed with a contoured upper surface, with the contouring chosen to match the experimental pressure distribution on the plate. The 2D mesh was constructed in a manner similar to the ZPG cases discussed above. The freestream turbulence conditions for the four T3C test cases are shown in Table 3. The values for k_T and ω in the simulation were chosen in order to match the measured streamwise decay of turbulent kinetic energy in the reference experiments.

The surface friction coefficient distribution is shown for each of the four cases in Fig. 7. For all cases, the model clearly indicates a laminar-to-turbulent boundary layer behavior and an excellent agreement with the experimental data in the fully laminar and fully-turbulent regions. For cases T3C2 and T3C3 (Figs. 7(*a*) and 7(*b*)), the model shows good prediction of the transition location to within 10–20%, with each case (both model and experiments) showing a decay of wall shear stress in the laminar adverse pressure gradient region and showing transition prior to boundary layer separation. In both cases the transition length is slightly underpredicted, similar to the behavior shown for the T3A case above.

For the T3C4 case (Fig. 7(*c*)), the experimental data seem to indicate that the boundary layer also transitions prior to separation, although there is only a single data point to indicate the transitional behavior. The model results for the T3C4 case indicate a laminar boundary layer separation due to the adverse pressure gradient, followed by the transition and reattachment of the boundary layer. Despite the apparently different behavior, the model shows prediction of the transition location to within about 20%. It is perhaps not surprising that the results show differences for this case in which transition and separation occur very close to one another.

For the T3C5 case (Fig. 7(*d*)), the flow transitions well upstream of the separation location due to the higher freestream turbulence intensity. The model predicts the transition location to within about 20%; however, the shear stress upstream of transition

Table 3 Leading-edge freestream conditions for T3C test cases

Case	Tu (%)	μ_T/μ
T3C2	3.0	11.0
T3C3	3.0	6.0
T3C4	3.0	8.0
T3C5	4.0	15.0

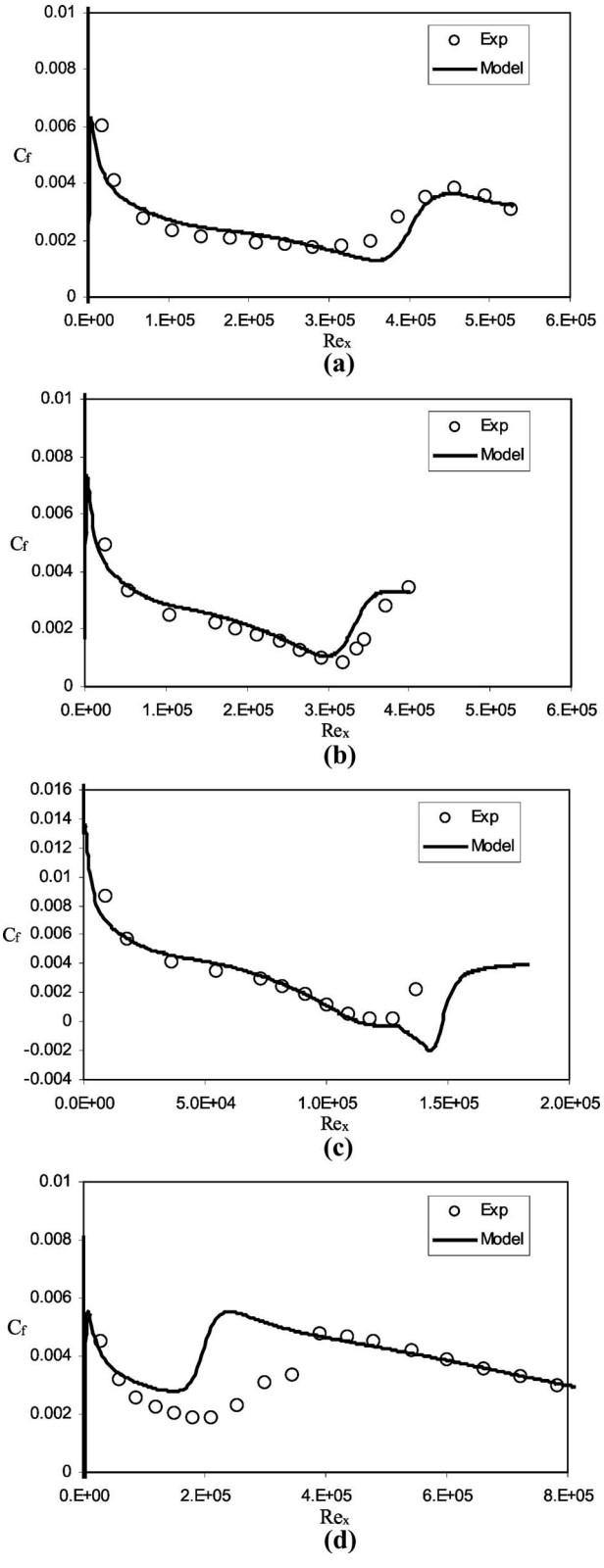

Fig. 7 Distribution of skin friction coefficient for flat plate cases with streamwise pressure gradient: (*a*) T3C2, (*b*) T3C3, (*c*) T3C4, and (*d*) T3C5

is overpredicted, and the model transition occurs too rapidly.

As above, the results compared to traditionally used eddy-viscosity models indicate a dramatic improvement, since fully-turbulent eddy-viscosity models would fail completely to resolve the laminar region and boundary layer transition. Taken in their entirety, the ERCOFTAC flat plate test cases highlight the improved predictive capability that is possible with a model specifically developed with the physics of transition taken into account.

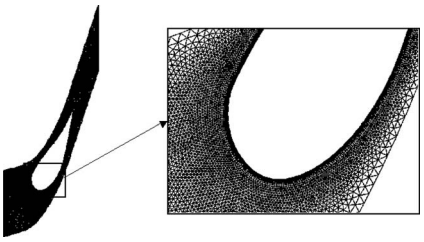

Fig. 8 Periodic domain and hybrid 2D mesh for VPI cascade test case

Airfoil Test Cases. One example of a realistic geometry for which transition is often an important factor is flow over airfoils. Relevant applications include gas turbine engines, aerodynamic vehicles, and wind turbines. Boundary layer transition directly influences the skin friction distribution and indirectly affects the separation and/or reattachment behavior, which can dramatically alter the force and moment distributions on lifting bodies. Likewise, transition plays a critical role in heat transfer, which is important for example in the turbine section of gas turbine engines downstream of the combustion chamber.

The new model has been applied to a number of airfoil test cases in order to assess predictive capability in terms of wall shear stress and heat transfer rates. Each of these cases is discussed briefly below.

VPI Cascade. The first validation case is a two-dimensional airfoil cascade of highly loaded turbine nozzle guide vanes, performed at the Virginia Polytechnic Institute and State University. The experiments were documented by Radomsky and Thole [49,50] and were performed with the purpose of providing code-validation quality data for CFD methods development. This experimental study is unique in that it provides data for a realistic high turning guide vane, with turbulence levels comparable to those exiting the combustion chamber of actual gas turbines. The geometry and flow conditions for this case, including freestream inlet turbulence quantities, were completely documented and provided for use in computational simulations.

An illustration of the geometry and mesh is shown in Fig. 8. The hybrid mesh contained 24,386 cells. The inlet air velocity was 5.85 m/s, which corresponds to a Reynolds number of 23,000 based on a chord length of 59.4 cm. Two test cases were run, corresponding to relatively high freestream turbulence levels of 10% and 19.5%. For the two cases, the inverse time-scale was chosen to correspond to a turbulent viscosity ratio (μ_T/μ) of 900 and 2100, respectively.

A constant heat flux boundary condition was applied on the airfoil surface, and the surface heat transfer coefficient was determined from the simulations and compared to the available experimental data. Figure 9 shows the model prediction versus measured data for the two freestream turbulence levels. The plot shows heat transfer coefficient (h) versus distance along the airfoil surface (from the stagnation point) normalized by chord length (s/C). Negative values of s indicate the pressure surface; positive values indicate the suction surface. The suction surface transition for both freestream levels is readily apparent in the data and in the model prediction. It is also apparent that the model predicts the beginning of transition near the trailing edge of the pressure surface. Overall, the model yields a reasonable agreement with the experimental data, although the higher turbulence case indicates too rapid transition predicted by the model, similar to the behavior shown in the T3C5 flat plate case above.

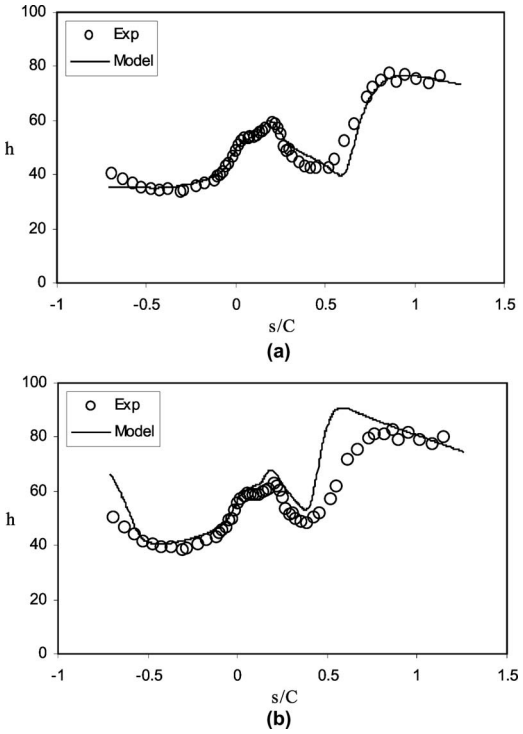

Fig. 9 Surface heat transfer coefficient distribution for VPI Cascade test cases: (*a*) $Tu_\infty = 10\%$ and (*b*) $Tu_\infty = 19.5\%$

VKI Cascade. The second airfoil test case corresponds to the experimental study of Arts et al. [51], performed at the von Karman Institute for Fluid Dynamics. The flow field is a 2D linear airfoil cascade, and the results were obtained in terms of the surface heat transfer coefficient distribution. The computational domain and mesh used for the CFD simulations are shown in Fig. 10. The mesh was comprised of 62,000 quadrilateral cells, unstructured in the farfield and structured in the near-wall region in order to resolve the boundary layer. Five total cases were run, three corresponding to a Reynolds number of 1×10^6 and two corresponding to a Reynolds number of 5×10^5. For the first three, the flowfield remained subsonic. For the last two, the experiments indicated that a shock was present on the suction side, which interacted with the developing boundary layer. The presence of the shock for the final two cases was confirmed in the CFD simulations here.

For each Reynolds number, varying levels of freestream turbulence were tested. The experiments included measurement of the freestream turbulence intensity, however no information regarding

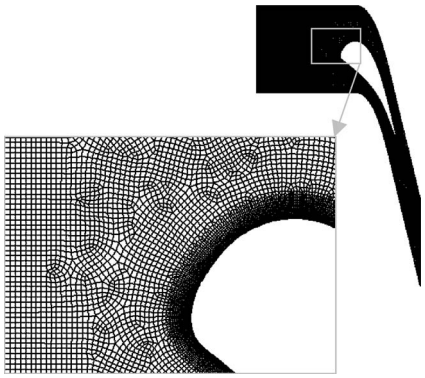

Fig. 10 Periodic domain and hybrid 2D mesh for VKI cascade test case

Table 4 Inlet freestream conditions for VKI test cases

Case	Re_C	Tu (%)	μ_T/μ
MUR 132	1×10^6	0.8	10.0
MUR 218	1×10^6	4.0	50.0
MUR 237	1×10^6	6.0	75.0
MUR 228	5×10^5	1.0	8.76
MUR 226	5×10^5	4.0	47.0

dissipation rate was obtained. In the simulations presented here, a turbulent length scale equal to 15% of the blade-to-blade pitch was chosen, with the resulting values of freestream turbulent viscosity ratio, as shown in Table 4. Because the inlet to the computational domain was placed upstream of the airfoil leading-edge, the turbulence quantities were found to decay, in some cases, significantly, before the freestream flow reached the airfoil, where the rate of decay in the simulations can be approximated as the solution to the following coupled equations:

$$U_\infty \frac{dk_T}{dx} = -\omega k_T \tag{45}$$

$$U_\infty \frac{d\omega}{dx} = -C_{\omega 2}\omega^2 \tag{46}$$

For example, cases MUR 218 and MUR 237 were found to decay such that the leading-edge turbulence intensity was 3.2% and 4.4%, respectively. In order to determine the influence of the freestream decay on the transition prediction, a second set of simulations (denoted as Run 2) was run for these two cases, for which the inlet conditions were chosen using Eqs. (45) and (46) such that the freestream conditions listed in Table 4 were present at the leading-edge of the airfoil rather than at the computational inlet.

The results for the cases with no shock are shown in Fig. 11. For freestream turbulence intensity of 1% and 4%, the distribution of heat transfer coefficient is very similar, with laminar flow over the pressure surface and most of the suction surface. In both cases, transition occurs on the suction surface near the trailing edge, most likely triggered by the presence of an adverse pressure gradient in that region. This behavior is found in both the experiments and the computation, with the model predicting the transition initiation location to within about 10%.

For the case of 6% freestream turbulence, the experiments indicate that the boundary layer behavior changes considerably. The transition location moves well forward on the suction surface, and the heat transfer coefficient shows a significant increase on the pressure surface. The simulations with freestream conditions applied at the inlet (Run 1) show only a slight increase on the pressure side—versus the 4% turbulence case—and indicate that transition occurs near the trailing edge similar to the 4% case. However, the simulations with freestream conditions applied at the airfoil leading-edge (Run 2) show a dramatically different behavior, with transition initiating well upstream on the suction surface similar to the experiments. The pressure surface also shows transition, although this leads to significant overprediction of heat transfer coefficient near the trailing edge. These results highlight the sensitivity of transitional behavior to the freestream conditions, particularly for cases that display sudden qualitative changes in flow behavior as the freestream turbulence is increased. As the transition-sensitive model development becomes a greater focus for RANS-based CFD, it will be necessary to have available experimental data sets with detailed descriptions of the freestream turbulence characteristics, including turbulence intensity, length scale, and dissipation rate.

The results for the cases with a suction side shock are shown in Fig. 12. The distribution of heat transfer coefficient indicates a laminar boundary layer over the entire pressure surface and over

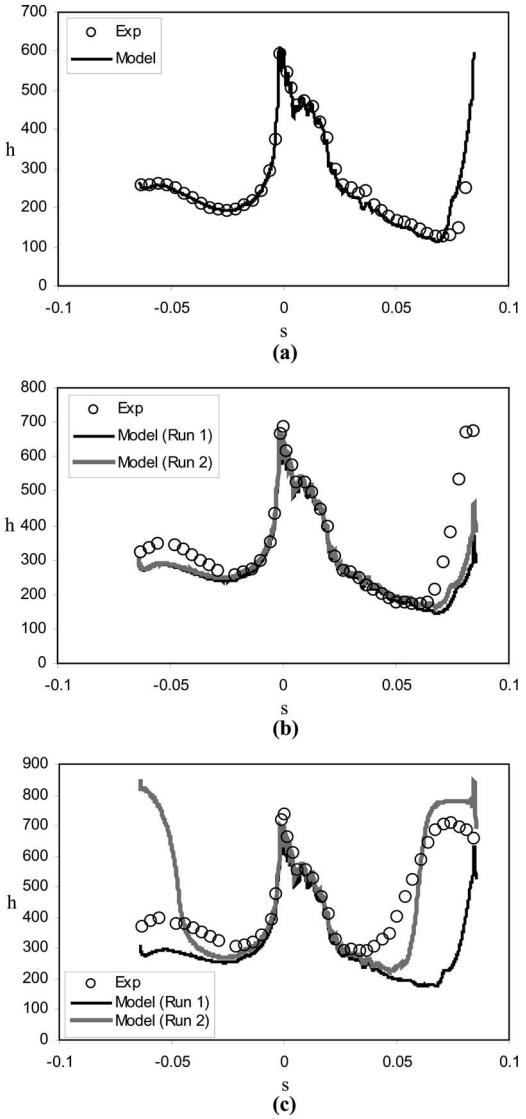

Fig. 11 Surface heat transfer coefficient distribution for VKI Cascade test cases with no suction side shock: (*a*) $Tu_\infty=1\%$, (*b*) $Tu_\infty=4\%$, and (*c*) $Tu_\infty=6\%$

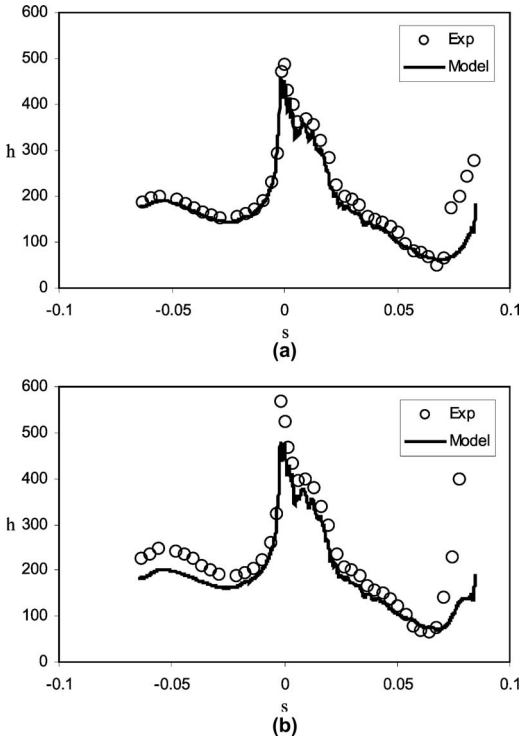

Fig. 12 Surface heat transfer coefficient distribution for VKI Cascade test cases with suction side shock: (*a*) $Tu_\infty=1\%$, and (*b*) $Tu_\infty=4\%$

most of the suction surface. In the experimental data, the boundary layer is seen to undergo transition near the trailing edge of the suction surface for both freestream turbulence levels due to the presence of the shock. The transition is incomplete, and fully-turbulent flow is not reached before the end of the airfoil surface. Similar behavior is indicated by the model, with transition predicted to initiate very close to the location shown in the experiments. The model transition is less rapid than in the experiments, but overall agreement is reasonable and superior to the fully-turbulent flow that would be predicted by commonly used-eddy viscosity models.

A-Airfoil. The third airfoil case is the Aerospatiale A-airfoil configuration at Reynolds number (based on chord length) of 2×10^6, Mach number of 0.15, and angle of attack (α) of 13.3 deg. This configuration has been well studied, both experimentally [52] and numerically [53] and is known to exhibit complex boundary layer transition and separation behavior.

The airfoil geometry and mesh are illustrated in Fig. 13. The mesh used was 2D structured C-type with a total of 65,000 cells. The inlet turbulence intensity for the simulations was 0.2%, and the turbulent viscosity ratio was 10.

CFD results were compared to experimental data in terms of skin friction coefficient on the upper (suction) surface and are shown in Fig. 14. The reported experimental data indicate that transition occurs on the suction surface at $s/C=0.12$. It is apparent in the figure that this transition location is well predicted by the model, and a fully-turbulent boundary layer is indicated downstream of this location.

S809 Wind Turbine Airfoil. The last airfoil case presented is the S809 airfoil that was specifically designed for wind turbine applications. The experimental measurements were obtained using a low-turbulence wind tunnel, and data are available in Refs. [54] and [55]. This configuration was run at Reynolds number (based on chord length) of 2×10^6 and a Mach number of 0.15. The interesting aspect of the experimental study is that the experimental values of transition location are available as a function of numerous angles of attack. This is valuable information since in real design applications engineers quite often conduct parametric studies of airfoil behavior as a function of different angles of attack. If the model can successfully be used for such purposes, then its

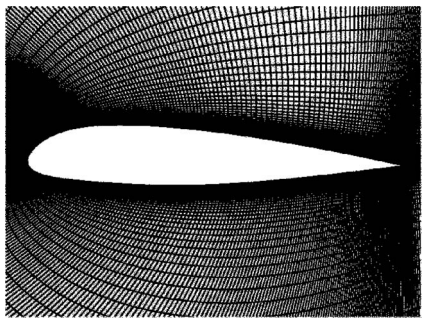

Fig. 13 Structured C-type 2D mesh for A-airfoil test case

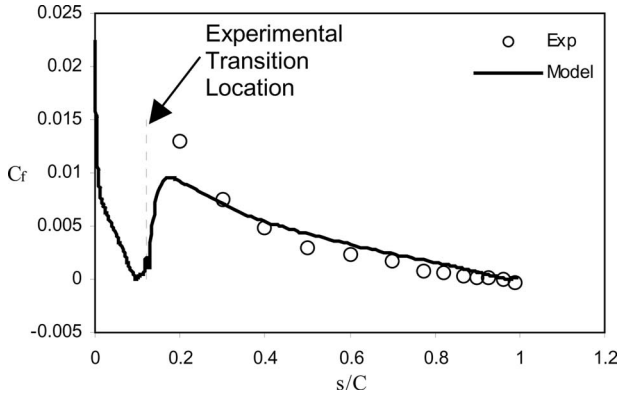

Fig. 14 Comparison of predicted and measured skin friction coefficients for the A-airfoil test case

practical merits would be significantly demonstrated.

The airfoil geometry and mesh are illustrated in Fig. 15. The mesh used was 2D structured C-type with a total of 77,000 cells. As for the A-airfoil case, the inlet turbulence intensity and the turbulent viscosity ratio were 0.2% and 10, respectively.

CFD results were compared to experimental data in terms of transition location versus angle of attack (α) on both suction and pressure sides, as shown in Fig. 16. In order to cover a wide range of attack angles, a total of 21 CFD runs were conducted ranging from 0 deg to 20 deg with a step of 1 deg. The reported experimental data indicate that transition location on suction side steadily moves toward the leading-edge up to $\alpha=5$ deg. This is followed by an accelerated movement of the transition location to the leading-edge in the range 5 deg $<\alpha<$ 9 deg. Beyond 9 deg, the transition location remains located at the vicinity of the leading-edge. It is apparent in the figure that transition location movement and behavior is well predicted by the model, both qualitatively and quantitatively (Fig. 16(*b*)). The experimental results on the pressure side (Fig. 16(*a*)) are less dramatic but are closely followed by the present model predictions.

Conclusions

The use of Reynolds-averaged Navier–Stokes simulation to predict both turbulent and transitional flows is a problem of substantial interest to designers and other end users of computational analysis tools. Recent efforts have focused on single-point models that display significant flexibility and ease of use for current generation CFD solvers. This paper has presented a physics-based (i.e., phenomenological) eddy-viscosity modeling approach based on the addition of one transport equation to a simple k-ω model framework. The additional transport equation represents the effects of pretransitional fluctuations, including Klebanoff modes and Tollmien–Schlichting waves that are the precursors to bypass and natural transition, respectively. The model is an improved

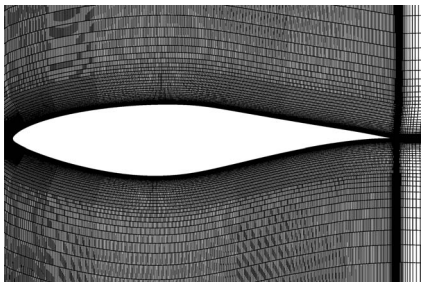

Fig. 15 2D mesh for S809 airfoil test case

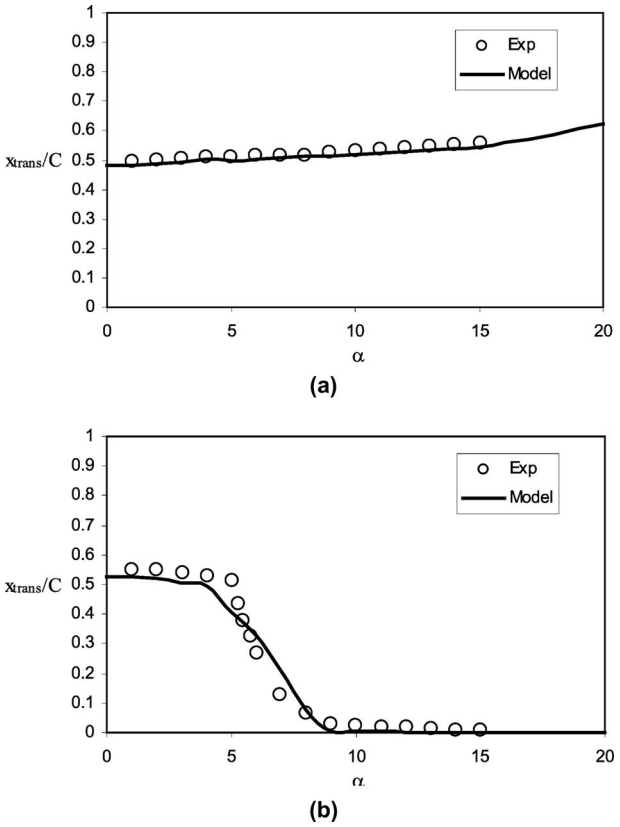

Fig. 16 Comparison of predicted and measured transition locations versus angle of attack for S809 airfoil test case: (*a*) pressure surface and (*b*) suction surface

version of the original phenomenological transition-sensitive k-ε model proposed by Walters and Leylek [17]. The new model has been implemented into the commercial code FLUENT (Ansys, Inc., Canonsburg, PA) and applied to several relevant test problems in order to highlight its performance for transitional flow prediction.

The results presented here indicate that the new model yields qualitatively correct transition behavior for a wide range of flow conditions. The test cases address the effects of freestream turbulence, pressure gradient, and surface curvature on the turbulence development. ZPG flat plate cases show excellent agreement with the experimental data from the ERCOFTAC database over a range of leading-edge freestream turbulence intensity from approximately 1% to 6%. The ZPG flat plate cases also show similar prediction of transition start location as three commonly used empirical correlations. Flat plate cases with complex favorable and adverse streamwise pressure gradients similarly show good agreement with ERCOFTAC experiments, although the complexity of the accelerating flowfield limited quantitative agreement of transition start location to within about 10–20%. Likewise, the model showed too short of a transition zone in some of the cases and that behavior was repeated in some of the airfoil cases. Future model improvement will address the transition zone behavior to produce more consistent prediction of this region. One possibility is the incorporation of an intermittency function into the model, although this would necessarily increase model complexity and empiricism. Alternative strategies may include the use of additional damping functions in the transition region or a modification of the transition production terms R_{BP} and R_{NAT}. Nevertheless, the flat plate results indicate that the new model provides useful predictive capability versus current generation RANS-based turbulence models.

Finally, the model was applied to a number of airfoil test cases available in the open literature. The airfoil test cases comprised a

wide range of geometries and flow conditions, including freestream turbulence conditions, Reynolds number, and angle of attack. The transitional behavior for each of these cases was well reproduced by the new model, with transition start location predicted to within approximately 10–20% for most of the cases.

The model results presented here show a dramatic improvement over traditional fully-turbulent models, without the need for empirical correlations or user prescribed transition information. While no simple modeling methodology will ever yield perfect predictive capability, these results suggest that the physics-based approach adopted here allows designers to significantly extend RANS-based computational analysis capability by providing realistic transitional modeling capability in a relatively simple eddy-viscosity framework.

Nomenclature

All model coefficients are tabulated in Table 1 of the text.

C = airfoil chord length
C_μ = turbulent viscosity coefficient
d = wall distance
D_T = anisotropic (near-wall) dissipation term for k_T
D_L = anisotropic (near-wall) dissipation term for k_L
f_{INT} = intermittency damping function
$f_{\text{NAT,crit}}$ = model function incorporating freestream turbulence effects on natural transition
f_W = inviscid near-wall damping function
f_{SS} = shear-sheltering damping function
f_ν = viscous near-wall damping function
f_ω = boundary layer wake term damping function in ω equation
$f_{\tau,l}$ = time-scale damping function
h = heat transfer coefficient
k_L = laminar kinetic energy
k_T = turbulent kinetic energy
$k_{T,l}$ = effective "large-scale" turbulent kinetic energy
$k_{T,s}$ = effective small-scale turbulent kinetic energy
k_{TOT} = total fluctuation kinetic energy, k_T+k_L
P_{kL} = production of laminar kinetic energy by mean strain rate
P_{kT} = production of turbulent kinetic energy by mean strain rate
Pr_θ = turbulent Prandtl number
R_{BP} = bypass transition production term
R_{NAT} = natural transition production term
Re_θ = momentum thickness Reynolds number
Re_T = turbulence Reynolds number
Re_τ = Reynolds number based on friction velocity and channel half-height
Re_x = local Reynolds number
Re_Ω = vorticity-based Reynolds number
S = magnitude of mean strain rate tensor
S_{ij} = strain rate tensor
s = distance along the airfoil surface (from the stagnation point)
T = temperature
t = time
Tu_∞ = freestream turbulence intensity
U_∞ = freestream mean velocity
u_i = velocity vector
v' = wall-normal freestream turbulence fluctuation magnitude
x = downstream distance
x_i = position vector
y^+ = wall distance normalized by inner scaling
α = thermal diffusivity
α_θ = turbulent thermal diffusivity
α_T = effective diffusivity for turbulence dependent variables
β_{BP} = bypass transition threshold function
β_{TS} = Tollmien–Schlichting threshold function
β_{NAT} = natural transition threshold function
δ = 99% boundary layer thickness
δ_{ij} = Kronecker delta
ε = farfield isotropic dissipation rate
φ_{BP} = model bypass transition parameter
φ_{NAT} = model natural transition parameter
η = wall-normal coordinate direction
λ_{eff} = effective (wall-limited) turbulence length scale
λ_T = turbulent length scale
ν = kinematic viscosity
ν_T = turbulent kinematic viscosity
$\nu_{T,s}$ = small-scale turbulent viscosity contribution
$\nu_{T,l}$ = large-scale turbulent viscosity contribution
Ω = magnitude of mean rotation rate tensor
ω = inverse turbulent time-scale
θ = boundary layer momentum thickness
ρ = density
μ = dynamic viscosity
μ_T = turbulent or "eddy"-viscosity

References

[1] Kalitzin, G., Wu, X., and Durbin, P. A., 2003, "DNS of Fully Turbulent Flow in a LPT Passage," Int. J. Heat Fluid Flow, **24**, pp. 636–644.
[2] Savill, A. M., 1993, "Some Recent Progress in the Turbulence Modeling of By-Pass Transition," *Near-Wall Turbulent Flows*, R. M. C. So, C. G. Speziale, and B. E. Launder, eds., Elsevier, Amsterdam, pp. 829–848.
[3] Savill, A. M., 2002, "By-Pass Transition Using Conventional Closures," *Closure Strategies for Turbulent and Transitional Flows*, Cambridge University Press, Cambridge, pp. 464–492.
[4] Wilcox, D. C., 1994, "Simulation of Transition With a Two Equation Turbulence Model," AIAA J., **32**, pp. 247–255.
[5] Hadzic, I., and Hanjalic, K., 1999, "Separation-Induced Transition to Turbulence: Second Moment Closure Modelling," Flow, Turbul. Combust., **63**, pp. 153–173.
[6] Rumsey, C. L., 2006, "Apparent Transition Behavior of Widely-Used Turbulence Models," *Proceedings of the 36th AIAA Fluid Dynamics Conference*, San Francisco, CA, June 5–8, 4, pp. 2625–2643.
[7] van Driest, E. R., and Blumer, C. B., 1963, "Boundary Layer Transition, Free Stream Turbulence, and Pressure Gradient Effects," AIAA J., **1**, pp. 1303–1306.
[8] Abu-Ghannam, B. J., and Shaw, R., 1980, "Natural Transition of Boundary Layers—The Effects of Turbulence, Pressure Gradient, and Flow History," J. Mech. Eng. Sci., **22**, pp. 213–228.
[9] Mayle, R. E., 1991, "The Role of Laminar-Turbulent Transition in Gas Turbine Engines," ASME J. Turbomach., **113**, pp. 509–537.
[10] Fasihfar, A., and Johnson, M. W., 1992, "An Improved Boundary Layer Transition Correlation," ASME Paper No. 92-GT-245.
[11] Praisner, T. J., and Clark, J. P., 2007, "Predicting Transition in Turbomachinery—Part I: A Review and New Model Development," ASME J. Turbomach., **129**, pp. 1–13.
[12] Dhawan, S., and Narasimha, R., 1958, "Some Properties of Boundary Layer During the Transition From Laminar to Turbulent Flow Motion," J. Fluid Mech., **3**, pp. 418–436.
[13] Greene, F. A., and Hamilton, H. H., 2006, "Development of a Boundary Layer Properties Interpolation Tool in Support of Orbiter Return to Flight," *Proceedings of the Ninth AIAA/ASME Joint Thermophysics and Heat Transfer Conference*, San Francisco, CA, June 5–8, 1, pp. 144–160.
[14] Kozulovic, D., and Lapworth, L., 2007, "An Approach for Inclusion of a Non-Local Transition Model in a Parallel Unstructured CFD Code," *Proceedings of the Fifth Joint ASME/JSME Fluids Engineering Conference*, San Diego, CA, July 30–Aug. 2, ASME Paper No. FEDSM2007–37162.
[15] Edwards, J. R., Roy, C. J., Blottner, F. G., and Hassan, H. G., 2001, "Development of a One-Equation Transition/Turbulence Model," AIAA J., **39**, pp. 1691–1698.
[16] Wang, C., and Perot, B., 2002, "Prediction of Turbulent Transition in Boundary Layers Using the Turbulent Potential Model," J. Turbul., **3**, N22.
[17] Walters, D. K., and Leylek, J. H., 2004, "A New Model for Boundary Layer Transition Using a Single-Point RANS Approach," ASME J. Turbomach., **126**, pp. 193–202.
[18] Suzen, Y. B., and Huang, P. G., 2000, "Modeling of Flow Transition Using an Intermittency Transport Equation," ASME J. Fluids Eng., **122**, pp. 273–284.
[19] Steelant, J., and Dick, E., 2001, "Modeling of Laminar-Turbulent Transition for High Freestream Turbulence," ASME J. Fluids Eng., **123**, pp. 22–30.
[20] Menter, F. R., Langtry, R. B., Likki, S. R., Suzen, Y. B., Huang, P. G., and Volker, S., 2006, "A Correlation-Based Transition Model Using Local

Variables—Part I: Model Formulation," ASME J. Turbomach., **128**, pp. 413–422.
[21] Menter, F. R., Langtry, R., and Volker, S., 2006, "Transition Modelling for General Purpose CFD Codes," Flow, Turbul. Combust., **77**, pp. 277–303.
[22] Walters, D. K., and Leylek, J. H., 2005, "A CFD Study of Wake-Induced Transition on a Compressor-Like Flat Plate," ASME J. Turbomach., **127**, pp. 52–63.
[23] York, W. D., Walters, D. K., and Leylek, J. H., 2003, "Conjugate Heat Transfer Simulation of an Internally-Cooled Turbine Vane With a Predictive Model for Boundary-Layer Transition," ASME Paper No. IMECE2003-41555.
[24] Holloway, D. S., Walters, D. K., and Leylek, J. H., 2004, "Prediction of Unsteady, Separated Boundary Layer Over a Blunt Body for Laminar, Turbulent, and Transitional Flow," Int. J. Numer. Methods Fluids, **45**, pp. 1291–1315.
[25] Walters, D. K., and Leylek, J. H., 2003, "Prediction of Boundary-Layer Transition Effects on Turbine Airfoil Profile Losses," ASME Paper No. IMECE2003-41420.
[26] Sveningsson, A., 2006, "Turbulence Transport Modelling in Gas Turbine Related Applications," Ph.D. thesis, Chalmers University of Technology, Sweden.
[27] Schlichting, H., and Gersten, K., 2000, *Boundary Layer Theory*, 8th ed., Springer-Verlag, Berlin.
[28] Matsubara, M., and Alfredsson, P. H., 2001, "Disturbance Growth in Boundary Layers Subjected to Free-Stream Turbulence," J. Fluid Mech., **430**, pp. 149–168.
[29] Klebanoff, P. S., 1971, "Effects of Free-Stream Turbulence on a Laminar Boundary Layer," Bull. Am. Phys. Soc., **16**, p. 1323.
[30] Jacobs, R. G., and Durbin, P. A., 2001, "Simulations of Bypass Transition," J. Fluid Mech., **428**, pp. 185–212.
[31] Lardeau, S., Li, N., and Leschziner, M. A., 2007, "Large Eddy Simulation of Transitional Boundary Layers at High Freestream Turbulence Intensity and Implications for RANS Modeling," ASME J. Turbomach., **129**, pp. 311–317.
[32] Mayle, R. E., and Schulz, A., 1997, "The Path to Predicting Bypass Transition," ASME J. Turbomach., **119**, pp. 405–411.
[33] Volino, R. J., 1998, "A New Model for Free-Stream Turbulence Effects on Boundary Layers," ASME J. Turbomach., **120**, pp. 613–620.
[34] Lardeau, S., Leschziner, M. A., and Li, N., 2004, "Modeling Bypass Transition With Low-Reynolds-Number Nonlinear Eddy-Viscosity Closure," Flow, Turbul. Combust., **73**, pp. 49–76.
[35] Volino, R. J., and Simon, T. W., 1997, "Boundary Layer Transition Under High Free-Stream Turbulence and Strong Acceleration Conditions: Part 2—Turbulent Transport Results," ASME J. Heat Transfer, **119**, pp. 427–432.
[36] Leib, S. J., Wundrow, D. W., and Goldstein, M. E., 1999, "Effect of Free-Stream Turbulence and Other Vortical Disturbances on a Laminar Boundary Layer," J. Fluid Mech., **380**, pp. 169–203.
[37] Johnson, M. W., and Ercan, A. H., 1999, "A Physical Model for Bypass Transition," Int. J. Heat Fluid Flow, **20**, pp. 95–104.
[38] Luchini, P., 2000, "Reynolds-Number-Independent Instability of the Boundary Layer Over a Flat Surface: Optimal Perturbations," J. Fluid Mech., **404**, pp. 289–309.
[39] Andersson, P., Berggren, M., and Henningson, D. S., 1999, "Optimal Disturbances and Bypass Transition in Boundary Layers," Phys. Fluids, **11**, pp. 134–150.
[40] Jacobs, R. G., and Durbin, P. A., 1998, "Shear Sheltering and the Continuous Spectrum of the Orr-Sommerfeld Equation," Phys. Fluids, **10**, pp. 2006–2011.
[41] Shih, T.-H., Liou, W. W., Shabbir, A., Yang, Z., and Zhu, J., 1995, "A New k-ε Eddy Viscosity Model for High Reynolds Number Turbulent Flows," Comput. Fluids, **24**, 227–238.
[42] Mathur, S. R., and Murthy, J. Y., 1997, "A Pressure Based Method for Unstructured Meshes," Numer. Heat Transfer, Part B, **31**, pp. 195–216.
[43] User Guide Fluent 6.3, Fluent Inc., Centerra Resource Park, 10 Cavendish Court, Lebanon, NH 03766, USA.
[44] Moser, R., Kim, J., and Mansour, N., 1999, "Direct Numerical Simulation of Turbulent Channel Flow up to Re_τ=590," Phys. Fluids, **11**, pp. 943–945.
[45] Hanjalic, K., Popovac, M., and Hadziabdic, M., 2004, "A Robust Near-Wall Elliptic-Relaxation Eddy-Viscosity Turbulence Model for CFD," Int. J. Heat Fluid Flow, **25**, pp. 1047–1051.
[46] Jaramillo, J. E., Perez-Segarra, C. D., Oliva, A., and Claramunt, K., 2007, "Analysis of Different RANS Models Applied to Turbulent Forced Convection," Int. J. Heat Mass Transfer, **50**, pp. 3749–3766.
[47] Coupland, J., 1990, ERCOFTAC Special Interest Group on Laminar to Turbulent Transition and Retransition: T3A and T3B Test Cases.
[48] Coupland, J., 1990, ERCOFTAC Special Interest Group on Laminar to Turbulent Transition and Retransition: T3C Test Cases.
[49] Radomsky, R. W., and Thole, K. A., 2000, "Flowfield Measurements for a Highly Turbulent Flow in a Stator Vane Passage," ASME J. Turbomach., **122**, pp. 255–262.
[50] Radomsky, R. W., and Thole, K. A., 2001, "Detailed Boundary-Layer Measurements on a Turbine Stator Vane at Elevated Freestream Turbulence Levels," ASME Paper No. 2001-GT-0169.
[51] Arts, T., Lambert de Rouvroit, M., and Rutherford, A., 1990, "Aero-Thermal Investigation of a Highly Loaded Transonic Linear Turbine Guide Vane Cascade," von Karman Institute for Fluid Dynamics, TN174.
[52] Gendre, P., 1992, "Maximum lift for a single-element airfoils—Experimental Results A-Airfoil," EUROVAL—A European Initiative on Validation of CFD Codes, Notes on Numerical Fluid Mechanics, W. Haase, F. Brandsma, E. Elsholz, M. Leschziner, and D. E. Schwamborn, eds., Vieweg, Braunschweig, Vol. 42.
[53] Schmidt, S., and Thiele, F., 2003, "Detached Eddy Simulation of Flow Around A-Airfoil," Flow, Turbul. Combust., **71**, pp. 261–278.
[54] Somers, D. M., 1989, "Design and Experimental Results for the S809 Airfoil," Airfoils, Inc., State College, PA.
[55] Somers, D. M., 1997, "Design and Experimental Results for the S809 Airfoil," NREL/SR-440-6918, January 1997.

Instantaneous Liquid Flow Rate Measurement Utilizing the Dynamics of Laminar Pipe Flow

Bernhard Manhartsgruber
Institute of Machine Design
and Hydraulic Drives,
Johannes Kepler University,
Altenbergerstrasse 69,
4040 Linz, Austria
e-mail: bernhard.manhartsgruber@jku.at

This paper deals with the utilization of the dynamic characteristics of laminar flow in circular pipes for the indirect measurement of flow rates. A discrete-time state space realization of the transmission line dynamics is computed via inverse Laplace transform and an identification and model reduction method based on the singular value decomposition. This dynamic system is used for the computation of the flow rate at one end of a pipe section. Special attention is paid to the identification of the speed of sound and the dimensionless dissipation number of the pipe section, since exact knowledge of these parameters is crucial for the reliability of the measurement results. First, experimental validation results are given in a limited range of operating frequencies between 100 Hz and 2000 Hz. Flow rate variations within ±1.2 l/min have been measured with an uncertainty of ±0.07 l/min at the 95% confidence level. The test fluid was mineral oil. [DOI: 10.1115/1.2969464]

1 Introduction

The accurate measurement of pressures and flow rates is important for the monitoring and control of hydraulic systems. Rapidly changing flow rates occur in various fluid power devices like high pressure piston pumps and fast switching valves. In many cases, exact knowledge of transient flow rates is important for the prediction of flow-induced forces on valve spools or pressure oscillations generated in the system.

While sensors are available for the precise measurement of rapid pressure transients, the measurement of transient flow rates is still a demanding problem. Positive displacement, turbine, and variable orifice flow meters feature bandwidth limitations due to the inertia of moving parts and nonlinearities due to mechanical friction. Simple flow chokes with differential pressure measurement either suffer from viscosity variations in the laminar flow region or have to be designed for turbulent flow conditions resulting in a large pressure drop at the flow meter. Flow rate sensors based on optical or ultrasonic techniques are often too expensive or difficult to install in high pressure applications.

The utilization of the dynamic characteristics of cylindrical chokes for the instantaneous measurement of flow rates has been studied in the past [1]. However, that approach does not include the identification of important fluid parameters such as viscosity and speed of sound. The parameter identification problem has been addressed by the introduction of an additional pressure sensor in the middle of a pipe section in Ref. [2]. The additional information can be used for parameter identification resulting in an optimal fit between the mathematical model and the real system behavior. While in Ref. [2] only one out of two important system parameters could be identified, this paper describes a frequency domain identification approach resulting in a better identification of the so-called "frequency-dependent friction" behavior of laminar pipe flow quantified by a dimensionless dissipation number.

Contributed by the Fluids Engineering Division of ASME for publication in the JOURNAL OF FLUIDS ENGINEERING. Manuscript received February 18, 2008; final manuscript received July 9, 2008; published online October 27, 2008. Assoc. Editor: James A. Liburdy.

2 Laminar Liquid Pipe Flow Model

The behavior of straight transmission lines with a rigid wall and a circular cross section filled with a weakly compressible Newtonian fluid can be described in the frequency domain using the two-port representation [3]:

$$\begin{bmatrix} \hat{p}_2(s) \\ \hat{Q}_2(s) \end{bmatrix} = \begin{bmatrix} \cosh(\gamma L) & -Z\sinh(\gamma L) \\ -\frac{1}{Z}\sinh(\gamma L) & \cosh(\gamma L) \end{bmatrix} \begin{bmatrix} \hat{p}_0(s) \\ \hat{Q}_0(s) \end{bmatrix} \quad (1)$$

with the propagation coefficient γ and the hydraulic impedance Z defined as

$$\gamma = \frac{s}{c_0}\sqrt{-\frac{J_0\left(\sqrt{-\frac{s}{\nu}}R\right)}{J_2\left(\sqrt{-\frac{s}{\nu}}R\right)}} \quad \text{and} \quad Z = Z_0\sqrt{-\frac{J_0\left(\sqrt{-\frac{s}{\nu}}R\right)}{J_2\left(\sqrt{-\frac{s}{\nu}}R\right)}} \quad (2)$$

The speed of sound is given by $c_0=\sqrt{(E/\rho)}$ and the characteristic impedance is $Z_0=(\sqrt{E\rho}/R^2\pi)$. Altogether, the input-output behavior depends on the geometric dimensions R and L of the pipe as well as on the mass density ρ, the bulk modulus of compressibility E, and the kinematic viscosity ν of the fluid. The derivation of the frequency domain model (Eqs. (1) and (2)) from the conservation laws of mass and momentum can be found in Ref. [4].

3 Measurement Principle

The basic idea of the current paper is the indirect measurement of flow rates using pressure sensors along a pipe section. Such a section with an inlet port (Index 0) and an outlet port (Index 2) is shown in Fig. 1. It features two pressures p_0 and p_2 as well as two flow rates Q_0 and Q_2 as port variables. Two out of these four variables can be prescribed as boundary conditions; the other two will be system outputs. Therefore, Eq. (1) represents only one out of six possibilities regarding the causality of pressure and flow rate at the ends of the pipe section. A formulation with prescribed pressure at both boundaries reads

$$\begin{bmatrix} \hat{Q}_0(s) \\ \hat{Q}_2(s) \end{bmatrix} = \frac{1}{Z}\begin{bmatrix} \coth(\gamma L) & -\operatorname{csch}(\gamma L) \\ \operatorname{csch}(\gamma L) & -\coth(\gamma L) \end{bmatrix} \begin{bmatrix} \hat{p}_0(s) \\ \hat{p}_2(s) \end{bmatrix} \quad (3)$$

A measurement of both port pressures p_0 and p_2 can be used for the computation of the flow rates at the ports. However, there are at least two problems to solve.

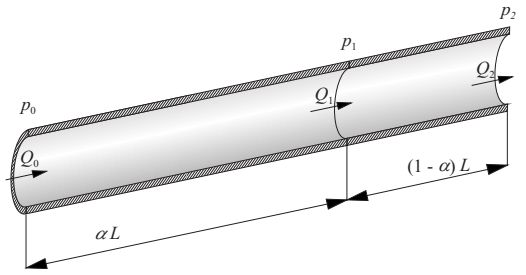

Fig. 1 Pipe section

- Some parameters of the dynamic model are not exactly known. In order to get reliable measurements, these parameters need to be identified before the computation of flow rates from pressure changes can be expected to give reliable results.
- Equation (3) states the relationship between flow rate and pressure in the frequency domain. For instantaneous measurements of transient flow rates, a time domain counterpart has to be found.

In order to identify unknown parameters in the system dynamics, a setup according to Fig. 1 has been proposed in Ref. [2]. A third pressure transducer (Index "1") is added within the pipe section. If only the flow rate at the inlet of the pipe section is to be measured, the dynamic model can be stated as

$$\begin{bmatrix} \hat{p}_1(s) \\ \hat{Q}_0(s) \end{bmatrix} = \begin{bmatrix} \dfrac{e^{\gamma(2-\alpha)L} - e^{\gamma\alpha L}}{e^{2\gamma L} - 1} & \dfrac{e^{\gamma(1-\alpha)L} - e^{\gamma(1+\alpha)L}}{e^{2\gamma L} - 1} \\ \dfrac{1}{Z}\dfrac{e^{2\gamma L} + 1}{e^{2\gamma L} - 1} & \dfrac{-1}{Z}\dfrac{2e^{\gamma L}}{e^{2\gamma L} - 1} \end{bmatrix} \begin{bmatrix} \hat{p}_0(s) \\ \hat{p}_2(s) \end{bmatrix} \tag{4}$$

Since all three pressure signals are measured, the unknown parameters can be identified by matching the first row of the theoretical right-hand side of Eq. (4) to the measured left-hand side.

4 Scaling of the Model

In order to choose a proper time scale and to reduce the number of parameters, the following scaling is used. Time is rescaled by the speed of sound and the length of the pipe section in the form

$$\tau = \frac{c_0}{L}t, \quad \tilde{s} = \frac{L}{c_0}s \tag{5}$$

Using the dimensionless dissipation number $Dn = (\nu L / c_0 R^2)$ [5] and the flow rate scaling

$$\tilde{Q}_0(\tau) = 8DnZ_0Q_0(t) \tag{6}$$

the transfer matrix model Eq. (4) reads

$$\begin{bmatrix} \hat{p}_1(s) \\ \hat{\tilde{Q}}_0(s) \end{bmatrix} = \begin{bmatrix} \dfrac{e^{\tilde{\gamma}(2-\alpha)} - e^{\tilde{\gamma}\alpha}}{e^{2\tilde{\gamma}} - 1} & \dfrac{e^{\tilde{\gamma}(1-\alpha)} - e^{\tilde{\gamma}(1+\alpha)}}{e^{2\tilde{\gamma}} - 1} \\ \dfrac{1}{\tilde{Z}}\dfrac{e^{2\tilde{\gamma}} + 1}{e^{2\tilde{\gamma}} - 1} & \dfrac{-1}{\tilde{Z}}\dfrac{2e^{\tilde{\gamma}}}{e^{2\tilde{\gamma}} - 1} \end{bmatrix} \begin{bmatrix} \hat{p}_0(s) \\ \hat{p}_2(s) \end{bmatrix} \tag{7}$$

with

$$\tilde{Z} = \sqrt{-\frac{J_0\left(\sqrt{-\frac{\tilde{s}}{Dn}}\right)}{J_2\left(\sqrt{-\frac{\tilde{s}}{Dn}}\right)}}$$

and $\tilde{\gamma} = \tilde{s}\tilde{Z}$.

5 Experiments

Figure 2 shows a simplified sketch of the experimental setup for the verification of the instantaneous flow rate measurement. A test pipe of steel with an outer diameter of 12 mm and an inner diameter of 8 mm is connected to an excitation device and a hydraulic servovalve. The excitation device features a housing containing a piston, which is actuated by a piezoelectric actuator. In order to maintain a constant mean pressure value in the pipe and a constant mean load on the piezoelectric actuator, the mean pressure values on both sides of the piston are controlled by two servohydraulic pressure control circuits. The pressure $p_0(t)$ is measured in the upper chamber of the excitation device. This upper chamber is located at the left-hand side of a pipe section with a length of $L = 1321$ mm. After one-third of this length, the pipe is equipped with a second pressure sensor for $p_1(t)$, and a third sensor for $p_2(t)$ is located at the end of the pipe section. From this point to the right, the pipe extends for another 300 mm and enters the pressure control manifold via an elbow fitting. The internal details of the pressure control are not shown in Fig. 2 because of the independence of the proposed measurement principle from the boundary conditions of the pipe section. In other words, the goal is to compute the flow rate at a boundary of the pipe section from the three pressure measurements only.

In order to verify the results, the design of the excitation device allows for some information on the flow rate $Q_0(t)$ to be collected. The movement of the piston within its housing is picked up by two accelerometers. After integration with respect to time, this gives the piston velocity and thus the flow rate into the upper chamber induced by the piston movement. The geometric dimensions of the upper chamber are small compared with the length of the pipe section. Therefore, wave propagation is neglected within this volume. However, the variation of the chamber pressure $p_0(t)$ with time results in a variation of the density of the hydraulic fluid within the chamber and thus in a difference between the flow rate given by the piston velocity and the flow rate entering the pipe section. This difference has to be accounted for by using the time derivative of the pressure signal $p_0(t)$ and the conservation of mass in the upper chamber (see Eq. (9)).

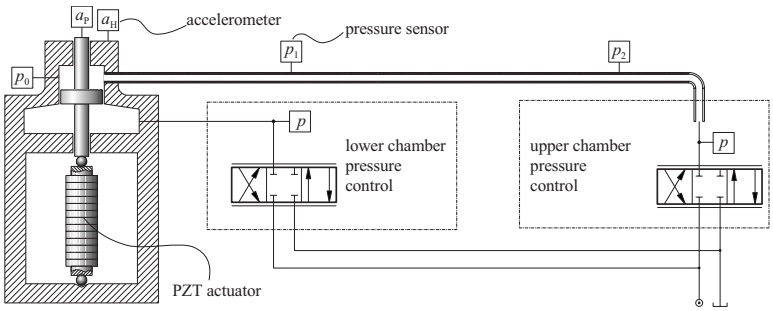

Fig. 2 Experimental setup

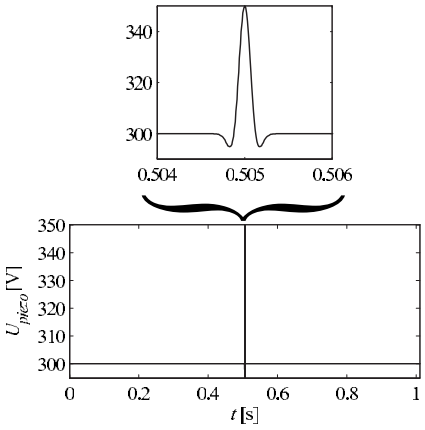

Fig. 3 Gaussian pulse excitation signal: whole period with a blowup of the pulse

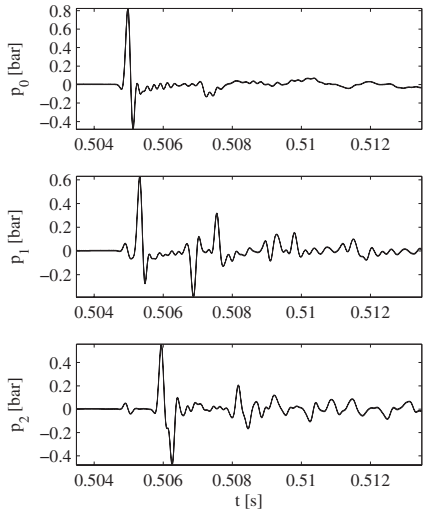

Fig. 4 Segment of measurement data

Measurements are taken from a periodic experiment where a constant voltage of 300 V applied to the piezoelectric transducer (PZT) actuator is superposed by a Gaussian pulse with an amplitude of 50 V and a bandwidth of 2000 Hz. A graphical representation of one period of this excitation signal is shown in Fig. 3. The pulse is repeated every 1.01 s. In the case of a periodically repeated experiment, this choice of period time allows for the partial cancellation of a possible 50 Hz noise picked up from electrical mains. The pressure signals p_0, p_1, and p_2 as well as the two accelerations a_P and a_H are measured with a sampling rate of 100 kHz for 20 periods of the excitation pulse. Figure 4 shows a segment of the measurement data beginning just before the application of the excitation pulse.

The availability of 20 periods allows for an error analysis in terms of a Type A experimental uncertainty according to ANSI/ASME PTC 19.1. At the given period time and sampling rate, each of the three pressure measurements consists of 20 times 101 000 sample values. For each of the 101 000 sample points, the mean value and standard deviation of the three pressures are computed. Standard deviations between $2.6 \cdot 10^{-3}$ bar and $1.1 \cdot 10^{-2}$ bar have been observed for the pressure signals having a typical amplitude of 0.5 bar. The pressure signals used during the rest of this paper are the mean values of 20 periods. Following the ISO uncertainty guide [6], the Type A uncertainty u_p for the mean pressure signals at the 95% confidence level is

$$u_p = 2\frac{\sigma_p}{\sqrt{20}}$$

where σ_p denotes the standard deviation of a pressure signal. Since this gives very small uncertainty values below 2.5×10^{-3} bar compared with the pressure amplitudes of about 0.5 bar, a graphical representation of the error is difficult. The data given in Fig. 4 consist of graphs having a line width exactly proportional to the 95% confidence interval.

The subsequent calculations for the identification of the speed of sound and the dimensionless dissipation number are formulated in the frequency domain. Thus, the time domain data are taken to the frequency domain by a fast Fourier transform (FFT). Figure 5 shows the magnitude spectra for the three pressure measurements. The FFT has been performed on each of the 20 measured periods, allowing for an uncertainty analysis of the spectral magnitude similar to the one performed in the time domain. Again, the line width in Fig. 5 corresponds to the 95% confidence interval. Before computing the FFT of each individual period, the measured signals are multiplied with a Kaiser window function of the form

$$w(k) = \frac{I_0\left(50\sqrt{1-\left(\frac{2k-101\,000+1}{101\,000-1}\right)^2}\right)}{I_0(50)}, \quad k = 0,1,\ldots,101\,000-1$$

i. e., with a window length equal to the number of samples per period and the Kaiser window parameter β=50.

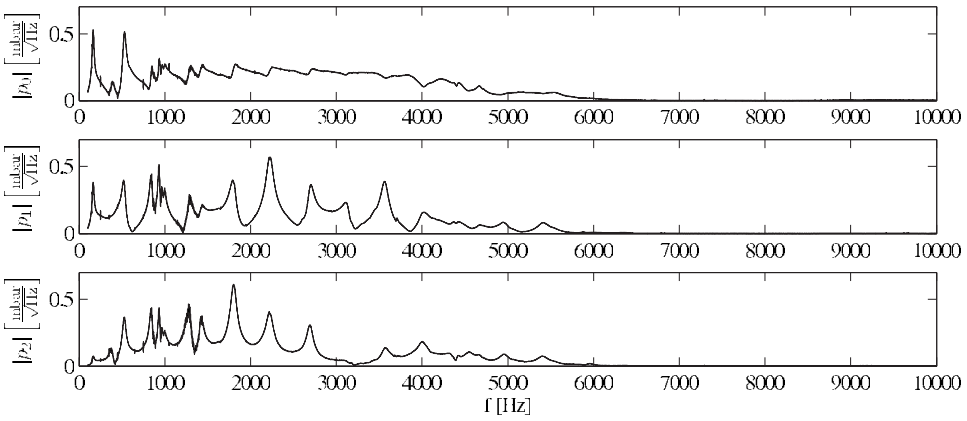

Fig. 5 Discrete amplitude spectra of the pressures p_0, p_1, and p_2

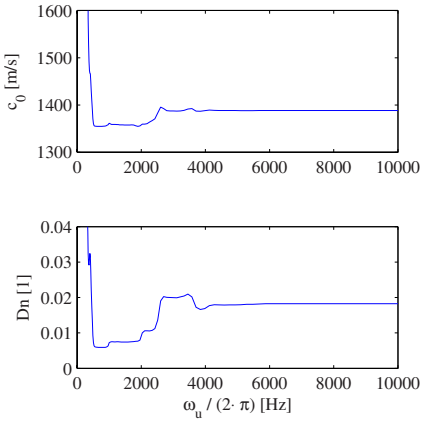

Fig. 6 Dependence of the identified parameters on the upper limit frequency

6 Parameter Identification

The identification of the speed of sound and the fluid viscosity is performed in the frequency domain by using the first row of the matrix in Eq. (7) for the formulation of the optimization problem.

$$\min_{c_0,Dn} \int_{\omega_l}^{\omega_u} \left| \frac{e^{\tilde{\gamma}(2-\alpha)} - e^{\tilde{\gamma}\alpha}}{e^{2\tilde{\gamma}} - 1} \hat{p}_0 + \frac{e^{\tilde{\gamma}(1-\alpha)} - e^{\tilde{\gamma}(1+\alpha)}}{e^{2\tilde{\gamma}} - 1} \hat{p}_2 - \hat{p}_1 \right|^2 d\omega \quad (8)$$

The frequency interval $[\omega_l, \omega_u]$ for which the quadratic error between the Laplace transform of the measured pressure signal p_1 and the value predicted from measurements of p_0 and p_2 is integrated in the optimization criterion has a large influence on the results. The integral in the optimization problem (8) is replaced by a sum of quadratic errors evaluated at the frequencies given by the discrete Fourier transform. This error sum is minimized by the Nelder and Mead simplex search algorithm [7] in the MATLAB optimization toolbox [8] using the routine "fminsearch" with default parameters.

The pressure signals have been picked up by piezoelectric pressure transducers (Kistler type 6005) that do not give information about steady-state pressure. For moderate frequencies greater than zero but well below the eigenfrequency associated with the first eigenmode of axial wave propagation in the pipe section, the measurement data contain little information about the unknown parameters because the spatial pressure distribution is nearly uniform. Thus, no significant contribution to the optimization criterion occurs in a frequency range $0 \leq \omega \leq \omega_l$, where ω_l is the lower limit frequency.

While small variations in the speed of sound dramatically change the shape of all transfer functions of the pipe section, the influence of the dissipation number is much weaker. Roughly speaking, the frequency at which a pole or zero occurs in the magnitude plot is shifted with the speed of sound resulting in a large deviation in terms of an error integral like in Eq. (8). A variation of the dissipation number mainly changes the height of the peaks resulting in a smaller contribution to the error norm. From the nature of the frequency-dependent friction phenomenon, the influence of the dissipation number increases with frequency. Therefore, the upper limit frequency must be high enough in order to include sufficient information about damping effects.

Figure 6 shows the resulting speed of sound and dissipation number for a lower limit frequency $\omega_l = 2\pi \cdot 50$ rad/s and upper limit frequencies $\omega_u = 2\pi \cdot 200, 2\pi \cdot 250, 2\pi \cdot 300, \ldots, 2\pi \cdot 10\,000$ rad/s. For an upper limit frequency below 4000 Hz, a strong influence of ω_u on the resulting parameters exists. While the pressure magnitude plots in Fig. 5 still show considerable excitation between 4000 Hz and 6000 Hz, the results shown in Fig. 6 do not change much above 4000 Hz. A comparison of the measured pressure p_1 against the value computed from the measurements of p_0 and p_2 by application of the appropriate transfer functions according to Eq. (4) is shown in Fig. 7.

In order to validate the proposed approach, the experimental setup is equipped with two accelerometers. One picks up the acceleration of the excitation piston while the other is mounted on the housing. The difference of the two acceleration signals is used in the following equation of continuity for the oil-filled upper chamber of the excitation device.

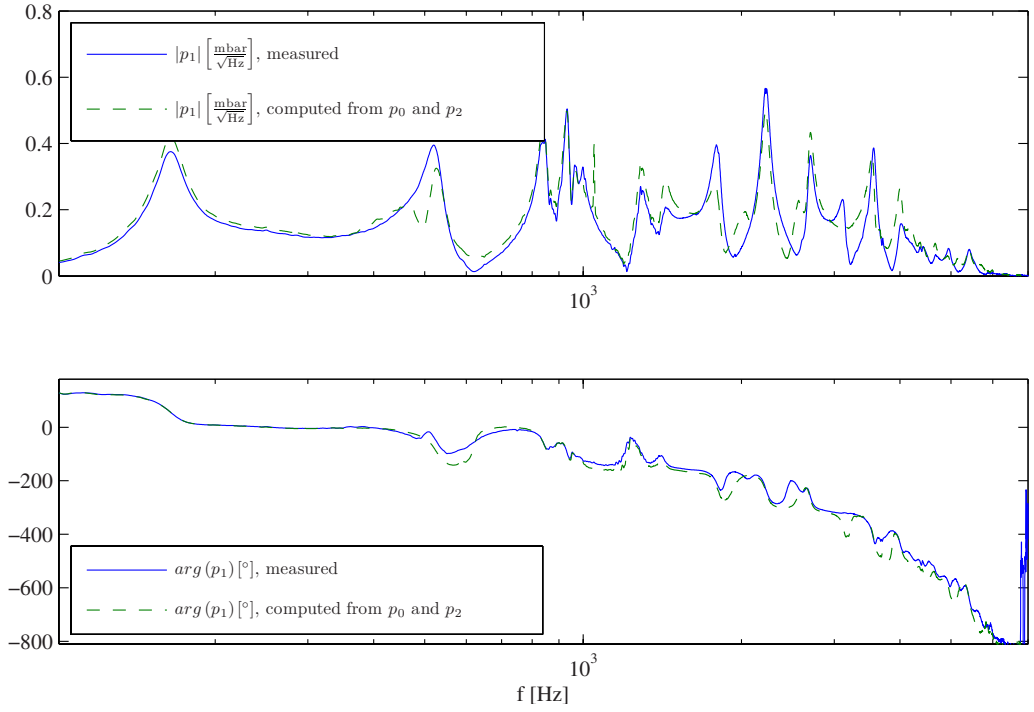

Fig. 7 Comparison of the measured pressure p_1 against the value computed from p_0 and p_2

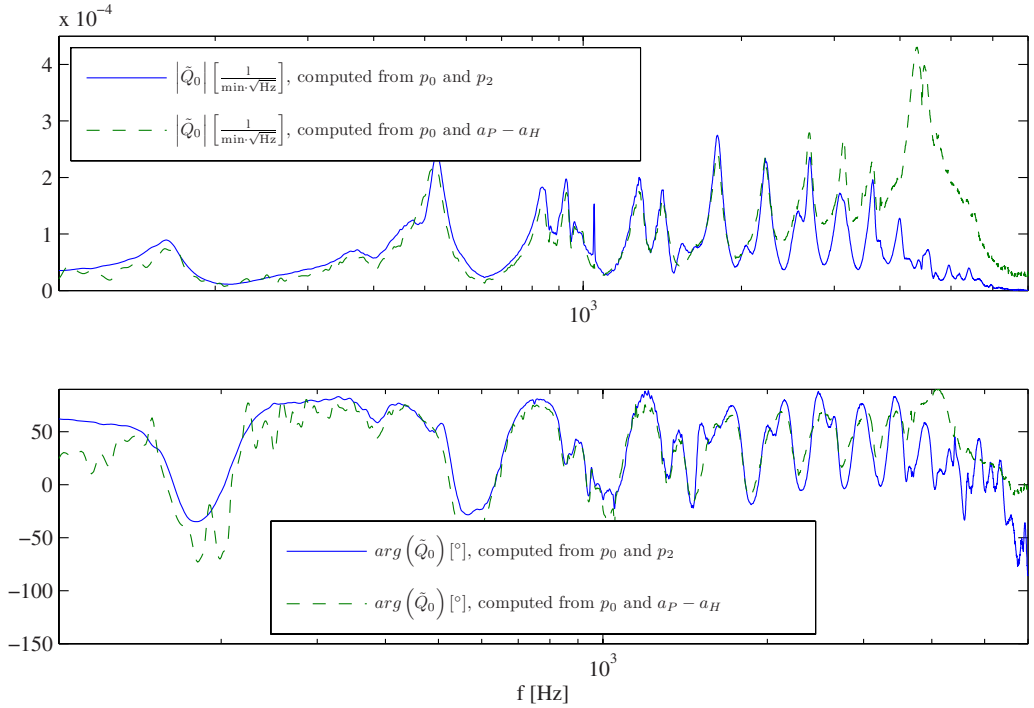

Fig. 8 The match between the left-hand side and right-hand side of Eq. (10)

$$\frac{V_0}{E_{fl}} s\hat{p}_0 = \frac{A_P}{s}(\hat{a}_P - \hat{a}_H) - \hat{Q}_0 \tag{9}$$

While the effective piston area A_p is known approximately, the hydraulic capacity V_0/E_{fl} of the upper chamber is unknown and has to be figured out from measurements before Eq. (9) can be solved for $\hat{Q}_0$. If the proposed measurement principle works, $\hat{Q}_0$ can be computed from $\hat{p}_0$ and $\hat{p}_2$ via Eq. (4). Substituting this into Eq. (9) yields

$$\frac{A_P}{s}(\hat{a}_P - \hat{a}_H) - \frac{V_0}{E_{fl}} s\hat{p}_0 = \hat{p}_0 \frac{1}{Z}\frac{e^{2\gamma L}+1}{e^{2\gamma L}-1} - \hat{p}_2 \frac{1}{Z}\frac{2e^{\gamma L}}{e^{2\gamma L}-1} \tag{10}$$

In case the parameters (V_0/E_{fl}) and A_P can be found such that Eq. (10) holds in a certain frequency range for measured values of $\hat{p}_0$, $\hat{p}_2$, $\hat{a}_P$, and $\hat{a}_H$, then the indirect flow rate measurement can be trusted in this frequency range. Of course the parameters (V_0/E_{fl}) and A_P should be realistic. Figure 8 shows the match between the left- and right-hand sides of Eq. (10) accomplished with a minimization of the sum of squared errors according to Eq. (8) for all frequencies between 100 Hz and 2000 Hz. The lower frequencies are corrupted by noise, and, for frequencies above 2000 Hz, a considerable error probably occurs due to the internal dynamics of the excitation device, which generates a difference between the acceleration picked up at the mounting points of the accelerometers and the effective piston acceleration. However in a region between 100 Hz and 2000 Hz, Eq. (10) is sufficiently fulfilled.

In order to give an uncertainty estimate for the final result of this paper, the uncertainty of the identified parameters c_0 and Dn has to be quantified. The identification procedure described above is influenced both by the measurement data for the pressure signals and by the values of the known parameters L, R, and α. The 95% confidence interval for these parameters is given in Table 1. A Monte Carlo simulation approach is used for the assessment of the uncertainty in the identified parameters: Each of the known parameters is represented by a number of ten values generated by a random number generator parametrized with a normal distribution with mean value and standard deviation given by Table 1. The resulting 10^3 parameter combinations are tried in the identification procedure. This gives 1000 values for both the speed of sound c_0 and the dissipation number Dn. Using the mean values and standard deviations for these 1000 identification outputs, the parameters can be given as

$$c_0 = 1388.1 \pm 1.5\frac{m}{s} \tag{11}$$

$$\mathrm{Dn} = 0.0182 \pm 0.0009 \tag{12}$$

at the 95% confidence level.

7 Time Domain Model

For instantaneous flow rate measurements, a time domain model corresponding to the second row of the matrix in Eq. (7) has to be found. Since this transfer matrix contains transcendental transfer functions, an exact realization in the time domain would require an infinite number of state variables. Therefore, the realization of the input-output behavior given by the transfer functions in Eq. (7) using a time domain model can only be an approximation. A number of different ways for such an approximation have been suggested in the literature.

A method of characteristics in the plane spanned by the time and the longitudinal coordinate can be used for the modeling of wave propagation in fluid transmission lines. The transcendental nature of Eq. (7) shows up in a frequency domain equation relating the pressure drop per unit length to the flow rate at the nodes. Zielke [9] approximated the corresponding weighting function by two matched series expansions and was able to calculate transient

Table 1 Known (with 95% confidence interval) physical parameters of the experimental setup

L	$(1321 \pm 2) \times 10^{-3}$	m	Length of the pipe section
R	$(4 \pm 0.1) \times 10^{-3}$	m	Internal radius of the pipe
α	$\frac{1}{3} \pm 5 \times 10^{-3}$	1	Location of the additional sensor
ρ	830 ± 10	$\frac{\mathrm{kg}}{\mathrm{m}^3}$	Mass density (mineral oil)

pipe flow. In Zielke's method, the weighting function is used in a convolution integral to give weight to past velocity changes. In every time step, this convolution has to be carried out over the whole interval from the start of the simulation to the actual time step. Therefore, the computational effort increases with each time step. This shortcoming has been eliminated by Suzuki et al. [10]. They replaced Zielke's convolution integral by a discrete-time dynamical system. The Zielke-Suzuki method gives a very good state space approximation of the frequency domain model at the price of a high model order [11].

Hullender and coworkers [12] applied modal approximation techniques to hydraulic and pneumatic transmission lines. These models are not as accurate as the Zielke-Suzuki method but require less computation time. One problem with modal approximation is the steady-state and low frequency (below the eigenfrequency associated with the first longitudinal eigenmode of the pipe section) model error.

Since the present paper focuses on a measurement application, a precise model of transient pipe flow is needed in order to get reliable measurement results. In the model construction process, the model error in terms of the maximum error of pressure and flow rate for certain test conditions should be known. Furthermore, the model should be computationally efficient, i.e., for a given tolerable approximation error, the system order should be as low as possible. The Zielke–Suzuki method is not suitable because it does not offer a tradeoff between the approximation error and the system order. Models derived from modal approximations also cannot guarantee a minimal system order.

Therefore, a direct calculation of the model using the inverse Laplace transform and a construction of the discrete-time state space model from the impulse response is used in this paper. The so-called fast inverse Laplace transform (FILT) in the version due to Hosono [13] has been used for the calculation of the step responses of the transfer matrix model in Eq. (7) in a preceding approach [2]. In the present paper, the algorithm of Weeks is used because of its better effectiveness for the computation of the function value at a high number of points in time as needed for the step response.

In the numerical inverse Laplace transform by the method of Weeks a function $f(t)$ is expanded into a Laguerre series.

$$f(t) = e^{\sigma t}\sum_{n=0}^{N-1} a_n e^{-bt} L_n(2bt)$$

where L_n denotes the Laguerre polynomial of degree n, and the coefficient a_n can be computed from

$$a_n = \frac{e^{-i(n\pi/2N)}}{2N}\sum_{j=-N}^{N-1}\left(b + ib\cot\left(\frac{j+\frac{1}{2}}{2N}\pi\right)\right) \times F\left(\sigma + ib\cot\left(\frac{j+\frac{1}{2}}{2N}\pi\right)\right)e^{-i(\pi/N)nj}$$

by the use of an FFT algorithm. The details both on the method and its implementation can be found in Ref. [14].

In order to compute the response of the flow rate $\tilde{Q}_0$ to unit steps of the pressures p_0 and p_2 according to Eq. (7), the two inverse Laplace transforms

$$h_1(\tau) = \mathcal{L}^{-1}\left(\frac{1}{\tilde{s}\tilde{Z}}\frac{e^{2\tilde{\gamma}}+1}{e^{2\tilde{\gamma}}-1}\right), \quad h_2(\tau) = \mathcal{L}^{-1}\left(-\frac{1}{\tilde{s}\tilde{Z}}\frac{2e^{\tilde{\gamma}}}{e^{2\tilde{\gamma}}-1}\right)$$

have to be carried out. The values of $h_1(\tau)$ and $h_2(\tau)$ are computed for $\tau = \Delta\tau, 2\Delta\tau, 3\Delta\tau, \ldots, N\Delta\tau$. A number of 2^{17} points was used in the FFT algorithm and the parameters in the method of Weeks were $\sigma = 0.01$ and $b = 1$. The time step $\Delta\tau$ was set to 1/20, which corresponds to 20 time steps per one wave travel time along the pipe length. A number of $N = 2000$ time steps were computed, resulting in the step response being available over a time interval of 100 wave travel times. The value for $\tau = 0$ is the trivial solution $h_1 = h_2 = 0$. The step response values can be arranged into a matrix $\mathbf{h}$ according to

$$\mathbf{h}_i = [h_1(\tau)h_2(\tau)]|_{\tau=i\Delta\tau}, \quad i = 0,1,2,\ldots,N \tag{13}$$

For the computation of a discrete-time state space system capable of reproducing the step response data given by the matrices $\mathbf{h}_i$ of Eq. (13) the method of Kung [15] is used. Since this method needs impulse response data, the impulse response $\mathbf{G}_i$ is generated from the step response by

$$\mathbf{G}_0 = \mathbf{h}_0$$

and

$$\mathbf{G}_i = \mathbf{h}_i - \mathbf{h}_{i-1}, \quad i = 0,1,2,\ldots,N$$

In a first step, the block Hankel matrices

$$\mathbf{H} = \begin{bmatrix} \mathbf{G}_1 & \mathbf{G}_2 & \mathbf{G}_3 & \cdots & \mathbf{G}_{\frac{N}{2}} \\ \mathbf{G}_2 & \mathbf{G}_3 & \mathbf{G}_4 & \cdots & \mathbf{G}_{\frac{N}{2}+1} \\ \mathbf{G}_3 & \mathbf{G}_4 & \mathbf{G}_5 & \cdots & \mathbf{G}_{\frac{N}{2}+2} \\ \vdots & \vdots & \vdots & \ddots & \vdots \\ \mathbf{G}_{\frac{N}{2}} & \mathbf{G}_{\frac{N}{2}+1} & \mathbf{G}_{\frac{N}{2}+2} & \cdots & \mathbf{G}_{N-1} \end{bmatrix},$$

$$\overline{\mathbf{H}} = \begin{bmatrix} \mathbf{G}_2 & \mathbf{G}_3 & \mathbf{G}_4 & \cdots & \mathbf{G}_{\frac{N}{2}+1} \\ \mathbf{G}_3 & \mathbf{G}_4 & \mathbf{G}_5 & \cdots & \mathbf{G}_{\frac{N}{2}+2} \\ \mathbf{G}_4 & \mathbf{G}_5 & \mathbf{G}_6 & \cdots & \mathbf{G}_{\frac{N}{2}+3} \\ \vdots & \vdots & \vdots & \ddots & \vdots \\ \mathbf{G}_{\frac{N}{2}+1} & \mathbf{G}_{\frac{N}{2}+2} & \mathbf{G}_{\frac{N}{2}+3} & \cdots & \mathbf{G}_N \end{bmatrix}$$

are formed from the impulse response data. The singular value decomposition $\mathbf{H} = \mathbf{U}\boldsymbol{\Sigma}\mathbf{V}^T$ is used for a reduction in the block Hankel matrix to

$$\mathbf{H}_n = \mathbf{U}(:,1{:}n)\Sigma(1{:}n,1{:}n)\mathbf{V}(:,1{:}n)^T$$

where n is the order of the resulting state space system. Using the QR decomposition, $\mathbf{H}_n$ is factored in the form $\mathbf{QR} = \mathbf{H}_n$. With the Moore-Penrose pseudoinverse of the first n columns of $\mathbf{Q}$ and the first n rows of $\mathbf{R}$, the system matrices of the state space system

$$\mathbf{x}_{k+1} = \mathbf{A}\mathbf{x}_k + \mathbf{B}\begin{bmatrix} p_0 \\ p_2 \end{bmatrix}_k \tag{14}$$

$$\tilde{Q}_{0,k} = \mathbf{C}\mathbf{x}_k \tag{15}$$

can be written as

$$\mathbf{A} = \mathbf{Q}(:,1{:}n)^{-1}\overline{\mathbf{H}}\mathbf{R}(1{:}n,:)^{-1}$$

$$\mathbf{B} = \mathbf{Q}(:,1{:}n)^{-1}\mathbf{H}_n, \quad \mathbf{C} = \mathbf{H}_n\mathbf{R}(1{:}n,:)^{-1}$$

The system order n is not known a priori. Given the impulse response data, the state space realizations are computed for increasing values of the system order. In every iteration, the maximum absolute error between the inverse Laplace transformed signal $\{\mathbf{h}_i\}$ and the step response of the state space realization is computed. The algorithm terminates when this error norm drops below a tolerance value of 10^{-4}. This corresponds to an approximation error of 0.01%, which is small enough to be neglected as compared with the experimental uncertainty.

The segment of measurement data shown in Fig. 4 is now resampled with a time step of $(1/20)(c_0/L)$ to fit into the time grid of the state space system (Eqs. (14) and (15)). Assuming zero initial conditions and feeding the resampled values for p_0 and p_2 through the state space system results in a sequence of values for

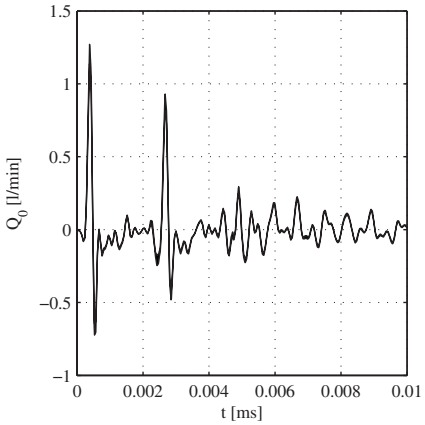

Fig. 9 Flow rate $Q_0(t)$ computed from measurements of $p_0(t)$ and $p_2(t)$

the flow rate $\tilde{Q}_0$. After a rescaling both in time from τ to t according to Eq. (5) and in flow rate from $\tilde{Q}_0$ to Q_0 according to Eq. (6), the flow rate signal is shown in Fig. 9.

The result of the flow rate calculation is influenced by the pressure signals p_0 and p_2 as well as by all parameters needed for the calculation of the matrices **A**, **B**, and **C** in the model (Eqs. (14) and (15)) and the scaling transformation (6). The uncertain parameters entering this calculation are the identified speed of sound c_0 and dissipation number Dn, the geometry parameters L and R, and the mass density ρ.

The mean values and standard deviations of these uncertain parameters are given in Table 1 and Eqs. (11) and (12), respectively. As some of the parameters enter the final result through extensive numerical computations, a Monte Carlo approach similar to the one described above is used for the uncertainty analysis. The maximum uncertainty observed for the final volumetric flow rate plotted in Fig. 9 is ± 0.067 l/min at the 95% confidence level. The line width in the graph resembles the confidence interval.

8 Conclusions and Outlook

The method of indirect flow rate measurement by using pressure sensors along a pipeline section and computing the flow rate at the boundary of the pipeline section by the well known frequency-dependent friction model has been shown to work at least in a certain range of frequencies. While in a preceding approach [2] the identification of crucial system parameters such as speed of sound and dissipation number turned out to be tedious in a time domain setting, a simple minimization of quadratic error norms of transfer functions gives good results in the frequency domain. Due to the assumption of a laminar flow model, the method is restricted to the case of laminar flow in the pipe section equipped with the three pressure transducers.

In order to verify the results experimentally, an excitation device was equipped with accelerometers to get information about the flow rate induced by a piston. This information can be trusted only at low frequencies where internal dynamics of the excitation device like resonant oscillations of the housing can be ruled out. For a proof of the validity of the proposed results, a direct measurement of the piston velocity relative to the housing will be tried in the near future.

In its current form, the proposed method can give information about very fast transient flow rates that occur in fluid power systems with pipeline sections like high pressure piston pumps attached to suction and delivery pipes or variable engine valve actuation systems with fast switching valves embedded in rather spacious hydraulic manifolds with long connecting bores.

Nomenclature

$\mathbf{A}, \mathbf{B}, \mathbf{C}$ = matrices of the linear model, Eqs. (14) and (15)
A_P = cross-sectional area of the excitation piston
E = bulk modulus of compressibility
$\underline{\mathbf{G}}$ = matrix of impulse response values
$\overline{\mathbf{H}}$ = shifted block Hankel matrix
$\mathbf{H}$ = block Hankel matrix
$\mathbf{H_n}$ = block Hankel matrix, reduced to order n
L = length of the pipe section
L_n = Laguerre polynomial of degree n
$\mathbf{Q}, \mathbf{R}$ = QR-decomposition of $\mathbf{H_n}$
R = internal radius of the pipe
$\mathbf{U}, \mathbf{V}$ = matrices in the singular value decomposition of $\mathbf{H}$
V_0 = upper chamber volume
$\tilde{Z}$ = scaled hydraulic impedance
Z = frequency-dependent hydraulic impedance
Z_0 = characteristic hydraulic impedance
$a_H(t)$ = measured acceleration of the housing
a_n = coefficients in the Laguerre series expansion
$a_P(t)$ = measured acceleration of the piston
b = parameter in the method of Weeks
c_0 = speed of wave propagation
$\mathbf{h}$ = matrix of step response values
$h_1(\tau), h_2(\tau)$ = step responses in scaled time
p_0, p_1, p_2 = pressure signals at the pipe section
$\tilde{s}$ = scaled Laplace variable
s = Laplace variable
t = time
α = scaled sensor location
γ = propagation coefficient
$\tilde{\gamma}$ = scaled propagation coefficient
ν = kinematic viscosity
ω_l, ω_u = lower and upper frequency limits
ρ = fluid density
Σ = diagonal matrix of singular values of $\mathbf{H}$
σ = parameter in the method of Weeks
$\Delta\tau$ = dimensionless time step
τ = scaled time variable
$\coth(\cdot)$ = cotangens hyperbolicus
$\operatorname{csch}(\cdot)$ = cosecans hyperbolicus
I_0 = modified Bessel function of the first kind
J_0, J_2 = Bessel functions of the first kind

References

[1] Yokota, S., Arai, K., and Nakano, K., 1989, "Instantaneous Flow Meter for Hydraulic Systems Utilizing the Dynamic Characteristics of Cylindrical Chokes," J. Jpn. Hydraul. Pneum. Soc., **20**(4), pp. 328–335.
[2] Manhartsgruber, B., 2003 "Instantaneous Liquid Flow Rate Measurement Using the Dynamic Characterisitics of Laminar Flow in Circular Pipes," *Proceedings of the Fourth ASME/JSME Joint Fluids Engineering Conference (FEDSM 2003)*, ASME, New York, ASME Paper No. FEDSM2003-45613.
[3] Stecki, J., and Davis, D. C., 1986, "Fluid Transmission Lines: Distributed Parameter Models, Part 1: A Review on the State of the Art," Proc. Inst. Mech. Eng., Part A, **200**, pp. 215–228.
[4] D'Souza, A. F., and Oldenburger, R., 1964, "Dynamic Response of Fluid Lines," ASME J. Basic Eng., **86**, pp. 589–598.
[5] Goodson, R. E., and Leonard, R. G., 1972, "A Survey of Modeling Techniques for Fluid Transients," ASME J. Basic Eng., **94**(2), pp. 474–482.
[6] ISO, 1993, *Guide to the Expression of Uncertainty in Measurement*, International Organization for Standardization, Geneva.
[7] Lagarias, J. C., Reeds, J. A., Wright, M. H., and Wright, P. E., 1998, "Convergence Properties of the Nelder-Mead Simplex Algorithm in Low Dimensions," SIAM J. Optim., **9**(1), pp. 112–147.
[8] MATLAB, 2004, *Optimization Toolbox User's Guide*, 5th ed., The MathWorks, Natick, MA.
[9] Zielke, W., 1968, "Frequency-Dependent Friction in Transient Pipe Flow," ASME J. Basic Eng., **90**(1), pp. 109–115.
[10] Suzuki, K., Taketomi, T., and Sato, S., 1991, "Improving Zielke's Method of Simulating Frequency Dependent Friction in Laminar Liquid Pipe Flow," ASME Trans. J. Fluids Eng., **113**(4), pp. 569–573.

[11] Manhartsgruber, B., 2001, "Computationally Efficient Time Domain Modeling of Fluid Transmission Lines," *Proceedings of the ASME Design Engineering Technical Conferences*, Pittsburgh, PA, Sept. 9–12, ASME, New York, ASME Paper No. DETC2001/VIB-21406.
[12] Hsue, C. Y.-Y., and Hullender, D. A., 1983, "Modal Approximations for the Fluid Dynamics of Hydraulic and Pneumatic Transmission Lines," *Fluid Transmission Line Dynamics 1983*, M. E. Franke and T. M. Drzewiecki, eds., ASME, New York, pp. 51–77.
[13] Hosono, T., 1981, "Numerical Inversion of Laplace Transform and Some Applications to Wave Optics," Radio Sci., **16**(6), pp. 1015–1019.
[14] Weeks, W. T., 1966, "Numerical Inversion of Laplace Transforms Using Laguerre Functions," J. Assoc. Comput. Mach., **13**(3), pp. 419–426.
[15] Kung, S. Y., 1978, "A New Identification and Model Reduction Algorithm via Singular Value Decomposition," *Proceedings of the 12th Asilomar Conference on Circuits, Systems and Computers*, Pacific Grove, CA, Nov. 6-8, pp. 705–714.

Grid Independence Via Automated Unstructured Adaptation

Ronald J. Chila
Rensselaer Polytechnic Institute,
110 8th Street,
Troy, NY 12180

Deborah A. Kaminski
Rensselaer Polytechnic Institute,
110 8th Street,
Troy, NY 12180

Grid independence is frequently an overlooked item in computational fluid dynamics (CFD) analyses. Results obtained from grid dependent solutions may prove to be costly, in that engineering design decisions can be made using potentially faulty information. An automated method for grid independence is developed for two-dimensional unstructured wall function grids. Grid independence is achieved via successive levels of adaptive refinement. Adaptive refinement is performed in an automated manner and is based on multiple field variables. Sensors are placed at strategic locations within the flow field, which are determined by examining the CFD solution of a uniform grid. Three cases are examined, the backward-facing step, flow over an asymmetric transonic airfoil, and hydrogen combustion in a channel. Grid independent solutions are obtained for all three cases. Results for each case compare well with experimental data and/or other numerical predictions. [DOI: 10.1115/1.3001099]

1 Introduction

It is quite common that uniform or embedded grid refinements are performed as substitutes for obtaining true grid independent solutions. In recent years grid adaptation was used as a vehicle for yielding an appropriate grid. While this is more scientific than doing a simple refinement, the adaptation is usually based on the gradient of a single field variable. Knowing which variable and gradient to choose can be difficult. Therefore, this approach does not necessarily ensure a grid independent solution.

Wall function based CFD grids present yet another challenge with respect to obtaining grid independent solutions. When utilizing wall functions, it is usually desired to keep y+ in the range of 30–100. When simple refinements or adaptation are used on wall function grids, there is always the danger of over-refining the cells adjacent to the walls. Over-refinement can potentially push the wall cells into the buffer zone (y+ between 5 and 30) or into the viscous sublayer (y+ less than 5) [1]. Low y+ values can have the effect of "linearizing" the velocity profile adjacent to the walls in question. The net outcome is spurious or incorrect results. Clearly wall function based grids present an additional challenge when attempting to achieve grid independence.

What is presented here is a novel approach toward using an automated adaptation methodology for obtaining grid independence. Moreover, y+ values are not allowed to dip below a value of 30, therefore avoiding the linearization of the logarithmic velocity profile adjacent to the wall. The automated methodology uses two-dimensional unstructured adaptation. Error estimates are based on the undivided differences in field quantities, and autogenerated sensor points are used for determining grid independence. The method uses a two-dimensional cell-based solver (FLUENT 6.0) to produce CFD solutions.

Walsh and Zingg [2] devised a method of unstructured adaptation for aerodynamic computations, based on undivided differences of the density and the Mach number. They utilized high aspect ratio triangular cells adjacent to airfoil walls to accommodate wall integration based turbulence models. The additional complexity associated with incorporating these "stretched" regions of the grid is substantial. Such complexities include issues with point insertion/connection and reduced accuracy of spatial discretization. Mavriplis [3] has also done extensive work in this area. The approach taken here avoids these issues, in that stretched cells are not utilized.

Marcum [4] utilized Euler based solvers and used adaptive methods to look at grid independence. What they found was that resolving flow field discontinuities (i.e., shock waves) via adaptive methods worked very well. However, the discontinuity locations were often in error. They attributed this to the fact that regions upstream and downstream of the discontinuity are sometimes neglected by the adaptive strategy. To overcome this, they proposed utilizing an error indicator based on the undivided differences in velocity magnitude, which was multiplied by a scale factor. The scale factor was essentially a cell size correction factor, which attempted to account for the disparity in neighboring cell sizes.

Warren et al. [5] developed a methodology for creating mixed element grids. This procedure focused on converting stretched triangular elements, which reside adjacent to wall boundaries to quadrilateral elements. While this lends itself to improving solver efficiency, via a reduction of the overall number of flux evaluations required for a given domain, performing adaptation on this type of grid is complicated. This type of grid generation methodology is common in the commercial code marketplace today. It should be stated that this approach is applicable to either wall function or wall integration based turbulence models.

This paper considers three separate cases: the backward-facing step, transonic flow over an asymmetric airfoil, and hydrogen combustion in a channel. The methodology developed is applied to each case and the results are presented and discussed.

2 Methodology

A method is developed by which a grid independent CFD solution may be obtained. The commercial CFD code FLUENT 6.0 is used in conjunction with the two-dimensional grid generator TRIANGLE [6]. TRIANGLE [6] uses a planar straight line graph (PSLG) as input. A variant of Rupert's Delaunay refinement algorithm [7] is implemented in TRIANGLE [6]. This is basically a point insertion algorithm, which successively refines Delaunay and constrained Delaunay triangulations. Rupert's methodology [7] also provides a means for shape and size guarantees on triangular elements.

TRIANGLE [6] and FLUENT are coupled via several FORTRAN programs, FLUENT journal files and UNIX KORN shell scripting. An

Contributed by the Fluids Engineering Division of ASME for publication in the JOURNAL OF FLUIDS ENGINEERING. Manuscript received November 26, 2007; final manuscript received July 4, 2008; published online October 28, 2008. Assoc. Editor: Rajat Mittal.

initial grid is created using TRIANGLE [6] from which cell and vertex files are extracted. The cell and vertex files are converted to NASTRAN format, via user FORTRAN code. The NASTRAN file is then imported into FLUENT 6.0 in an automated fashion via a FLUENT journal file. The CFD problem is set up with the same journal file and a solution is run to convergence. Field data are then output to external files. The field variable data are then fed to another piece of user FORTRAN that calculates solution error estimates. The error estimates are then utilized to determine how the initial grid is refined. Regions of large error receive the greatest grid refinement. This is accomplished by calculating new cell areas based on the error estimates.

An error indicator is developed for the purpose of error estimation. According to Lohner [8], the error indicator should possess the following characteristics

(1) The error indicator should be fast (no noticeable CPU tax).
(2) The error indicator should be dimensionless (ability to monitor several parameters at once).
(3) The error indicator should be bounded.

The following error indicator is used for error estimation purposes:

$$\Delta = |\varphi_1 - \varphi_2|/(\varphi_{\max} - \varphi_{\min}) \quad (1)$$

where φ is any specified field variable and $\varphi_{\max}$ and $\varphi_{\min}$ are the maximum and minimum values in the domain. This error indicator is computed at each of the three edges of a triangular cell (Subscripts 1 and 2 indicate the nodes for that edge). The maximum value of Δ is then used as the representative error estimate for the triangular cell in question. Once error estimates have been established for all cells within the domain, cells with the largest error are tagged for refinement. The area of each tagged cell is then multiplied by a fractional scaling factor, thereby reducing the area of each tagged cell. The new cell areas are output to an external file and then used by TRIANGLE [6] in the next adaptation cycle. TRIANGLE will then refine the grid, as per the new cell area values. The refinement process is repeated until a grid independent solution is obtained.

Grid independence is determined by using "sensor" points placed in the flow domain. Field quantities are extracted at these sensor points during each cycle of the adaptation process and stored in a file. Sensor point generation is accomplished by solving the problem in question using a "sufficiently fine" uniform grid. The density of the uniform grid is determined by first finding the shortest edge in the PSLG representation of the geometry. A cell size is then prescribed by setting cell edge length for the uniform grid to some percentage of the shortest PSLG edge length. It was found that 15% yields sufficiently fine uniform grids. A CFD analysis is performed and a converged solution is produced for the uniform grid. Error estimates are calculated for the uniform grid via the aforementioned procedure. Cells residing within the top 10% of the error estimate population are used for sensor placement. Sensors are then defined at the centroid locations of the cells with the greatest errors. It should be stated that all field quantities are considered for error estimation. The field quantity displaying the greatest error is used for error estimation. The sensor definitions are then exported and used in the aforementioned automated adaptation process. Sensor data are queried at the end of each adaptation cycle and compared against a preset sensor tolerance. The sensor tolerance will be user and problem dependent, in that it is essentially a function of how "grid independent" the user wishes the solution to be. A sensor tolerance of 0.01 (1% difference in field quantities between successive adaptation cycles) would be a stringent requirement on grid independence. The sensor tolerances used for the case studies in this paper are set according to what is perceived to be practical. If the difference in field variables values between successive cycles is less than the user specified sensor tolerance, then grid independence is achieved.

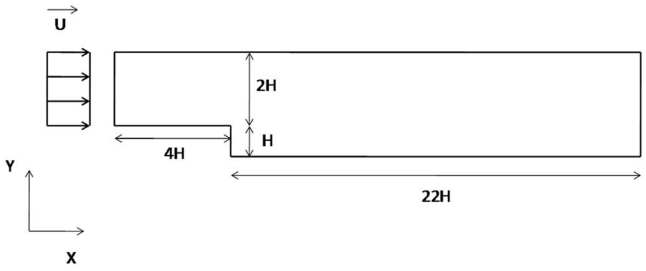

Fig. 1 Backward-facing step geometry

3 Results and Discussion

3.1 Backward-Facing Step. The first case investigated is the backward-facing step. The geometry under investigation is depicted in Fig. 1. The Reynolds number based on the step height is (Re_H=59,000). The initial grid, which is shown in Fig. 2, is extremely coarse. It will be demonstrated that achieving grid independence is not dependent on the cell density of the initial grid.

The problem that is solved is a steady viscous flow of an ideal gas (air). The realizable k-ε turbulence model is employed [9]. The energy equation is solved with viscous dissipation accounted for. All wall boundaries are adiabatic and there is a single inlet and single outlet.

The methodology described in Sec. 2 was employed for the backward-facing step problem. The results show that it takes seven adaptation cycles to achieve grid independence. The 99 sensor points used in determining grid independence are shown in Fig. 3.

Error estimates were calculated for all field quantities throughout the adaptation process. However, the field quantity with the largest error was used for determining whether or not the solution was grid independent. A graph of the mean error estimates for all field quantities is shown in Fig. 4.

Where mean error is defined as

$$\Delta_{\mathrm{mean}} = (\text{Sum of cell errors})/(\text{Total no. of cells}) \quad (2)$$

The velocity error dominates for the backward-facing step and is used in determining grid independence. It is interesting to note the exponential decay of the mean error as the number of cells is increased from adaptation cycle to adaptation cycle. A listing of cell density is shown as a function of adaptation cycle in Table 1. The final adapted grid has 42,920 triangular cells and is depicted in Fig. 5.

All field variables were used for the automated grid adaptation process. Therefore, the user is not required to "guess" which field variable will move the solution toward grid independence. This is handled automatically. Data extracted from the sensor points

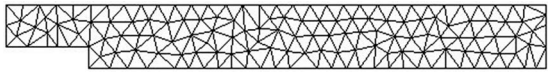

Fig. 2 Original coarse grid for backward-facing step

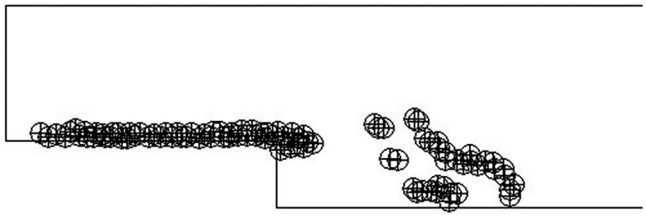

Fig. 3 Sensor placement for backward-facing step case

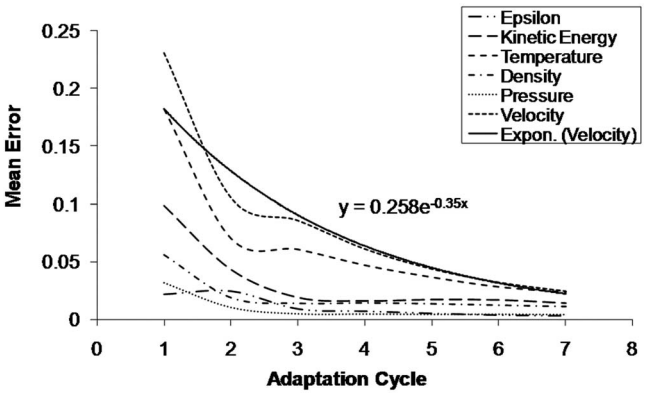

Fig. 4 Mean error versus the adaptation cycle for backward-facing step

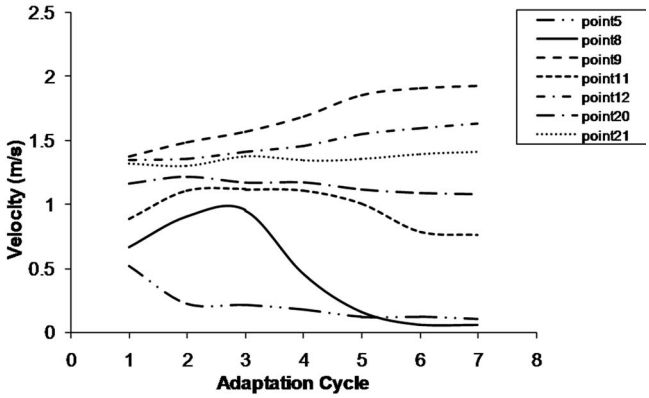

Fig. 6 Sensor point data (velocity) versus the adaptation cycle for backward-facing step

shown in Fig. 6., are utilized to determine grid independence.

Once the sensor point velocity difference (between successive adaptation cycles) is less than a sensor tolerance of 0.01 m/s at all sensor locations, a grid independent solution is obtained. The sensor tolerance used is, of course, problem and situation dependent and in essence, drives the number of adaptation cycles. Seven adaptation cycles may be excessive for larger problems. Here however, the entire process can be run in approximately 8 CPU hours, on a single CPU HP-3600 workstation. Evidence of grid independence for this case is shown in Fig. 6.

It is evident that the velocity data extracted at the sensor points changes only minimally, in accord with the preset sensor tolerance, between adaptation cycles 6 and 7. Even in the reattachment zone (point 8 in Fig. 6), the velocities have leveled off. Starting with an extremely coarse initial grid, it was possible to automatically obtain a grid independent solution without any user intervention. Therefore, it is possible to achieve a grid independent solution for the backward-facing step, utilizing the methodology described herein. This is an important step toward automating the CFD process. As previously stated, grid independence often only receives a cursory consideration in most industrial applications. Enabling an analyst to perform this task automatically lends credibility to any analysis.

Table 1 Cell count for given adaptation cycles (backward-facing step)

Adaptation cycle	No. of cells
1	243
2	862
3	2672
4	7716
5	15,354
6	26,366
7	42,920

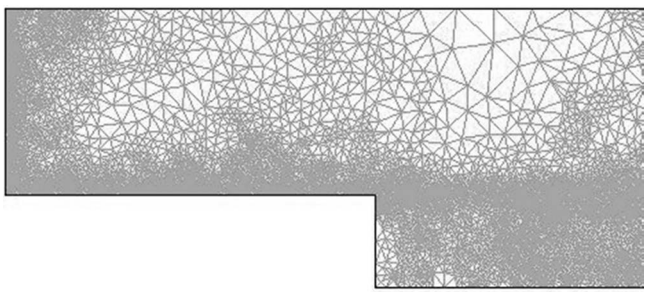

Fig. 5 Final adapted grid for backward-facing step

However, it remains to be shown that y+ values are controlled, as we have been using wall functions in our near wall treatment. A FORTRAN code was developed in such a manner that no refinement would take place, if a given y+ value dropped below a value of 30. This would ensure that we remained within the log-law region and grid independence would be attainable. Figure 7 shows the y+ history as a function of adaptation cycle. The values clearly level off at a y+ of 30.

Obtaining a grid independent solution is not very meaningful if the result sought is incorrect. The result sought in this instance is the correct prediction of the reattachment point (point of zero wall shear), for the backward-facing step. Our CFD model mimics the work of Kim [10]. Kim [10] predicted experimentally that the reattachment point occurs at a distance of $(7.0H+/-0.5H)$, downstream of the step. Figure 8 shows a chart of the reattachment length versus the adaptation cycle. It is clear upon examining this chart that the grid independent solution obtained via the automated process produces an accurate prediction for the reattachment point.

A plot of the stream function is shown in Fig. 9. The recirculation zone just downstream of the step is displayed prominently. The automated process described herein has worked successfully for the backward-facing step. The process can start with a coarse initial grid, produce a grid independent solution and the correct result for this particular problem.

The robustness of the process was tested by running the backward-facing step at two additional Reynolds numbers (Re_H =47,000 and Re_H=117,000). This was done to test any potential sensitivities of the process to boundary conditions and mean flow characteristics. The same sequence of steps was performed for the

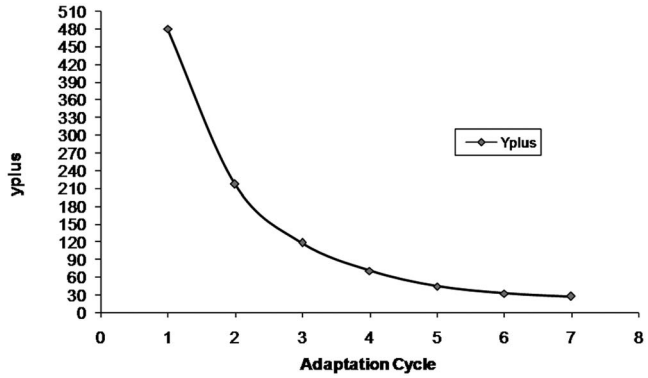

Fig. 7 y+ versus the adaptation cycle for backward-facing step

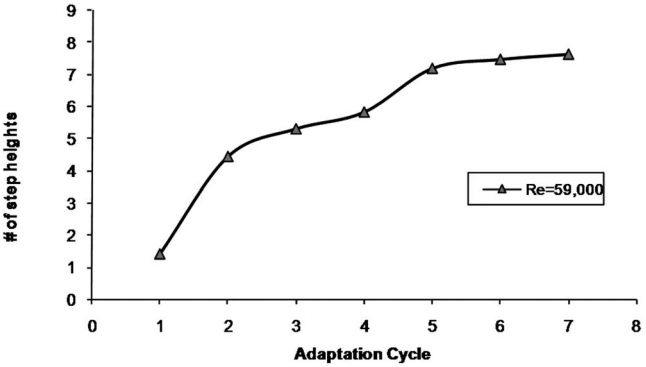

Fig. 8 Reattachment length versus the adaptation cycle for backward-facing step

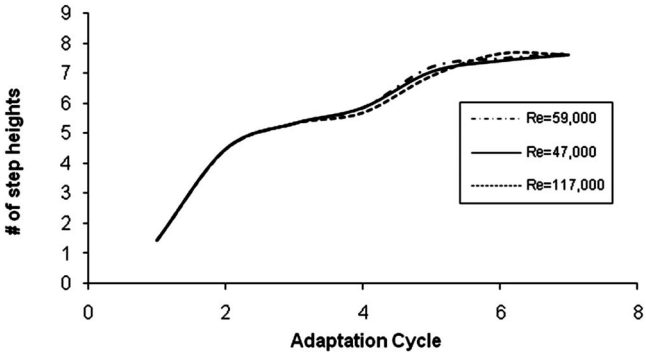

Fig. 10 Reattachment length versus the adaptation cycle for various Reynolds numbers for backward-facing step

two additional cases, and the same initial grid was utilized. The only difference between the cases was the inlet boundary condition. The magnitude of the uniform velocity profile was adjusted to obtain the aforementioned Reynolds numbers. Grid independence was obtained for both of these additional Reynolds numbers.

Once again, a grid independent solution does not mean much without predicting the correct result. Decreasing and increasing the Reynolds number does not have much of an effect with respect to predicting the reattachment length. The reattachment length predictions for all three Reynolds numbers considered are essentially identical. This is evident upon inspection of Fig. 10.

The solution obtained via the methods described herein was compared with a solution from a uniform unstructured triangular grid. The uniform grid had a total of 45,000 triangular cells. The y+ values of the uniform grid were maintained in the range of (30–100) to ensure a fair comparison to the adapted grid solution. The case with (Re_H=59,000) was repeated for the uniform grid. No adaptation was performed. The uniform grid was run to convergence and the reattachment length was computed and compared with the adapted grid solution.

The uniform grid solution yields a reattachment length of 5.5H. This is not nearly as accurate as the adapted grid prediction of 7.6H, when compared with the experimental result of 7.0H+/−0.5H. Therefore, optimal sizing and placement of the triangular cells not only yield a more accurate answer, but a grid independent solution as well. Mean error estimates were calculated for the uniform grid utilizing the same algorithm from the automatic process. The mean error estimates were found to be 20% higher for the uniform grid, as compared with the final adapted grid. It should be noted that the overall triangular cell count for the uniform grid and the final adapted grid were essentially the same (45,000 cells versus 42,920 cells).

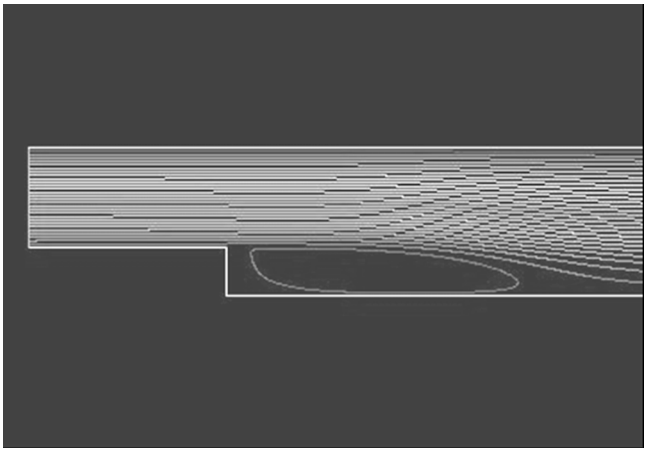

Fig. 9 Contours of the stream function for backward-facing step

3.2 RAE 2822 Airfoil. The second case examined was that of the transonic flow over the RAE 2822 airfoil. The problem at hand is the steady viscous transonic flow of an ideal gas (air) over a nonsymmetric airfoil. The energy equation is solved with viscous dissipation accounted for. All walls are adiabatic and the realizable k-ε turbulence model is utilized. Wall functions are used for wall treatment. The mainstream Mach number is 0.729 and the angle of attack is 2.31 deg. The overall domain extends 21 chord lengths in the x and y directions. The airfoil is situated in the center of this square domain. There is a single inlet and a single outlet. The inlet is a total pressure boundary and the outlet is a static pressure boundary. The top and bottom boundaries of the domain are designated as symmetry planes.

The goal was to apply the automated grid independence process to the RAE 2822 airfoil, to obtain a grid independent solution, and to compare this with the numerical predictions of Slater [11] and the experimental data of Cook [12]. The automated grid independence (AGI) process ran for nine adaptation cycles for the RAE 2822 airfoil. The overall process took approximately 18 CPU hours on a single CPU HP-3600 workstation. Table 2 shows the triangular cell count versus the adaptation cycle for the RAE 2822 airfoil.

The aforementioned automatic process for defining and locating sensor points is used for the RAE 2822 airfoil. A total of 33 sensor points are used for determining grid independence and are clustered around the airfoil, as shown in Fig. 11. The sensor point data was extracted at each adaptation cycle step. Velocity was once again found to be the predominant source of error and was used as the indicator of grid independence. The y+ values were controlled in the same fashion as in the backward-facing step problem. Therefore, an optimal wall function grid is obtained. A sample of velocities extracted at sensor points, for each given adaptation

Table 2 Cell count per adaptation cycle for RAE 2822 airfoil

Adaptation cycle	No. of cells
1	11,116
2	18,760
3	30,210
4	49,374
5	81,984
6	132,284
7	193,158
8	257,446
9	320,174

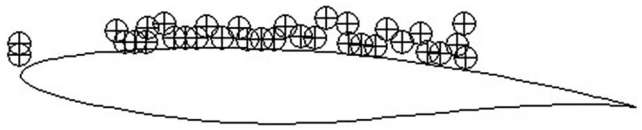

Fig. 11 Sensor point locations for the RAE 2822 airfoil

cycle, is shown in Fig. 12.

Figure 13 shows pressure coefficient predictions, along the airfoil surface. It compares extremely well with the experimental data of Cook [12]. The automated process once again produces a grid independent solution that matches experimental data very well. Contours of pressure, as predicted by Slater [11] using the WIND code, are shown in Fig. 14. A contour plot of pressure around the RAE 2822 airfoil using the process herein is shown in Fig. 15. Qualitatively, the pressure contour predictions compare well with Slater [11]. One difference between the numerical predictions is that Slater [11] prescribes mean flow angles that define the angle of attack. In the current analysis the airfoil was rotated by 2.31 deg, and a uniform inlet velocity profile was implemented.

3.3 Hydrogen Combustion in a Channel. In an attempt to demonstrate the versatility of the automated process, a reacting flow problem was chosen. The problem chosen is the work of DalBello [13], which is another NPARC validation case. DalBello [13] used the WIND code to attempt to match the work of Mani et al. [14]. Mani et al. used the NASTD code to compare with closed form solutions produced with a Runge–Kutta scheme. Therefore, we will not have the benefit of comparison to experimental data in this case. The physical situation in question is shown in Fig. 16.

The physics of the problem are as follows: steady, laminar, reacting, and incompressible ideal gas (density is a function of temperature only). A single step reaction is defined for the combustion of hydrogen with oxygen, and is as follows:

$$0.5O_2 + H_2 \Rightarrow H_2O \tag{3}$$

The work of DalBello [13] and Mani et al. [14] employed more complex reaction definitions, with more species. It was our intent to model the combustion in as simple a manner as possible, focusing on the grid independence aspects and see how well we could match the referenced predictions. The reaction rate exponents were determined empirically using a set of computational experiments, since exact values were not available for this specific problem. The boundary conditions consisted of an inlet, an outlet, and two slip walls. The inlet conditions are shown in Table 3.

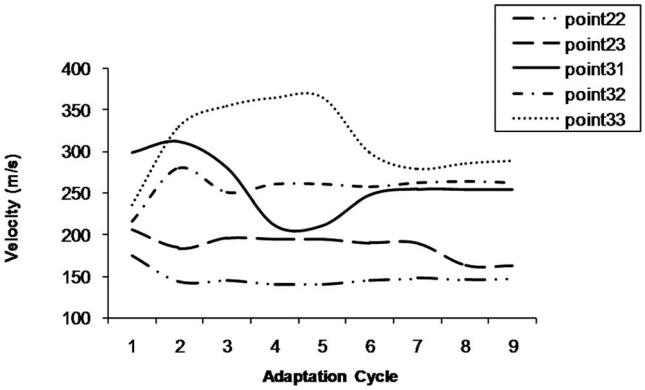

Fig. 12 Sensor point data (velocity) versus adaptation cycle for the RAE 2822 airfoil

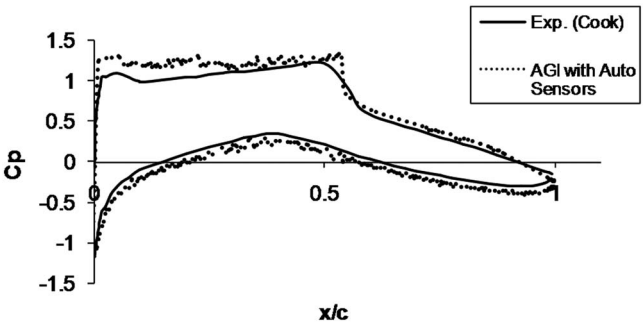

Fig. 13 Pressure coefficient prediction versus experimental data for the RAE 2822 airfoil

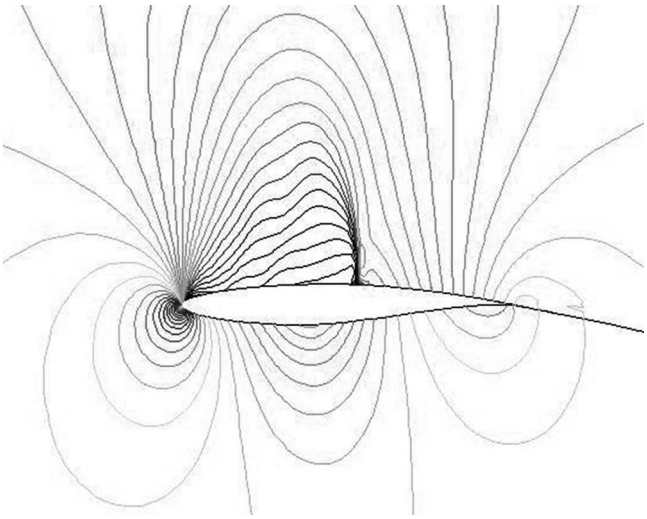

Fig. 14 Pressure contour predictions of Slater [11]

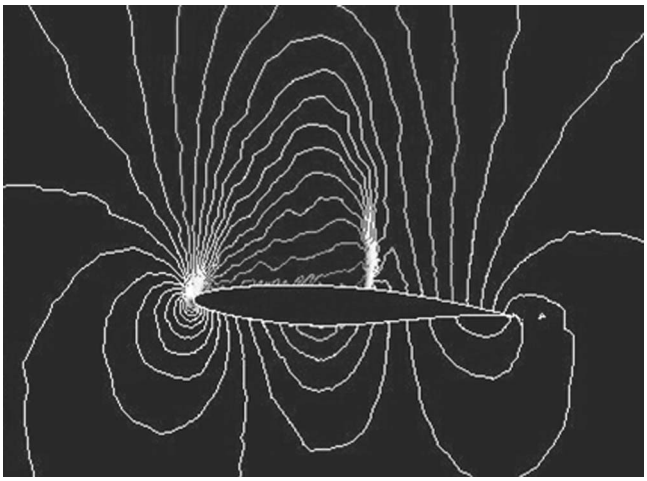

Fig. 15 Pressure contour predictions for the RAE 2822 airfoil

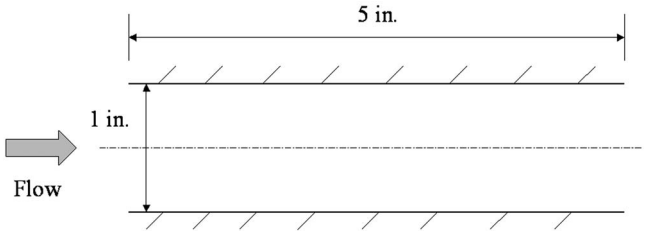

Fig. 16 Combustion channel geometry

Table 3 Inlet conditions for combustion channel

Velocity	600 m/s
Temperature	2500 R
H_2 mass fraction	0.0069
O_2 mass fraction	0.9931
H_2O mass fraction	0.0

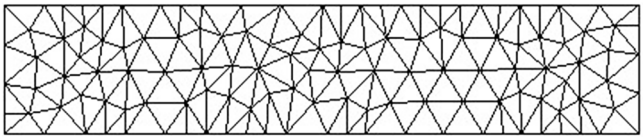

Fig. 17 Combustion channel initial grid

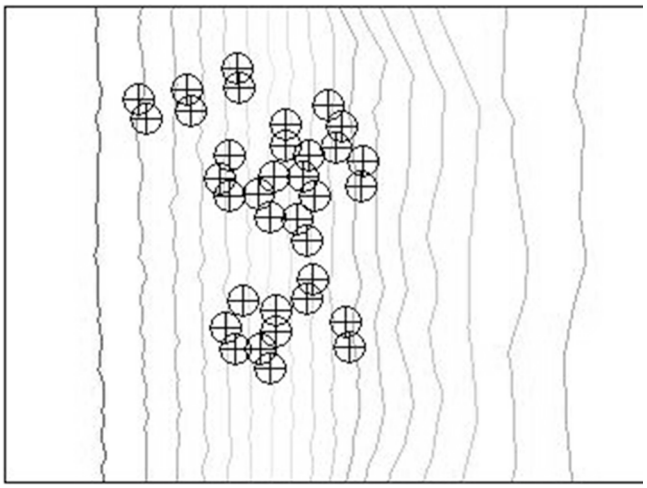

Fig. 18 Sensor point locations for combustion channel (overlay on H_2 mass fraction contours)

Application of these inlet conditions result in a mainstream Mach number of 1.82, which is consistent with the work of DalBello [13]. The outlet condition is at 0.0 psi (gauge). The challenge here was to obtain a grid independent solution and to predict the correct ignition point. The initial grid is shown in Fig. 17.

There were 35 sensors automatically generated and used for determining grid independence. A total of four adaptation cycles were performed and H_2 mass fraction was used as the indicator of grid independence. In this particular case, the choice of indicator of grid independence was not critical. This is true in that the mean error for all field variables behaved similarly. The sensor point locations are shown in Fig. 18 and the final adapted grid in Fig. 19.

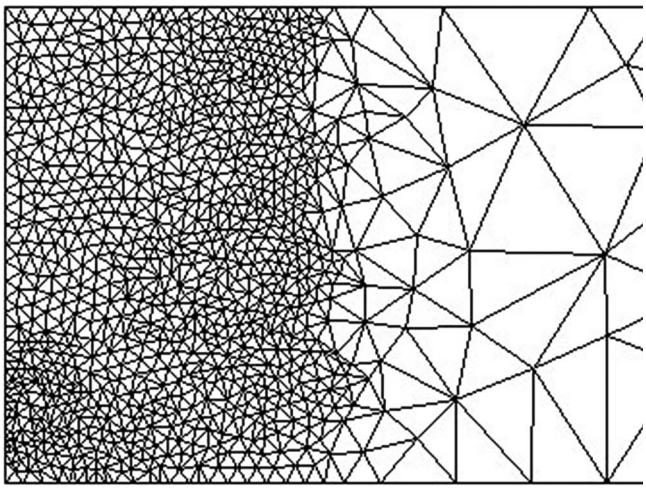

Fig. 19 Final adapted grid for the combustion channel

Grid independence is achieved in two adaptation cycles. The mass fraction values at the sensor locations do not vary much with the addition of more triangular cells. The flow field is established quickly, in response to the chemical reaction. Chemical kinetics seem to dominate, especially in the absence of turbulence (i.e., laminar flow). The pressure drop across the channel is minimal as well. Therefore, we arrive at a grid independent solution quickly in this case.

The results of DalBello [13] are shown in Fig. 20. The results from the automated process are shown in Figs. 21 and 22. The predictions of species mass fractions along the centerline of the channel are in reasonable agreement with the work of DalBello [13]. The H_2O and O_2 predictions are slightly higher. This can be attributed to the fact that we considered only three species and a single step reaction, as compared with seven species and an eight-step reaction. Another difference to be noted is the steepness of the curves in the ignition zone. The curves in DalBello's work are

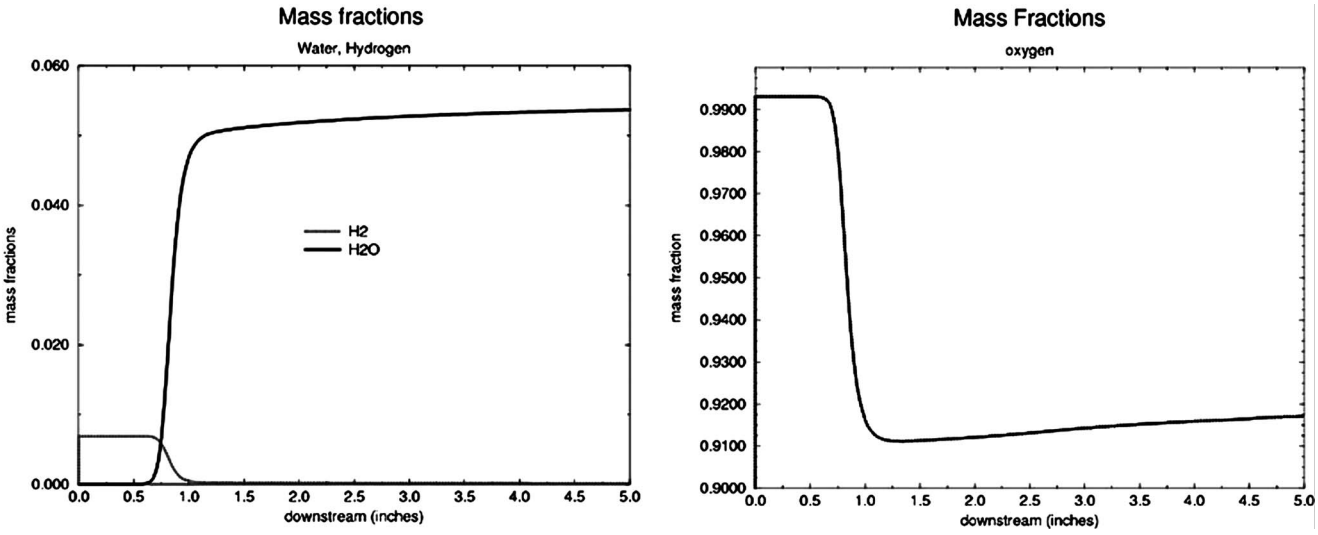

Fig. 20 Results of DalBello [13]

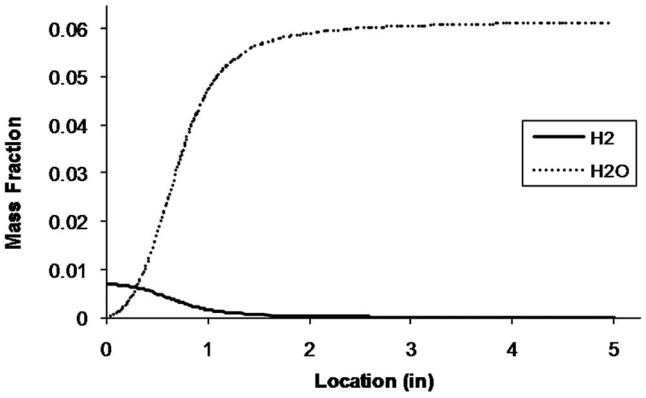

Fig. 21 Predictions of H_2 and H_2O concentrations at the centerline of the combustion channel

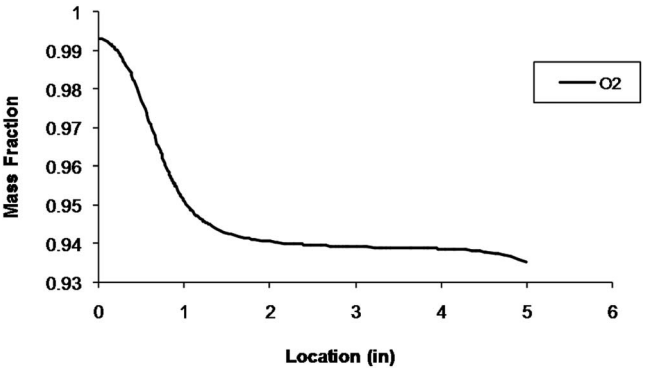

Fig. 22 Predictions of O_2 concentrations at the centerline of the combustion channel

nearly step functions, whereas our predictions are more gradual. The work of Mani et al. [14] are somewhere in between.

4 Conclusions

This paper presents a method in which grid independent solutions may be sought in an automated fashion. A CFD analysis is performed on a uniform grid for a given problem. Sensor points are generated automatically via utilization of error estimates of field quantities from the uniform grid solution. The sensor points are then used in an automated unstructured grid adaptation process. Adaptation is performed in accord with error estimates based on the undivided differences in field variables. The methodology is applied to three very different case studies. The results obtained with the method proposed are quite promising, in that they match the work of the references cited very well.

The hope is that the importance of grid independence is conveyed to the analyst. We have tried to devise a vehicle for obtaining grid independent solutions on grids utilizing wall function based wall treatments. This is an important point to note, in that in general, obtaining grid independence on wall function grids is not possible. This statement is true, if y+ values are not controlled in a systematic fashion. To the best of our knowledge, a methodology to achieve this end does not exist, other than what is presented here.

A natural outgrowth of the work presented herein is the extension to three-dimensional problems. This can be accomplished in two ways. The first would be to find a three-dimensional grid generation program and leverage the algorithms established for the current work. The geometry translation and error estimation routines would require modification to accommodate tetrahedral elements. Another approach would be to implement a modified version of the error estimation algorithm within a commercial CFD code such as FLUENT. At the time this work was performed, there was no practical means for doing this via user coding (user defined function (UDFs)) in FLUENT. The custom error estimates could be used in conjunction with the grid refinement capabilities within the commercial code to perform the adaptation.

References

[1] Burmeister, L. C., 1983, *Convective Heat Transfer*, Wiley, New York.
[2] Walsh, P. C., and Zingg, D. W., 2001, "Solution Adaptation of Unstructured Grids for Two-Dimensional Aerodynamic Calculations," AIAA J., **39**(5), pp. 831–837.
[3] Mavriplis, D. J., 1990, "Adaptive Mesh Generation for Viscous Flows Using Delaunay Triangulation," J. Comput. Phys., **90**, pp. 271–291.
[4] Marcum D. L., 1995, "Generation of Unstructured Grids for Viscous Flow Applications," Paper No. AIAA 95-0212.
[5] Warren G. P., Anderson W. K., Thomas J. L., and Krist S. L., 1991, "Grid Convergence for Adaptive Methods," Paper No. AIAA-91-1592-CP.
[6] Shewchuk, J. R., 1996, "Triangle: Engineering a 2D Quality Mesh Generator and Delaunay Triangulator," *Proceedings of the First Workshop on Applied Computational Geometry*, ACM, pp. 124–133.
[7] Ruppert, J., 1995, "A Delaunay Refinement Algorithm for Quality 2-Dimensional Mesh Generation," J. Algorithms, **18**(3), pp. 548–585.
[8] Lohner, R., 1989, "Adaptive H-Refinement on 3-D Unstructured Grids for Transient Problems," Paper No. AIAA 89-0365.
[9] Shih, T. H., Zhu, J., and Lumley, J., 1993, "A Realizable Algebraic Stress Model," *Proceedings of the Symposium on Turbulent Shear Flow*, Kyoto, Japan, Paper No. 3.5.
[10] Kim, J. J., 1978, "Investigation of Separation and Reattachment of a Turbulent Shear Layer: Flow Over a Backward Facing Step," Ph.D. thesis, Stanford University, Stanford, CA.
[11] Slater, J. W., 1998/2002, "RAE 2822 Transonic Airfoil: Study No. 1," NPARC Validation Study, Sept. and Dec.
[12] Cook, P. H., MacDonald, M. A., and Firmin, M. C. P., 1979,"Aerofoil RAE 2822—Pressure Distributions, Boundary Layer and Wake Measurements, Experimental Database for Computer Program Assessment," AGARD, Report No. AR 138.
[13] DalBello, T., 2002, "Channel Combustion: Study No. 1," NPARC Validation Study, Mar.
[14] Mani, M., Bush, R. H., and Vogel, P. G., 1991, "Implicit Equilibrium and Finite-Rate Chemistry Models for High Speed Flow Applications," Paper No. AIAA-91-3299-CP.

The Influence of Slip Boundary Conditions on Peristaltic Pumping in a Rectangular Channel

X. Mandviwalla

R. Archer

Department of Engineering Science,
The University of Auckland,
Private Bag 92019,
Auckland 1001, New Zealand

The flow of an incompressible fluid is modeled in a channel of a rectangular cross section with two symmetric peristaltic waves propagating on the top and bottom. A low Reynolds number and a long wavelength are assumed. The effect on pumping of the inclusion of slip boundary conditions on the side walls is investigated. [DOI: 10.1115/1.3001107]

Keywords: peristaltic pumping, slip

1 Introduction

Peristaltic pumping of a fluid involves the progression of waves traveling along the boundaries of an enclosing tube or channel. In human physiology peristalsis is used to transport fluids and solids around the body, such as the flow of urine in the ureter. Peristalsis is also found in medical devices (e.g., drug delivery) and industrial applications where the pumping fluid should not be in contact with the pump's machinery, as it is corrosive or is required to be kept sanitary. Fundamental modeling work on peristaltic pumping was developed and published in the 1960s and 1970s to study pathologies in the ureter and small blood vessels. Fung and Yih [1] developed an analytic solution to a two-dimensional tube with infinite trains of peristaltic waves on both the top and bottom. Fung and Yih [1] assumed that the peristaltic wave amplitude is small compared with the radius of the tube. Shapiro et al. [2] also developed an analytic solution for two-dimensional peristaltic flow. In contrast to Fung and Yih [1], their method assumed a long peristaltic wavelength (in comparison to the channel radius) as well as a zero Reynolds number (viscous forces are dominant). Subba Reddy et al. [3] expanded the work of Shapiro et al. [2] to three dimensions to consider the effect of lateral walls in a rectangular channel.

Slip conditions at a boundary refer to the velocity of the fluid at a solid-liquid interface not being equal to the velocity of the solid. Physically this condition can be obtained by chemically increasing the hydrophobicity or the wetting angle of the solid boundaries. Slip can also be observed in rarefied gas flows in microelectromechanical systems (MEMS) technologies. For our purposes we impose Navier's slip condition on the side wall boundaries, as presented below in Eq. (1) [4]. The variable l_{Slip} is defined as the slip length and is a material property of the solid boundaries. Specifically, it is the distance beyond the fluid-solid interface at which the velocity extrapolates to zero. If l_{Slip} is equal to zero, then Eq. (1) will return to the traditional no-slip condition

$$\mathbf{u} - (\mathbf{u}\cdot\mathbf{n})\mathbf{n} = l_{\text{Slip}}\{\mathbf{E}\cdot\mathbf{n} - [(\mathbf{E}\cdot\mathbf{n})\cdot\mathbf{n}]\mathbf{n}\} \tag{1}$$

where $\mathbf{u}$ is the velocity vector (m s^{-1}), $\mathbf{n}$ is the unit normal, l_{Slip} is the slip length (m), and $\mathbf{E}$ is the rate of the strain tensor $(1/2(\nabla\mathbf{u}+\nabla^T\mathbf{u}))$.

Chu and Fang [5] presented a solution using slip boundary conditions for rarefied gas flow in a two-dimensional channel. This work was based on the theory of Fung and Yih [1].

The current study is based on the theory of Shapiro et al. [2] where a three-dimensional solution for a rectangular channel was obtained. The work of Subba Reddy et al. [3] is extended to include slip boundary conditions.

The aim of this paper is to investigate the effects of slip on fluid flow by adding Navier's slip boundary conditions to the side walls of a rectangular channel undergoing peristalsis. Interest in this problem came from work done to model fluid flow in conducting polymer based micropumps [6]. An analytical solution was sought in order to help understand the benefits of pursuing surface modification to induce slip flow in the micropump designs.

2 Model Formulation

The model geometry is a channel of the rectangular cross section measuring $2a$ in height and $2d$ in width (Fig. 1). Peristaltic waves are present on the top and bottom of the channel. Equation (2) below represents the waves. The variables presented in Eq. (2) are illustrated in Fig. 1.

$$Z = H(X,t) = \pm a \pm b\cos\frac{2\pi}{\lambda}(X - ct) \tag{2}$$

where X and Z are Cartesian coordinates, a is the half height of the channel (m), b is the amplitude of the wave (m), c is the speed of the wave (m s^{-1}), t is the time (s), and λ is the wavelength (m).

The ratio of the wave amplitude to the wavelength is considered to be small. Consequently, the pressure is considered to be uniform over every channel cross section, allowing for the use of a wave-frame traveling at velocity c. Equation (3) shows how the variables in the laboratory frame (X, Y, Z) are transformed into the moving wave-frame (x, y, z)

$$X = X - ct, \quad y = Y, \quad z = Z, \quad u = U - c, \quad w = W$$

$$p(x,z) = P(X,Z,t) \tag{3}$$

where u and w are wave-frame velocities for the x and z directions, respectively (m s^{-1}), U and W are the laboratory frame velocities for the X and Z directions, respectively (m s^{-1}), P and p are the pressures in the laboratory and wave-frame, respectively (Pa).

Working in the wave-frame we employ the following nondimensional quantities:

$$\delta = \frac{a}{\lambda}, \quad \bar{x} = \frac{x}{\lambda}, \quad \bar{z} = \frac{z}{a}, \quad \bar{w} = \frac{w}{c\delta}, \quad \bar{u} = \frac{u}{c}$$

$$\bar{t} = \frac{ct}{\lambda}, \quad h = \frac{H}{a}, \quad \phi = \frac{b}{a}, \quad \bar{p} = \frac{a^2 p}{\mu c\lambda}, \quad \bar{l}_{\text{Slip}} = \frac{l_{\text{Slip}}}{d}$$

where d is the channel half width (m), H is the wave surface (m), and μ is the dynamic viscosity (kg m^{-1} s^{-1}).

The velocity in the z direction (w) is further scaled down by a factor (δ) when compared with the x direction (u). This is a consequence of the long wave assumption, and is similarly seen in the theory of shallow water waves [7].

We assume that the fluid contained within the channel has a constant viscosity and is incompressible. The Navier–Stokes and continuity equations with our nondimensional variables (without bars) are presented as

$$\text{Re}\left(u\frac{\partial u}{\partial y} + w\frac{\partial u}{\partial z}\right) = -\frac{dp}{dx} + \delta^2\frac{\partial u^2}{\partial x^2} + \beta^2\frac{\partial^2 u}{\partial y^2} + \frac{\partial^2 u}{\partial z^2}$$

Contributed by the Fluids Engineering Division of ASME for publication in the JOURNAL OF FLUIDS ENGINEERING. Manuscript received April 2, 2008; final manuscript received September 16, 2008; published online October 24, 2008. Assoc. Editor: Rajat Mittal.

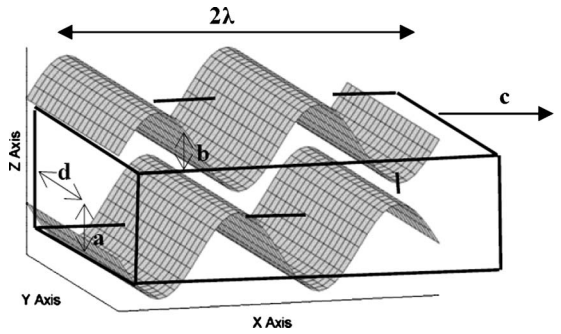

Fig. 1 An illustration of the model geometry

$$\mathrm{Re}\ \delta^2\left(u\frac{\partial w}{\partial y}+w\frac{\partial w}{\partial z}\right)=-\frac{dp}{dx}+\delta^2\left(\delta^2\frac{\partial w^2}{\partial x^2}+\beta^2\frac{\partial^2 w}{\partial y^2}+\frac{\partial^2 w}{\partial z^2}\right)$$

$$\frac{dp}{dy}=0$$

$$\frac{du}{dx}+\frac{dw}{dz}=0 \tag{4}$$

where Re is the Reynolds number ($\rho ac\delta/\mu$) and β is the aspect ratio of the channel (a/d).

By further assuming that the Reynolds number is small (Re $\ll 1$) and the wavelength is long ($\delta \ll 1$). We can simplify the equations to the following:

$$\beta^2\frac{\partial^2 u}{\partial y^2}+\frac{\partial^2 u}{\partial z^2}=\frac{dp}{dx} \tag{5}$$

$$\frac{\partial u}{\partial y}+\frac{\partial w}{\partial z}=0 \tag{6}$$

The corresponding no-slip conditions on the top and bottom of the channel are shown as

$$u=-1 \quad \text{at} \quad z=\pm 1\pm\phi\cos 2\pi x \tag{7}$$

The slip conditions on the side walls are shown in Eq. (8). The imposition of slip in the x-direction (but not in the z-direction) on the side walls of the channel (but not on the top and bottom) was inspired by design/fabrication considerations for a proposed microfluidic peristaltic pump.

$$u=-\frac{l_{\mathrm{Slip}}}{2}\frac{\partial u}{\partial y}-1 \quad \text{at} \quad y=1, \quad u=+\frac{l_{\mathrm{Slip}}}{2}\frac{\partial u}{\partial y}-1 \quad \text{at} \quad y=-1 \tag{8}$$

We can transform Eq. (5) into Laplace's equation (Eq. (10)) by introducing the variables $x=x'$, $y=\beta y'$, and $z=z'$ and by substituting Eq. (9).

$$u=u'-1-\frac{1}{2}\frac{dp}{dx'}(h^2-z'^2) \tag{9}$$

$$\frac{\partial^2 u'}{\partial y'^2}+\frac{\partial^2 u'}{\partial z'^2}=0 \tag{10}$$

The corresponding boundary conditions become

$$u'=0 \quad \text{at} \quad z'=\pm h(x') \tag{11}$$

$$u'=\mp\frac{l_{\mathrm{Slip}}}{2}\frac{\partial u'}{\partial y}+\frac{1}{2}\frac{dp}{dx'}(h^2-z'^2) \quad \text{at} \quad y'=\pm\frac{1}{\beta} \tag{12}$$

By introducing $u'(y',z')=Y(y)Z(z)$ we can substitute and separate Eq. (10) into two parts.

$$\frac{1}{y'}\frac{d^2Y}{dy'^2}=\alpha^2, \quad \frac{1}{z'}\frac{d^2Z}{dz'^2}=-\alpha^2 \tag{13}$$

By solving these equations we can arrive at the solution below.

$$u'=(A\cosh\alpha y'+B\sinh\alpha y')(C\cos\alpha z'+D\sin\alpha z') \tag{14}$$

Substituting the boundary condition shown in Eqs. (11) and (12), results in the two equations below.

$$(A\cosh\alpha y'+B\sinh\alpha y')(C\cos(\alpha h)+D\sin(\alpha h))=0$$

$$(A\cosh\alpha y'+B\sinh\alpha y')(C\cos(-\alpha h)+D\sin(-\alpha h))=0 \tag{15}$$

The solution is treated as the sum of an infinite series, as shown as

$$u'=\sum_{n=1}^{\infty}U_n=\sum_{n=1}^{\infty}\left(F_n\cosh\left(\frac{\alpha_n y'}{h}\right)+G_n\sinh\left(\frac{\alpha_n y'}{h}\right)\right)\cos\left(\frac{\alpha_n z'}{h}\right) \tag{16}$$

where

$$\alpha_n=\frac{(2n-1)\pi}{2}$$

$$F_n=A_nC_n$$

$$G_n=A_nB_n$$

Combining solutions and substituting slip boundary conditions yields

$$\sum_{n=1}^{\infty}X_n=\sum_{n=1}^{\infty}W_n+\frac{1}{2}\frac{dp}{dx}(h^2-z'^2)$$

$$\sum_{n=1}^{\infty}X_n^*=-\sum_{n=1}^{\infty}W_n^*+\frac{1}{2}\frac{dp}{dx}(h^2-z'^2) \tag{17}$$

where

$$X_n=\left(F_n\cosh\left(\frac{-\alpha_n}{h\beta}\right)-G_n\sinh\left(\frac{-\alpha_n}{h\beta}\right)\right)\cos\left(\frac{\alpha_n z'}{h}\right)$$

$$W_n=\frac{l_{\mathrm{Slip}}}{2}\left(F_n\frac{\alpha_n}{h}\sinh\left(\frac{-\alpha_n}{h\beta}\right)+G_n\frac{\alpha_n}{h}\cosh\left(\frac{-\alpha_n}{h\beta}\right)\right)\cos\left(\frac{\alpha_n z'}{h}\right)$$

$$X_n^*=\left(F_n\cosh\left(\frac{\alpha_n}{h\beta}\right)-G_n\sinh\left(\frac{\alpha_n}{h\beta}\right)\right)\cos\left(\frac{\alpha_n z'}{h}\right)$$

$$W_n^*=\frac{l_{\mathrm{Slip}}}{2}\left(F_n\frac{\alpha_n}{h}\sinh\left(\frac{\alpha_n}{h\beta}\right)+G_n\frac{\alpha_n}{h}\cosh\left(\frac{\alpha_n}{h\beta}\right)\right)\cos\left(\frac{\alpha_n z'}{h}\right)$$

By using orthogonality and integrating by parts we arrive at the solution below (Eq. (18)). Note that the application of the boundary conditions gives $G_n=0$.

$$u'=\sum_{m=1}^{\infty}\frac{dp}{dx}\frac{-2h^2(-1)^m}{\alpha_m^3\cosh\left(\frac{\alpha_m}{h\beta}\right)+\frac{l_{\mathrm{Slip}}}{2}\frac{\alpha_m}{h}\sinh\left(\frac{\alpha_m}{h\beta}\right)}\times\cosh\left(\frac{\alpha_m y'}{h(x)}\right)\cos\left(\frac{\alpha_m z'}{h(x)}\right) \tag{18}$$

Substituting back into Eq. (9) results in the solution given by

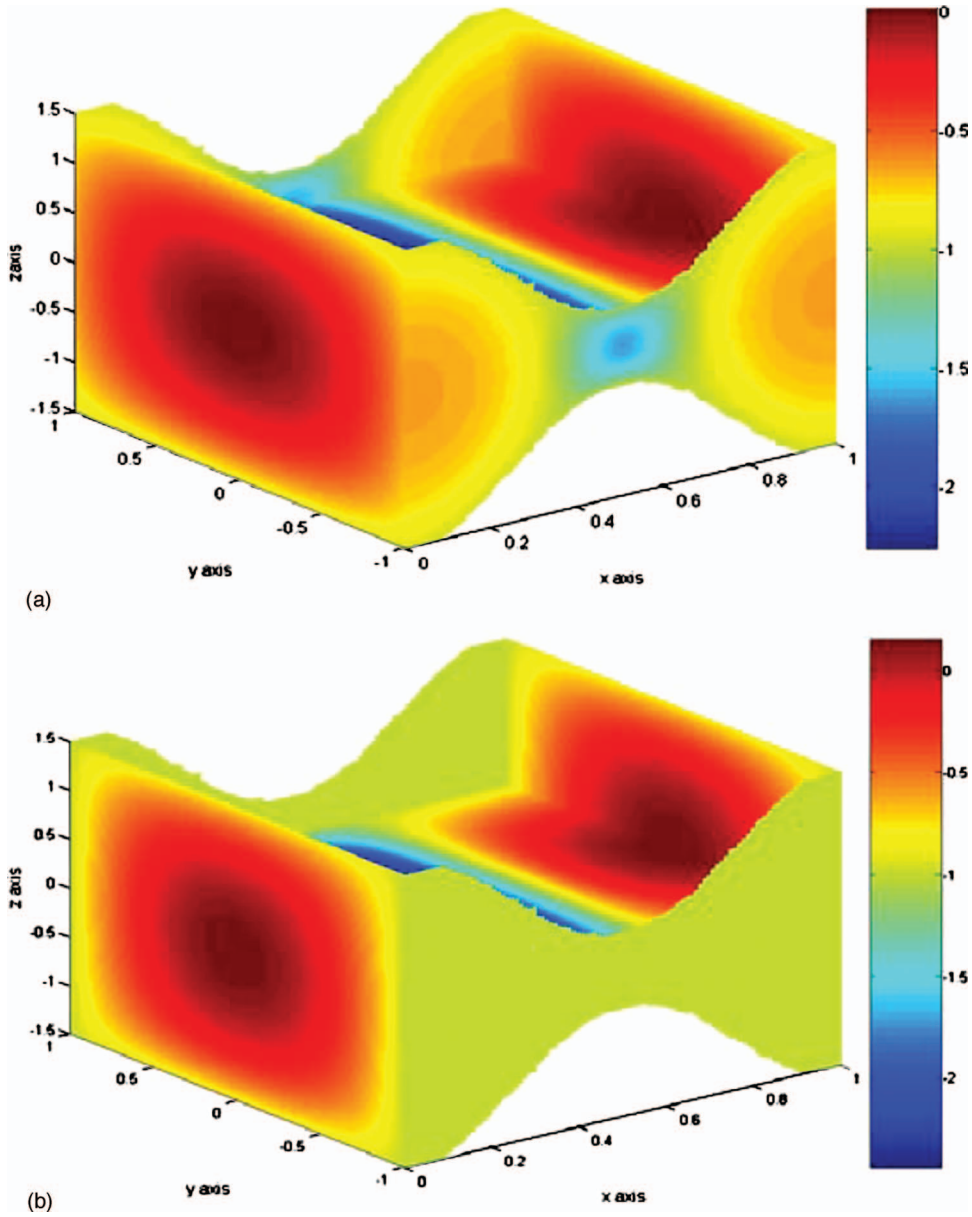

Fig. 2 (***a***) **Shows a solution involving a nondimensional slip length of 0.5 for the side walls and** (***b***) **shows a no-slip solution.** ϕ**=0.6 and** β**=1 for both solutions.**

$$u = -1 - \frac{1}{2}\frac{dp}{dx}(h^2 - z^2) + \sum_{m=1}^{\infty} \frac{dp}{dx} \times \frac{-2h^2(-1)^m}{\alpha_m^3 \cosh\left(\frac{\alpha}{h\beta}\right) + \frac{l_{\text{Slip}}}{2}\frac{\alpha_m}{h}\sinh\left(\frac{\alpha_m}{h\beta}\right)} \cosh\left(\frac{\alpha_m y}{\beta h}\right)\cos\left(\frac{\alpha_m z}{h}\right) \tag{19}$$

This reduces to Subba Reddy's solution when $l_{\text{slip}}=0$. The solution reduces to the 2D solution of Shapiro et al. [2] when l_{slip} is infinite. The pressure gradient (dp/dx) is found in a similar fashion to Ref. [3], which involves integrating the velocity in a quadrant (a quarter of the channel cross section) to find an average flux. The result is rearranged for dp/dx and presented in

$$\frac{dp}{dx} = \frac{Q - 1 + h(x)}{P} \tag{20}$$

where Q is the average flux over a wave period T.

$$p = \sum_{m=1}^{\infty} \frac{-2h(x)^2(-1)^m}{\alpha_m^3 \cosh\left(\frac{\alpha_m}{h(x)\beta}\right) + \frac{l_{\text{Slip}}}{2}\frac{\alpha_m}{h(x)}\sinh\left(\frac{\alpha_m}{h(x)\beta}\right)} \sinh\left(\frac{\alpha_m}{\beta h}\right) \times \left(\frac{\beta h(x)^2}{\alpha_m^2}\right)(-1)^m - \frac{h(x)^3}{3}$$

The pressure drop Δp along a wave is calculated by integrating Eq. (20) with respect to x. This is performed numerically due to the difficulty in evaluating the integral analytically.

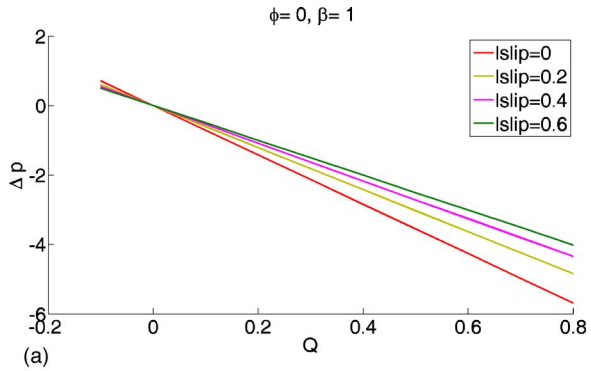

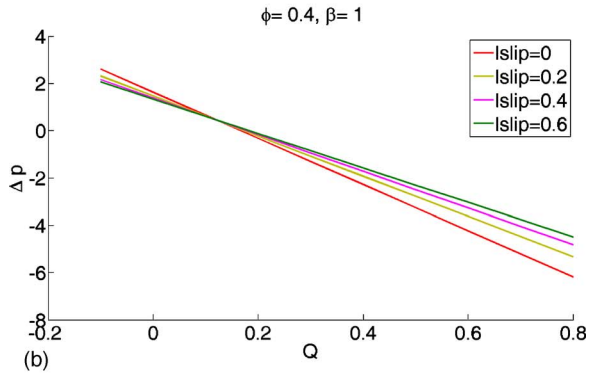

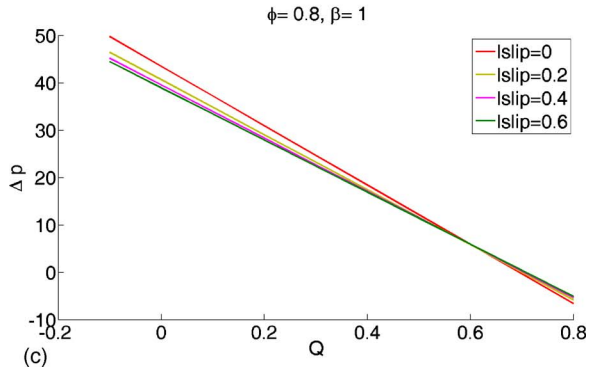

Fig. 3 Plots (*a*)–(*c*) relate the pressure drop (Δp) and the average flux (Q) for varying nondimensional slip lengths (l_{Slip} =0,0.2,0.4,0.6). All plots solve for a channel with a square cross section in *x-z* (β=1). (*a*) Plots ϕ=0, which result in a Poiseuille flow as no peristaltic wave is present, (*b*) plot results with ϕ=0.4, and (*c*) plot results with ϕ=0.8.

3 Results

Figure 2(*a*) shows velocity slices for the rectangular channel. A relatively large nondimensional slip length of 0.5 was selected to show the velocity contours on the side walls. The velocity is still in the nondimensional form and is active in the wave-frame. Therefore, a velocity of −1 is essentially a true velocity of zero in the fixed frame. The contrasting no-slip solution is shown in Fig. 2(*b*), where the side wall is green indicating a wave-frame velocity of −1.

One method to analyze pumping performance is to consider the relationship between pressure and flux. Figure 3 plots three graphs for pressure drop versus the average flux for three nondimensional slip lengths (l_{Slip}=0, l_{Slip}=0.2, l_{Slip}=0.4). The three graphs relate to values of ϕ=0, 0.4, and 0.8 respectively.[1] The channel being modeled has a square cross section in the *y-z* plane (β=1).[2] In Fig. 3(*a*) no peristaltic wave is present (ϕ=0). The lines of the graph cross at (0,0) indicating that when the pressure drop is zero no flux is present. Negative values of Δp relate to favorable pressure drops, which induce flow in the positive direction. Alternatively, positive values of Δp describe gradients opposing the positive direction of flow. From Figs. 3(*b*) and 3(*c*) it can be observed that by introducing peristaltic pumping (increasing ϕ), the plots tend to shift upward toward positive values of Δp. With a value of ϕ=0.4 in Fig. 3(*b*), positive fluxes between 0 and 0.04 relate to positive pressure drops. By increasing the wave to a large amplitude of ϕ=0.8, we can see in Fig. 3(*c*) that all the flux values between 0 and 0.5 relate to positive pressure drops. Therefore, by increasing the ratio of the wave amplitude to the channel half height, we are further enabling the peristaltic wave to generate a positive flow against a larger undesirable (positive) pressure. It should be noted that the average flux values at zero pressure drop in Figs. 3(*b*) and 3(*c*) relate to flows generated solely from peristalsis.

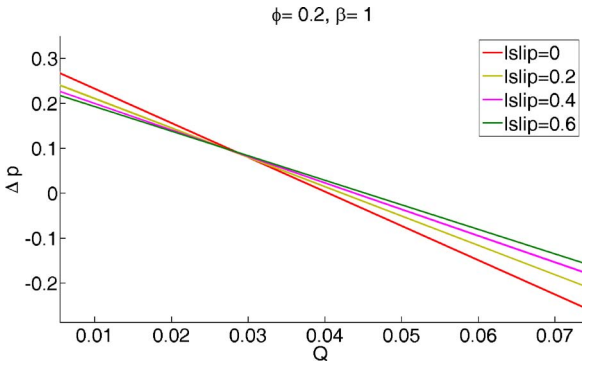

Fig. 4 A blow-up of the intercept for the solution ϕ=0.2 and β=1

With the inclusion of the slip in all three plots the lines on the plot form a fan. The lines tend to intersect in a region, which shifts upward with respect to Δp as ϕ is increased.

In Fig. 3(*a*) where no peristalsis is present, it is evident that the inclusion of a slip length at the boundary reduces the favorable pressure drop required to induce a particular average flux. This can be observed from the plot by the lines below (Δp=0). Similarly, the same is true for flow with an undesirable negative direction and a positive pressure drop shown by the lines above Δp =0.

With the inclusion of the peristaltic waves Figs. 3(*b*) and 3(*c*), one can observe that the average flux below Δp=0 is also induced by smaller pressure drops with an increasing slip length. The intersection of the lines tends to be above Δp=0.

Figure 4 presents a blow-up of a typical intersection for the solution ϕ=0.2 and β=1. The intercept is approximately at Δp =0.09. The lines to the right of the intercept above Δp=0 indicate that the increasing slip length allows for a stronger positive flow against higher opposing pressure gradients. However data to the left of the intercept show that the pump's ability to force fluid against a positive pressure gradient is reduced as the slip length increases. This is a consequence of the fluid's increased ability to flow backward with additional slip at the boundary. Therefore, attention must be paid to the effect on increased backflow when considering slip as a means of improving pumping.

[1] $\phi=b/a$, where b is the amplitude of the peristaltic wave and a is the height of the channel.

[2] $\beta=a/d$ where a is the height of the channel and d is half the width of the channel.

Acknowledgment

The authors wish to acknowledge financial support from the New Zealand Foundation for Research, Science and Technology via a grant held by the Polymer Electronics Research Centre at the University of Auckland.

References

[1] Fung, Y. C., and Yih, C. S., 1968, "Peristaltic Transport," ASME J. Appl. Mech., **35**, pp. 669–675.
[2] Shapiro, A. H., Jafferin, M. Y., and Weinberg, S. L., 1969, "Peristaltic Pumping With Long Wavelengths at Low Reynolds Number," J. Fluid Mech., **37**, pp. 799–825.
[3] Subba Reddy, M. V., Mishra, M., Sreenadh, S., and Rao Ramachandra, A., 2005, "Influence of Lateral Walls on Peristaltic Flow in a Rectangular Duct," ASME J. Fluids Eng., **127**, pp. 824–827.
[4] Leal, G. L., 2007, *Advanced Transport Phenomena: Fluid Mechanics and Convective Transport Processes*, Cambridge University Press, Cambridge.
[5] Chu, K.-H. W., and Fang, J., 2000, "Peristaltic Transport in a Slip Flow," Eur. Phys. J. B, **16**, pp. 543–547.
[6] Archer, R. A., and Mandviwalla, X., 2007, "CFD as a Design Tool for a Conducting Polymer Micropump," *Proceedings of the 16th Australasian Fluid Mechanics Conference*, Gold Coast, Australia.
[7] Dean, R. G., and Dalrymple, R. A., 1991, *Water Wave Mechanics for Engineers and Scientists*, World Scientific, Singapore.